

VOLCANIC ARCHITECTURE OF THE HOUNDÉ AND BOROMO GREENSTONE BELTS, WEST-AFRICA: IMPLICATIONS FOR TERRANE EVOLUTION

Gloria Awo Senyah
MPhil

Submitted in fulfilment of the requirements for the degree of
Doctor of Philosophy



School of Earth and Atmospheric Sciences
Faculty of Science
Queensland University of Technology
2021

Keywords

Basalt petrogenesis
Birimian greenstone belts
Lithostratigraphy
Paleoproterozoic crustal evolution
Tectonic setting
Titanite geochronology
Volcanic architecture
West African Craton

Abstract

The early Paleoproterozoic era represents a major time of change in Earth's geological history, including establishing distinct mantle reservoirs, widespread preservation of continental crust, many juvenile crust-forming events, as well as sustained oxygenation of the atmosphere. Despite the prominent changes within this timeframe, there are relatively few studies on the processes that led to these vital changes. In this study, the 2.35–2.1 Ga supracrustal rocks of the Houndé and Boromo greenstone belts of the West African craton are investigated to unravel their petrogenetic history and the geodynamic processes associated with their formation. These rock assemblages represent some of the best-preserved Paleoproterozoic units emplaced after extensive Archean crust-forming events. Detailed lithofacies analysis, geochemical, petrological, and geochronological data are employed to constrain the volcanic architecture and provide a new lithostratigraphic framework, magmatic history and age of these rocks.

The lithostratigraphy of the Houndé and Boromo belts have been divided into three sequences: (1) a Lower sequence composed of thick (> 5 km) subaqueous coherent mafic lavas and syn-volcanic intrusions, (2) an Upper sequence comprising subaqueous to emergent mafic-intermediate coherent lavas, associated intrusions and volcaniclastic rocks, and (3) a locally overlying epiclastic fluvialite Quartz-rich sedimentary association. The Lower sequence comprises laterally extensive mafic lava sheet flows, forming a large igneous province, whereas discrete composite volcanic systems characterise the Upper sequence. The Quartz-rich sedimentary association was deposited in a fault-bounded basin hosted within the Lower and Upper sequences in the Houndé belt. The volcanic stratigraphic architecture of the Lower and Upper sequences across both belts illustrates a non-layer cake stratigraphy with no unconformities. The boundary between these lithostratigraphic units has been truncated by crustal-scale faults and lithological discontinuities. Major and trace element whole-rock geochemical data of the least altered coherent rock samples (assessed for element mobility) were used to probe the magmatic history. The Lower sequence is characterised by moderately evolved high Fe-tholeiites with depleted light rare earth element (LREE), flat to nominally enriched-LREE Chondrite normalised patterns. Incompatible elements correlated with MgO and MELTS fractional

crystallisation modelling of the Lower sequence basalts is consistent with origins from ~40% late-stage fractionation of clinopyroxene and plagioclase of anhydrous parental magmas at relatively shallow depths. Key incompatible trace element ratios are consistent with a heterogeneous mantle-plume source with no indication of crustal contamination. All of these characteristics are most similar to ocean flood basalts. On the contrary, the Upper sequence is characterised by diverse tholeiitic and calc-alkaline rocks with predominately LREE-enriched and minor LREE depleted Chondrite-normalised signatures, exhibiting prominent Nb-Ta depletion relative to high field strength elements. These rocks evolved from fractional crystallisation of mainly plagioclase and minor clinopyroxene and assimilation fractional crystallisation of large-ion lithophile element (LILE)-enriched crustal component in relatively deeper magma chambers. The rocks of the Upper sequence originated from hydrous melting of a subduction-modified depleted mantle source, similar to volcanic island arcs. Whole-rock Sm-Nd isotopic data and in-situ LA-ICPMS U-Pb titanite ages, coupled with published ages, provide a constraint on the timing of development of the Lower and Upper sequence of both belts in four distinct stages: Stage 1- ~2350 Ma represents the onset of subaqueous mantle-plume related magmatism (Lower sequence); Stage 2- 2212–2160 Ma represents subduction-related magmatism in one or more island arc settings (Upper sequence); Stage 3- 2160–2124 Ma represents subduction driven accretion of Stage 1 and 2 lithological packages and E-W compressional deformation (D1), and Stage 4- post-2124 Ma represents the uplift and erosion of granitic bodies and fluvial deposition of the Quartz-rich sedimentary association into fault-bounded basins.

This research supports an allochthonous accretion of the Lower sequences juxtaposed with the island arc terranes of the Upper sequences of Houndé and Boromo belts, implying a geodynamic evolution analogous to that of modern accretionary orogens. Both belts display comparable lithostratigraphy, tectonic setting and ages, implying similar geological history. Lower sequence basalts were formed by co-existing primitive, depleted and enriched mantle source reservoirs, indicating well-established mantle heterogeneity by the Paleoproterozoic era.

Table of Contents

Keywords	i
Abstract	ii
Table of Contents	iv
List of Figures	vi
List of Tables	xv
List of Abbreviations.....	xvi
Statement of Original Authorship.....	xvii
Acknowledgements	xviii
Chapter 1: Introduction	1
1.1 Background.....	1
1.2 What is a greenstone belt?.....	2
1.3 Greenstone belts and their implications on the geodynamic evolution of the Precambrian eon.....	8
Chapter 2: Geological setting of the Paleoproterozoic Birimian domain of the West African Craton.....	11
2.1 Overview of the West African Craton	11
2.2 Geological setting of the Birimian domain.....	13
2.3 Geological setting of the Houndé and Boromo greenstone belts, Southwest Burkina Faso	23
2.4 Research Problems.....	28
Chapter 3: Lithostratigraphy of the Houndé and Boromo greenstone belts	30
3.1 Introduction.....	30
3.2 Methodology	31
3.3 Results.....	34
3.4 Conclusions.....	72
Chapter 4: Whole-rock geochemistry	75
4.1 Introduction.....	75
4.2 Methodology	76
4.3 Results.....	80
4.4 Petrogenesis	111
4.5 Conclusions.....	134
Chapter 5: Age constraints on the Eburnean tectonothermal event in the Houndé and Boromo belts	136
5.1 Introduction.....	136
5.2 Methodology	138

5.3	Results	139
5.4	Discussion.....	148
5.5	Conclusion	150
Chapter 6: Geological synthesis and Conclusions.....		151
6.1	Reconstruction of the development of the Houndé and Boromo greenstone belts	151
6.2	Autochthonous vs Allochthonous origin.....	161
6.3	Implications of the Paleoproterozoic evolution of the Houndé and Boromo belts	163
6.4	Conclusions	166
Bibliography		168
Appendices		197
Appendix A : Chapter 3		197
Appendix B : Chapter 4.....		204
Appendix C : Chapter 5.....		234

List of Figures

- Figure 1-1 Global distribution of cratons, shields and orogens (Furnes et al., 2015). Greenstone belts are situated in cratons and shields which occupies a vast coverage of the continents and are typically bordered by Phanerozoic assemblages.....4
- Figure 1-2 Generalised lithostratigraphic subdivisions of Precambrian greenstone belts illustrating principal lithological assemblages. Modified after Anhaeusser et al. (1969); Anhaeusser (2014).5
- Figure 2-1 Geology of the Man-Leo shield of the southern West African Craton (WAC) showing the Archean Kénéma-Man domain and Paleoproterozoic Baoulé-Mossi domain, Kayes and Kédougou-Kéniéba inliers (KKI) adapted from Boher et al. (1992); Kouamelan et al. (1997); Milési et al. (2004). Inset map shows map location with reference to continental Africa (above) and the WAC boundary showing the Reguibat shield in the north and Man-Leo Shield in the south (below). Abbreviation of major structures: Sassandra Fault (SF), Grenville-Ferkessedougou-Bobo-Dialoussو fault (GFBF), Ouango-Fitini (OF), Markoye shear zone (MSZ) and Pan-African suture zone (PA). Abbreviation of greenstone belts and sedimentary basins: Houndé (HO), Boromo (BO), Banfora (BA), Lawra (LW), Goren (GO), Bui (BU), Ashanti (AS), Sefwi (SW), Haute Comoé basin (HC), and Kibi-Winneba (KW).....13
- Figure 2-2 Summary chart of some published geochronological data for emplacement ages and metamorphic ages in the Birimian domain modified after Pouclet et al. (2006); Lebrun et al. (2016). Each country column represents the location where samples were obtained. Geochronological data sources are presented in Table 2.1. Note: the majority of the age data was obtained from intrusive rocks with only a few emplacement ages for volcanic rocks.18
- Figure 2-3 Geological map of the Houndé and Boromo greenstone belts, SW Burkina Faso showing the distribution of rock types and some published radiometric ages. Modified after BGRM SIGAfrique (Milési et al., 2004). Geochronological data sources are presented in Table 2-3.26
- Figure 2-4 Simplified lithostratigraphy sections of the Houndé and Boromo belts of western Burkina Faso. Adapted from Baratoux et al. (2011). TH- tholeiitic mafic units, THM- tholeiitic megacrystic basalts, TRAN- transitional mafic and intermediate volcanic sequences, CA- calc-alkaline volcanic sequences.....27
- Figure 3-1 Simplified geological map of the Houndé and Boromo greenstone belts showing outcrop locations visited during this study and field transects. Inset showing study area location within the West African Craton. Map (including inset) modified from Milési et al. (2004). Map data source Chorlton (2007).....32

Figure 3-2 Pie charts illustrating the percentage abundances of mineral phases obtained from XRD analyses of selected lithologies from both belts. The results of the XRD analysis are presented in Appendix A Table A- 2.	40
Figure 3-3 Photographs of A) Drill core showing at least 20 meters of massive aphyric basalt. B) Cross-section of well-preserved pillow aphyric basalt showing rounded pillow tops, eastward facing direction (408564, 1208185). C) Strongly foliated massive aphyric basalt intruded by unfoliated quartz-feldspar porphyritic dacite D) Massive plagioclase-porphyritic basalt (442536, 1115143).	41
Figure 3-4 Field photographs of A) Crystal-rich (~70%) massive feldspar megacrystic basalt showing plagioclase macrocrysts (~7cm) in fine-grained mafic groundmass (479149, 1142288). B) Crystal-poor massive feldspar megacrystic basalt transitioning into a massive aphyric basalt (492534, 1140459). Red circle showing feldspar macrocrysts. C) Massive pyroxene-porphyritic basalt showing the characteristic blocky pyroxenes contained in pale-green fine-grained groundmass (477203, 1228672). D) Massive gabbro showing coarse-grained texture (480737, 1233035). E) Massive hornblende-plagioclase porphyritic andesite showing ~5mm euhedral relict plagioclase crystals and ~3mm hornblende crystal. An arrow pointing to plagioclase glomerocrysts (452512, 1219633). F) Massive quartz-feldspar porphyritic dacite. Red circle showing quartz crystal (450423, 1234344).	42
Figure 3-5 Crossed-polarised light thin-section microphotographs of A) Sparsely distributed tabular gray plagioclase microphenocrysts in a fine-grained groundmass of aphyric massive basalt. The second interference coloured mineral is epidote (450352, 1228077). B) Calcite-filled amygdules in aphyric pillow basalt (438773, 1204815). C) Mosaic image of feldspar megacrystic basalt showing sericite-altered feldspar macrocryst contained in a fine-grained groundmass. D) Plagioclase-porphyritic basalt contained in an altered groundmass. E) Pyroxene-porphyritic basalt showing prismatic pyroxene and plagioclase glomerocrysts contained in fine-grained groundmass (416765, 1203940). F) Plane polarised image of E) highlighting resorbed crystal boundary of glomerocryst.	43
Figure 3-6 Thin-section microphotographs of A) Plane & B) crossed polarised light images of typical equigranular gabbro made up of plagioclase (tabular grey) and pyroxene converted to chlorite (anhedral first-order interference colours (478715, 1235136)). C) Plane & D) crossed polarised light images of gabbro showing sector zoning in pyroxene in center of the image (480737, 1233035) E) Plane & F) Crossed polarised images of dolerite with acicular actinolite crystals poikilitically enclosed by plagioclase (463438, 1215053)	44
Figure 3-7 Thin-section photomicrograph of A) Crossed polarised image of Hornblende-plagioclase porphyritic andesite showing zoned hornblende phenocryst contained in a siliceous microcrystalline groundmass. B) Plane polarised light image of A) highlighting	

abundant opaque mineral in the groundmass. C) Plane polarised image of quartz-feldspar porphyritic dacite showing euhedral resorbed quartz phenocryst and altered plagioclase phenocrysts in fine-grained sericitised groundmass (450423, 1234344). D) Crossed polarised image of altered plagioclase phenocryst and quartz phenocrysts exhibiting embayment in quartz-feldspar porphyritic dacite 45

Figure 3-8 Classical Bouma Sequence showing the subdivisions of a complete turbiditic sequence by Bouma (1962). The planar bedded mudstone-siltstone represent (Td & Te) subdivision and the massive-graded (Ta). Image obtained from Shanmugam (1997)..... 47

Figure 3-9 (A) Drill core of thick (~15m) succession of planar bedded mudstone-siltstone lithofacies (CHDD0007- 409915, 1222184). (B). Section of drill core showing graded siltstone interval (~5 cm) (C) Drill core of wavy planar-bedded tuff showing poorly defined bedding. D) Close-up outcrop photograph of C) showing low-angle cross-beds (red arrow) bound by planar beds (494802, 1088212). E) Outcrop photo of massive tuff-lapilli sandstone pointing to feldspar-porphyritic clast, feldspar crystals, and fine-grained matrix (499706, 1141971). F) Diffuse bedding is seen in massive tuff-lapilli sandstone..... 49

Figure 3-10 Plane-polarised photomicrographs of massive tuff-lapilli sandstone. A) Crystal-poor subfacies with fine-grained matrix (409915, 1222184). B) Crystal-rich subfacies showing feldspar-porphyritic fragments and abundant feldspar framework crystals. Plag = plagioclase (498686, 1131147). Blue outline=amygdaloidal aphyric basalt; red outline= feldspar-porphyritic basalt. Note: the absence of quartz..... 50

Figure 3-11 A) Outcrop photo of massive monomictic breccia showing large (>7 cm) of pyroxene-porphyritic basalt (417284, 1236194). B) Outcrop photo of graded monomictic breccia showing angular to cuspatate-shaped, grey, and holohyaline volcanic fragments of various sizes (1 cm to > 10cm). C) Drill core photo of B) monomictic breccia showing the base of succession (Red bar) truncating wavy to planar-bedded tuff lithofacies. D) Outcrop photo of graded polymictic conglomerate showing an interval of well-sorted lithic fragments and abundant intermediate volcanic clasts. E) Drill core of graded polymictic conglomerate showing the thickness (~ 5m) of beds (CHDD00007 409915, 1222184)..... 53

Figure 3-12 Outcrop photographs of massive polymictic conglomerates lithofacies. A) & B) Show a variety of matrix-supported surrounded to rounded lithic clasts comprising dominantly of plagioclase-porphyritic lithofacies and rare chert (Red circle) in medium to a fine-grained matrix (499706,1141971) (442994,1228410). 54

Figure 3-13 A) high-angle cross-bedding in quartz-rich sandstone (west-facing) (446432, 1228123). B) Thin (< 1cm) planar bedding in quartz-rich sandstone with bedding defined by dark bands of heavy minerals. C) Diffusely bedded pebbly sandstone. Outlined in red are mudstone rip-up clasts, which form less than 5% of lithic fragments. D) Poorly-sorted matrix-supported conglomerate. E) & F) Crossed-polarised and

Plane-polarised photomicrographs of quartz-rich sandstone lithofacies showing abundant (>70%) polycrystalline quartz and micaceous matrix.....	56
Figure 3-14 Equal area stereographic projections of field structural measurements plotted for A) LFA-1 and B) LFA-2 of the Houndé and Boromo belts showing the general orientation of bedding and foliation. B) LFA-2 of the Houndé and Boromo belts showing the general orientation of bedding and foliations	63
Figure 3-15 A) Sharp contact between coherent pyroxene-porphritic basalt and planar bedded mudstone-siltstone. B) Peperitic contact between quartz-feldspar porphyritic dacite lithofacies and unconsolidated planar bedded mudstone-siltstone in CHDD00010 (413318, 1210000).....	64
Figure 3-16 Local geology of study area-Map A (location in inset) with outcrop sites, field transects, structural measurements and stratigraphic sections (HE-1-4) reconstructed from field transects. Coordinate system- WGS 84 UTM zone 30N. Total magnetic intensity map courtesy Gryphon Minerals.....	66
Figure 3-17 Local geology of study area-Map B (location in inset) with outcrop site, field transects, structural measurements and stratigraphic sections (HE-5 & 6) reconstructed from field transects. Coordinate system- WGS 84 UTM zone 30N	67
Figure 3-18 Local geology of study area-Map C (location in inset) with outcrop sites, field transects, drill cores (CHDD0007 and CHDD00010), structural measurements and stratigraphic sections (HW-7 & 8) reconstructed from field transects. Coordinate system- WGS 84 UTM zone 30N. Regional vertical derivative aeromagnetic map from WAXI database 2016.....	68
Figure 3-19 Local geology of study area-Map D (location in inset) with field transects, structural measurements and stratigraphic sections (BO-1-3) reconstructed from field transects. Coordinate system- WGS 84 UTM zone 30N. Regional radiometric map from WAXI database 2016.....	69
Figure 3-20 Local geology of study area-Map E (location in inset) with outcrop sites, field transects, structural measurements and stratigraphic sections (BO-4 & 5) reconstructed from field transects. Coordinate system- WGS 84 UTM zone 30N. Aeromagnetic map from Volta Resources website http://www.voltaresources.com/s/Gaoua.asp	70
Figure 3-21 Local geology of study area-Map F (location in inset) with outcrop sites, field transects, drill core (KRND416), structural measurements, and stratigraphic sections (BO-6) reconstructed from field transects. Coordinate system- WGS 84 UTM zone 30N. Aeromagnetic map from Centamin website https://www.centamin.com/exploration/burkina-faso/regional-geology).	71
Figure 3-22 Summary figure of the stratigraphic architecture of the lithofacies associations of the Houndé and Boromo belts. The general stratigraphy is subdivided into Lower and Upper volcanic sequences	

depicting two major volcanic cycles. Legend is the same as Figure 3-21.	74
Figure 4-1 Plot of relative concentrations of zirconium (Zr) and hafnium (Hf) from LA-ICPMS and acid digestions ICPMS methods (denominator value). Values close to the 1:1 line depict a good correlation between both analytical measurements. Values plotting above and below 0.8 ratio show LA-ICPMS methods generally have significantly higher and lower zirconium and hafnium concentrations, respectively.	78
Figure 4-2 Weathering index ternary plots for igneous rocks after Ohta and Arai (2007). (A) corresponds to coherent volcanic lithofacies of the Lower Sequence and Upper sequence and (B) plots for the intrusive lithofacies (Gabbro and Dolerite). Dash lines represent weathering profiles, and the solid line shows the trend of fresh igneous rocks: M-fresh mafic rocks, F-fresh felsic rocks, W-weathered igneous rock. The majority of the rocks fall along the fresh igneous rock trend.	86
Figure 4-3 Isocon diagram of altered and unaltered compositions from Lower volcanic Sequence of the Boromo and Houndé belts following element mobility method of Grant (1986), (2005). Altered and unaltered compositions were selected based on LOI. Line of best fit isocon defined by pre-selected immobile elements (solid green line). 1:1 isocon line (grey broken line). The analyses were achieved using the MS Excel worksheet designed by López-Moro (2012). Oxides/elements above the isocon line have gained while those below have lost abundance. Oxides and elements concentrations have been scaled to fit the plots following López-Moro (2012). Inserts have higher relative abundances compared to the majority of the oxides and elements.....	87
Figure 4-4 Plot of La/Sm against Gd/Yb Chondrite normalised ratios illustrating the range and variation of the four recognised geochemical groups within the study area. Top panel illustrates variations in the Lower sequence while bottom panel shows that of the Upper sequence for both belts. Three outlier samples with $(La/Sm)_N > 3$ have been omitted from the plot.....	94
Figure 4-5 Primitive Mantle-normalised multi-element diagrams for rocks of the Lower volcanic sequence of the Houndé and Boromo belts showing the three distinct geochemical groups. Note: Pronounced negative Nb-Ta and Ti anomalies in some of the Group 1L rocks. No Group 4 signatures belong to the Lower sequence Normalising values from Sun and McDonough (1989).	95
Figure 4-6 Primitive Mantle-normalised multi-element diagrams of rocks of the Upper volcanic sequence of the Houndé and Boromo belts exhibit three distinct geochemical groups. Note: pronounced negative Nb-Ta and Ti anomalies in rocks of Group 1 and Group 4. No Group 2 signatures were sampled in the Upper sequence. Normalising values from Sun and McDonough (1989). Note change in scale on the y-axis from Figure 4-5.	96

Figure 4-7 Primitive Mantle-normalised multi-element diagrams for the Intrusive units of the Houndé and Boromo belts. The gabbros and dolerites exhibit all four distinct geochemical groups. Note: pronounced negative Nb-Ta and Ti anomalies in some rocks of Group 1 and all Group 4. Normalising values from Sun and McDonough (1989).....	97
Figure 4-8 Geochemical classification diagrams of Jensen (1976) showing the diversity of rock types in the (A) Lower volcanic sequence; High-Fe tholeiites, (B) Upper volcanic sequence; minor high-Mg and high-Fe tholeiites and calc-alkaline. Legend below.....	98
Figure 4-9 Th-TiO ₂ classification for rocks of the (A) lower volcanic sequence, (B) Upper volcanic sequence, (C) Gabbros and dolerites of both belts illustrating the abundance of Th relative to TiO ₂ . Plot demarcations follow Barnes et al. (2012); Hayman, Thébaud, et al. (2015) where Low-Th= Th/TiO ₂ < 0.75; High-Th= Th/TiO ₂ > 1.5. Rocks of the Lower sequence consistently have Low Th-TiO ₂ ratios while the Upper sequence is intermediate to high-Th compositions. Symbol legend same as Figure 4-8.....	100
Figure 4-10 Box and whisker plots, showing the range of magnesium numbers (Mg#) for the rocks of the Lower, Upper sequences and the gabbro-dolerite lithofacies. The top and bottom of whiskers represent minimum and maximum values in each subset; the black line is the median value, and the black dot is the mean value. Details of the box and whisker plots are presented in Appendix B Table A-16.	101
Figure 4-11 Binary plots of selected major elements against MgO for the volcanic rocks showing variation. Two pyroxene-porphyritic basalt samples from the UVS with MgO ~15 wt. % have been omitted to deskew the plot. All gabbros and dolerites have been omitted to enhance comparison between volcanic rocks only.	102
Figure 4-12 Binary plots of selected trace elements against MgO for the volcanic rocks showing variation. Intrusive rocks have excluded to deskew the plots.....	103
Figure 4-13 ¹⁴³ Nd/ ¹⁴⁴ Nd vs ¹⁴⁷ Sm/ ¹⁴⁴ Nd pseudo-isochron plots of Lower sequence rocks (A) Select samples from the Boromo belt yielding an age of 2369 ± 76 Ma (MSWD = 2.3) (B) Select samples from the Houndé belt yielding an age of 2313 ± 34 Ma (MSWD = 16). Error margins are 2 sigma standard deviation and expressed by the outline of ellipses. Grey boundaries around the regression line are the error on the isochron. Age calculation was done using the online version of IsoplotR by Vermeesch (2018).	107
Figure 4-14 Summary of the spatial distribution of geochemical groups within the Houndé and Boromo belts. For the Lower sequence, Group 3L dominates the Houndé belt and is underlain by Group 2L in the south. In contrast, Group 2L dominates the Boromo belt and in places overlain by Group 1L with the south similar to the southern Houndé succession. In the Upper sequence of both belts, Group 4U dominates	

and is underlain by Group 1U. In the southern part of the Houndé belt, Group 3U of the Upper sequence dominates. 110

Figure 4-15 Fractional crystallisation modelling results for key major elements.

Liquid lines of descent generated at varying pressures and initial H₂O content of starting composition at constant *fO*₂ indicated by Model 1 to Model 4. The models are compared to Group 1L to Group 3L of the Lower volcanic sequence. Markers indicate 10% increments of fractionation. Model 1: 1 kbar anhydrous magma condition Model 2: 5 kbar anhydrous magma condition Model 3: 1 kbar hydrous magma condition (1% H₂O in starting composition) Model 4: 5 kbar hydrous magma condition (1% H₂O in starting composition) 119

Figure 4-16 Fractional crystallisation modelling results for key major elements.

Liquid lines of descent generated at varying pressures and initial H₂O content of starting composition at constant *fO*₂ indicated by Model 1 to Model 4. The models are compared to Group 1U, Group 3U and Group 4U of the Upper volcanic sequence. Group 1 has too few samples to define a geochemical trend. Markers indicate 10% increments of fractionation. 120

Figure 4-17 Plots of cumulative crystal proportions against the temperature of

best-fit MELTS simulated fractional crystallisation models for Groups 1L, 2L & 3L (A, B & C, D) of the Lower sequence and Groups 3U and 4U (E & F) of the Upper sequence. Note: Group 3L of the Lower sequence fits Model 1 and Model 2 fractional crystallisation hence two diagrams. Also, Group 1L of the Upper sequence could not be matched with any model due to a lack of trend. Starting temperatures are calculated liquidus temperature of the parental magma. Crystal label: Cpx-clinopyroxene, Plag-plagioclase..... 121

Figure 4-18 Primitive mantle normalised trace element diagrams for Group 1L,

2L, and 3L of the Lower sequence showing calculated liquid line of descent of best fit MELTS generated, fractional crystallisation models. Markers represent 10% incremental crystal fractionation. Note: Ti was not modelled due to a lack of reliable input parameters. 122

Figure 4-19 Primitive mantle normalised trace element diagrams for Group 3U

and 4U of the Upper sequence showing calculated liquid line of descent of best fit MELTS generated fractional and assimilation fractional crystallisation models. Markers represent 10% incremental crystal fractionation. Group 4U was modelled by assimilation of a ratio of r=0.2 of the Upper continental crust (Rudnick & Gao, 2014)..... 123

Figure 4-20 Th/Yb against Nb/Yb vector diagram showing the trajectory of

calculated fractional crystallisation based on the most primitive composition (parental magma composition) of each geochemical group. The fractional crystallisation pathways of each group demonstrate that it is unlikely to produce the geochemical variation of one group from another through crystal fractionation. Markers represent 10% fractionation of variable proportions of olivine, clinopyroxene, and plagioclase (see Figure 4-17 for the relative abundance of mineral assemblage). UCC= Upper continental crust by Rudnick and Gao (2014). 124

- Figure 4-21 Incompatible trace element ratio plots of all geochemical groups in the study illustrating the trace element characteristics of the mantle source from which the rocks were derived characteristics. (A) La/Yb against Th/Ta plot after Condie (1994). Top panel: Samples of the Lower sequence with Groups 2L and 3L & 3U plotting along the PM-Enriched source hypothetical mixing line while Group 1 plots near the PM-DMM source composition. Bottom panels are samples of the Upper sequence with Group 4U plotting along the Arc mantle-UCC line with high Th-Ta ratios indicative of crustal contamination or subduction zone enrichment. Group 3L & 3U plots near the E-MORB composition and trend towards the Arc mantle composition while Group 1 plots on the PM-DMM line indicating a moderately depleted mantle source compared to modern DMM. 130
- Figure 4-22 ϵ Nd against (A) Time showing the variation of Nd-isotopic ratios with time and (B) La/Nb illustrating mantle source signatures for the select Nd-isotope analysed samples of Group 1-3 of the Lower sequence and Group 4 of the Upper sequence. La/Nb > 1.4 signifies crustal contamination of mantle source. CHUR- Chondritic uniform Earth and Depleted mantle evolution line after DePaolo et al. (1991). 133
- Figure 5-1 Plane polarised light image of (A) GS_030 of the hornblende-plagioclase porphyritic andesite lithofacies from the Houndé belt and (B) Gs_041 Gabbro from the Boromo belt. Representative reflected light image (C) and (D), and SEM BSE (E) and (F) images showing texture and mineral inter-relationship of titanite in samples Gs_030 and Gs_041, respectively. The titanites form reaction rims around the primary titanium-bearing minerals ilmenite and hornblende as well as inclusion. Hbl-hornblende, CPx-clinopyroxene, Pl-plagioclase, Ttn-Titanite, ilm- Ilmenite. 141
- Figure 5-2 Th/U against U plot for spot analysis of sample Gs_030 and Gs_041 showing a relatively lower concentration of U in Gs_041 compared to Gs_030. Th/U ratios are consistent with that for metamorphic titanites (0.05–10) for the given U concentrations, according to Olierook et al. (2019). 147
- Figure 5-3 U–Pb ages of titanite in (A) Gs_030; hornblende-plagioclase porphyritic andesite from Houndé belts and (B) Gs_041-gabbro from Boromo belt. Left column: Tera-Wasserburg Concordia (A) and (B) Concordia diagrams showing spot analyses of LA-ICPMS; the error of ellipses are 2σ . (C) $^{206}\text{Pb}/^{238}\text{U}$ weighted mean ages; the error bars are 2σ . Diagrams and age calculations achieved using IsoplotR software by Vermeesch (2018). 148
- Figure 6-1 Schematic representation of the geodynamic evolution of the Paleoproterozoic Houndé and Boromo greenstone belts in sequential order; Ocean Plateau Stage: Emplacement of abundant tholeiitic flood basalt assemblages of the Lower sequence onto an oceanic crust with magma production by a mantle plume. Island Arc building Stage: Tholeiitic and calc-alkaline subduction-related magmatism in an island arc setting (Upper sequence). 159

Figure 6-2 Schematic representation of the tectonic evolution of the Caribbean-Colombian Cretaceous igneous province according to White et al. (1999). Here, the Caribbean plateau is rimmed by volcanic arc terranes in a complex subduction accretion setting, similar to the geodynamic model proposed for the Houndé and Boromo belts in this study. 162

List of Tables

Table 1-1 Summary of evidence for autochthonous and allochthonous models of greenstone formation and crustal growth.	7
Table 2-1 Compilation of published magmatic and metamorphic ages across portions of the WAC presenting rock type, methods and references used in Figure 2-2	19
Table 2-2 Summary of evidence for tectonic models of the Birimian Supergroup	22
Table 2-3 List of radiometric age data displayed in Figure 2-3	27
Table 3-1 Summary of the lithofacies associations and interpretation of the paleodepositional environmental present in the Houndé and Boromo belts.....	61
Table 4-1 Major and trace element geochemical data of representative samples of the Houndé belt. Values are normalised to 100%.	82
Table 4-2 Major and trace element geochemical data of representative samples of the Boromo belt. Values are normalised to 100%.....	84
Table 4-3 Key geochemical characteristics of the Lower and Upper volcanic Sequence and associated Intrusive lithofacies.	104
Table 4-4 Whole-rock Sm-Nd isotope data of selected samples from the Lower (LVS), Upper volcanic sequences (UVS), and intrusive lithofacies of the Houndé and Boromo belts.	106
Table 5-1 U-Pb isotopic data of titanite spot analyses from GS_030	142
Table 5-2 U-Pb isotopic data of titanite spot analyses from GS_041	145

List of Abbreviations

AFC	Assimilation Fractional Crystallisation
ALS	Australian Laboratory Services
BABB	Back Arc Basin Basalt
BSE	Back Scatter Electron
CAMP	Central Atlantic Magmatic Province
CFB	Continental flood Basalt
CHUR	Chondritic Uniform Reservoir
CRM	Certified Reference Material
DMM	Depleted MORB Mantle
EDS	Energy Dispersive Spectroscopy
EM	Enriched Mantle
GPS	Geographical Positioning System
HFSE	High Field Strength Element
HIMU	High μ (U/Pb)
HREE	Heavy Rare Earth Elements
IAB	Island Arc Basalt
ICPMS	Inductively Coupled Mass Spectrometer
LILE	Large Ion Lithophile Element
LLD	Liquid Line of Descent
LOI	Loss on Ignition
LREE	Light Rare Earth Element
MORB	Mid Ocean Ridge Basalt
MREE	Middle Rare Earth Element
MSWD	Mean Standard Weighted Deviation
OIB	Ocean Island Basalt
PM	Primitive Mantle
QFM	Quartz Fayalite Magnetite
REE	Rare Earth Element
RSC	Recycled Subduction Component
SDC	Subduction-derived Component
SEM	Scanning Electron Microscope
TTG	Tonalite Trondhjemite Granite
UCC	Upper Continental Crust
UTM	Universal Transverse Mercator
WAC	West African Craton
WAXI	West African Exploration Initiative
WGS	World Geographic System
XRD	X-ray Diffraction
XRF	X-ray Florescence

Statement of Original Authorship

The work contained in this thesis has not been previously submitted to meet requirements for an award at this or any other higher education institution. To the best of my knowledge and belief, the thesis contains no material previously published or written by another person except where due reference is made.

Signature: [QUT Verified Signature](#)

Date: 28/10/2021

Acknowledgements

The journey to completing this thesis has been long and winding, filled with some ups and downs. During the lowest moments, this biblical scripture kept me motivated: “I can do all things through Christ who strengthens me.” Philippians 4:13 NKJV.

I express sincere appreciation to my supervisors, Dr Patrick Hayman and Prof David Gust, for their guidance, advice, encouragement throughout the PhD journey and critically reviewing and proofreading this thesis. I particularly appreciate Dr Patrick Hayman for granting me the opportunity to be part of this research project and for giving me the necessary training required to attain the objectives of this research. I want to greatly thank Dr David Murphy for mentoring in Titanite petrography and in-situ geochronology, although not officially my supervisor. Prof Balz Kamber and Trinity College, Dublin, are thanked greatly for freely analysing 30 samples as quality control on the geochemical data obtained at QUT. I appreciate Charlotte Allen and Christoph Schrank for insightful discussions about different aspects of this research.

I am grateful for financial support towards tuition and cost of living through the QUT Postgraduate Research Award (QUTPRA). Funding for the research through the West African Exploration Initiative (WAXI) is much appreciated. I thank the sponsors and coordinators of the WAXI project for liaising with the appropriate institutions (i.e., IRD and the University of Ouagadougou) in Burkina Faso to make the fieldwork possible. I thank Pascal Ouiya, Diarra Ahmed and Mr Daouda for their assistance with fieldwork at various times. I acknowledge the QUT EAS and CARF technical staff for assistance at various analytical techniques, especially Karine Moromizato, Dr Sunny Hu, Gus Luthje, Dr Sam Ghidan, Will Stearman, Fiona Kallus, Dr Sanjleena Singh, and Donald McAuley. I thank the Isotopia Lab at Monash University for Sm-Nd analysis.

Finally, I am grateful for the support of my family, especially Prof Jonathan Opata. I wouldn’t have progressed without your constant prayers and encouragement. I thank my friends, EAS HDR colleagues (2016-2020 cohort), and church family for making this journey much bearable.

Chapter 1: Introduction

1.1 BACKGROUND

The Earth's outermost layer comprises two dramatically contrasting layers, the continental and the oceanic crust. The continental crust is approximately 40 km thick and averagely andesitic in composition (e.g., Taylor and McLennan, 1985, Rudnick and Gao, 2003, Arculus, 2006). The oldest preserved continental crust is the ~ 4.0 (billion years ago) Ga Acasta Gneiss complex of the Slave Craton in Canada (Reimink et al., 2016). The oceanic crust, on the other hand, is relatively thinner (~7km), predominantly basaltic (mafic) and young (< 200 million years ago-Ma) (Rudnick and Gao, 2003). Despite vast knowledge of the current physical and chemical properties of the crust (i.e., chemical composition, age, rheology etc.), there are indications that the Earth has undergone many changes since its inception leading to the evolution of the lithosphere, mantle, atmosphere, and hydrosphere.

A compilation of radiometric ages suggests at least 60-70% of the presently preserved continental crust had been generated by 3.0 Ga (Cawood et al., 2013; Hawkesworth et al., 2013). The oldest continental crust probably evolved from the melting of the early Earth's mafic outer shell (Smithies et al., 2021). Through time, there appears to be a progressive slow-down in the production of juvenile continental crust attributed to changes in the Earth's geodynamic processes through time (e.g. Condie et al., 2011; Arndt & Davaille, 2013). But because of the poor preservation and scarcity of geologically ancient rocks, the geodynamic processes that contributed to the formation and evolution of the continental crusts through time is poorly understood.

It is also widely accepted that the state of the mantle, which is the solid-molten layer below the crust, has evolved through time from a Chondritic composition to a more heterogeneous nature (Patchett et al., 1982; Ogg et al., 2016; Korenaga, 2018). The state of the mantle today has been investigated in many studies using various techniques, including geochemical variations in ocean basalts. From these studies, many distinct mantle reservoirs (e.g. Primitive mantle, Depleted mantle, Enriched

mantle) from which the various ocean basalt types are derived have been recognised (Hofmann, 1997; Stracke et al., 2005). However, the origin of the mantle heterogeneity is much debated due to the lack of well-preserved uncontaminated mantle-derived rocks to provide direct evidence of mantle evolution through time. Some studies have found a correlation between the onset of global-scale subduction and the origin of mantle heterogeneities. This is depicted by an increase in the proportion of large ion lithophile elements (LILE) in mantle-derived basalts between 3.2–2.7 Ga (Campbell & Griffiths, 1993; Cagnard et al., 2011; Condie et al., 2016; Condie & Shearer, 2017; Ganne & Feng, 2017; Gamal El Dien et al., 2020). These researchers assert that the global establishment of subduction regime is responsible for the re-introduction and redistribution (via mantle convection) of LILE back into the mantle. In contrast, Bédard (2017) argues that only until the end of Archean (i.e. 2.5 Ga) was modern-style plate tectonics established and suggests the early Earth was characterised by punctuated mantle overturn events which led to extensive crustal growth and periodic homogenisation of the mantle followed by episodic stagnant-lid intervals (~300–500 my). If this is the case, then the enriched mantle reservoirs recognised in modern basalts could not have persisted in the pre-Proterozoic era.

Therefore, the origin of distinct mantle reservoirs, crustal growth and preservation and the onset of modern-style plate tectonics appears to be interrelated but, albeit poorly understood. Some of the questions which remain unresolved include the geological mechanisms associated with the growth of the continental crust in the early Earth and the influence of plate tectonics on its rate of formation and preservation (van Hunen et al., 2008; Hawkesworth et al., 2013; Hawkesworth et al., 2018). Therefore, to fully understand the geological evolution of the solid Earth and its mantle, it is prudent to investigate rocks of the early Earth that are today preserved as greenstone belts in stable continental fragments known as craton/shields (Figure 1-1).

1.2 WHAT IS A GREENSTONE BELT?

Some of the oldest rocks on Earth are preserved in tectonically stable parts of the continental crust known as cratons and shields (Figure 1-1). These regions are made up of Archean and Proterozoic in granite-greenstone terranes characterised by curvilinear to variably shaped, spatially and temporally related volcano-sedimentary and intrusive rock assemblages (de Wit & Ashwal, 1995; de Wit, 2004; Furnes et al., 2015). Thurston (2002) defines greenstone belts as stratified lithological assemblages

deposited in a common setting within a discrete-time frame. The term 'greenstone' is coined from the green colouration imparted on the rocks due to greenschist metamorphic minerals such as chlorite, actinolite and epidote (Vearncombe et al., 1986; de Wit, 2004). Commonly, a high length to breadth aspect ratio gives greenstones belts a regional-scale linear appearance (Grachev & Fedorovsky, 1981), hence the term 'belt'. Greenstone belts vary in sizes, from small, Isua Greenland-75 km², to large Lapland-50,000 km² (Furnes et al., 2015).

There are more than 250 recognised greenstone belts worldwide of diverse dimensions and ages (Furnes et al., 2015). Typically, greenstone belts share common similarities in their volcano-sedimentary successions, structure and metamorphism aside from local variations (Anhaeusser et al., 1969; Grachev & Fedorovsky, 1981). The typical stratigraphy of greenstone belts comprises a lower ultramafic group, a middle greenstone group (tholeiitic basalts, minor ultramafic rocks, andesites, intermediate-felsic volcanic, volcaniclastic rocks and chert), overlain by an upper sedimentary group (pelitic, psammitic and coarse clastic rocks) (Anhaeusser, 2014) (detail in Figure 1-2). Basalts are the dominant constituents of most greenstone belts (e.g., Kalgoorlie Terrane (Swager, 1997); Superior Province (Polat & Kerrich, 2001); Barberton Greenstone Belt Furnes et al. (2013); Birimian Supergroup (Sylvester & Attoh, 1992)). The true stratigraphic thicknesses of greenstone belts are difficult to determine due to complex structural deformation and extensive erosion. According to Condie (1994), the mafic assemblages of most Archean greenstone belts are thicker, have a higher proportion of basalt-komatiites and a higher ratio of lava flow to fragmental assemblages compared to Proterozoic greenstone.

Greenschist facies metamorphism is prevalent in most greenstone belts. However, metamorphic grades from granulite through amphibolite to prehnite-pumpellyite have been reported in many places (Anhaeusser, 2014). Greenstone belts are often intruded by granitic rocks and exhibit contact metamorphic aureoles. Studies have highlighted many structural styles characteristic of greenstone domains. The structural style of greenstone belts differs from place to place, with most Archean granite-greenstone terranes exhibiting a dome and keel structure (e.g. Barberton Greenstone Terrane, Anhaeusser et al. (1969); East Pilbara Terrane, Van Kranendonk et al. (2015)). The keels are relative thin bands of mafic rocks assemblages (greenstone

belts) wrapped around the intruded, often larger granitoids. Other greenstone belts are essentially stacked sheets with large cross-sectional aspects rather than deep synclinal keels (e.g. de Wit & Ashwal, 1995). These thrust faulted stacked sequences bears similarities with Phanerozoic orogens (e.g. West Pilbara Terrane, Hickman (2004)). It is worth noting that many greenstone belts have been described by more than one structural style expounding on the complexity in unravelling their geological history.

Greenstone belts are important sources of economic minerals (e.g. Gold in the Superior Province, Birimian Supergroup, Kalgoorlie Terrane; Goldfarb et al. (2001)). Various styles of ore deposits have been discovered in greenstone belts, including volcanogenic massive sulphide (VMS), komatiite-hosted Cu-Ni-platinum group elements (PGE), intrusion (including pegmatite)-hosted Cu-Ni-Cr-PGE-rare metals, and orogenic gold (Goldfarb et al., 2001; Thurston, 2015).

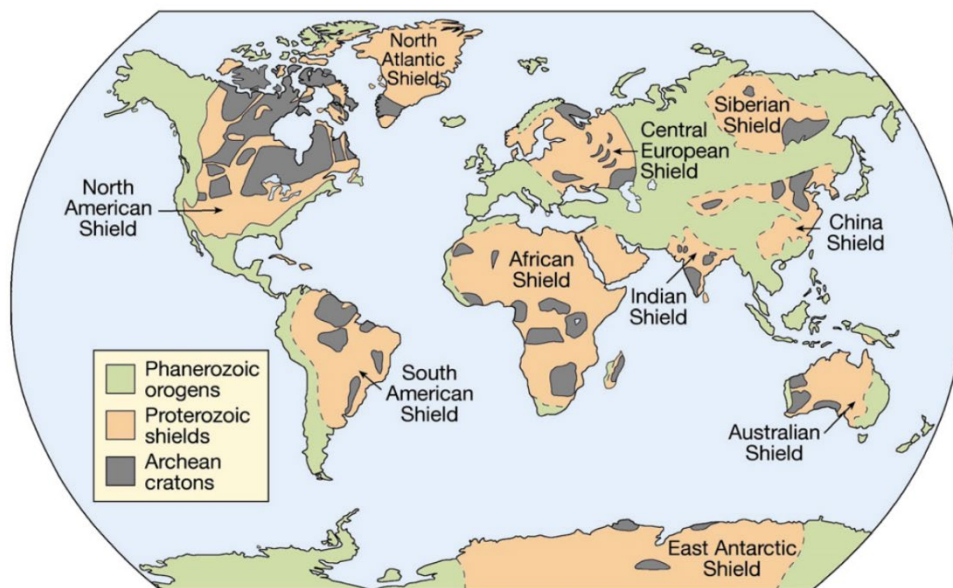


Figure 1-1 Global distribution of cratons, shields and orogens (Furnes et al., 2015). Greenstone belts are situated in cratons and shields which occupies a vast coverage of the continents and are typically bordered by Phanerozoic assemblages.

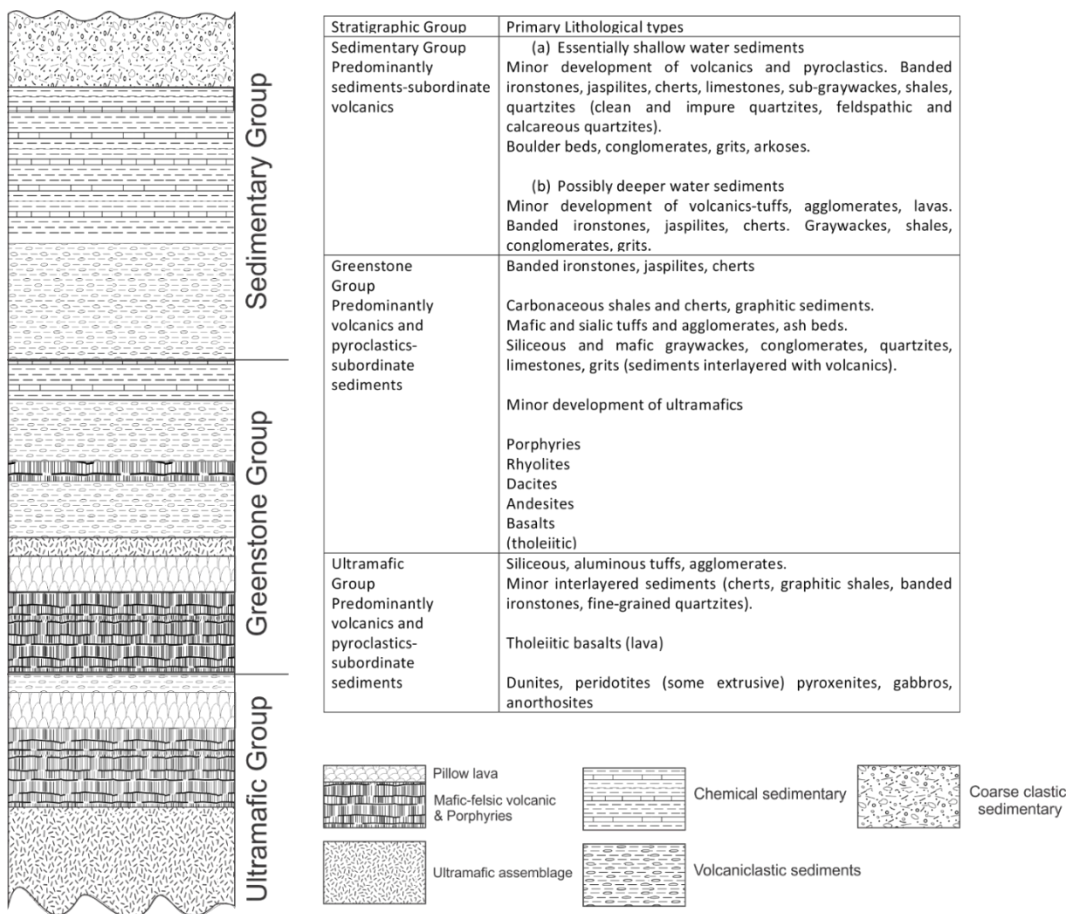


Figure 1-2 Generalised lithostratigraphic subdivisions of Precambrian greenstone belts illustrating principal lithological assemblages. Modified after Anhaeusser et al. (1969); Anhaeusser (2014).

1.2.1 Development of greenstone belts

In recent times, there has been a growing number of studies on greenstone belts to provide insight into their geodynamic evolution, thereby providing insights into the geological evolution of the Earth, albeit with significant disagreements (e.g. Cawood et al., 2006; Van Kranendonk, 2011; Gerya, 2014; Furnes et al., 2015). Some of the key controversies boil down to the tectonic setting in which the greenstone belt formed and the implication of the proposed models to the early Earth's evolution. It is now widely accepted that greenstone belts originate from a myriad of tectonic settings, and no single tectonic regime explains the features associated with all greenstone belts. Many models have been suggested for how greenstone belts formed (e.g., Drip tectonics; van Hunen et al., 2008). However, two commonly cited models are the allochthonous and autochthonous models (Vanderhaeghe et al., 1998). A summary of some of the geological evidence supporting both models is presented in Table 1-1.

The allochthonous model is defined by the lateral accretion of proto-crusts in a subduction setting (Smithies et al., 2005; Barley et al., 2008; Furnes et al., 2015; Polat et al., 2015). Proponents of the allochthonous model base arguments on characteristic features which resemble subduction-related products in the rock record. For example, the occurrence of ultra-high pressure metamorphic mineral assemblages such as the prehnite-pumpellyite facies have been attributed to the high-pressure metamorphic regime common in the accretionary prism of subduction zones (Brown, 2010). Also, crustal-scale structures, including thrust faults and regional-scale folding, are akin to compressional tectonics facilitated by lateral propagation of the subducting plate (Polat et al., 2015). Abundant high-magnesium calc-alkaline volcanic assemblages within greenstone belts with similar geochemical compositions as Boninites and Adakites are interpreted as melts generated in response to hydration of the subduction wedge mantle (Kerrich & Polat, 2006; Thurston, 2015). These rocks assemblages combined with the structural and metamorphic features mentioned above provide evidence for subduction-related geodynamic processes. However, their impression within the ancient rock record begs the question of their uniqueness to plate tectonic processes only.

On the other hand, the autochthonous model argues for in-situ growth with younger, evolved successions deposited on older units forming a layer-cake stratigraphic succession (Thurston, 2002). This model invokes plume-initiated within plate tectonic setting often deformed by vertical gravity-driven tectonics (Rey et al., 2003; Van Kranendonk et al., 2013; Thurston, 2015; Bédard, 2017; Ciborowski et al., 2017). Gravity-driven tectonic regime produces dome and keel structures which are difficult to explain by lateral movement in a convergent plate-tectonic regime (e.g. East Pilbara granite-greenstone terrane, Hickman (2004)). Others argue the high thermal regime during the Archean could not have permitted the successful operation of modern-style plate tectonics, thereby favouring the autochthonous model of greenstone belt formation (e.g. Bédard (2013); Gerya (2014)). Some of the geological features that support this model include a regional basement complex and unconformity and progressive crustal contamination signatures up stratigraphy (Swager, 1997). Inherited isotopic signatures and crustal xenolith (and xenocrystic zircons) manifest the presence of a pre-existing sialic basement suggestive of in-place accumulation of magmas (Abbott & Mooney, 1995; Kamber, 2015). The presence of

high-magnesium volcanic rocks known as Komatiite is an indicator of mantle plume-driven magmatism in a within plate setting, and most greenstone belts with such rocks are interpreted as forming by the autochthonous model (e.g., Pilbara and eastern Kaapvaal cratons; Van Kranendonk et al., 2015).

Table 1-1 Summary of evidence for autochthonous and allochthonous models of greenstone formation and crustal growth.

Criteria	Autochthonous models	Allochthonous models
Principal rock assemblage	Thick pelagic sedimentary cover ¹ , voluminous Komatiite and Fe-tholeiite ³	High Mg-andesite ¹ , Hydrous melts (e.g. anorthosites) ¹¹ , high Nb basalts, Boninites, Adakites
Geochemical signatures	High Ni, Cr, Fe High Ni-Mg number ratio ^{1, 2, 10} Low ratios Th/Ta<2; La/Yb<5 ¹ . High degrees partial melting ¹⁰	Nb-Ta depletion ¹ , Low Th/Ta>5; La/Yb>2. Low Ni-Mg number ratio ²
Regional structures	Gravitational tectonics & diapiric granitoids ^{4,5} . mantle wind ⁶ Radiating dyke swarms ¹⁰ . Dome and keel ¹³	Poly-phased fold and thrust ¹¹ , Syn-tectonic TTG plutons. Ophiolites ¹²
Basement	Unconformities mostly present with basement (subaqueous/subaerial sediments) ³ . Pre-existing continental crust ¹³	Basement contact mostly tectonic ⁹
Tectonic setting	Within-plate setting, e.g. Oceanic plateau (OP), continental flood basalts (CFB),	Subduction related- island arc, continental margin arc, convergent zone accretionary prism
Crustal growth	Vertical accretion in place ⁵ Pulsed magmatism ¹³	Lateral plate-tectonic style accretion of exotic blocks
Mode of magmatism	Plume generated, adiabatic decompression melting	Mantle wedge, slab melting, decompression melting at back-arc.
Others	Delaminated lower crust in seismic images. ⁶ Inherited zircons from lower stratigraphic units ^{9, 13} Short magmatic period ¹⁰	Metamorphic core complex ⁷ Ophiolites, blueschist Fossil subduction slabs in seismic images ⁸

References: 1. Abbott and Mooney (1995); 2. Condie (1994); 3. Thurston (2015); 4. Anhaeusser (2014); 5. Van Kranendonk et al. (2014); 6. Bédard (2013); 7. Brown (2010); 8. Stern (2005); 9. Thurston (2002); 10. Ciborowski et al. (2017); 11. Polat et al. (2015); 12. Furnes et al. (2015); 13. Kamber (2015)

1.3 GREENSTONE BELTS AND THEIR IMPLICATIONS ON THE GEODYNAMIC EVOLUTION OF THE PRECAMBRIAN EON

Since greenstone belts comprise rock assemblages formed within the Archean to Proterozoic era, they reflect the geodynamic processes that operated in the early Earth. Additionally, because rock assemblages of greenstone belts formed within discrete timeframes, they captured key physical and chemical changes that occurred as they formed through time, inferred from variances in the rock record. For example, the decrease in the proportion of high MgO volcanic rocks (i.e., Komatiites) in greenstone belts through time have been attributed by some to a progressive reduction in the ambient mantle temperature (Condie & O'Neill, 2011). Other researchers have attributed the decline in the mantle temperature to increased mantle convection cycles linked with cold subducting crust and delaminated lithosphere sinking into the mantle (Davies, 1992; Cawood et al., 2006).

There is also an apparent increase in the abundance of dyke swarms, kimberlites, and aulacogens in the rock record with time, denoting an increase in the mechanical strength of the continental crust (Windley, 1984; Korenaga, 2013) reminiscent of the progressive cooling of the Earth's internal temperatures. Presently, continental crust growth occurs at convergent zones, where the newly formed crust of various origins is accreted onto existing crust and reworking of older continental margins by plate tectonic mechanisms. However, it has been noted that the rate of addition of new material to the existing crust by subduction accretion-convergence regime is minimal (Condie, 2013). Hence, some argue that the plate tectonic style of crustal growth can not solely account for the continental crust volume at present (Windley, 2003).

Moreover, the timing of the onset of modern-style plate tectonics is also widely debated, with many reporting dates as early as the Archean (ca. 3.0 Ga; Van Kranendonk, 2007; Van Kranendonk, 2011) to about 800 Ma (< 1.0 Ga; Stern & Gerya, 2018). Consequently, there is no clear correlation on the influence of modern-style plate tectonics on the growth of the continental crust in the early Earth. Therefore, there is the notion that there must have been other mechanisms that operated in the early Earth to produce and stabilise the oldest continental crusts. There is also the long-standing debate on the evolution of the crust and its implications on the origin of the chemical heterogeneity of the mantle. The chemical (also isotopic) compositional variability of uncontaminated oceanic basalts of various ages reveals

that the mantle comprises distinct components that reflect its evolution through time (Patchett et al., 1982; Campbell & Griffiths, 1993; Yan et al., 2020). According to Patchett et al. (1982), the fragments of crust that formed before ~3.0 Ga preserved evidence of a largely Chondritic mantle ($\epsilon_{\text{Hf}}=0$) until ~2.8 Ga where both Chondritic and residual mantle ($\epsilon_{\text{Hf}}=0$ to +14) arose and diversified even further with time. This compositional diversity, driven by mantle-convection cycles, is characterised by substantive incompatible element depletion and enrichment of the mantle through partial melting and re-fertilisation by recycled crust and lithosphere (Hofmann, 1997; Stracke et al., 2005; Sobolev et al., 2007). Due to the recognised heterogeneities, the mantle has been categorised into many distinct source regions. Some of the common ones based on geochemistry include the Primitive mantle; which is similar to the composition of the bulk silicate Earth (BSE), Depleted mantle, and Enriched mantles (EM I, EM II, HIMU etc.); representing re-fertilised deeper mantle reservoirs tapped by mantle plumes (White, 2015; Stracke, 2016).

Of particular interest to this study are the changes which occurred within the early Paleoproterozoic era (~2.4–2.0 Ga). This era was subject to major juvenile crustal growth and preservation of continental crust (Barley et al., 2005; Reddy & Evans, 2009), following the extensive crust forming events of the Archean. A collation of high precision U-Pb zircon crystallisation ages from Precambrian rocks shows anomalous peaks representing periods of crustal growth (Hawkesworth et al., 2010; Arndt & Davaille, 2013; Condie, 2013; Hawkesworth et al., 2013). Some of these peaks are reported at 2.5, 2.1 and 1.9 Ga (Arndt & Davaille, 2013), consistent with major global geodynamic events within the early Paleoproterozoic era. Another peculiar change detected is the sustained rise of atmospheric oxygen is estimated to have occurred around 2.4 Ga, followed by evidence of extensive oxidative weathering products in the rock record (Barley et al., 2005; Reddy & Evans, 2009). This period was also characterised by transition from predominantly granulite facies ultrahigh temperature metamorphism of the Neoarchean to the prevalence of eclogite facies-high-pressure metamorphism in the Proterozoic to Cambrian (Brown, 2010).

However, the lack of well-exposed and easily datable juvenile supracrustal rocks in the Paleoproterozoic hinders interpretations of Earth history between 2.4-2.2 Ga (Barley et al., 2005; Zhao et al., 2006), with much of these investigations centred on

well-preserved Archean rocks. Therefore, to better understand crustal growth mechanisms, the evolution of the mantle and the influence of modern-style plate tectonics in the early Proterozoic, the mode of development of Paleoproterozoic greenstone belts must be fully understood. This will require integrating multi-scaled, multi-faceted analytical data backed by physical evidence from the geological record to propose a robust model on a case by case basis. Lithostratigraphy coupled with geochemistry and robust radiometric dating has proven to be a useful tool in the reconstruction of the evolution of greenstone belts (e.g. Barley et al., 2008; Hayman, Thébaud, et al., 2015).

This study will investigate the origin of the Paleoproterozoic Houndé and Boromo greenstone belts of the West African Craton (WAC) to assess the geodynamic processes leading to their formation and its implications on Earth's evolution. The WAC represents one of the best regions to study the first post-Archean crustal growth event, which coincides or shortly follows many major changes on Earth.

Chapter 2: Geological setting of the Paleoproterozoic Birimian domain of the West African Craton

2.1 OVERVIEW OF THE WEST AFRICAN CRATON

The West African Craton (WAC) is located in the western part of Africa. According to Grenholm et al. (2019), the WAC is estimated to cover $2800\text{ km} \times 16000\text{ km}$. The basement rocks of the WAC are exposed in three separate Precambrian granite-greenstone shields. These are the Reguibat Shield to the north, also known as the Northern WAC, the Man-Leo Shield/Southern WAC to the south, and the Kayes Kédougou-Kéniéba inliers (KKI) (Figure 2-1). The central part of the WAC, between the Reguibat and Man-Leo shields, is covered by the Neoproterozoic Taoudenni sedimentary basin (Abouchami et al., 1990). The extreme northern and south-eastern margins of the WAC are also covered by relatively smaller Neoproterozoic sedimentary basins known as the Tindouf and Volta basins, respectively. Contacts between the overlying sedimentary basins and the Precambrian supracrustal have not been observed. However, geophysical surveys detect lateral extension of the WAC beneath the sedimentary covers (Wilson, 1969; Boher et al., 1992).

The Reguibat and Man-Leo shields are composed of Archean and Paleoproterozoic domains. In both shields, the Archean domains are found on the west and the Paleoproterozoic domains on the east. The Archean domains of the WAC consist of 3.3-2.7 Ga basement rocks known as Tiris-Amsaga and Kénéma-Man domains of the Reguibat and Man-Leo shields, respectively (Gasquet et al., 2003). On the other hand, the Paleoproterozoic domains consist of 2.3-1.9 Ga supracrustal rocks known as the Baoulé-Mossi domain in the Man-Leo shield and the Eglab domain of the northern Reguibat shield (Merabet et al., 2016; Grenholm et al., 2019). The north-south trending transcurrent Sassandra Fault in the Man-Leo shield/southern WAC marks the western border of the Paleoproterozoic Baoulé-Mossi with the Archean Kénéma-Man domains (Kouamelan et al., 1997; Egal et al., 2002) (Figure 2-1). The

nature of the contact between the Archean Kénéma-Man and Paleoproterozoic Baoulé-Mossi domains is highly debated. Kouamelan et al. (1997) interpret the Paleoproterozoic Ity-Toulépleu massif occurrence, west of the Sassandra Fault, as evidence for reworking and thinning of the Archean crust due to underplating of juvenile Paleoproterozoic magmatism. On the other hand, Wane et al. (2018) propose continental subduction of the Archean Kénéma-Man domain underneath the Baoulé-Mossi during the Birimian orogeny at ~2.1 Ga. Both models indicate extensive juvenile magmatism in the Baoulé-Mossi domain with input from the older Archean Kénéma-Man supported by detrital and xenocrystic zircons of Archean age (Parra-Avila et al., 2016; Petersson et al., 2018).

The WAC is established to have experienced multiple tectonic events before its stabilisation at about 1.7 Ga after crustal thickening and the cessation of magmatism (Feybesse et al., 2006). Although the WAC has generally remained stable since about 1.7 Ga, its margins were reactivated during the 600–500 Ma Pan-African orogenic event during the assembly of the Gondwana supercontinent (Ennih & Liégeois, 2008). It has been suggested, based on the similarity of age and lithological succession, that WAC is the equivalent of the São Luis Craton of South America and was subsequently detached during the breakup of the Pangea Supercontinent (Klein et al., 2005). Across the WAC, about twenty-five unique sets of Neoarchean to Quaternary mafic dyke swarms have been identified by Jessell et al. (2015).

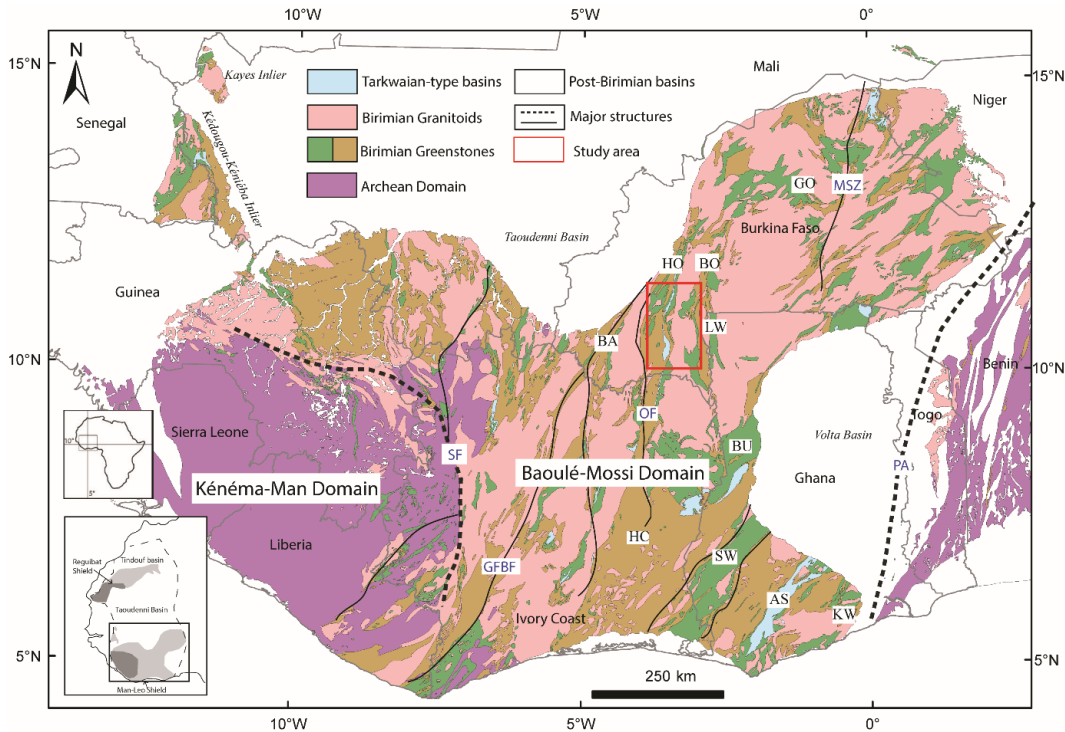


Figure 2-1 Geology of the Man-Leo shield of the southern West African Craton (WAC) showing the Archean Kénéma-Man domain and Paleoproterozoic Baoulé-Mossi domain, Kayes and Kédougou-Kéniéba inliers (KKI) adapted from Boher et al. (1992); Kouamelan et al. (1997); Milési et al. (2004). Inset map shows map location with reference to continental Africa (above) and the WAC boundary showing the Reguibat shield in the north and Man-Leo Shield in the south (below). Abbreviation of major structures: Sassandra Fault (SF), Grenville-Ferkessedougou-Bobo-Dialouso fault (GFBF), Ouango-Fitini (OF), Markoye shear zone (MSZ) and Pan-African suture zone (PA). Abbreviation of greenstone belts and sedimentary basins: Houndé (HO), Boromo (BO), Banfora (BA), Lawra (LW), Goren (GO), Bui (BU), Ashanti (AS), Sefwi (SW), Haute Comoé basin (HC), and Kibi-Winneba (KW).

2.2 GEOLOGICAL SETTING OF THE BIRIMIAN DOMAIN

The Baoule-Mossi domain, hereafter called the Birimian domain, comprises Paleoproterozoic supracrustal rocks collectively called the Birimian Supergroup (Leube et al., 1990). Magmatic accretion of the Birimian domain is estimated to have occurred between 2350–1900 Ma (Taylor et al., 1992), a period of over three hundred million (300 m.y.), which was punctuated by polycyclic deformational and metamorphic events from ~2160 to ~1980 Ma (Feybesse et al., 2006; Baratoux et al., 2011). Generally, the Birimian Supergroup is characterised by linear-curvilinear greenstone belts commonly oriented northeast-southwest to north-south in the central and eastern parts of the Birimian domain; and northwest-southeast in the western part of the domain. The greenstone belts commonly comprise volcanic and volcano-

sedimentary rocks intruded by multiple syn to post emplacement granitoids, with intermittent shallow and deep water sedimentary basins (Abouchami et al., 1990; Boher et al., 1992; Pohl & Carlson, 1993) (Figure 2-1).

2.2.1 Lithostratigraphy of the Birimian Domain

There is no unequivocal evidence of a basement complex underlying the Birimian Supergroup. However, there are reports of the involvement of older (Neoarchean) crustal material in the genesis of the Birimian magmas (Feybesse et al., 2006; Petersson et al., 2018). For example, the Winneba granitoid of southern Ghana yield an Sm-Nd model age of ~2600 Ma, suggesting a significant contribution from an Archean precursor (Leube et al., 1990; Taylor et al., 1992). Even though there are pockets of rocks with evidence for older crustal influence in juvenile magmas, the source and timing of contamination are poorly understood. Due to poor outcrop exposure and lack of extensive radiometric dating, there is yet to be a consensus on the lithostratigraphic relationships of the Birimian supracrustal rocks across the entire Birimian domain. In places where the stratigraphy of the Birimian Supergroup has been studied in detail, it is generally subdivided into three principal groups (Mériaud et al., 2020). These are the Lower Birimian, Upper Birimian and Tarkwaian Groups (Figure 2-2).

The Lower Birimian Group is considered the basal supracrustal succession of the Birimian Supergroup and dominated by thick sequences of volcanic lavas (pillowed in most places) and subordinate volcano-sedimentary rocks (Feybesse et al., 2006). In places, the Lower Birimian is locally capped by rare cherts, manganese, carbonates and quartzites deposits (e.g., Nangodi belt, Attoh (1982); Mako Series, Dabo et al. (2017)). The thickness of the Lower Birimian Group in most places is greater than 4500 m (e.g. Dixcove belt, south-western Ghana; Sylvester and Attoh (1992)). This succession is interpreted have been emplaced in a deep subaqueous environment based on the presence of abundant pillow basalts and chemical sedimentary beds (Abouchami et al., 1990; Hein et al., 2004; Attoh et al., 2006). Geochemically, the volcanic units are compositionally tholeiitic, ferroan with unfractionated rare earth elements pattern (Béziat et al., 2000; Pouclet et al., 2006; Dampare et al., 2008). There are very few published ages that constrain the age of emplacement of the Lower Birimian Group. However, magmatic accretion of the

Lower Birimian Group is estimated to predate 2270 Ma based on ages of granitoid intrusions (e.g., 2270 Ma Fada N'Gourma granodiorite; Parra-Avila et al. (2016))

The Upper Birimian Group is dominantly made up of clastic sedimentary deposits intercalated with volcanic rocks (Feybesse et al., 2006; Pouclet et al., 2006; Roddaz et al., 2007). This succession is predominately made up of intermediate-felsic lavas (pillowed and massive) with minor mafic lavas basalts; ultramafic and mafic intrusions interbedded with fine-coarse grained intermediate pyroclastic, volcanogenic, epiclastic, and chemical sedimentary units (Pouclet et al., 2006; Roddaz et al., 2007). Geochemically, the volcanic rocks of the Upper Birimian Group are typically calc-alkaline with high magnesium basalts/andesite compositions (Roddaz et al., 2007). Crystallisation ages within the Upper Birimian Group range between 2200-2160 Ma (Davis et al., 1994; Baratoux et al., 2011). The contact relationship between the Lower and Upper Birimian groups is not well documented due to lack of exposure. In places, the transition between the Lower Birimian and the Upper Birimian is in places marked by approximately 200m thick manganiferous jaspilite, beds of chert and Fe-Ca-Mg carbonate rocks (e.g. Nangodi belt, Ghana (Sylvester & Attoh, 1992); Boromo-Goren belt, Burkina Faso (Hein et al., 2004)). The Upper Birimian is at least 3000 meters thick (e.g. Nangodi belt Attoh (1982)). Sedimentary structures such as graded beds and cross-bedding suggest a deltaic to a turbiditic depositional environment for the sedimentary deposits (Hein et al., 2004).

The Tarkwaian Group predominantly comprises clastic sedimentary rocks restricted to only a few localities in the Birimian domain. The type-locality name originates from the Tarkwa valley of Ghana, where it was first described (Pohl & Carlson, 1993). This stratigraphically distinct sedimentary group has been indiscriminately applied to many conglomeratic deposits of the Upper Birimian, causing errors in their geological interpretations. The Tarkwaian Group unconformably overlies the Upper Birimian (Leube et al., 1990; Davis et al., 1994), defined by an angular unconformity made up of polymictic conglomerates of the Kawere subgroup. Components of the Tarkwaian sedimentary units were derived from the Birimian greenstones and associated granitic intrusions with a high proportion of fragments from the underlying granitoids and felsic intrusive units (Davis et al., 1994; Bossière et al., 1996; Smith et al., 2016). The thickness of the Tarkwaian group is

estimated to be greater than 2000 m (Pigois et al., 2003; Baratoux et al., 2011). The Tarkwaian group is generally a fining upward sequence interpreted to have been deposited into long, narrow intramontane basins resulting from rifting of the greenstone belts (Leube et al., 1990; Davis et al., 1994). The depositional environment of the Tarkwaian conglomerate is interpreted as alluvial fans reworked by braided stream channels (Smith et al., 2016). The Tarkwaian Group is estimated to have been deposited between 2132 Ma to 2097 Ma (Bossière et al., 1996; Pigois et al., 2003).

The Birimian Supergroup includes several generations of tonalite-trondhjemite-granodiorites (TTG), potassic granites, diorites and alkaline syenites (Tapsoba et al., 2013). Few granitoids with emplacement ages corresponding to the Lower Birimian Group exist in northern Ghana (~2258 Ma; de Kock et al. (2011), ~2213; Sakyi et al. (2014)) and north-eastern Burkina Faso (~2253 Ma; Tshibubudze et al. (2015)). The majority of the Birimian granitoids were emplaced between 2195–2150 Ma (Tapsoba et al., 2013), contemporaneous with periods of volcanism in the Upper Birimian Group. There is a wide range of geochemical compositions of the Birimian granitoids. Notably, the early granitoids (>2200 Ma) are typically ferroan with high Yb, Y and Nb (TTG compositions), while the younger, more abundant granitoids are typically granitic with higher K, Th and Rb contents (Sakyi et al., 2014; Grenholm et al., 2019). According to Block et al. (2016), early granitoids originated from crustal recycling of an older proto-crust between 2350–2210 Ma while the younger (2210–2150 Ma) granitoids preserve evidence for hydrous melting of a metasomatised source.

The Birimian Supergroup is crosscut by many dyke swarms and sills. Recent studies by Jessell et al. (2015); Baratoux et al. (2019) place the age of dyke swarms within the Birimian domain in four discrete cycles. The first notable dyke swarms age 1800-1700 Ma are interpreted to be related to the assembly of Nuna supercontinent; secondly, 1600-1500 Ma- the onset of the breakup of Nuna; 900-800 Ma break up of Rodina supercontinent, and subsequently ~200 Ma Central Atlantic Magmatic Province (CAMP) linked to the opening of the Atlantic ocean.

2.2.2 Structural and Metamorphic evolution of the Birimian Domain

The Birimian Supergroup has been subjected to structural deformation coupled with regional scale amphibolite-greenschist facies metamorphism during the Eburnean tectonothermal events. The Eburnean events occurred between 2160 Ma to 1980 (Feybesse et al., 2006; Baratoux et al., 2011) in two broad phases; an early

deformational phase (Eoeburnean/Eburnean I/Tangaean event 2160–2120 Ma) followed by a later event, Eburnean II between 2100–1980 Ma (Grenholm et al., 2019). The Eburnean I event is characterised by contractional deformation (denoted by D1) and crustal thickening associated with medium to high-grade (upper greenschist–amphibolite) metamorphism (McFarlane et al., 2019). This deformational phase resulted in regional-scale NE–SW to N–S alignment of greenstone belts and subvertical tilting (Lombo, 2010). Early deformation (D1) is defined largely by S1 penetrative foliation, which is often parallel to primary bedding (Baratoux et al., 2015). Some studies have identified a poorly defined pre-D1 event associated with N–S shortening within the greenstone belts and constrained by syn-tectonic granitoids at about 2180 Ma (Perrouty et al., 2012; McCuaig et al., 2016). The question remains as to whether the Eburnean I is the earliest deformational event to affect rocks of the Lower Birimian Group.

The second phase of the Eburnean event (Eburnean II) has been attributed to NW–SE transcurrent tectonic movement and is responsible for D2 and D3 deformational cycles (Feybesse et al., 2006; Block et al., 2016). According to Baratoux et al. 2011, D2 is defined by brittle to brittle-ductile anastomosing steeply dipping shear zones, whereas D3 is marked by fold-generated brittle shear zones as well reactivation of earlier faults. The transition between Eburnean I (D1) and Eburnean II (D2-3) deformational cycles are marked by the opening of the Tarkwaian Group sedimentary basin and represented by strike-slip faults parallel to S2 shear zones (Bossière et al., 1996; Baratoux et al., 2011).

Regional metamorphism of the Birimian Supergroup is characterised by amphibolite to greenschist facies conditions with localised high temperature-pressure granulite facies conditions at granitoid intrusive aureoles (Block et al., 2016). Recent studies by Ganne et al. (2011) record relic high-pressure, low-temperature blueschist metamorphic assemblages in the Fada N’Gourma region north-eastern Burkina Faso, which have not been reported elsewhere in the Birimian domain. Peak regional metamorphism correspond to the Eburnean I and II tectonothermal events, respectively (see Figure 2-2). Timing of Eburnean I associated metamorphic regime is constrained by U-Pb zircon rim age of 2153 ± 6 Ma by Tshibubudze et al. (2015) from granites of the Oudalan-Goroul belt in north-eastern Burkina Faso. Subsequent metamorphic

regimes associated with Eburnean II span ages between 2120–2000 Ma across the Birimian domain (de Kock et al., 2011; Parra-Avila et al., 2016)

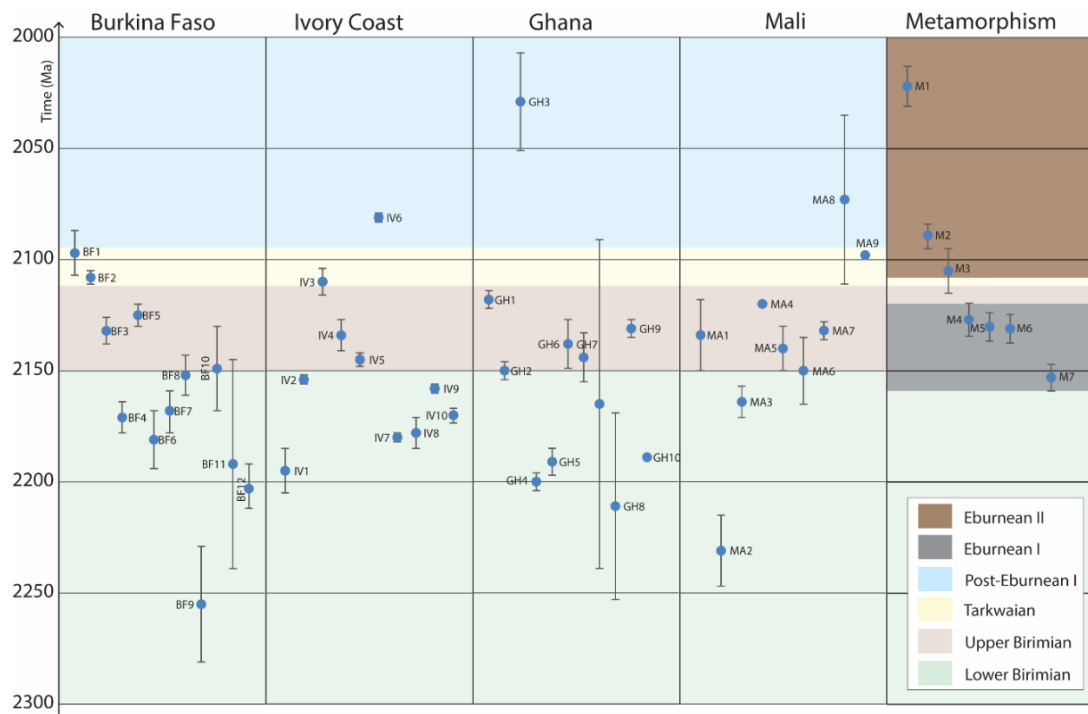


Figure 2-2 Summary chart of some published geochronological data for emplacement ages and metamorphic ages in the Birimian domain modified after Pouclet et al. (2006); Lebrun et al. (2016). Each country column represents the location where samples were obtained. Geochronological data sources are presented in Table 2.1. Note: the majority of the age data was obtained from intrusive rocks with only a few emplacement ages for volcanic rocks.

Table 2-1 Compilation of published magmatic and metamorphic ages across portions of the WAC presenting rock type, methods and references used in Figure 2-2

	Lithology	Reported Age	+/-	Material	Isotopic system	Reference
BF1	Diorite	2097	10	Zircon	U-Pb	Castaing et al. (2003)
BF2	Granite	2108	3	Zircon	U-Pb	Castaing et al. (2003)
BF3	Granite	2132	6	Zircon	U-Pb	Castaing et al. (2003)
BF4	Rhyolite-Dacite	2171	7	Zircon	U-Pb	Castaing et al. (2003)
BF5	Granite	2125	5	Zircon	U-Pb	Parra-Avila et al. (2016)
BF6	Tonalite	2181	13	Zircon	U-Pb	Parra-Avila et al. (2016)
BF7	Volcaniclastic	2168	10	Zircon	U-Pb	Parra-Avila et al. (2016)
BF8	Granodiorite	2152	9	Zircon	U-Pb	Tapsoba et al. (2013)
BF9	Granite	2255	26	Zircon	U-Pb	Tshibubudze et al. (2013)
BF10	Diorite	2149	19	Zircon	U-Pb	Tshibubudze et al. (2015)
BF11	Granodiorite	2192	47	Zircon	U-Pb	Tshibubudze et al. (2015)
BF12	Granite	2203	12	Zircon	U-Pb	Tshibubudze et al. (2015)
IV1	Granite	2195	10	Zircon	U-Pb	Delor et al. (1995)
IV2	Tonalite	2154	1	Zircon	U-Pb	Gasquet et al. (2003)
IV3	Granodiorite	2110	6	Zircon	U-Pb	Hirdes et al. (1996)
IV4	Granodiorite	2134	7	Titanite	U-Pb	Hirdes et al. (1996)
IV5	Granodiorite	2145	3	Titanite	U-Pb	Hirdes et al. (1996)
IV6	Granite	2081	1	Zircon	U-Pb	Hirdes et al. (2007)
IV7	Andesite	2180	2	Zircon	U-Pb	Hirdes et al. (2007)
IV8	Volcaniclastic	2178	7	Zircon	U-Pb	Kouamelan (1997)
IV9	Rhyolite-Dacite	2158	1	Zircon	U-Pb	Lüdtke et al. (1999)
IV10	Lapilli-tuff	2170	5	Zircon	U-Pb	Lüdtke et al. (1999)
GH1	Diorite	2118	4	Zircon	U-Pb	de Kock et al. (2011)
GH2	Granodiorite	2150	4	Zircon	U-Pb	de Kock et al. (2011)
GH3	Kimberlite	2029	22	Rutile	U-Pb	Delor et al. (2004)
GH4	Granodiorite	2200	4	Zircon	U-Pb	Feybesse et al. (2006)
GH5	Shallow intrusive	2191	6	Zircon	U-Pb	Parra-Avila et al. (2016)
GH6	Granite	2138	11	Zircon	U-Pb	Sakyi et al. (2014)
GH7	Granodiorite	2144	11	Zircon	U-Pb	Sakyi et al. (2014)
GH8	Granite	2165	74	Zircon	U-Pb	Sakyi et al. (2014)
GH9	Granodiorite	2211	42	Zircon	U-Pb	Sakyi et al. (2014)
GH10	Lapilli-tuff	2131	4	Zircon	U-Pb	de Kock et al. (2011)
GH11	Rhyolite-Dacite	2189	1	Zircon	U-Pb	Hirdes and Davis (1998)
MA1	Detrital	2134	16	Zircon	U-Pb	Parra-Avila et al. (2016)
MA2	Detrital	2231	16	Zircon	U-Pb	Parra-Avila et al. (2016)
MA3	Monzonite	2164	7	Zircon	U-Pb	Feybesse et al. (2006)
MA4	Granodiorite	2120	0	Zircon	U-Pb	Parra-Avila et al. (2016)
MA5	Syenite	2140	10	Zircon	U-Pb	Parra-Avila et al. (2016)
MA6	Monzonite	2150	15	Zircon	U-Pb	Liégeois (1990)
MA7	Diorite-Gabbro	2132	4	Zircon	U-Pb	McFarlane et al. (2011)
MA8	Volcaniclastic	2073	38	Whole-rock	Rb-Sr	Liégeois et al. (1991)
MA9	Rhyolite-Dacite	2098	5	Zircon	U-Pb	Liégeois et al. (1991)
M1	Granodiorite	2022	9	Zircon	U-Pb	Tshibubudze et al. (2015)
M2	Granodiorite	2089	6	Zircon	U-Pb	Parra-Avila et al. (2016)

Table 2-1 continued

	Lithology	Reported Age	+/-	Material	Isotopic system	Reference
M3	Granodiorite	2105	10	Zircon	U-Pb	de Kock et al. (2011)
M4	Migmatite	2127	7.4	Monazite	U-Pb	Block et al. (2015)
M5	Migmatite	2130.2	6.4	Monazite	U-Pb	Block et al. (2015)
M6	Granofels	2131	6.4	Monazite	U-Pb	Block et al. (2015)
M7	Granite	2153	6	Zircon	U-Pb	Tshibubudze et al. (2015)

2.2.3 Geodynamic evolution of the Birimian Domain

Many studies have vastly debated the evolution of the Birimian domain with contrasting models to explain the geodynamic processes responsible for the emplacement of the Birimian Supergroup. Much effort into understanding the evolution is because the Birimian domain represents a well-preserved extensive Paleoproterozoic juvenile magmatic event that can provide valuable insight into that era of Earth's evolution. A compilation of the proposed tectonic models for the evolution of the Birimian domain can be summed up under two contrasting scenarios (summarised in Table 2-2). These are the contrasting allochthonous and autochthonous origins of greenstone belts and are highlighted below:

The allochthonous model— this model suggests lateral accretion of volcanic arc successions in an arc-back-arc setting and with time transitioned into a collisional orogen docking subduction-derived protocrusts onto an Archean nucleus (Sylvester & Attoh, 1992; Béziat et al., 2000; Dampare et al., 2008; Baratoux et al., 2011). Geochemical signatures similar to volcanic successions derived from modern-style plate tectonic settings have been the foremost evidence cited by proponents of this model. For instance, trace element trends such as negative Nb–Ta anomalies and abundant calc-alkaline rocks have led to suggestions of subduction-related origin (Tapsoba et al., 2013; Senyah et al., 2016). Other evidence, such as rare high-pressure-low temperature metamorphic assemblage in few locations, has been likened to metamorphic facies obtained in a subduction wedge (Ganne et al., 2011). A seemingly north-westward younging of emplacement ages has been interpreted as progressive accretion of younger protocrust resulting in the spatio-temporal variations in the supracrustal succession (Hirdes & Davis, 2002; Grenholm et al., 2019).

The autochthonous model—In this model, the Birimian Supergroup is proposed to have accreted in-situ, thereby generating progressively younger successions within

an oceanic basin (Abouchami et al., 1990; Pouclet et al., 2006; Lombo, 2009) or an intra-continental rift setting (Leube et al., 1990; Vidal & Alric, 1994). According to Lombo (2010), the ubiquitous occurrence of unfractionated chondrite-normalised REE patterns of tholeiitic basalts across the Birimian domain is evidence for extensive plume-generated magmas in a rift setting comparable to the Nauru oceanic plateau. Dome and keel structures and associated deformational features in the Nassian domain, Ivory Coast, are interpreted as diapiric uprising of TTGs with subsequent sagduction of greenstones (Vidal et al., 2009), suggesting there was primarily no influence from horizontal convergent tectonic forces.

A major hindrance to the understanding of the evolution of the Birimian greenstone belts is the over-reliance on geochemical tectonic discrimination proxies with little regard for lithostratigraphy. The geochemical approach is based on comparing the geochemistry of the Birimian rocks to well-documented Phanerozoic sequences emplaced in different tectonic settings. There have been many studies that suggest rocks of the early vary markedly from those generated in recent times (Sylvester & Attoh, 1992; Van Kranendonk, 2007). This problem is exacerbated by the lack of enough robust emplacement ages to characterise each volcanic event. Both models proposed for the evolution of the Birimian domain are supported by tangible evidence but without a stratigraphic framework from which to interpret these geochemical signatures. Hence the magmatic history of the Birimian greenstone belts remains unresolved.

Table 2-2 Summary of evidence for tectonic models of the Birimian Supergroup

Criterion	Allochthonous model	Autochthonous model
Tectonic environment	Oceanic Island arcs ^c , arc-oceanic plateau accretion ^{e f}	Intra-plate oceanic flood basalts/ oceanic plateau ^{h, i} , Continental rift ^k
Principal lithologies	Lava flows (tholeiitic, ultramafic-mafic, calc-alkaline), volcaniclastics	Mafic bimodal volcanic and volcano-detrital units ^g
Origin of magmas	Melting of the subducting slab, mantle wedge	Deep mantle plumes through immature crust ^h
Provenance of sedimentary units	Marginal marine setting (not derived from a pre-Birimian source) ^d . late orogenic compression basin (lower Tarkwaian group) ^m	Locally derived devoid of older crust components ^g
Geochemical signatures	LILE and Pb enrichment ^{c e} , HFSE depletion, high Ce/Nb, Th/Nb	Slightly depleted– Flat LREE (similar to Archean tholeiites) ^a
Metamorphism	Blueschist facies 10-12kbar 400-450 ^b	Homogenous metamorphic conditions across the terrane ^j
Structures	Regional NE-SW crustal shortening ⁱ ,	Diapiric structures around domical plutons ^j

References: a. Sylvester and Attoh (1992), b. Ganne et al. (2011), c. Dampare et al. (2008), d. Hein et al. (2004), e. Béziat et al. (2000), f. Baratoux et al. (2011) g. Abouchami et al. (1990), h. Lombo (2009), i. Pawlig et al. (2006) j. Vidal et al. (2009), k. Leube et al. (1990), l. Tapsoba et al. (2013), m. Lebrun et al. (2016).

2.3 GEOLOGICAL SETTING OF THE HOUNDÉ AND BOROMO GREENSTONE BELTS, SOUTHWEST BURKINA FASO

The Boromo and Houndé belts are two adjacent NNE-SSW trending greenstone belts in SW Burkina Faso (Figure 2-3) and cover about 30,000 km². The Boromo belt (eastern part of the study area) extends into northern Ghana, where it is called the Lawra belt. The Houndé belt (western part of the study area) extends southwards into the Ivory Coast, known as Ouango-Fetini and Téhini greenstone belts. The geology of the two belts is generally similar to other Birimian belts elsewhere. They are composed of ~2.2–2.0 Ga volcanic, volcaniclastic and metasedimentary rocks with associated syn to post volcanic, granitic intrusions (Castaing et al., 2003).

The lithostratigraphic succession of the Boromo and Houndé belts are generally similar. They both comprise a roughly 5 km thick mafic-ultramafic basal sequence comprising massive and pillow basalts, including a distinctive feldspar-megacrystic basalt unit intercalated with gabbros, pyroxenites, and amphibolites (Baratoux et al., 2015). There are no ages for this basal unit. This basal sequence is presumed to be the oldest succession based on field relationships. The basal sequence is generally tholeiitic in composition with mostly unfractionated rare earth element abundances, although the transitional basalts show slight light rare element enrichment (Baratoux et al., 2011; Nanema et al., 2017). Because there is no age constraint on the basal sequence, it is generally assumed that this unit in both belts formed simultaneously based on their similar lithological assemblages and stratigraphy.

Within the Boromo belt, the basal tholeiitic unit is overlain by an approximately five-kilometre-thick intermediate-felsic, dominantly calc-alkalic in composition and made up of andesitic to rhyolitic lavas, tuffs, and pyroclastic flows intercalated with epiclastic volcano-sediments (Béziat et al., 2000; Lombo, 2009; Baratoux et al., 2011; Metelka et al., 2011; Augustin et al., 2016). However, in the Houndé belt, the calc-alkaline units are located near the western margin and are separated from the basal tholeiitic units by sedimentary rocks. Rhyolite in the westernmost unit of the Boromo belt yield 2171 ± 7 Ma (zircon, U-Pb), a rhyodacite from the western Houndé belt yield 2176 ± 4 Ma (zircon Pb-Pb), and various suites of granitoid yield ages ranging from 2195–2097 Ma (Baratoux et al., 2011 and references therein).

The youngest succession, ‘Tarkwaian group’, in this region, unconformably overlies the greenstone succession in a 100 km long, 1-5 km wide basin on the eastern margin of the Houndé belt (Bossière et al., 1996) (Figure 2-3). This succession comprises feldspathic sandstone, phyllites, and conglomerates (Koffi et al., 2016). Crossbedding and graded bedding structures in some places indicate a westward younging direction for the Tarkwaian sedimentary succession (Baratoux et al., 2011). Detrital zircons from rhyolite pebbles from Tarkwaian conglomerates yield three distinctive ages populations (2170, 2150, and 2124 Ma) which probably reflect at least three episodes of magmatism (Bossière et al., 1996). This sedimentary package is described as a fluvial post-orogenic unit deposited in intracontinental rift basins (Bossière et al., 1996; Koffi et al., 2016) but their sedimentological relationship with the underlying mafic-intermediate packages is unclear.

Just like other Birimian greenstone belts, the evolution of the Houndé and Boromo greenstone belts are proposed to have formed in two contrasting scenarios: a) subduction-related accretion of island arcs (Béziat et al., 2000; Baratoux et al., 2011), and b) mantle-plume accretion of oceanic plateaus (Augustin & Gaboury, 2017). According to Baratoux et al. (2011), the compositional range of basalts with tholeiitic (oceanic crust or plateaus) and calc-alkaline bimodal (volcanic arcs) signatures represents accretion in a subduction setting. This subduction-accretion model is also supported by Koffi et al. (2017); Nanema et al. (2017). But a delineation of these contrasting accreted blocks has not been accomplished. For example, while the ultramafic rocks of Loraboué in the Boromo belt possess strong island arc signatures like LILE enrichment and depleted HFSE (Béziat et al., 2000), the mafic tholeiitic basalts of the Mana district with abundant Fe-rich tholeiitic basalts with flat REE signatures are attributed to plume-generated oceanic plateaus (Augustin & Gaboury, 2017). These claims generally lack supporting field evidence and lithostratigraphic constraints but rather rely heavily on geochemistry.

According to (Baratoux et al., 2011), three distinctive deformational events are imprinted in the greenstone belts and surrounding granitoids. A pre-Eburnean D₁ collisional event occurred at about 2160 Ma and is mostly expressed by bedding-parallel foliation localised shear zones. The late stages of D₁ facilitated the opening and deposition of the Tarkwaian sedimentary basin rocks. This first phase of deformation is followed by a D₂ deformational phase characterised by E-W

compression is constrained by syn-tectonic granitoids dated between 2113–2097 Ma. The D₂ is characterised by steeply dipping NNE–ENE trending shear zones. Lastly, a localised D₃ transpressional event resulted in reverse faults, kink fold, and crenulation cleavage (Baratoux et al., 2011; Baratoux et al., 2015). The rocks of the study area have been affected by regional greenschist facies metamorphism with localised amphibolite-granulite facies metamorphism synchronous with deformational tectonic events (Koffi et al., 2017). Recognition of the early D1 event in both Lower and Upper Birimian rocks may suggest that both were emplaced in the same tectonic setting with a relatively short time gap between them.

The Boromo and Houndé belts host several deposits of economic minerals, including the massive sulphide zinc-silver deposit at Perkoa (Schwartz & Melcher, 2003), the Bagassi gold deposit (Hein, 2015), the 2165 Ma porphyry copper, and the 2100–2040 Ma lode gold of the Gaoua district (Le Mignot et al., 2014; Le Mignot et al., 2017). The diversity in the style of mineralisation reflects the tectonic setting and depositional environment (Goldfarb et al., 2001) and a robust knowledge of this are important for exploration targeting.

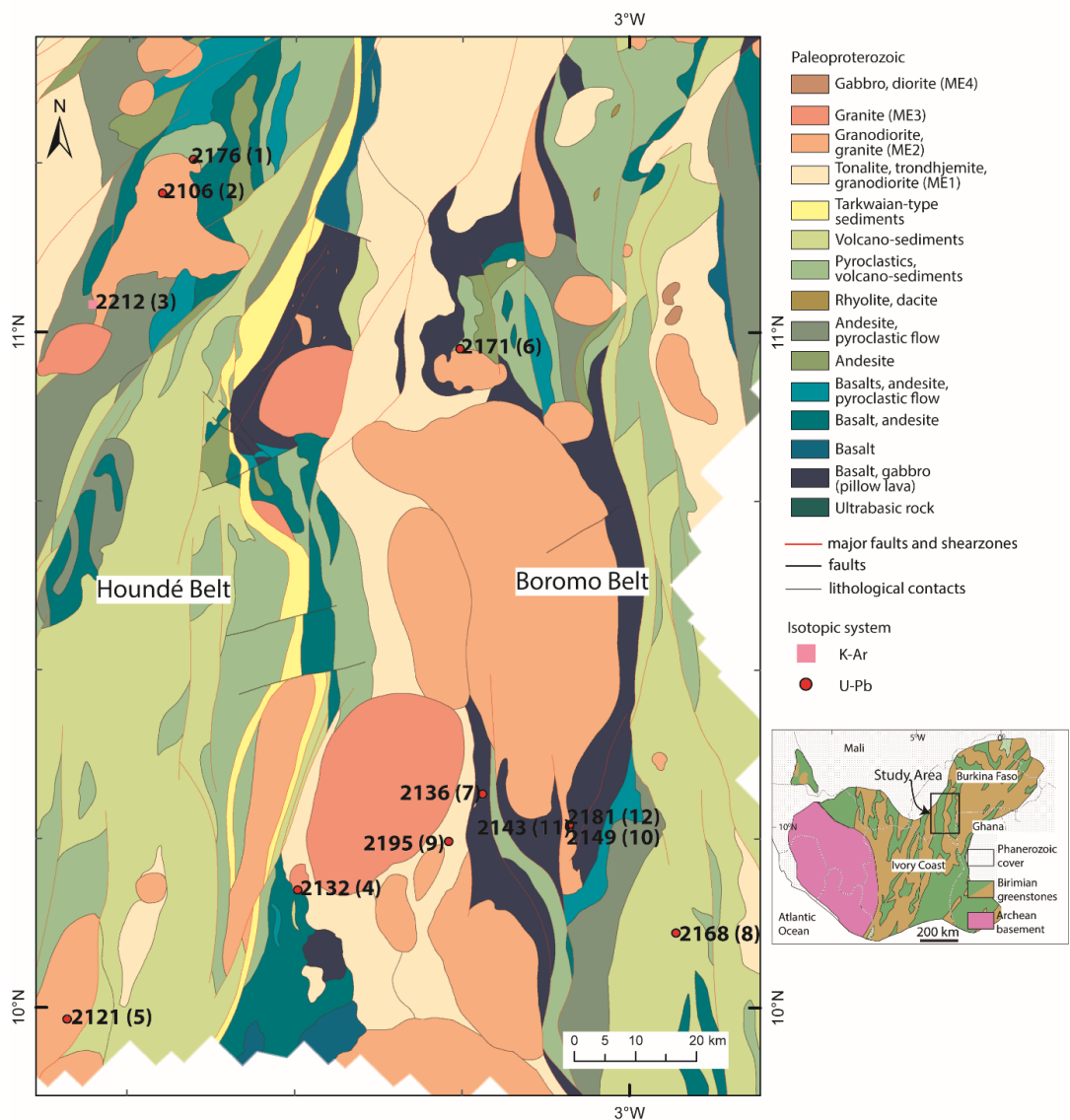


Figure 2-3 Geological map of the Houndé and Boromo greenstone belts, SW Burkina Faso showing the distribution of rock types and some published radiometric ages. Modified after BGRM SIGAfrique (Milési et al., 2004). Geochronological data sources are presented in Table 2-3.

Table 2-3 List of radiometric age data displayed in Figure 2-3

	Lithology	Reported Age	+/-	Material	Isotopic system	Reference
1	Rhyolite	2176	4	Zircon	U-Pb	Castaing et al. 2003, in Baratoux et al. 2011
2	Tonalite-trondhjemite-granodiorite	2106	7	Zircon	U-Pb	Castaing et al. 2003, in Baratoux et al. 2011
3	Rhyolite	2212	31	Amphibole	K-Ar	Castaing et al. 2003, in Baratoux et al. 2011
4	Granite	2132	3	Zircon	U-Pb	Bruguier, WAXI2 2011
5	Granite	2121	8	Zircon	U-Pb	Bruguier, WAXI2 2011
6	Rhyolite	2171	7	Zircon	U-Pb	Castaing et al. 2003, in Baratoux et al. 2011
7	Granite	2136	4	Zircon	U-Pb	Parra-Avila et al. (2016)
8	Volcano-sediment	2168	10	Zircon	U-Pb	Parra-Avila et al. (2016)
9	Trondhjemite	2195	6	Zircon	U-Pb	Bruguier, WAXI2 2011
10	Granodiorite	2149	7	Zircon	U-Pb	Parra-Avila et al. (2016)
11	Aplite	2143	5	Zircon	U-Pb	Parra-Avila et al. (2016)
12	Tonalite, foliated	2181	13	Zircon	U-Pb	Parra-Avila et al. (2016)

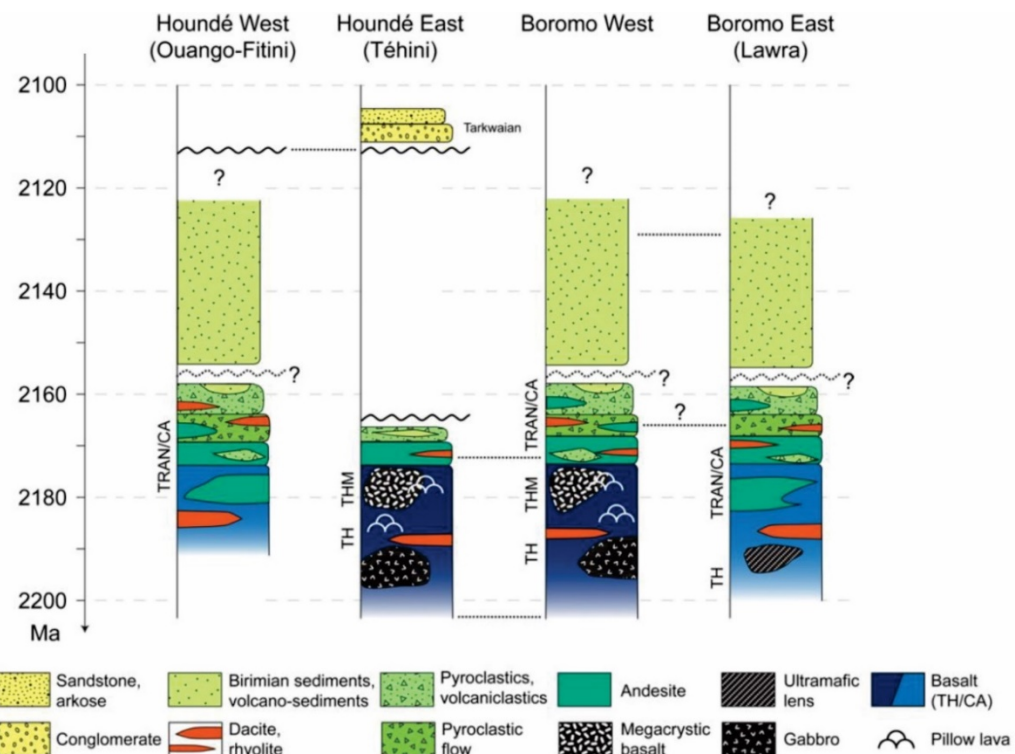


Figure 2-4 Simplified lithostratigraphy sections of the Houndé and Boromo belts of western Burkina Faso. Adapted from Baratoux et al. (2011). TH- tholeiitic mafic units, THM- tholeiitic megacrystic basalts, TRAN- transitional mafic and intermediate volcanic sequences, CA-calc-alkaline volcanic sequences.

2.4 RESEARCH PROBLEMS

The Houndé and Boromo greenstone belts, like their Birimian counterparts, are missing links to a better understanding of their geodynamic evolution, which is critical to an overall understanding of geodynamic changes in the Paleoproterozoic era. Many studies have been done to characterise the deformational history and geochemistry of the rocks. But without geological context, including that of the paleodepositional environment, stratigraphic relationships coupled with geochemical fingerprinting, reconstruction of their geodynamic evolution remains inconclusive and speculative.

Some vital questions arise from the literature review of the study area. These are:

- What is the volcanic architecture of the Boromo and Houndé greenstone belts, and what are their spatial and temporal relationships? If the lithostratigraphy of the Boromo and Houndé Belts is the same, does this imply similar geological history?
- What are the geochemical distinctions within the volcanic sequences of both belts? What is the implication(s) for the relationship between both belts? Texturally similar volcanic rocks could be genetically distinct.
- What constraints can be placed on the evolution of the magmatic rocks of the Boromo and Houndé belts? Did a pre-existing continental crust play a role in terrane evolution? Magmatic rocks reflect mantle source conditions and magma diversification process as the magma evolves. Geochemical fingerprinting gives indications of the mantle source conditions and crustal contamination.
- What are the implications of the geological history of the Houndé and Boromo greenstone belts on Paleoproterozoic geodynamics? Does their magmatic and tectonic history reflect a shift in the geodynamic evolution of the Earth?

2.4.1 Aim and objectives of the study

The principal aim of the study is to reconstruct the stratigraphy and volcanic architecture of the Houndé and Boromo greenstone belts to provide a framework for understanding the magmatic evolution and tectonic setting of both greenstone belts. This research will test this hypothesis: It is hypothesised that the Houndé and Boromo

greenstone belts are allochthonous terranes accreted in a subduction-accretion setting. A sub-hypothesis will investigate whether the allochthonous terranes are solely volcanic arcs (island or continental) against a myriad of exotic blocks. The critical test is to identify lithofacies akin to composite volcanoes with geochemical and petrological signatures associated with subduction-related magmatism. These objectives will be followed to help achieve the research aim:

- Reconstruct the volcanic facies architecture and paleodepositional environment of the Boromo and Houndé greenstone belt successions. This will be achieved by rock observation, facies analysis, and geochemical fingerprinting of rock types. (Research question 1).
- Geochemically characterise the coherent lithofacies to enable fingerprinting of distinct units across the study area. (Research question 2).
- Use the petrography and geochemistry of these distinct units to unravel the magmatic history. (Research question 3).
- Determine the magmatic age of the basal unit of both belts. (Research question 3).
- Integrate all findings to articulate a model that best explains the development of the Houndé and Boromo belts, tectonic setting, and its implications on the geodynamic evolution in the Paleoproterozoic era.

Chapter 3: Lithostratigraphy of the Houndé and Boromo greenstone belts

3.1 INTRODUCTION

Reconstruction of ancient volcanic successions is a challenging task. Precambrian volcanic successions are even more arduous to unravel due to limited continuous rock exposure, complex tectonic disruptions, and granitoid intrusions (Ayer et al., 2002; Barley et al., 2008; Thurston et al., 2008). An effective way to overcome this difficulty is by applying the principles of physical volcanology to help (1) identify the dynamics of volcanism; (2) recognise mechanisms responsible for the deposited/emplaced volcanic products; (3) determine the setting/environment of volcanism; and (4) understand relationships between syn-volcanic and post-emplacement deposits (Fisher, 1984; Cas & Wright, 1987; McPhie et al., 1993). Following this approach is important for identifying distinct facies and facies associations, which are the essential building blocks for unravelling the volcanic history. The relative timing of events using marker horizons (e.g. paleosols and unconformities) and robust radiometric dating are vital for stratigraphic correlation (Martí et al., 2018). This approach is not only useful for unravelling volcanic history but provides a stratigraphic framework for targeting and understanding controls of mineral deposits (Mueller, Chown, et al., 2000 and references therein). Furthermore, cryptic regional structures can be unveiled through stratigraphic correlation (e.g. Rosa et al. (2008); Rogers et al. (2014); Hayman, Hull, et al. (2015)).

The stratigraphy of the Houndé and Boromo greenstone belts is poorly understood and therefore restrains the reconstruction of their magmatic history. In this study, the principles of volcanology have been applied to sections of the Houndé and Boromo greenstone belts to unravel the volcanic history and provide a stratigraphic framework for investigating the magmatic evolution of both belts. To achieve the aim of this study, the following objectives were executed:

- Identify distinct facies and facies associations to determine the paleodepositional environment and mechanism of volcanism to reconstruct the volcanic architecture.

- Determine the relative timing of events to reconstruct the stratigraphy
- Propose a stratigraphic model for the Houndé and Boromo belts

3.2 METHODOLOGY

3.2.1 Fieldwork and sampling

Before fieldwork, relevant peer-reviewed literature on the study area was studied to inform on locations suitable for fieldwork and where field data was lacking. Subsequently, outcrop location, geochemical, structural, and geophysical data were collated from the 2016 West African Exploration Initiative (WAXI) database to plan fieldwork and sampling regime. Subsequently, fieldwork was done in October-November 2016 and January-February 2018 during the dry season. Based on the reconnaissance desk study, fourteen field transects were planned to cover the field areas of interest fully. The field transects were designed to run perpendicular to the strike of bedding to access the base and top contacts of each lithological unit. The orientation of transects also allowed for the estimation of the thickness of each lithological unit. A systematic approach was followed at each outcrop station to allow for consistency in field data. This included (1) recording outcrop location using a Garmin handheld GPS; (2) measure and record petrographic (e.g., texture, mineralogy) and structural features; (3) photographs of important field features were taken; and (4) collection of representative rock samples at key localities. A similar procedure was followed when using drill cores. The rock samples collected were processed for petrographic and geochemical analysis. The location of the outcrops and field transects is shown in Figure 3-1 and Appendix A Table A- 1.

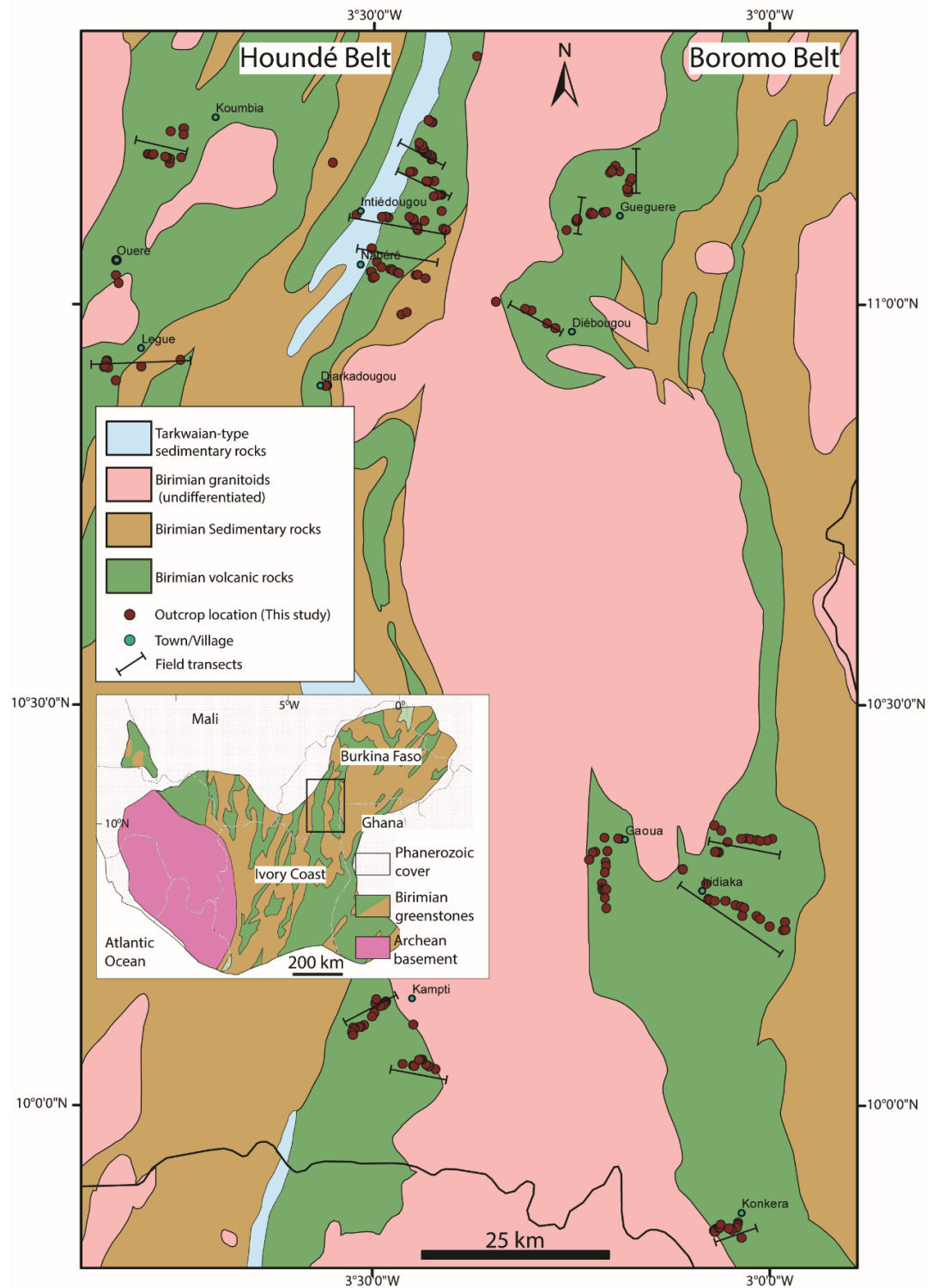


Figure 3-1 Simplified geological map of the Houndé and Boromo greenstone belts showing outcrop locations visited during this study and field transects. Inset showing study area location within the West African Craton. Map (including inset) modified from Milési et al. (2004). Map data source Chorlton (2007).

3.2.2 Analytical methods

Optical Microscopy

Thin (~5mm) billets of representative rock samples were mounted on glass slides and prepared into 30 microns polished/covered thin sections for micro-petrographic studies. The thin section preparation was done at the sample preparation lab at QUT CARF's Banyo Precinct. The thin sections were studied using the Leica DM6000 light microscope fitted with a camera for photomicrography. The purpose of the micro-petrographic studies was to document primary and secondary mineral phases and textures for rock classification.

X-Ray Diffraction (XRD)

Powder X-ray diffraction analysis was carried on nineteen samples for mineral phase identification. Before analysis, the samples were micronised using the McCrone mills to reduce the samples to fine powders (less than 5 μm) and dried overnight at 40 °C. Subsequently, the powdered samples were mounted on disks, pressed, and analysed by the Panalytical X'Pert vertical diffractometer using Corundum as the internal standard. The XRD data collected was reduced using the HighScore software followed by Rietveld refinement for phase identification and quantitative analysis. The results of this analysis are important for identifying and quantifying the alteration and metamorphic mineral phases. Results of the Rietveld refinement is presented in Table A- 2.

3.3 RESULTS

The rocks investigated in this study have been presented in two descriptive categories: coherent and fragmental lithologies following Cas et al. (2009). The coherent rocks are rocks formed by the cooling of molten magma, and the fragmental units are rocks made up of components derived from pre-existing rocks, juvenile clasts, and crystals (Cas & Wright, 1987; McPhie et al., 1993). Coherent lithological names are based on mineralogical and textural characteristics following Le Maitre et al. (2002), while the fragmental rocks are descriptive following Cas et al. (2009). Key features of sixteen major lithologies, including seven coherent and nine fragmental facies, are described below. The prefix ‘meta’ is omitted from the rock names to emphasise the protolith. Due to poor rock exposure and limited drill core, top and bottom contact relationships of most lithofacies could not be established. Additionally, the thickness of each lithofacies has been calculated using outcrop width and dip of primary bedding where possible. A summary of the major lithofacies is presented in Table A- 3.

3.3.1 Descriptions and interpretations of Coherent lithologies

Massive and Pillow Aphyric Basalts

The commonest rock type observed is aphyric basalt, constituting more than 50% of rocks in the study area. In most places, the thickness of aphyric basalts is on the order of 10’s of meters (Figure 3-3 A). The only contacts observed were sharp intrusive contacts with quartz-feldspar porphyritic dacites (Figure 3-3 C). The aphyric basalts are strongly foliated in most places, with the prominent foliation aligning roughly with the few primary bedding measurements.

The aphyric basalts are typically pale to dark green and massive or pillowed (Figure 3-3 B). The massive aphyric basalts are the dominant lithology and appear to be interdigitated with the less common aphyric pillow basalts. The massive aphyric basalts are typically non-vesicular and lack obvious internal variations. The pillows are rounded at the rim and taper into space between underlying pillows. Often, the pillows are rimmed by a devitrified glass layer (~5 mm thick) and exhibit radial joints. The inter-pillow spaces are commonly occupied by monomictic breccia (<5cm) of cryptocrystalline mafic clasts. The cross-sectional width of most pillows varies from 20–40 cm on the short axis but may exceed 50 cm when strongly deformed. The cores

of some pillows are characterised by vesicles infilled with silica and calcite (Figure 3-5 B).

The aphyric basalts are aphanitic to microporphyritic, consisting of plagioclase laths (10–15%; 0.5–1 mm) and subhedral green mineral with second-order interference colours (Figure 3-5 A). Based on the XRD analysis, the aphanitic varieties are made up of ~25% actinolite, 13% albite, 12% epidote, and other minor phases (Figure 3-2). These minerals presumably replaced primary groundmass olivine, plagioclase, and pyroxenes.

Massive and pillow plagioclase-porphyritic basalt

The plagioclase-porphyritic basalts are the second most abundant coherent lithofacies observed in the study area. Outcrops indicate a minimum thickness of 10 meters, while extrapolation between outcrops would make some more than 100 meters thick. No lithological contacts were observed. The plagioclase-porphyritic basalts are typically pale green and predominantly massive with few pillowed intervals (Figure 3-3 D). The plagioclase-porphyritic basalts are made up of relict plagioclase phenocrysts (30–50% 2–5 mm) set in microcrystalline groundmass (Figure 3-5 D). Often, the plagioclase crystals occur as glomerocrysts clusters with irregular resorbed boundaries (Figure 3-5 D). The groundmass of the plagioclase-porphyritic basalt is typically altered to sericite. The plagioclase phenocrysts have often undergone saussuritisation.

Massive Feldspar Megacrystic Basalt

The massive feldspar megacrystic basalts are rare and the only outcrop in a few places. They are generally pale to dark green, massive, and about 500 meters thick. Although not observed in this study, pillowed varieties are described in Baratoux et al. (2011). The massive feldspar megacrystic basalts contain prominent 5–10 cm milky white subhedral relict plagioclase crystals that are dispersed in a dark green fine-grained groundmass (<0.5 mm) (Figure 3-4 A & Figure 3-5 C). Feldspar abundance is variable, from typically ~15% to as much as 70%, and the lithofacies is gradational into aphyric massive basalt (Figure 3-4 B). The groundmass of the feldspar megacrystic basalts is fine-grained, and XRD analysis quantifies the groundmass as approximately 30% epidote, ~20% albite, 13% chlorite, and 7% actinolite (Figure 3-2). Quartz and epidote veinlets are usually present in most units.

Massive Pyroxene-porphyritic Basalt

The pyroxene-porphyritic basalts are rare, massive and dark green with thicknesses of a few tens of meters. The pyroxene-porphyritic basalts comprise ~30% 1-5 mm dark green blocky pyroxene phenocrysts in a fine-grained groundmass (Figure 3-4 C). Small amounts of plagioclase phenocrysts (<5%; ~3 mm) are present in some places. The phenocrysts often occur as glomerocrysts and are interpreted as clinopyroxenes based on their inclined extinction (Figure 3-5 E). The pyroxenes usually have resorbed edges, and some show sector zoning (Figure 3-5 F). The primary minerals of the pyroxene-phyric basalts are mostly altered to actinolite (37%), albite (26%), and chlorite (13%) (Figure 3-2).

Interpretation

The pillow basalts are indicative of subaqueous lava flows (Fisher, 1984). The massive basalts, on the other hand, are interpreted as subaqueous sheet flows. High-level intrusions of mafic magma can cool sufficiently quickly to produce aphyric textures and can be texturally identical to lavas. However, relatively thick mafic intrusions (>~100 m), even high-level ones, crystallise coarser-grained textures (doleritic to gabbroic) that are unknown in any unambiguous mafic lava (Hayman et al. 2019). Well-studied subaerial mafic extrusions, on the other hand, commonly display internal vesicle zonation and enable them to be readily distinguished from high-level intrusions (Self et al., 1996). Basalts that are >100's m thick, without coarser textures, strongly suggests an extrusive origin, while the lack of internal zonation is best explained by formation at depths sufficient to suppress vesiculation (Cas & Simmons, 2018). The association with pillow basalts is further support for a subaqueous origin.

Although internal contacts were not observed, the thick massive basalts must represent stacked flows. Typically, basaltic lava flows in large igneous provinces have average thicknesses of 15-50 meters thick (e.g. Columbia River basalts; Self et al., 1996), which is envisaged as a typical flow thickness for the massive and pillow basalts in this study, implying 10's to 100's of individual lava flows are stacked on top of one another. The pillow flows indicate low effusion rates, while the massive flows are formed by a high magma influx (Sager et al., 2011).

In terms of textural origin, the presence of phenocrysts is an indication of prolonged magma storage. The plagioclase phenocrysts imply magma storage at

relatively shallow depths under relatively low pressure (0-100MPa) and low temperature (~1100 °C) conditions (Cawthorn & Ashwal, 2009), before eventual eruption on the seafloor. The pyroxene phenocrysts suggest relatively deep magma storage conditions ($T = \sim 1200$ °C $P = 25\text{kb}$) (Cox et al., 1979; Gill, 2010). Furthermore, glomeroporphyritic texture may indicate a change in magma conditions (e.g. chemistry or temperature (Hogan, 1993)), leading to the agglutination of crystals. Feldspar megacrystic basaltic lavas are common in large igneous provinces (e.g. Deccan Traps; Higgins & Chandrasekharam, 2007; Sheth, 2016), mid-ocean ridge spreading centres and off-ridge seamounts (Lange et al., 2013; Valer et al., 2017), and Archean greenstone belts (e.g. Agnew greenstone belt, Hayman, Thébaud, et al., 2015). Many experimental studies have shown the megacrysts are commonly non-cogenetic with their host basalts (Valer et al., 2017) and ascribe the origin of the megacrysts to crystal-rich mush, which subsequently becomes entrained in an erupting mafic magma (Sheth, 2016).

Gabbro, Dolerite and Ultramafic lithofacies

The gabbros (>5 mm groundmass crystals) are generally massive, dark green, and observed in outcrops extending more than 10-20 meters with an estimated thickness of a few tens of meters. The gabbros comprise equigranular interlocking subhedral clinopyroxenes (~5mm, 30-50%) and tabular plagioclase (3-5 mm, 40%) (Figure 3-6 A & B). The pyroxenes are often altered to actinolite and chlorite (Figure 3-2).

The dolerites (1-5 mm groundmass crystals) are dark-green and massive, with thickness not exceeding a few meters. Contact relationships with surrounded rocks could not be established; however, some dolerites include basalt lithic fragments. The dolerites are predominantly medium-grained, composed of subhedral resorbed pyroxene crystals (~3 mm, 40%) and tabular plagioclase (2-3 mm, 30-40%). Some dolerites are composed of acicular hornblende crystals (1-3 mm, ~30%) instead of pyroxenes (Figure 3-5 E & F).

The ultramafic lithofacies is poorly preserved and rare. The thickness and contact relationship with surrounding units are unclear as they are very weathered. They are strongly foliated and magnetic. The relict texture is orthocumulate with ~20% subhedral mineral with abundant reddish-brown iron-oxide minerals. Thin sections of

this lithofacies could not be obtained because of their crumbly weathered nature. The primary minerals of the ultramafic rocks have been overprinted by talc (40%), actinolite (35%), and chlorite (16%) (Figure 3-2), indicating olivine was a major mineral phase.

Interpretation

The consistently coarse interlocking texture (>3mm) of the gabbro and dolerite lithofacies suggest they are intrusive as against ponded mafic lavas (Hayman et al., 2019). The ultramafic lithofacies are possibly differentiated zones of the mafic coarse-grained intrusives, where olivine accumulated.

Massive Hornblende-plagioclase porphyritic Andesite

The hornblende-plagioclase porphyritic andesites are typically pale-green (Figure 3-4 E), massive, and less than a meter thick. They do not exhibit strong deformational overprint and are predominantly made up of ~3 mm dark green prismatic hornblende (~20%), and in places, plagioclase (~5mm, ~30%) phenocrysts crystals contained in a microcrystalline groundmass (Figure 3-5). The hornblende phenocrysts often exhibit simple crystal zoning and twining (Figure 3-7 A), whereas the plagioclase crystals form glomerocrysts. In places, this lithofacies includes rare foliated aphyric basalt lithic clasts. The groundmass of the hornblende-plagioclase porphyritic andesites consists of microcrystalline plagioclase laths and acicular actinolite and abundant (~5) opaque iron-oxide accessory phases (Figure 3-7 B). The primary phases have been altered to actinolite, chlorite, and albite, with quartz occupying interstitial spaces.

Interpretation

Andesitic lavas are often thick, voluminous flows and are commonly associated with autobreccia. However, the hornblende-plagioclase porphyritic andesites observed are relatively thin (< 1 m) and lack an associated fragmental facies; they are more likely to be intrusions.

Massive Quartz-feldspar porphyritic Dacite

The quartz-feldspar porphyritic dacites are massive, only a few tens of centimetres thick and have sharp crosscutting contacts with their hosts; aphyric basalts (Figure 3-3 C). They are typically unfoliated and made up of tabular relict plagioclase (~30% 2-3 mm) and quartz (~30%, ~5 mm) contained in gray medium-grained

siliceous groundmass (Figure 3-7 C & D). The plagioclase phenocrysts are altered to sericite and only preserve remnant polysynthetic twinning (Figure 3-7 D). The quartz phenocrysts, on the other hand, are euhedral and exhibit embayments (Figure 3-7 C & D).

Interpretation

This lithofacies represents high-level intrusions of dacite into lithified crust based on the sharp nature of contacts and the presence of embayed quartz (Folk, 1974). In contrast to their hosting aphyric basalts, lack of foliation suggests they were emplaced later, perhaps post-deformational magmatic phase.

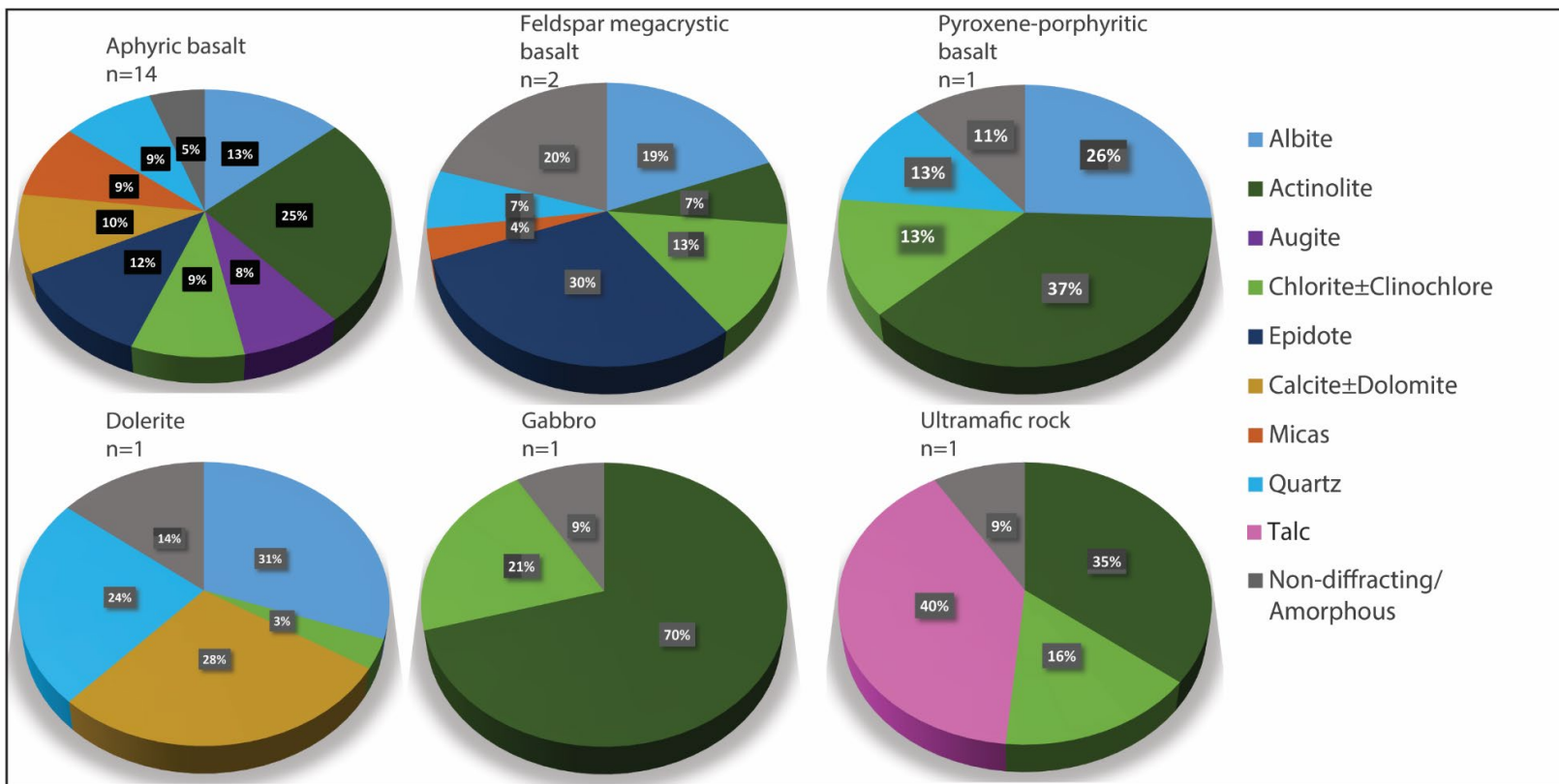


Figure 3-2 Pie charts illustrating the percentage abundances of mineral phases obtained from XRD analyses of selected lithologies from both belts. The results of the XRD analysis are presented in Appendix A Table A- 2.

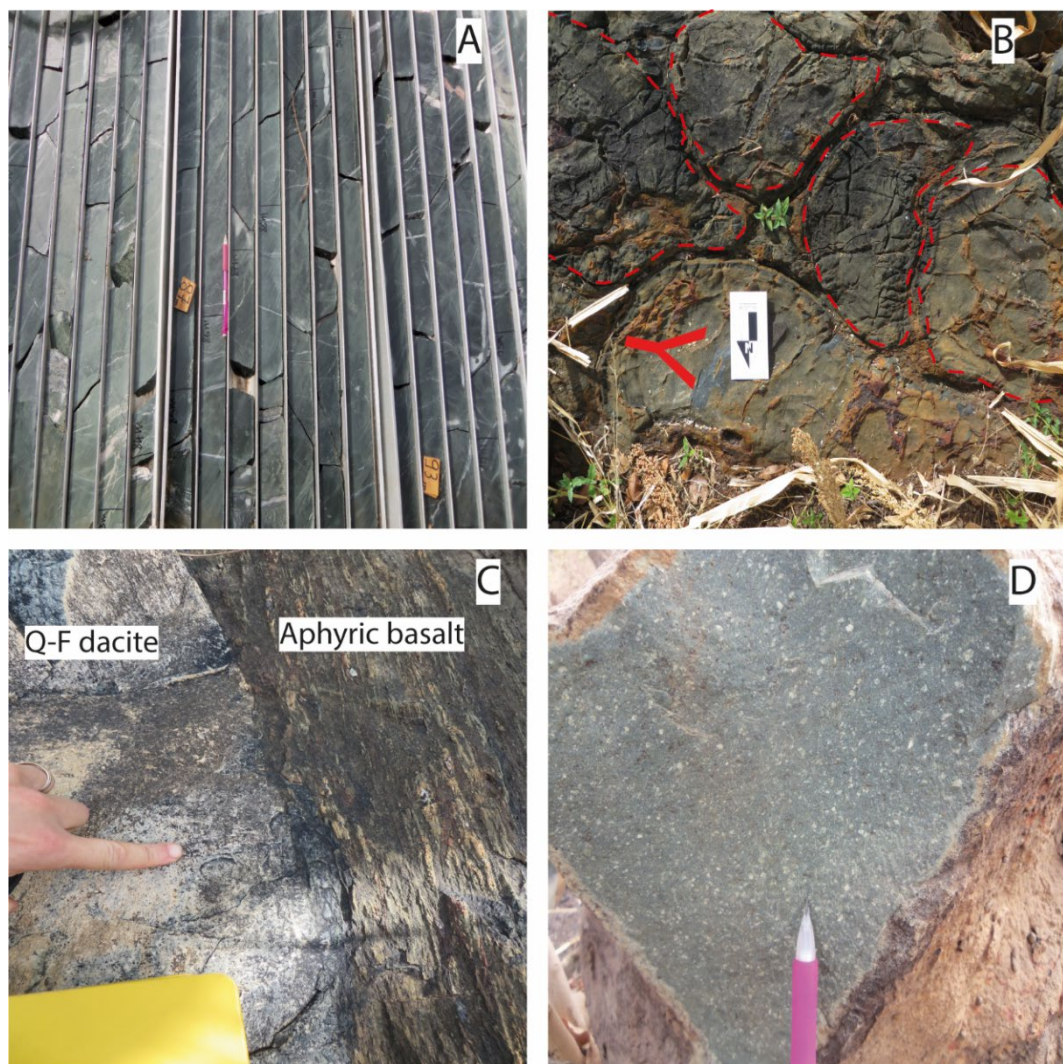


Figure 3-3 Photographs of A) Drill core showing at least 20 meters of massive aphyric basalt. B) Cross-section of well-preserved pillow aphyric basalt showing rounded pillow tops, eastward facing direction (408564, 1208185). C) Strongly foliated massive aphyric basalt intruded by unfoliated quartz-feldspar porphyritic dacite D) Massive plagioclase-porphyritic basalt (442536, 1115143).



Figure 3-4 Field photographs of A) Crystal-rich (~70%) massive feldspar megacrystic basalt showing plagioclase macrocrysts (~7cm) in fine-grained mafic groundmass (479149, 1142288). B) Crystal-poor massive feldspar megacrystic basalt transitioning into a massive aphyric basalt (492534, 1140459). Red circle showing feldspar macrocryst. C) Massive pyroxene-porphyritic basalt showing the characteristic blocky pyroxenes contained in pale-green fine-grained groundmass (477203, 1228672). D) Massive gabbro showing coarse-grained texture (480737, 1233035). E) Massive hornblende-plagioclase porphyritic andesite showing ~5mm euhedral relict plagioclase crystals and ~3mm hornblende crystal. An arrow pointing to plagioclase glomerocrysts (452512, 1219633). F) Massive quartz-feldspar porphyritic dacite. Red circle showing quartz crystal (450423, 1234344).

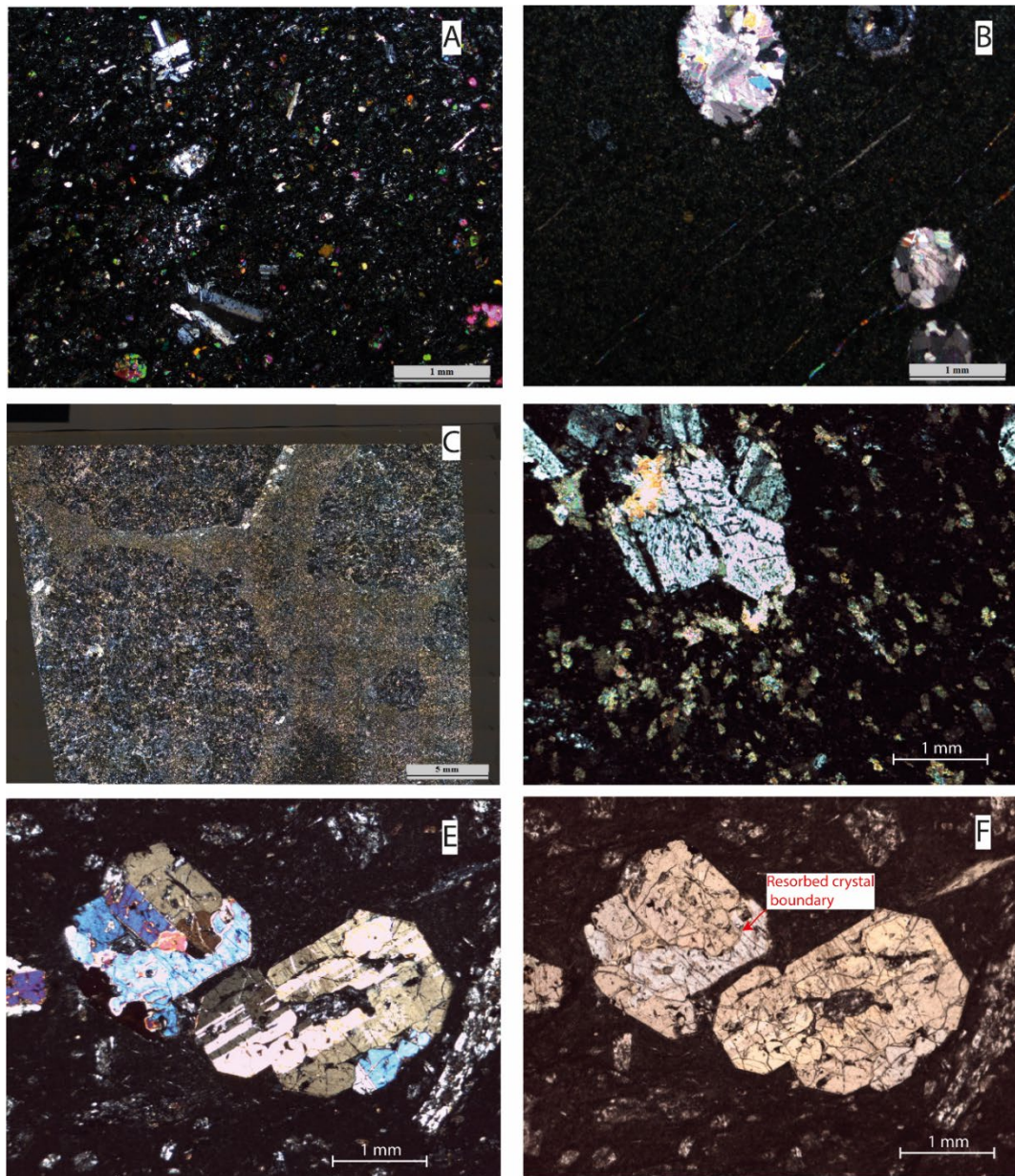


Figure 3-5 Crossed-polarised light thin-section microphotographs of A) Sparsely distributed tabular gray plagioclase microphenocrysts in a fine-grained groundmass of aphyric massive basalt. The second interference coloured mineral is epidote (450352, 1228077). B) Calcite-filled amygdules in aphyric pillow basalt (438773, 1204815). C) Mosaic image of feldspar megacrystic basalt showing sericite-altered feldspar macrocryst contained in a fine-grained groundmass. D) Plagioclase-porphyritic basalt contained in an altered groundmass. E) Pyroxene-porphyritic basalt showing prismatic pyroxene and plagioclase glomerocrysts contained in fine-grained groundmass (416765, 1203940). F) Plane polarised image of E) highlighting resorbed crystal boundary of glomerocryst.

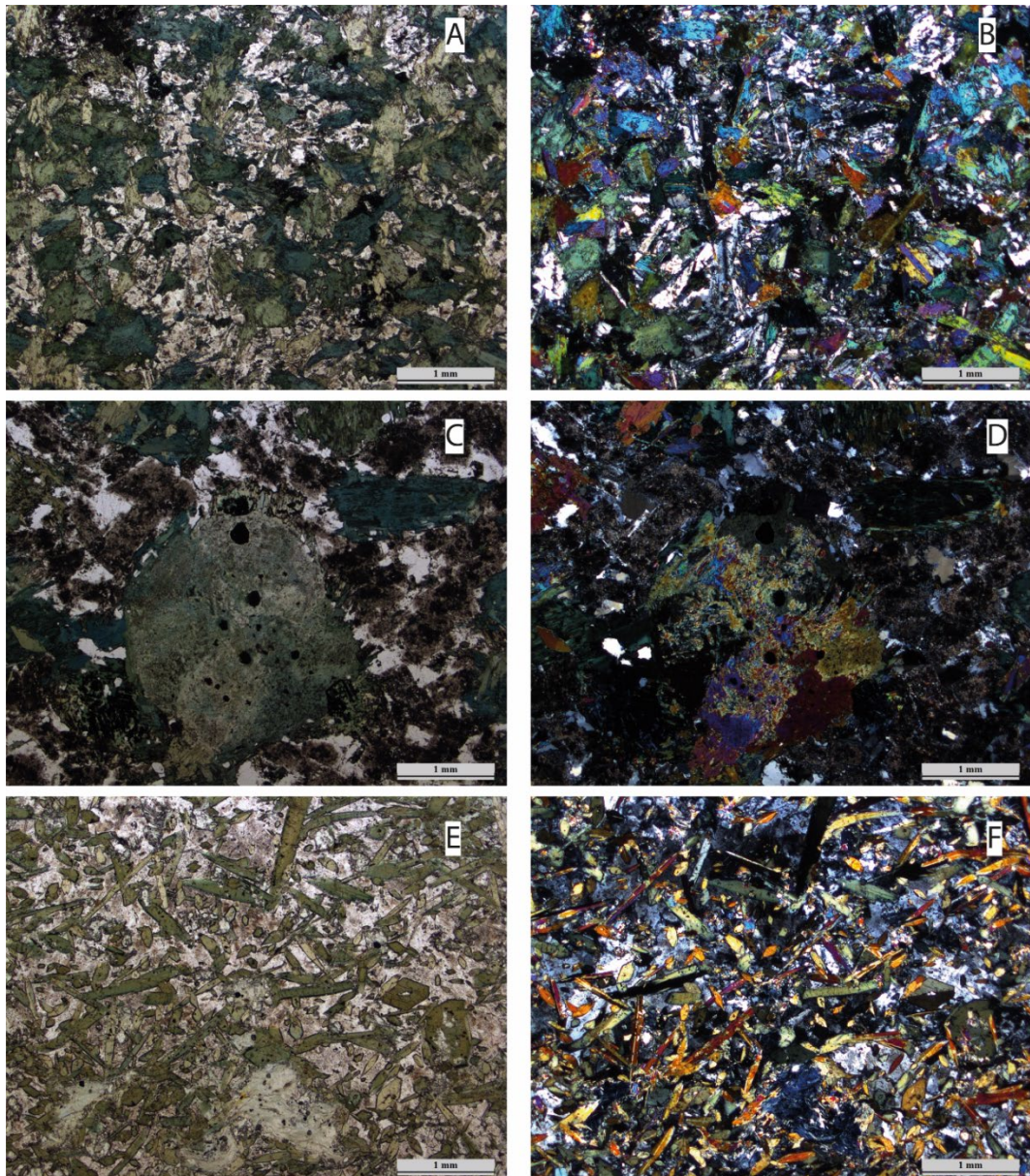


Figure 3-6 Thin-section microphotographs of A) Plane & B) crossed polarised light images of typical equigranular gabbro made up of plagioclase (tabular grey) and pyroxene converted to chlorite (anhedral first-order interference colours (478715, 1235136)). C) Plane & D) crossed polarised light images of gabbro showing sector zoning in pyroxene in center of the image (480737, 1233035) E) Plane & F) Crossed polarised images of dolerite with acicular actinolite crystals poikilitically enclosed by plagioclase (463438, 1215053)

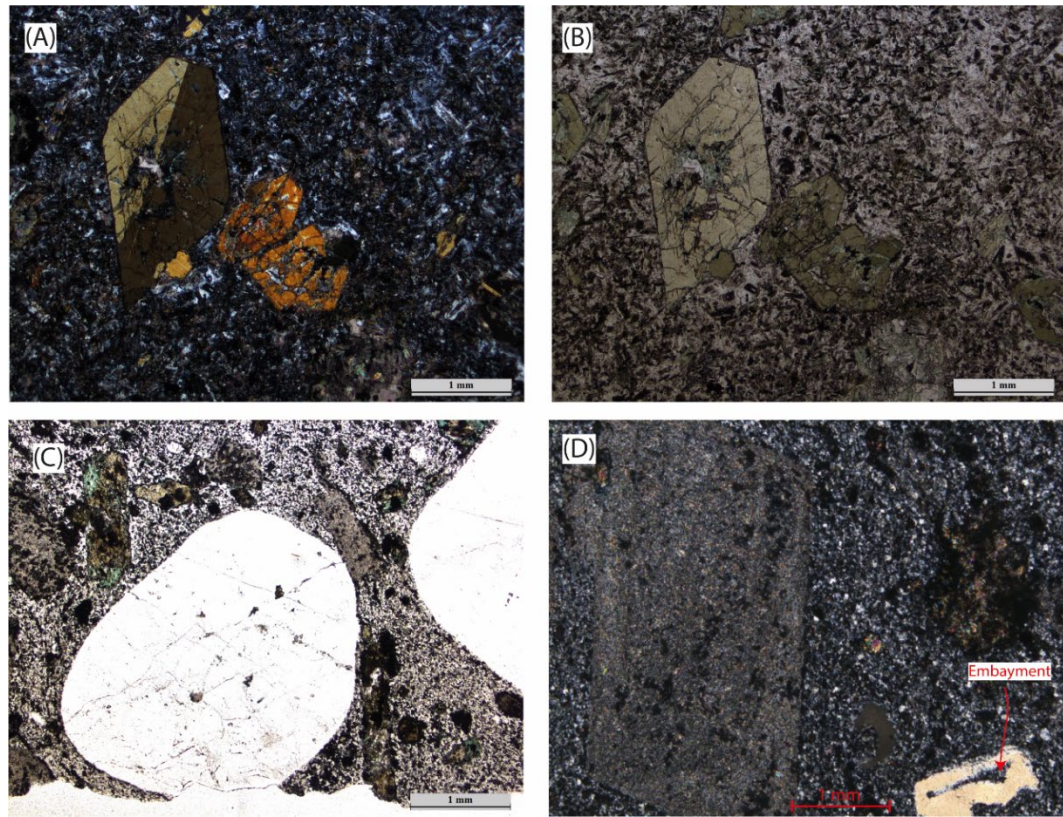


Figure 3-7 Thin-section photomicrograph of A) Crossed polarised image of Hornblende-plagioclase porphyritic andesite showing zoned hornblende phenocryst contained in a siliceous microcrystalline groundmass. B) Plane polarised light image of A) highlighting abundant opaque mineral in the groundmass. C) Plane polarised image of quartz-feldspar porphyritic dacite showing euhedral resorbed quartz phenocryst and altered plagioclase phenocrysts in fine-grained sericitised groundmass (450423, 1234344). D) Crossed polarised image of altered plagioclase phenocryst and quartz phenocrysts exhibiting embayment in quartz-feldspar porphyritic dacite

3.3.2 Descriptions and interpretations of Fragmental lithologies

Planar bedded mudstone-siltstone

The planar bedded mudstones-siltstones are commonly dark grey with rare cream-coloured varieties. In places, the mudstone beds are carbonaceous with a dull metallic sheen and strongly deformed. The transition from mudstone to siltstone beds commonly is sharp. Mudstone-siltstone beds are a few centimetres (1-3 cm) thick and typically form successions between 10-20 meter thicknesses (Figure 3-9 A). Rare coarser intervals are made up of feldspar microlites and minor lithic clast. No quartz was observed.

Massive to graded siltstone

The massive to graded siltstones are commonly grey with thicknesses of about 5cm (Figure 3-9 B). Overall thickness exceeds 10 meters. The massive beds are well-sorted and often transition into normally graded beds. Coarser intervals comprise feldspar crystals (~1 mm) in a fine grey matrix. No quartz grains were observed. The massive-graded siltstone is intercalated with the planar bedded mudstone-siltstone lithofacies.

Interpretation

The black colouration of the mudstone facies is characteristic of sediments deposited in an anoxic environment where oxidation weathering is inhibited, such as deep marine settings (Reading, 1996). The planar bedded mudstone-siltstone are products of suspensions settling due to the consistently fine texture and lack of internal structure (Shanmugam, 1997). The grading in the massive to graded siltstone lithofacies, coupled with lack of traction bed forms, is evidence of mass debris flow transport of sediments (Fisher, 1984). The lines of evidence presented are characteristic of turbidites as described by (Bouma, 1962). The planar bedded mudstone-siltstone beds represent the background environmental condition – low energy, anoxic deep marine setting (Mueller & Dimroth, 1987). In contrast, the massive-graded siltstone beds represent episodic mass flow deposits via turbidity current (Figure 3-8).

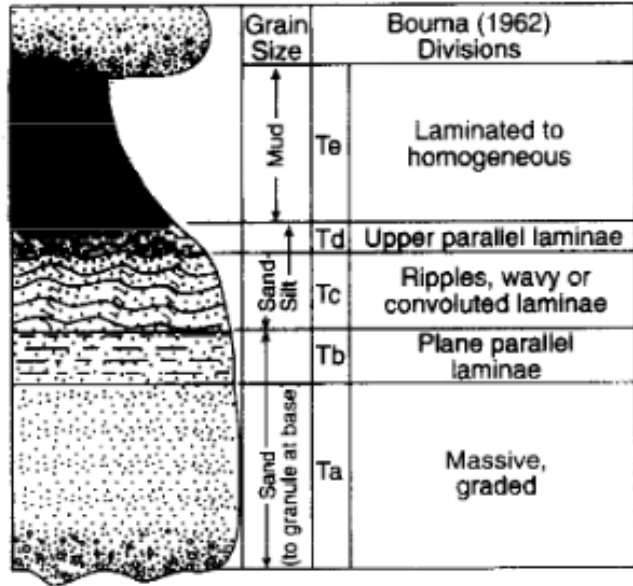


Figure 3-8 Classical Bouma Sequence showing the subdivisions of a complete turbiditic sequence by Bouma (1962). The planar bedded mudstone-siltstone represent (Td & Te) subdivision and the massive-graded (Ta). Image obtained from Shanmugam (1997)

Wavy to planar-bedded tuff

This facies is pale green with homogenous clay/ash-sized particles and characterised by wavy to planar beds that are at least 1 meter thick and form an overall succession roughly 10 meters thick. Asymmetrical centimetre-scale low-angle ($<20^\circ$) cross-beds truncated by the wavy layers are notable but rare features (Figure 3-9 C&D). The top contact of this lithofacies is truncated by the monomictic breccia lithofacies (Figure 3-11 C).

Interpretation

The preferred interpretation for the origins of this lithofacies is by pyroclastic processes, but the lack of detail on the clast origins makes it difficult to be certain. Cross-beds (antidunes) are formed by a unidirectional sediment-laden tractional current in the upper flow regime, which can occur in fluvial, marine, and volcanic environments (McPhie et al., 1993; Boggs, 2006). Hummocky cross-stratification, also characterised by low-angle and wavy bed forms, forms in subaqueous environments above wave-base during storm events (Boggs, 2006). The monomictic nature of the components implies a primary volcanic origin, as opposed to epiclastic origins, and would imply this lithofacies formed by pyroclastic surges. Fragmentation, in such a

case, would be by phreatomagmatic and transport by low-density currents (Cas et al., 1990).

Massive tuff-lapilli sandstone

The massive tuff-lapilli sandstone is dark grey with an average bed thickness of about 50 cm. This lithofacies is poorly sorted and typically massive; however, some units exhibit diffuse bedding (Figure 3-9 E&F). This lithofacies is mostly coarse-grained matrix-supported and comprises sub-rounded and angular lithic fragments of (20-40%, ~5 mm) feldspar-porphyritic and minor aphyric amygdaloidal volcanic clasts. Broken feldspar crystals (2–5mm) also make up the framework of this lithofacies (Figure 3-10 A&B) and are contained within a fine-grained grey altered matrix. There are two subfacies of the massive tuff-lapilli sandstone lithofacies based on the abundance of framework feldspar crystals. These are (1) the crystal-poor (feldspar <20%) matrix-supported, and (2) crystal-rich (feldspar ~40%) framework-supported subfacies (Figure 3-10 A & B).

Interpretation

The massive sandstones are made up of juvenile magmatic fragments sourced from an intermediate volcano (e.g. andesite/dacite) on account of abundant subhedral feldspar crystals and no ferromagnesian minerals. The massive internal character is consistent with transport and deposition by mass flow processes (Fisher, 1984). The sub-rounded nature of clasts and polymictic provenance most likely reflects epiclastic origins for this lithofacies.



Figure 3-9 (A) Drill core of thick (~15m) succession of planar bedded mudstone-siltstone lithofacies (CHDD0007- 409915, 1222184). (B). Section of drill core showing graded siltstone interval (~5 cm)

(C) Drill core of wavy planar-bedded tuff showing poorly defined bedding. D) Close-up outcrop photograph of C) showing low-angle cross-beds (red arrow) bound by planar beds (494802, 1088212).

E) Outcrop photo of massive tuff-lapilli sandstone pointing to feldspar-porphyritic clast, feldspar crystals, and fine-grained matrix (499706, 1141971). F) Diffuse bedding is seen in massive tuff-lapilli sandstone.

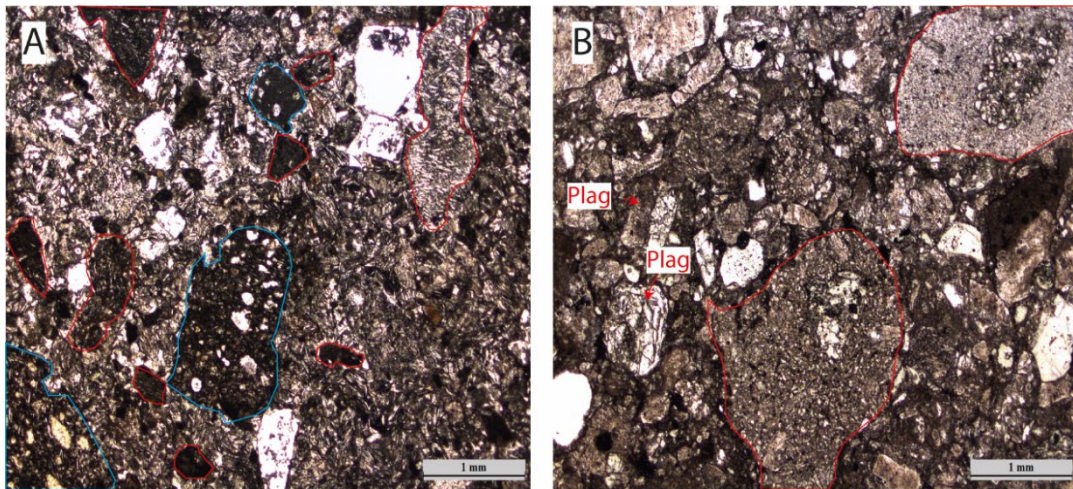


Figure 3-10 Plane-polarised photomicrographs of massive tuff-lapilli sandstone. A) Crystal-poor subsurfaces with fine-grained matrix (409915, 1222184). B) Crystal-rich subsurfaces showing feldspar-porphyritic fragments and abundant feldspar framework crystals. Plag = plagioclase (498686, 1131147). Blue outline=amygdaloidal aphyric basalt; red outline= feldspar-porphyritic basalt. Note: the absence of quartz.

Massive monomictic breccia

This lithofacies is massive, poorly sorted, and matrix-supported. Thickness and distribution are poorly constrained because of poor exposure, but this lithofacies is at least several meters thick and extends for a few 10's of meters. The massive monomictic breccia is made up of angular lithic fragments more than 7 cm in size. These lithic fragments are pyroxene-porphyritic basalts contained in a pale green fine to a medium-grained altered matrix (Figure 3-11 A). The clasts and matrix consist of prismatic pyroxenes crystals (2-3 mm, ~30%).

Interpretation

The preferred interpretation of the massive monomictic breccias is by mass wasting of the massive pyroxene-porphyritic basalt and transport by mass flows and en-mass deposition. The fragments of the monomictic breccias are similar to massive pyroxene-porphyritic basalt lithofacies on account of crystal abundance and texture. The massive and poorly sorted character of this lithofacies indicates transport and deposition through mass flows and en-mass freezing. Epiclastic and pyroclastic origins (dome collapse) were considered to account for the dense, large, and angular nature of the clasts. However, the absence of features indicative of hot emplacement (e.g., cooling joints) indicates an epiclastic origin is more likely (Mueller, Garde, et al., 2000). Other fragmentation modes were considered but rejected; quench

fragmentation of mafic magma produces cuspatate and smaller (<3 cm in size) clasts, while autobrecciation of mafic clasts produces blocky and angular clasts that are typically vesicular (McPhie et al., 1993). The most likely setting for the origins of this lithofacies is in and around over-steepened portions of volcanic edifices of the pyroxene-porphyritic basalt similar to volcanic debris-avalanche deposits (McPhie et al., 1993; Stewart & McPhie, 2006).

Graded volcanic breccia/conglomerates

The graded volcanic breccia/conglomerates range from ~1 to 10 meters thick and consist of volcanic fragments up to 10 cm in size. Top contacts are gradational into bedded mudstone-siltstone lithofacies, and the bases truncate underlying sedimentary lithologies (Figure 3-11 C&E). These graded volcanic breccias and conglomerates are typically clast-supported. Lithic fragment types and their proportions vary; some varieties are essentially monomictic, being dominated by 1-10 cm sized, angular to cuspatate-shaped, grey, and holohyaline volcanic fragments (Figure 3-11 B). In contrast, other varieties are polymictic, being dominated by sub-rounded clasts of feldspar-porphyritic basalts/andesites and aphyric (often flow banded) dacite/rhyolite clasts (Figure 3-11 D). The feldspar-porphyritic fragments comprise ~1 mm phenocrysts and range in abundance from 10-40%. The matrix of both varieties is typically light grey and lacks free crystals.

Interpretation

Graded beds form from density currents in standing water. However, the texture and composition of clasts indicate important differences about clast origins before entrainment into subaqueous mass flows. The grey angular to cuspatate-shaped volcanic clasts is interpreted as being basaltic to andesitic in origin. Their common angular to cuspatate-shapes is most consistent as products of quench fragmentation, making them hyaloclastite (Cas & Wright, 1987; McPhie et al., 1993). Hyaloclastite can be differentiated from autobreccia by the texture and size of fragments. Clasts produced by autobrecciation are typically blocky and relatively large (>5 cm), and the larger clasts likely have such origins. Epiclastic origins for the grey volcanic clasts are rejected because of their shapes and because epiclastic deposits tend to be more polymictic.

Breccias and conglomerates dominated by sub-rounded intermediate volcanic clasts represent re-deposited detritus derived from an emergent volcanic source. The abundance of plagioclase crystals in the clasts, and the absence of quartz, indicates an intermediate volcanic source (andesite to dacite). The rounded nature of clasts indicates they have spent a prolonged time in a fluvial or beach setting before eventual entrainment into subaqueous mass flows (Hayman et al., 2020). Angular clast populations (e.g., hyaloclastite and flow banded clasts) spent little to no time in a surface environment before entrainment.

Massive polymictic conglomerate

This lithofacies is poorly sorted, matrix-supported and massive, with intervals of poorly defined diffused bedding. Bedding thickness is averagely 50 cm and extends for at least several 10's of meters. This lithofacies is made up of 2–10 cm well-rounded lithic fragments contained in a pale green matrix (Figure 3-12 A). The lithic fragments include several varieties of porphyritic clast, of variable proportions and sizes of phenocrysts (mainly feldspar and hornblende), as well as aphanitic light grey volcanic and rare chert clasts (Figure 3-12 B). The matrix is fine to medium-grained and crystal-free.

Interpretation

This lithofacies is interpreted as the product of debris flows. The massive and poorly sorted character indicates transport and deposition were by mass flow processes. The phenocryst populations of the porphyritic volcanic lithic clasts are consistent with derivation from various intermediate volcanic sources. Aphanitic grey volcanic clasts are likely intermediate as well, and the chert clast indicative of sedimentary origin. The well-rounded nature of the clasts indicates prolonged abrasion in a fluvial or nearshore environment. Emergent intermediate volcanoes must have dominated the environment from which these clasts were sourced.



Figure 3-11 A) Outcrop photo of massive monomictic breccia showing large (>7 cm) of pyroxene-porphyritic basalt (417284, 1236194). B) Outcrop photo of graded monomictic breccia showing angular to cuspatate-shaped, grey, and holohyaline volcanic fragments of various sizes (1 cm to > 10cm). C) Drill core photo of B) monomictic breccia showing the base of succession (Red bar) truncating wavy to planar-bedded tuff lithofacies. D) Outcrop photo of graded polymictic conglomerate showing an interval of well-sorted lithic fragments and abundant intermediate volcanic clasts. E) Drill core of graded polymictic conglomerate showing the thickness (~ 5m) of beds (CHDD00007 409915, 1222184).



Figure 3-12 Outcrop photographs of massive polymictic conglomerates lithofacies. A) & B) Show a variety of matrix-supported subrounded to rounded lithic clasts comprising dominantly of plagioclase-porphyritic lithofacies and rare chert (Red circle) in medium to a fine-grained matrix (499706,1141971) (442994,1228410).

Quartz-rich sandstone

This lithofacies comprises three sub-facies: massive, planar, and cross-bedded quartz-rich sandstones (Figure 3-13 A, B & C). Bedding thickness ranges from about 10 cm for the planar bedded sandstones to ~1 m for the massive and cross-bedded sandstones. The cross-beds in this lithofacies are consistently high angled and westward-facing (Figure 3-13 A). The planar bedded units are defined by alternating bands of dark, heavy minerals and pink arkosic layers (<1 cm). This lithofacies is characteristically made up of abundant framework quartz crystals (>50%) and rare (~5%) mud rip-up clasts (Figure 3-13 C). The matrix comprises sericite and accessory minerals (Figure 3-13 E & F). The quartz crystals are sub-rounded, often polycrystalline, and show undulatory extinction.

Quartz-rich polymictic conglomerate

The quartz-rich polymictic conglomerate lithofacies are interbedded with the quartz-rich sandstone lithofacies. Contact between the quartz-rich sandstone and polymictic conglomerate is gradational. The thickness of a conglomerate bed may exceed one meter. The conglomerates are massive, matrix-supported, and poorly-sorted (Figure 3-13 D) and made up of well-rounded granite lithic clasts (~20%, 5cm), polycrystalline quartz, and minor quartz-feldspar porphyritic clasts contained in sand-sized quartz-rich matrix identical to the sandstone lithofacies.

Interpretation

Components of the quartz-rich polymictic conglomerate and sandstone were sourced from plutonic rocks due to abundant granite clasts and polycrystalline quartz and are interpreted as mature epiclastic sedimentary deposits based on the absence of mud in the matrix. The well-rounded clasts and high-angle cross-beds are consistent with deposition from tractional processes under a unimodal current, which are common in a fluvial system (Folk, 1974).

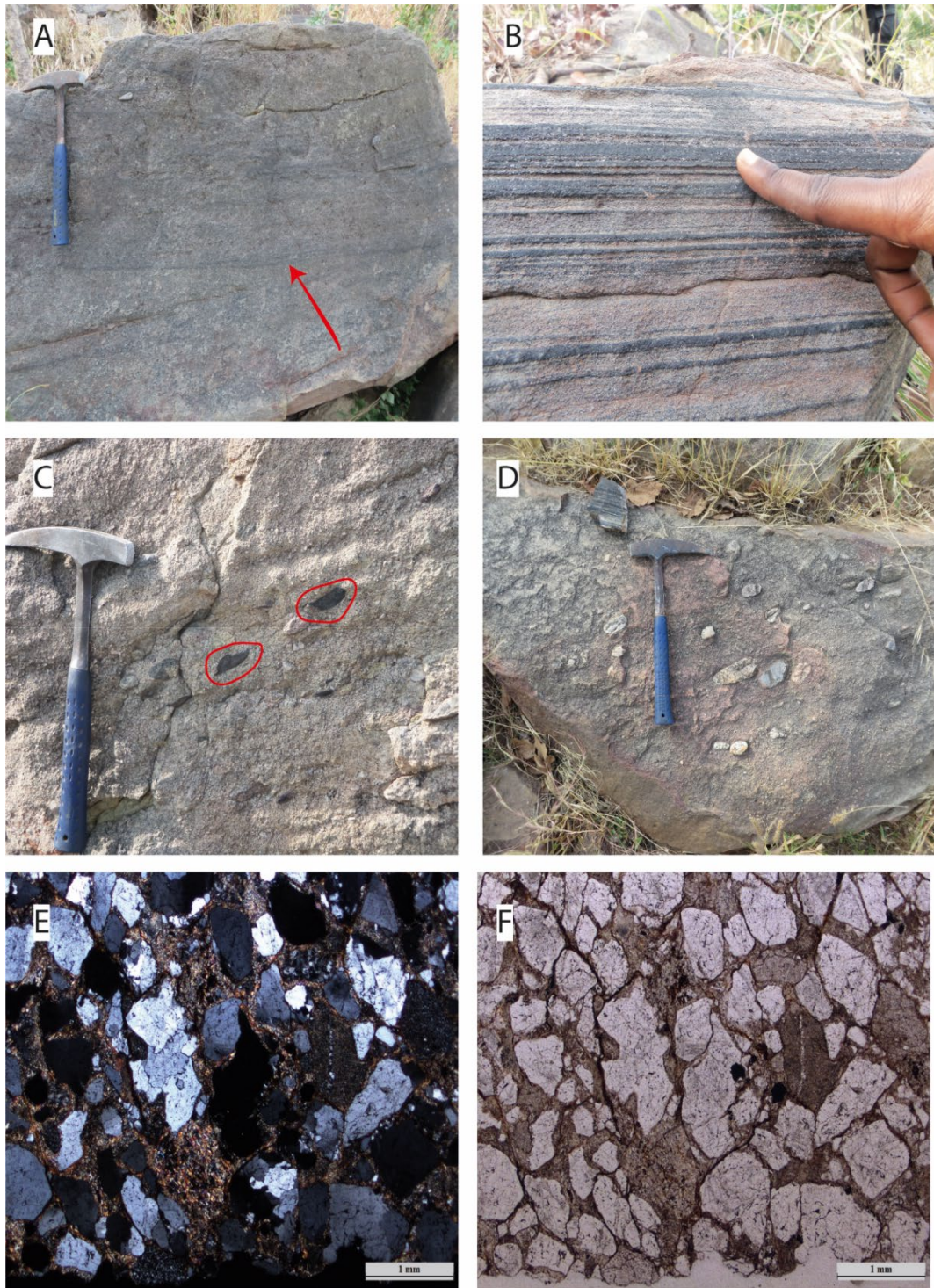


Figure 3-13 A) high-angle cross-bedding in quartz-rich sandstone (west-facing) (446432, 1228123). B) Thin (< 1cm) planar bedding in quartz-rich sandstone with bedding defined by dark bands of heavy minerals. C) Diffusely bedded pebbly sandstone. Outlined in red are mudstone rip-up clasts, which form less than 5% of lithic fragments. D) Poorly-sorted matrix-supported conglomerate. E) & F) Crossed-polarised and Plane-polarised photomicrographs of quartz-rich sandstone lithofacies showing abundant (>70%) polycrystalline quartz and micaceous matrix.

3.3.3 Description and interpretation of the Lithofacies associations (LFA)

The principal lithofacies of the Houndé and Boromo belts fall into one of four distinct associations based on the mode of emplacement, mode of fragmentation and deposition, the environment of deposition, and provenance of the fragmental rocks. The lithofacies associations have been mapped out along field transects to provide insight into the volcanic architecture and stratigraphy of the Houndé and Boromo belts. A summary of the key characteristics and interpretations of each lithofacies association is presented in Table 3-1.

Coherent Basalt association (LFA-1)

This lithofacies association is made up dominantly of coherent mafic lavas with subordinate intrusions. The coherent basalt association includes the massive and pillowd aphyric basalts, massive plagioclase-microporphyritic, feldspar megacrystic basalts, and associated dolerite, gabbro, and ultramafic lithofacies. The massive pyroxene-porphyritic basalts, hornblende-plagioclase porphyritic andesite, and quartz-feldspar porphyritic dacites are commonly hosted in this association but are excluded because of their post-deformational and intrusive origins (e.g., strongly deformed aphyric basalt intruded by quartz-feldspar porphyritic dacites; Figure 3-3 C)

The LFA-1 is restricted along the eastern margin of the Houndé belt (Map A; Figure 3-16 and Map B; Figure 3-17) and the western and central parts of the Boromo belt (Map D; Figure 3-19, Map E; Figure 3-20 and Map F; Figure 3-21). The lithofacies which make up this succession are present at all five sites, except for the massive feldspar megacrystic basalts, which are only found south of the study area in areas of Map B of the Houndé belt, and Map E and F of the Boromo belt (Figure 3-17, 19 and 20). Based on the stratigraphic reconstruction of LFA-1, massive and pillow aphyric basalts are the most dominant facies, and the plagioclase-porphyritic and feldspar megacrystic basalts are rare. Notably, the feldspar is typically found near the base of the succession and commonly transition into pillow aphyric basalts (BO-4 and BO-5 in Figure 3-19). The associated gabbros, dolerites, and ultramafic lithofacies are mostly found near the base of the succession (e.g., HE-3, HE-4; Figure 3-6), although some intrude the middle to upper parts of the succession (BO-1; Figure 3-19).

Because primary bedding measurements are rare, the effects of stratigraphic thickening and duplication are poorly constrained, the apparent thickness of the

association is presented as a maximum true stratigraphic thickness. Across the five sites where LFA-1 occurs, the thickness ranges from 4000 to 6000 meters. Younging direction, as judged from pillows in the coherent basalt association and sedimentary structures from lithofacies outside of the basaltic association, is westward in the Houndé Belt and eastward in the Boromo Belt. Stratigraphic sections constructed from field transects HE-3 in the Houndé belt, and BO-5 in the Boromo belt reveal the LFA-1 constitutes a thick succession of at least 5000 meters (Figure 3-16 & Figure 3-19). No repeated marker horizons have been observed within these transects to identify stratigraphic duplication unambiguously.

The LFA-1 is interpreted to have been emplaced in a subaqueous setting due to interdigitated pillow lavas (Fisher, 1984). Additionally, the paucity of vesicles and thickness (100's m) of massive basalt indicate deep water conditions (>1000 m) where hydrostatic pressures exceed 20 MPa and vesiculation of exsolved volatiles is prohibited (Cas & Simmons, 2018). The lack of interbedded sedimentary intervals suggests that there were no nearby emergent landmasses. The dolerite, gabbro, and ultramafic lithofacies are interpreted as synvolcanic intrusions because of the similarity of deformational intensity to the basalt hosts. They appear to be mostly concordant (sill-like) in geometry and may represent feeders to overlying extrusions. The estimated thickness (~5000 m) and a rough estimate of the areal extent (>10,000 km²) of the LFA-1 in both belts are consistent with dimensions of large igneous province according to Bryan and Ernst (2008).

Therefore, LFA-1 is interpreted as extensively constructed deepwater mafic lava flow fields.

Mafic-intermediate volcanic Association (LFA-2)

The mafic-intermediate volcanic lithofacies association (LFA-2) comprises massive and pillow aphyric basalt, plagioclase-porphyritic basalt, pyroxene-porphyritic basalt, massive hornblende-plagioclase porphyritic andesite, and quartz-feldspar porphyritic dacite lithofacies. The coherent aphyric and porphyritic lithofacies are interleaved with gabbros and dolerites and the following fragmental lithofacies: wavy to planar bedded tuff, massive tuff-lapilli sandstone, massive and graded monomictic and polymictic breccia/conglomerates lithofacies. Textures and pillows are notably well preserved compared to those of LFA-1. The lithofacies which make up LFA-2 were observed in the Houndé belt in the west (Map C; Figure 3-18), in the

south (Map B; Figure 3-17), and the Boromo belt (Map D; Figure 3-19). Based on field transects (HE-5, HE-6 HW-7, and BO-5), this lithofacies association is estimated to have an apparent thickness of about 4000 meters. However, this thickness is likely broken up by intervals of LFA-3, which is generally poorly preserved.

The depositional setting of LFA-2 is subaqueous based on the presence of pillows, graded beds, and common association with bedded mudstone-siltstone of LFA-3. Many massive breccias and conglomerates lack associated lithologies with internal diagnostic structures to constrain the depositional environment. The presence of sub-rounded to rounded intermediate volcanic clasts in the graded volcanic conglomerate lithofacies indicates emergent volcanic islands within the depositional basin (Hayman et al., 2020). Most of the fragmental lithologies are polymictic, intermediate in provenance (notably quartz crystals are rare to absent), and consistent with epiclastic origins. It is not possible to form a complete reconstruction of the internal architecture of this lithofacies association on account of the sporadic nature of outcrop and scope of the study, but two areas with a higher density of data are useful for providing more detail.

At Ouere (Map C), the examination of one drill hole (CHDD0007) and field traverse (HW-8) through the same sequence provides a detailed picture for a small period of the construction of LFA-2 (Figure 3-18). The LFA-2 in this location predominantly comprises sub-rounded intermediate volcanic clasts representing a fluvial or nearshore environment. The sediments were subsequently remobilised and deposited into deeper waters either by turbidity currents (forming the graded bedded polymictic conglomerates) or debris flows (massive polymictic conglomerate). The grey angular to cuspatate volcanic clasts (interpreted as hyaloclastite) is also common in this association. Hyaloclastite commonly forms when lavas enter the sea or when lavas erupt at relatively shallow depths (<1000 m; Cas and Simmons (2018)). The angular-cuspatate shaped clasts have subsequently been remobilised by turbidity currents, forming the graded monomictic breccias. The depth and proximity to the volcanic island are difficult to constrain. However, if the wavy to planar-bedded tuff is indeed a product of a subaqueous base surge from a pyroclastic eruption, then the depth could be deeper than a storm wave base up to ~1000 meters depth. At far greater depths, explosive fragmentation by magma-water interaction is not possible because the

expansion of steam is minimal under such pressures (Cas & Simmons, 2018). The conglomerates and breccias are interbedded with the planar bedded mudstone-siltstones in CHDD0007, indicating periods of magmatic quiescence and cessation of mass/debris flows.

North of Ouere, the field transect HW-7 records a similar history of mass wasting of a volcanic edifice (Figure 3-18). Here, the massive monomictic breccia (with pyroxene-porphyritic lithic clast) lithofacies proximal to coherent massive pyroxene-porphyritic basalt is interpreted as debris-avalanche deposits. This establishes that there were pyroxene-porphyritic basaltic volcanic edifices that collapsed, producing the breccias. Various mafic to intermediate volcanic lithic clasts and lack of extensive lateral continuity indicate discrete volcanic centres. The presence of conglomerates in this lithofacies association is evidence for emergent volcanic edifices.

Therefore LFA-2 is reported as deep-shallow water mafic to intermediate lava fields intercalated with synchronous volcaniclastic deposits and associated resedimented products forming discrete emergent volcanic edifices such as stratovolcanoes and tuff cones.

Fine-grained sedimentary Association (LFA-3)

This lithofacies association is composed of the planar bedded mudstone-siltstone and massive-graded siltstone lithofacies. The fine-grained sedimentary lithofacies is interdigitated with LFA-2 and (seemingly) forming a large poorly exposed area in the central and south Houndé belt and south Boromo belt (Figure 3-18). Drill core CHDD0007 intercepts more than 20 meters of LFA-3. The overall thickness of LFA-3 is difficult to constrain due to intense folding (e.g., Map F; Figure 3-21). An intermediate provenance is interpreted for LFA-3 based on the abundance of feldspar crystals and paucity of quartz grains within the coarser intervals. Planar beds and the absence of symmetrical ripples reflect the depositional environment must have been low-energy and below wave base with some sediment transport by turbidity current (Bouma, 1962; Mueller & Dimroth, 1987).

Quartz-rich sedimentary Association (LFA-4)

This lithofacies association comprises quartz-rich sandstone and polymictic conglomerate and, in contrast to the other lithofacies associations (LFA-1, 2 and 3), is sourced primarily from felsic plutonic lithologies. This sedimentary succession was

only observed in the Houndé belt (Map A; Figure 3-16). The thickness of the entire succession may exceed 2000 meters. Primary bedding is consistently westward-facing with shallow dipping ($\sim 20^\circ$) roughly north-south trending beds. The presence of large cross-beds, coupled with the absence of graded beds, is consistent with a fluvial system (Krapež et al., 2008). This suggests a predominantly subaerial depositional setting for the LFA-4. This lithofacies association has a similar quartz-rich provenance to the Tarkwaian sedimentary group described by Bossière et al. (1996); Koffi et al. (2016) in western Burkina Faso and Pigois et al. (2003) in south-western Ghana. But temporal data is needed before ascribing this to the Tarkwaian group of the Birimian Supergroup with confidence.

Table 3-1 Summary of the lithofacies associations and interpretation of the paleodepositional environmental present in the Houndé and Boromo belts.

Lithofacies association (LFA)	Interpretation
Coherent basalt association (LFA-1)	
Massive and pillow aphyric basalt, massive plagioclase-microporphyritic and feldspar megacrystic basalts interleaved with dolerite, gabbro, and ultramafic lithofacies	Deepwater effusive mafic volcanism. Flood basalts
Mafic-Intermediate volcanic association (LFA-2)	
Massive and pillow aphyric basalt, plagioclase-porphyritic basalt, pyroxene-porphyritic, hornblende-plagioclase porphyritic andesite, quartz-feldspar porphyritic dacite interleaved with gabbros and dolerites, and Wavy to planar bedded tuff, massive tuff-lapilli sandstone, massive monomictic breccias, and massive to graded volcanic breccias/conglomerates	Subaqueous effusive and pyroclastic mafic-intermediate emergent volcanic centres, associated mafic intrusive rocks, and epiclastic deposits
Fine-grained sedimentary association (LFA-3)	
Planar bedded mudstone-siltstone, Massive-graded siltstone	Distal low-energy, deepwater setting, sediment transport by turbidity current
Quartz-rich sedimentary association (LFA-4)	
Quartz-rich sandstone and Polymictic conglomerate	Post-magmatic sedimentary basins. Fluvial setting

3.3.4 Foliation measurements and other structural observations

Structural data were collected from the dominant foliation at most field sites and magnetic lineaments in various geophysical datasets. Bedding measurements (S_0) are rare, especially in LFA-1; however, most outcrops preserve a pervasive foliation (S_1). These data are plotted on stereonets for all sites in the LFA-1, while all sites are combined for the LFA-2-3 in the Boromo and Houndé belts, respectively (Figure 3-14).

Although data on primary bedding (S_0) is limited, few bedding measurements have been obtained from pillow lavas. In the Houndé belt, general bedding trends northeast-southwest, dips are averagely sub-vertical ($\sim 60^\circ$), and generally westward-facing (Figure 3-14 A). On the other hand, bedding in the LFA-1 in the Boromo belt is eastward facing and generally trends northeast-southwest and northwest-southeast with dips of about 50° . In the case of LFA-2, the primary bedding in both belts trends north-south and northeast-southwest with sub-vertical dips. In the Boromo belt, the primary bedding is consistently eastward facing, while in the Houndé belt, bedding is westward facing on the eastern margin and eastward facing on the western margin. The bedding orientation in the Houndé belt is indicative of synclinal folding (Figure 3-14 B). Two contrasting foliation orientations are common to both LFA-1 and LFA-2; a bedding parallel (S_1) and a cross-cutting foliation (referred to as S_2 in this study). The S_2 foliation orients roughly east-west and north-south dipping.

Aeromagnetic geophysical data of varying quality were obtained for the area of Map A, C, D, E, and F (Figure 3-16–21). Magnetic lineaments are prominent in LFA-1 and 2 and difficult to discern in LFA-3 and LFA-4. The most prominent lineaments for LFA-1 are observed in the total magnetic intensity (TMI) of map area A in the Houndé belt (Figure 3-16). Here the lineaments roughly trend between 035° – 040° (NE-SW) and are truncated by LFA-4. The general trend of the LFA-1 geophysical lineament is consistent with S_0 primary bedding and S_1 foliation measurements. Magnetic lineaments in the LFA-2 of the Houndé belt roughly trend 020 – 030° and correspond to S_0 and S_1 (Map C; Figure 3-18). Notably, S_2 foliation orientation does not have an obvious magnetic signature.

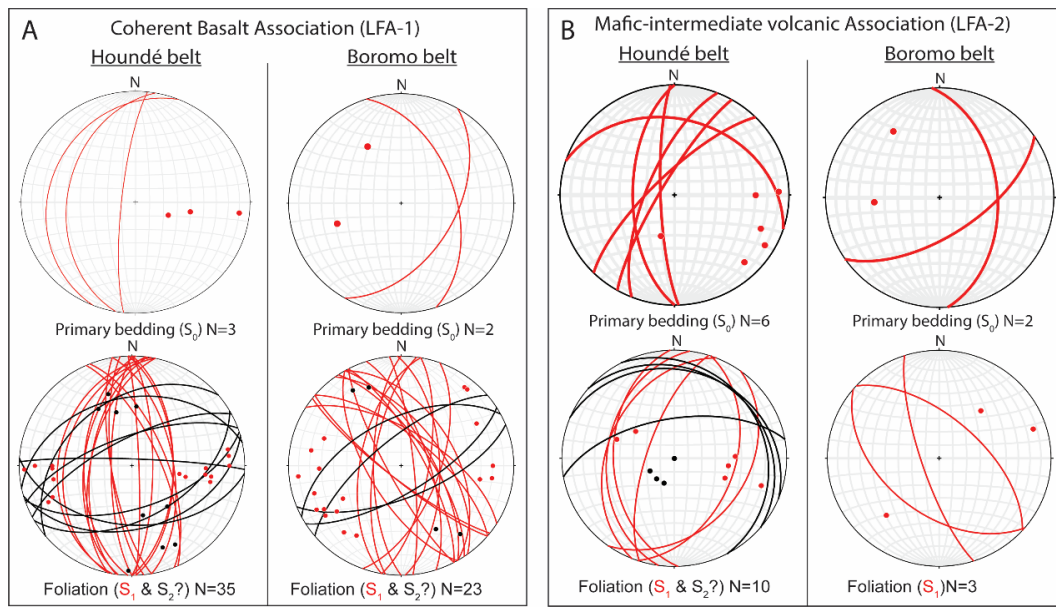


Figure 3-14 Equal area stereographic projections of field structural measurements plotted for A) LFA-1 and B) LFA-2 of the Houndé and Boromo belts showing the general orientation of bedding and foliation.

3.3.5 Nature of contacts bounding lithofacies associations

Here the nature of the contacts between the lithofacies associations is considered. Bounding contacts for the LFA-1 were not observed. However, field mapping and geophysical datasets indicate the lower bounding contact is always with felsic plutonic bodies (e.g., HE-4; Figure 3-16, BO-3; Figure 3-19). Neither apophyses nor basal breccias were observed to help distinguish late granitic intrusions that post-date mafic volcanism versus granitic plutons that form the basement of LFA-1. The upper contact based on geophysical data is truncated by the lower contact of LFA-4 in Map A (Figure 3-16). It appears to be discordant based on the bedding and foliation orientation. In the southern part of the Houndé belt (Map B; Figure 3-17), general bedding in the LFA-2 is discordant to the LFA-1, and the lower bounding contact is with LFA-3. This observation also occurs south of the Boromo belt (Map F; Figure 3-21). In other places, however, LFA-1 is overlain by LFA-2, although not directly observed (e.g. BO-2 in Map D; Figure 3-19, BO-4 and BO-5 in Map E; Figure 3-20).

On the western margin of the Houndé belt, the lower contact of LFA-2 is close to granitic rocks, based on field mapping and geophysics. Here it is unclear if the granite represents a basement or is intrusive into LFA-2 (Figure 3-18). The lower

contact of the LFA-3 is complex to unravel but appears to have a tectonically-strained contact with the LFA-1 in drill core KRND416 (Map F; Figure 3-21) and elsewhere transitional and interdigitated with graded beds of LFA-2 (CHDD0007; Figure 3-18). In the area of Map C, there is evidence of a syn-depositional intrusion of coherent pyroxene-porphyritic basalt and quartz-feldspar porphyritic dacite of LFA-2 into wet unconsolidated mudstones of LFA-3 represented by ductile peperitic contacts (Figure 3-15). The top contact of LFA-4 was not observed; however, based on reconstructed Map A (Figure 3-16), it appears to be in contact with the base of LFA-2.

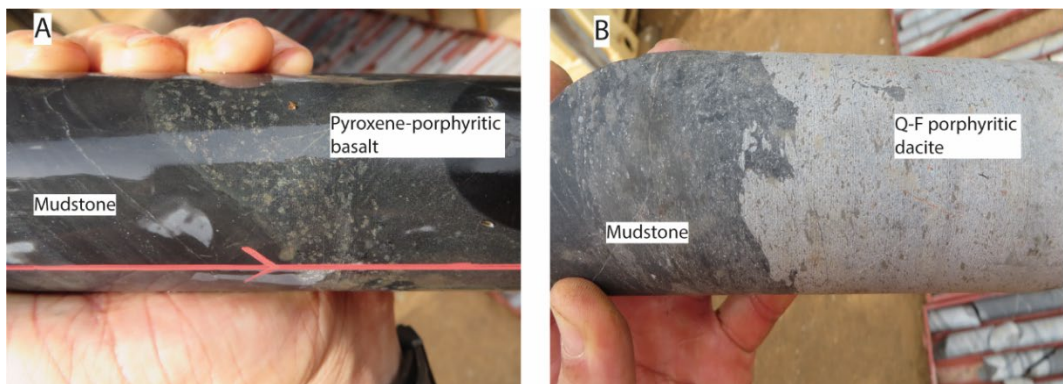


Figure 3-15 A) Sharp contact between coherent pyroxene-porphyritic basalt and planar bedded mudstone-siltstone. B) Peperitic contact between quartz-feldspar porphyritic dacite lithofacies and unconsolidated planar bedded mudstone-siltstone in CHDD00010 (413318, 1210000).

3.3.6 Relative timing

The relative timing of events is established using cross-cutting relationships, differences in deformation histories, as well as provenance and summarised in (Figure 3-22). LFA-1 likely forms the oldest supracrustal package observed in the study area. There is no field evidence (e.g., apophyses) to indicate that adjacent granitic rocks are intrusive. However, the absence of basal breccias and in comparison with other greenstone belts in the WAC, most granitic rocks are syn-D1 (~ 2160 Ma) or younger intrusions (Baratoux et al., 2011). LFA-1 seems to have experienced more intense deformational events not recorded by the other lithofacies associations, perhaps a pre-D1 event. Baratoux et al. (2011) and Tshibubudze et al. (2015) observed cryptic pre-D1 deformational event (thus >2160 Ma) in greenstones of south-western and north-eastern Burkina Faso perhaps contemporaneous with earlier deformation suggested for LFA-1.

The LFA-1 includes several coherent lithofacies of the LFA-2 (i.e., hornblende-plagioclase porphyritic andesites and quartz-feldspar porphyritic dacite) that lack pervasive foliations indicating intrusion after LFA-1 experienced an earlier deformational event. With matching intermediate character to similar lithofacies in the LFA-2, these intrusions may represent feeders to their overlying extrusive counterparts. The cross-cutting relationship of feeder dykes of LFA-2 in LFA-1 indicates the two associations were juxtaposed at some point during the formation of LFA-2. Thus LFA-1 presumably outdates LFA-2. The LFA-3 is commonly interdigitated with LFA-2, which implies they are contemporaneous, and this is supported by similar syn-depositional intrusions. Additionally, the absence/paucity of quartz crystals in the matrix and lithic clasts is an indication that LFA-3 precedes any felsic magmatism. On the other hand, LFA-4 consists of abundant quartz crystal (framework and matrix), which links it to extensive erosion of granitic bodies (felsic magmatism), and therefore post-dates LFA-2 and LFA-3, hence the youngest supracrustal succession.

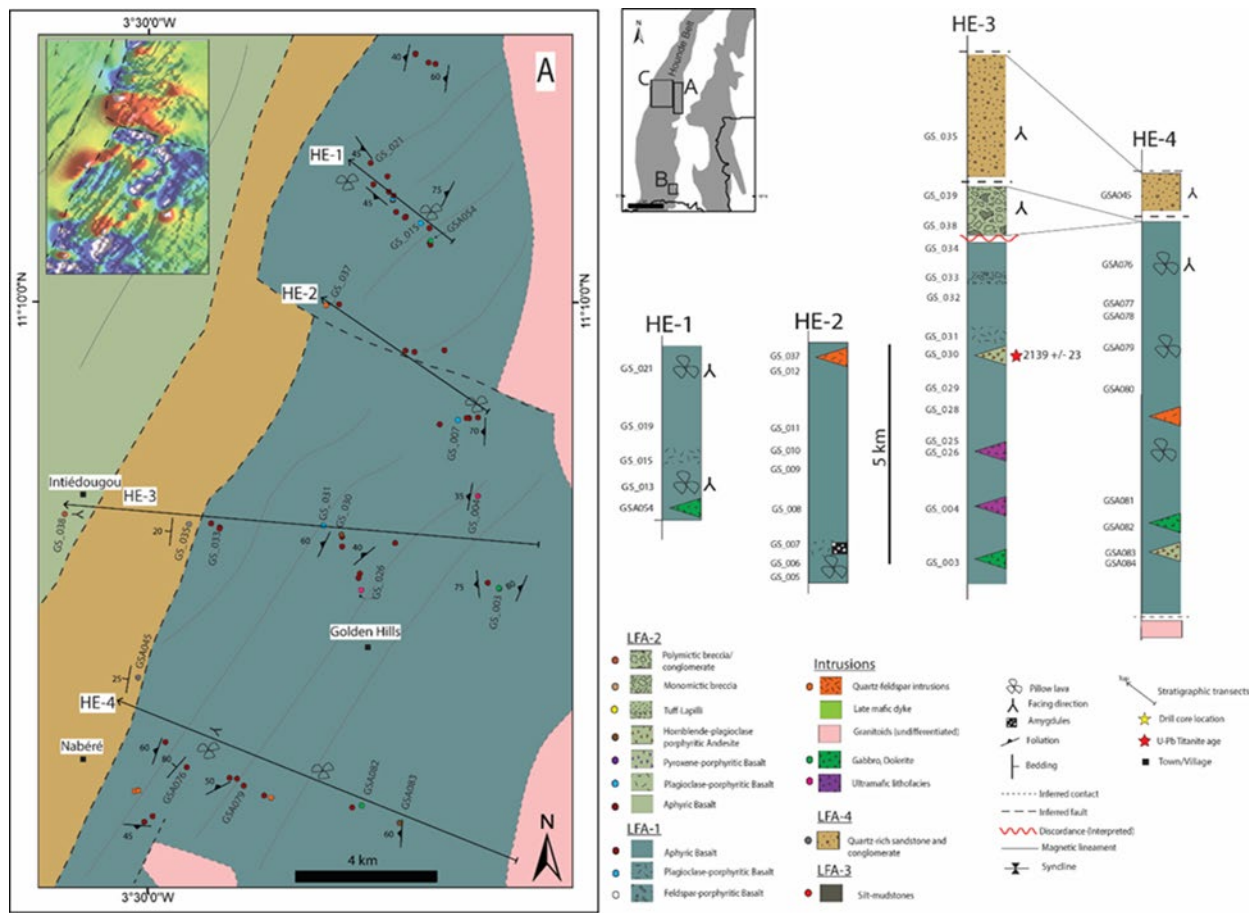


Figure 3-16 Local geology of study area-Map A (location in inset) with outcrop sites, field transects, structural measurements and stratigraphic sections (HE-1-4) reconstructed from field transects. Coordinate system- WGS 84 UTM zone 30N. Total magnetic intensity map courtesy Gryphon Minerals.

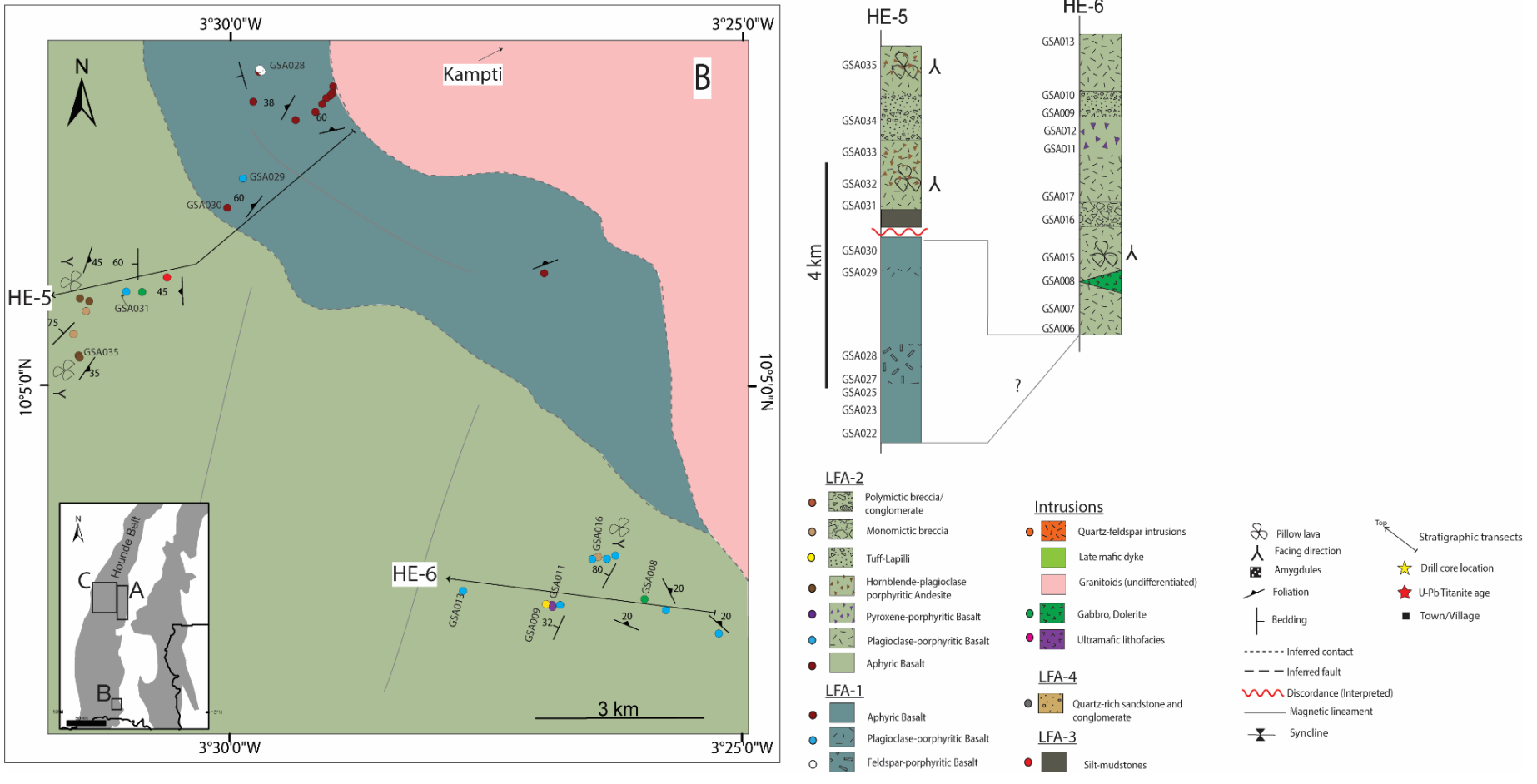


Figure 3-17 Local geology of study area-Map B (location in inset) with outcrop site, field transects, structural measurements and stratigraphic sections (HE-5 & 6) reconstructed from field transects. Coordinate system- WGS 84 UTM zone 30N

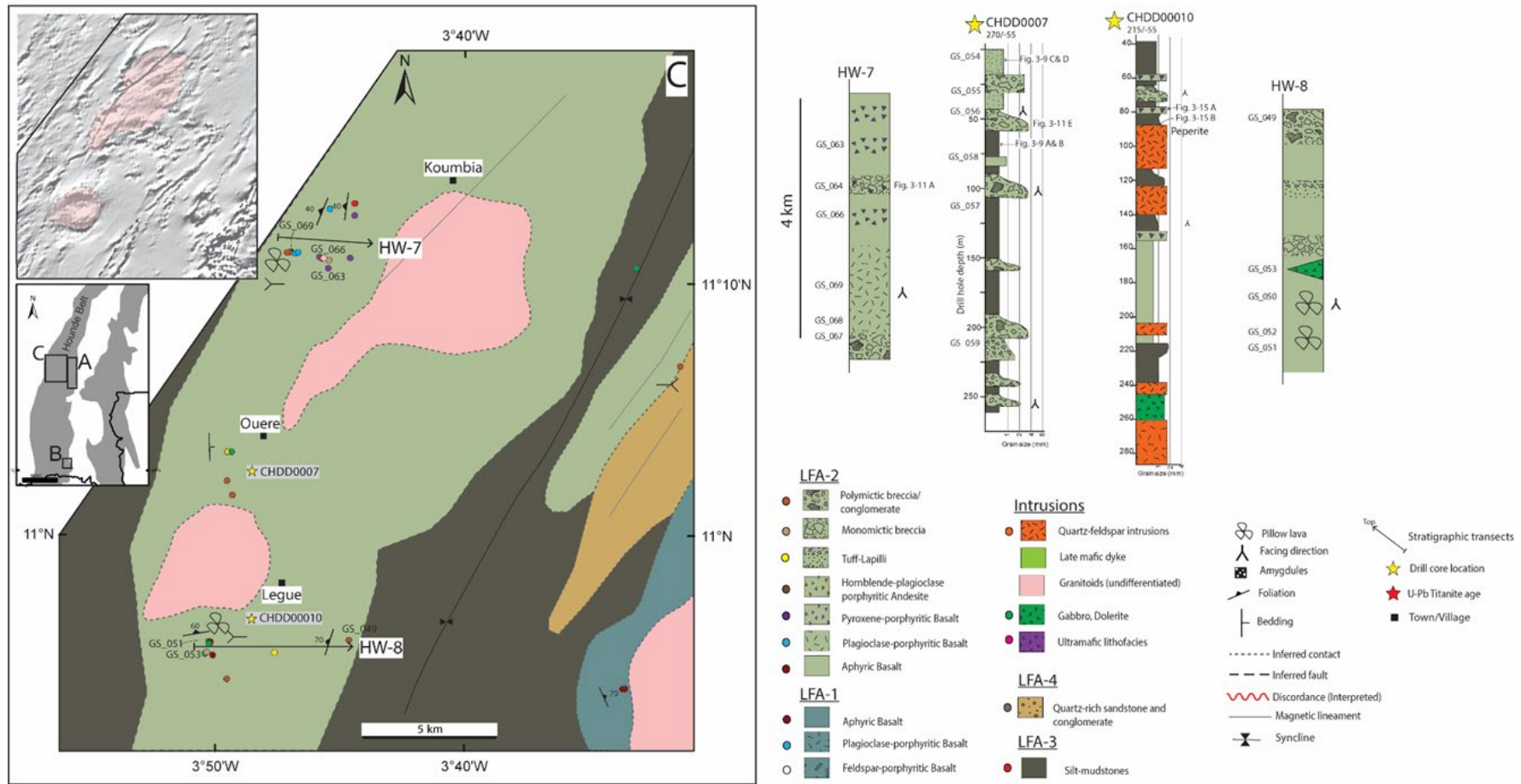


Figure 3-18 Local geology of study area-Map C (location in inset) with outcrop sites, field transects, drill cores (CHDD0007 and CHDD00010), structural measurements and stratigraphic sections (HW-7 & 8) reconstructed from field transects. Coordinate system- WGS 84 UTM zone 30N. Regional vertical derivative aeromagnetic map from WAXI database 2016.

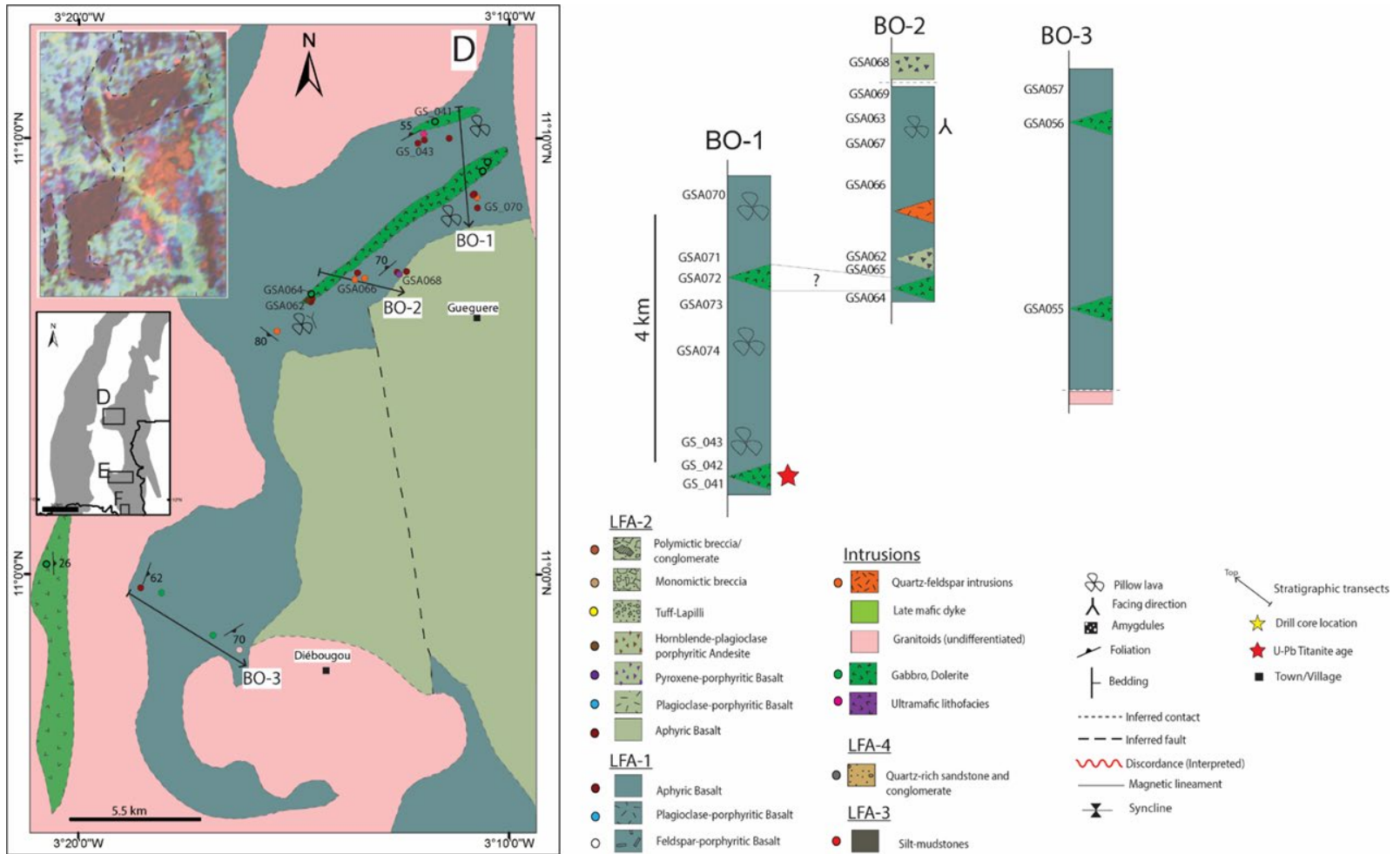


Figure 3-19 Local geology of study area-Map D (location in inset) with field transects, structural measurements and stratigraphic sections (BO-1-3) reconstructed from field transects. Coordinate system- WGS 84 UTM zone 30N. Regional radiometric map from WAXI database 2016.

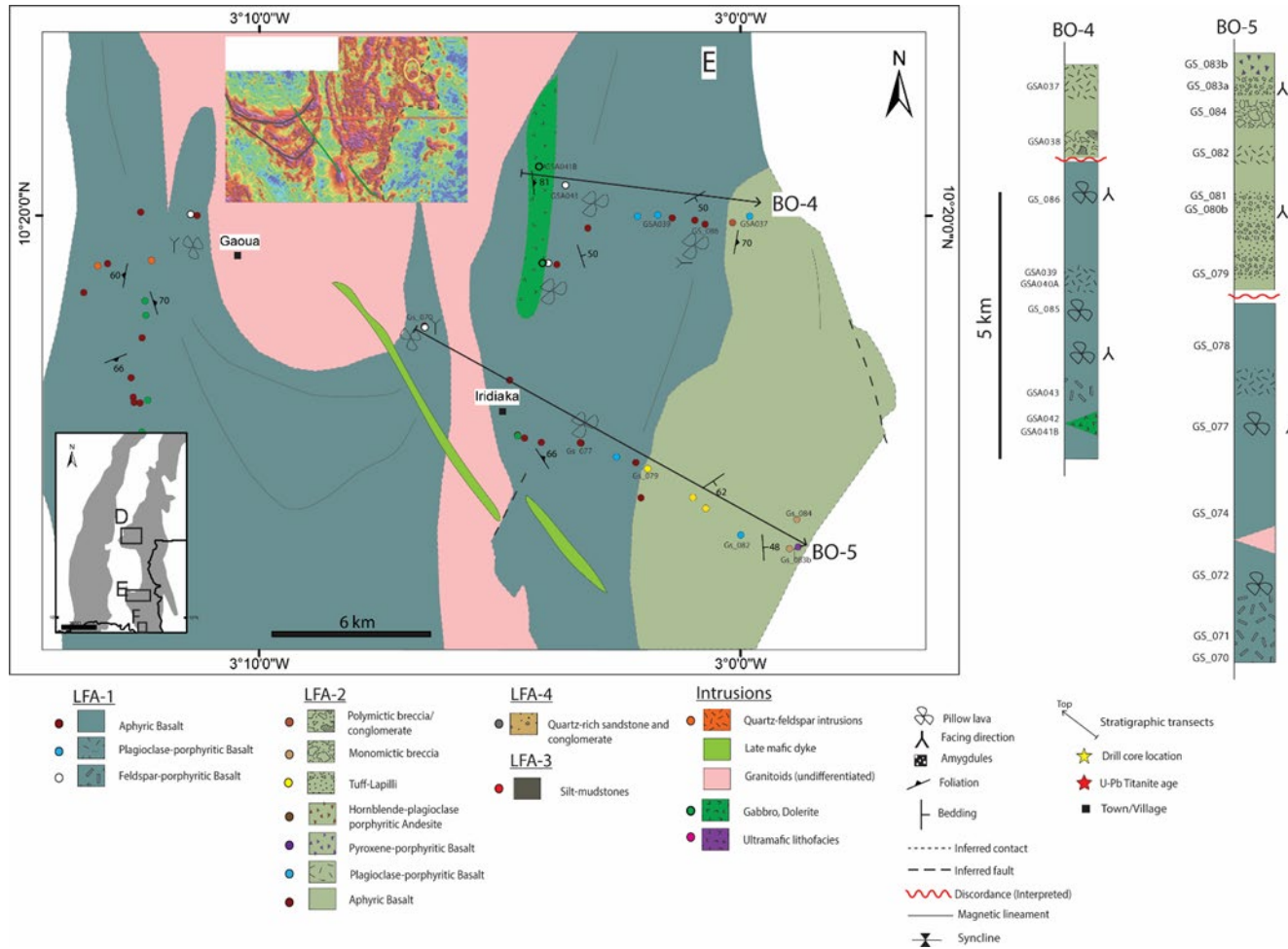


Figure 3-20 Local geology of study area-Map E (location in inset) with outcrop sites, field transects, structural measurements and stratigraphic sections (BO-4 & 5) reconstructed from field transects. Coordinate system- WGS 84 UTM zone 30N. Aeromagnetic map from Volta Resources website
<http://www.voltaresources.com/s/Gaoua.asp>

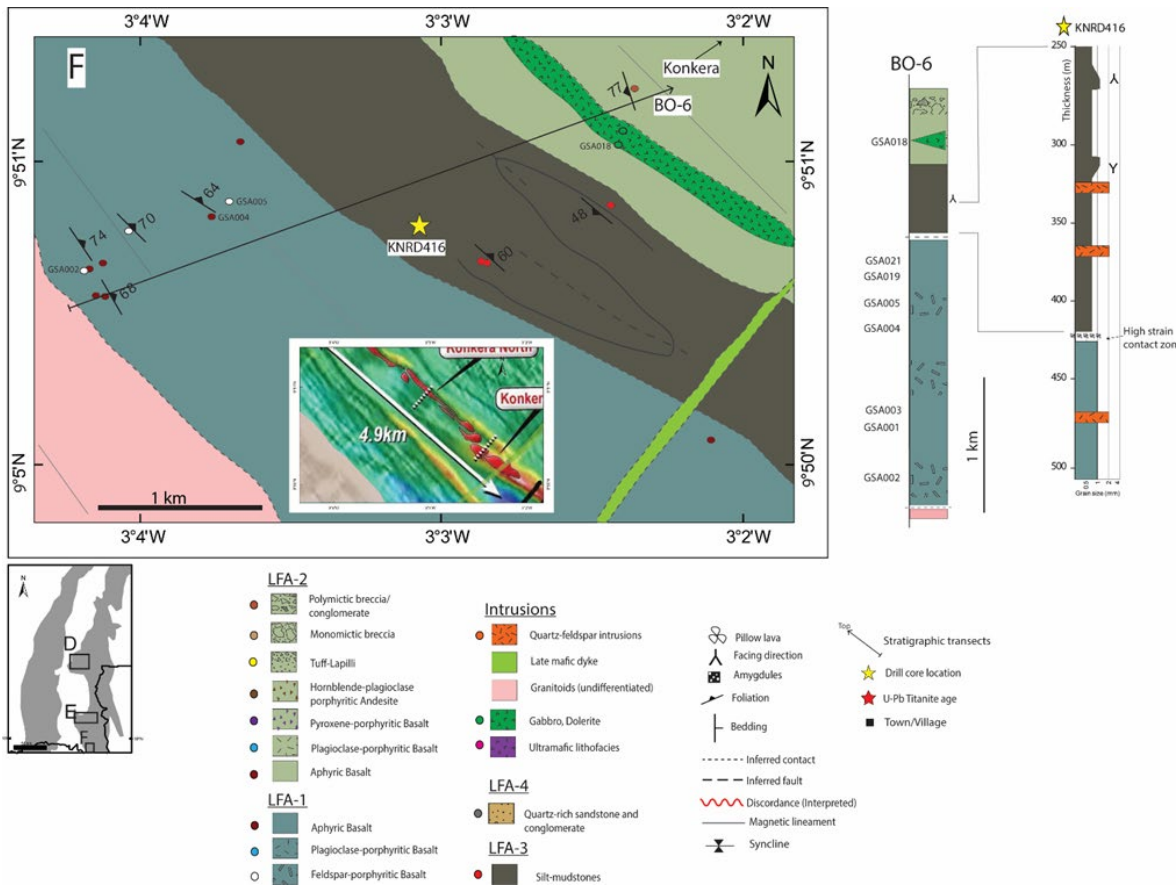


Figure 3-21 Local geology of study area-Map F (location in inset) with outcrop sites, field transects, drill core (KNRD416), structural measurements, and stratigraphic sections (BO-6) reconstructed from field transects. Coordinate system- WGS 84 UTM zone 30N. Aeromagnetic map from Centamin website
<https://www.centamin.com/exploration/burkina-faso/regional-geology>.

3.4 CONCLUSIONS

- Four main lithofacies associations have been identified:
 - Coherent basalt association (LFA- 1), which is prominently made up of subaqueous flood basalts emplaced in deep water depositional setting with no evidence for emergent landmass (no extra-basinal influence)
 - Mafic-intermediate volcanic association (LFA-2), composed of coherent subaqueous basalts and andesites, and several volcaniclastic and epiclastic fragmental lithofacies with evidence of mass wasting of intermediate emergent volcanic edifices.
 - Fine-grained sedimentary association (LFA-3) represents background sedimentation in a distal anoxic deepwater environment with sediment supply from intermediate volcanic sources (no quartz crystal).
 - Quartz-rich sedimentary association (LFA-4) comprises quartz-rich epiclastic sedimentation in a fluvial setting with sediment supply from the erosion of granitic bodies and deposited in fault-bounded basins.
- Reconstruction of relative timing reveals:
 - LFA-1 is the oldest supracrustal succession based on the facing direction of the lithofacies, inference of an earlier deformational overprint, and apparent absence in successive overlying lithofacies associations.
 - LFA-2 succeeds LFA-1 based on intrusive relationship. The contact between both associations is represented by a structural discordance.
 - LFA-3 is contemporaneous with LFA-2 due to their interdigitated succession, syn-depositional intrusion, and common deformational history (folding).
 - LFA-4 is the youngest of the succession based on the influx of plutonic quartz, which is not present in underlying successions, representing post-magmatic sedimentary basin formation and unroofing of granitic bodies.
- The Houndé and Boromo greenstone belts form a broad mirror image of each other with similar lithofacies associations and volcano-sedimentary successions except for LFA-4, which only forms in the Houndé Belt. The

common stratigraphic assemblages between both belts indicate similar lithological provenance and depositional environment. The LFA-1 forms the basal Lower volcanic sequence, whereas the LFA-2 and LFA-3 form the Upper volcanic sequence (Figure 3-22).

- The occurrence of abundant porphyritic lithofacies in LFA-2 compared to LFA-1 suggests contrasting magma differentiation and storage conditions.
- Common folding history in the Upper volcanic sequence (LFA-2 and 3) observed in the Houndé belt does not affect the basal Lower volcanic sequence (LFA-1). This points to a crustal-scale discordance which may be explained by forming the Lower and Upper volcanic sequence in different basins and subsequently juxtaposed during late-stage volcanism in the Upper volcanic sequence. This is supported by the juxtaposition of the youngest succession of the stratigraphy (LFA-4) onto the oldest basal succession (LFA-1), suggestive of an important crustal-scale fault.
- The volcanic architecture of the Houndé and Boromo belts can be summarised as:
 - A basal Lower sequence representing extensive effusive mafic volcanism in a deep water environment distal from terrestrial landmass forming thick and laterally continuous volcanic provinces.
 - The basal Lower sequence is juxtaposed with the Upper sequence, represented by deep to shallow water mafic-intermediate effusive and pyroclastic volcanism with associated volcaniclastic and epiclastic deposits forming discrete emergent volcanic edifices.
 - The paleodepositional environment emerges above sea level, where the subaerial Quartz-rich sedimentary association is deposited in a post-deformation basin.

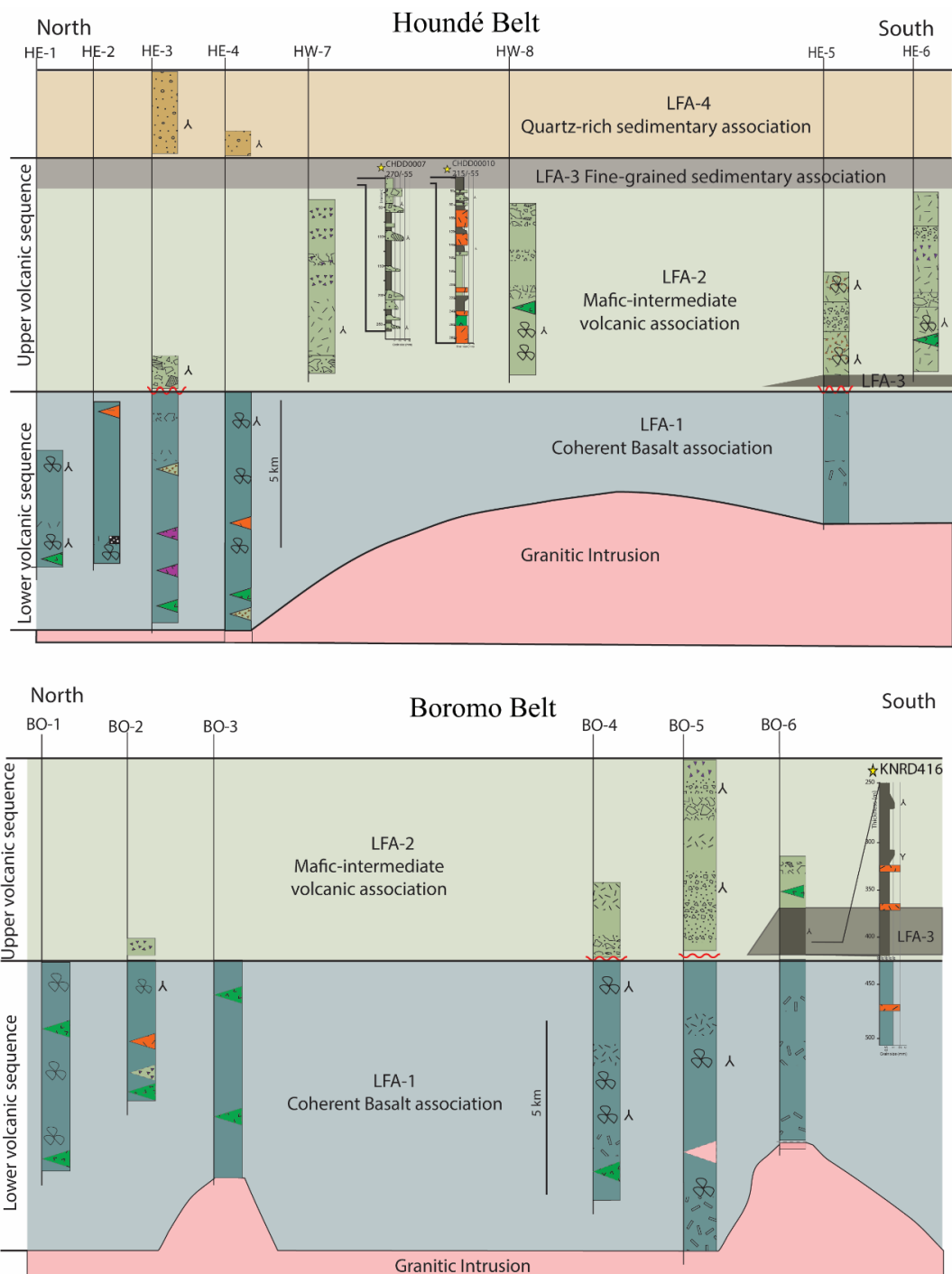


Figure 3-22 Summary figure of the stratigraphic architecture of the lithofacies associations of the Houndé and Boromo belts. The general stratigraphy is subdivided into Lower and Upper volcanic sequences depicting two major volcanic cycles. Legend is the same as Figure 3-21.

Chapter 4: Whole-rock geochemistry

4.1 INTRODUCTION

Geochemical data is a vital tool in detecting many geological processes. For instance, incompatible trace element ratios in uncontaminated basalts help constrain mantle source characteristics (Condie, 2015). In recent times, geochemical fingerprinting has proven useful in unravelling inconspicuous volcanic stratigraphy and tracing mineral resources, especially by defining associated alteration patterns (MacLean & Barrett, 1993). Additionally, geochemical data, within reasonable constraints, has been efficient in deducing the petrogenetic history of rocks. This can be achieved through well-established thermodynamic modelling techniques controlled by experimental petrological parameters (e.g. Villiger, 2004; Vogel et al., 2008; Gleeson et al., 2017).

In this section, the major, trace (including rare earth elements) and Sm-Nd isotope data will be used to fingerprint and investigate the petrogenetic history of the Lower and Upper volcanic sequences of the Houndé and Boromo belts. The primary objectives of this section are to:

- Geochemically fingerprint, distinguish and document key characteristics of the Lower, Upper volcanic sequence and associated intrusive rocks. Fingerprinting the rocks within the volcanic assemblages of each belt will allow regional stratigraphic correlation within each and perhaps across the belts. The geochemical characteristics of rocks from each volcanic sequence will also help ascertain the accuracy of the geological boundaries inferred from fieldwork and volcanological analysis (Chapter 3).
- Use the Sm-Nd isotopic data to constrain the timing of emplacement of rocks from the Lower Sequence of each belt. This information will be valuable as there are no published magmatic ages for the rocks of the Lower Sequence in the Houndé and Boromo belts to date.
- Gain insights into the petrogenetic history of the volcanic rocks. The characteristics of the mantle source and the pathway of differentiation will

be investigated using the least evolved rock compositions as tracers for primary melt and mantle source characteristics. The information obtained from this investigation, coupled with the outcomes of the volcanological analysis, will assist in unravelling the geological history of the rocks of both belts.

4.2 METHODOLOGY

One hundred and thirty-nine (139) coherent volcanic and intrusive rock samples were analysed for major and trace element chemistry. Twelve representative samples, six (6) from each belt, were analysed for Sm-Nd isotopic ratios. Among the six samples from each belt, five were selected from the Lower sequence and one from the Upper sequence. Details of the sampling strategies and analytical techniques are presented below.

4.2.1 Analytical methods

Before geochemical analyses, the samples were trimmed to remove weathered patches and hydrothermal veins using a rock saw. The suitable samples were then crushed and pulverised to about 75 microns particle size to achieve homogeneity using a rock jaw crusher and an agate mill, respectively, at the QUT CARF sample preparation laboratory at Banyo. Some samples (~50) were pulverised using the tungsten carbide mill by the Australian Laboratory Services (ALS) in Brisbane. Duplicate samples were introduced in all analysis batches to ascertain data quality except for the Sm-Nd isotope analyses. In the case of the Sm-Nd isotope data, the Sm and Nd trace element concentrations measured during the isotope analyses were compared with independent trace element analysis to test for the integrity of that data.

Major and trace element analysis

Major element geochemical analyses were executed on fused glass discs using the PANalytical AXIOS Wavelength X-ray Fluorescence (XRF) Spectrometer at the QUT CARF X-Ray and particles laboratory. The XRF fused discs were made by mixing approximately 1.15 g of sample powder with 8.84 g of Claisse lithium tetraborate, lithium metaborate, and lithium iodide flux ($49.75\% \text{ Li}_2\text{B}_4\text{O}_7 + 49.75\% \text{ LiBO}_2 + 0.50\% \text{ LiI}$). Each sample-flux mixture was then ignited in platinum crucibles at 1050 °C in a multi-sample Claisse The OX electronic fusion instrument. Loss on ignition (LOI) was measured by igniting about 2 g of sample powder in ceramic

crucibles at 1050 °C, and the new weight was measured to determine loss of volatiles. Major element detection limits are presented in Appendix B Table A- 4.

Trace element (including rare earth elements) chemistry presented in this study was determined by the sample digestion method. About 50 mg of sample powder was transferred into Teflon Savillex vials and digested in the following steps:

Step 1- 3 ml double distilled HNO₃ and 1 ml HF were added to each powder sample, capped, and allowed to heat up to 100 °C on a hot plate for about 24 hours. The solution was allowed to dry down uncapped for about six hours until a dry sample cake formed.

Step 2- 1 ml HCL and 1 ml Milli-Q® purified water was added to the dry sample cake and dried down.

Step 3- 1 ml HNO₃ and 1 ml Milli-Q® water and heated at 120 °C overnight and allowed to dry down.

Step 4- For the final stage of the sample digestion process, 0.5 ml HNO₃ and 4.5 ml Milli-Q® were added to the dry sample, capped, and heated at 100 °C overnight to allow the dry sample to re-dissolve into a clear solution.

The final solution was sonicated for 30 minutes to homogenise and then transferred into a 125 ml HDPE tube, weighed to determine the weight of aliquot, and diluted to 1000 times dilution factor using Microlab Hamilton system calculated from the weight of aliquot. The final solution was transferred to a 10 ml tube and re-homogenised in a centrifuge. Each batch of 10 unknowns consisted of two certified reference materials (CRM: AGV-2, W2 at QUT; BHVO-2, JA-2 at TCD), instrument blanks, and procedural blanks. Analyses of unknowns and CRMs were carried out on Agilent 8800 Triple Quadrupole Inductively Coupled Plasma Mass Spectrometer (ICP-MS) at QUT CARF, Brisbane and Trinity College Dublin (TCD) (30 samples including duplicates). Instrument detection limits and uncertainty are presented in Appendix B Table A-4. All certified reference materials are within ±5% analytical uncertainty. Most of the analysed samples and elements with poor reproducibility were not used subsequently.

The trace element data obtained through the acid digestion method (described above) was compared to preliminary data obtained via the Laser Ablation-

ICPMS method (LA-ICPMS on fused glass disks). The data from both methods used for the verification is presented in Table A-9B of the Appendix. The rationale for this was to verify the concentrations of Zr and Hf, which seemingly measured unexplainably anomalous concentrations relative to elements with similar compatibilities in some of the analysed samples. The outcome of the comparison showed that some of the values are similar (thus within error $\pm 5\%$), but the remaining results are either significantly higher or lower than the LA-ICPMS values (Figure 4-1). The comparison does not provide a conclusive answer as to whether the Zr and Hf elemental values are erroneously anomalous or whether they represent a geological phenomenon. This is because some duplicate results from both methods are within error while others are exponentially dissimilar. For this reason, Zr and Hf will not be relied on for petrological interpretations.

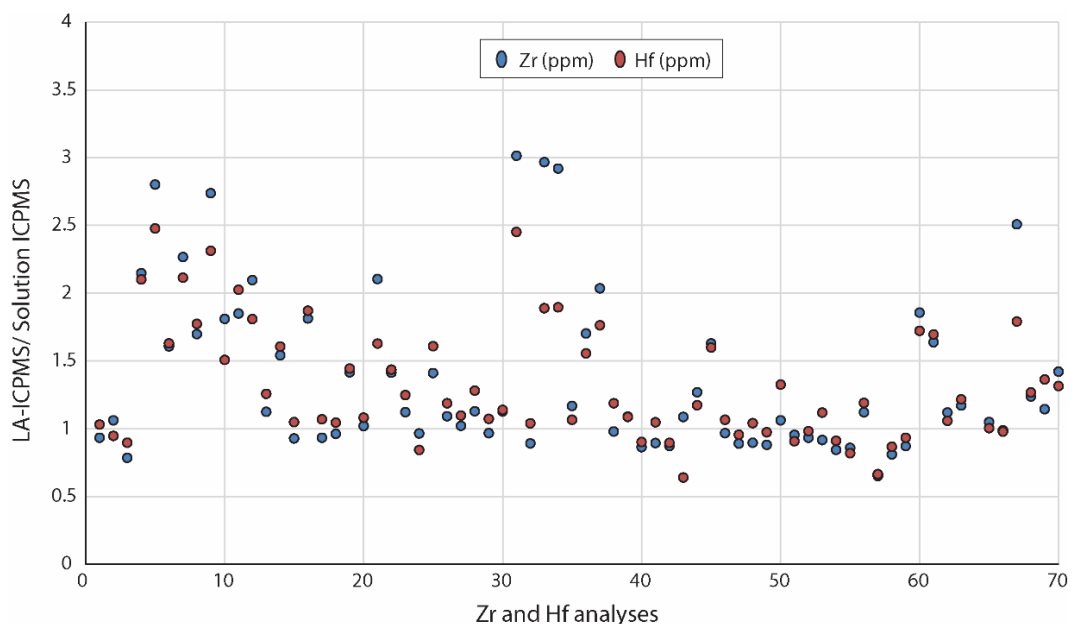


Figure 4-1 Plot of relative concentrations of zirconium (Zr) and hafnium (Hf) from LA-ICPMS and acid digestions ICPMS methods (denominator value). Values close to the 1:1 line depict a good correlation between both analytical measurements. Values plotting above and below 0.8 ratio show LA-ICPMS methods generally have significantly higher and lower zirconium and hafnium concentrations, respectively.

Sm-Nd isotope analysis

Twelve powder samples were analysed at the Isotopia Lab of Monash University, Melbourne, for samarium-neodymium isotope ratios. Only two samples from the Upper sequence were selected for Nd isotope analysis; the remaining ten belong to the Lower sequence. Only a few rocks were selected from the Upper sequence because the focus of the Sm-Nd isotope analysis was for constraining the age of rocks of the Lower sequence, and hence the rocks of the Upper sequence are solely for isotopic comparison. The report obtained from the Isotopia Lab indicated the samples were digested by concentrated HNO₃: HF (4:1) and solutions spiked with ¹⁵⁰Nd/¹⁴⁹Sm enriched tracer following the method of Pin and Zalduogui (1997). ¹⁴³Nd/¹⁴⁴Nd and ¹⁴⁷Sm/¹⁴⁴Nd ratios were measures on Tritonplus Thermal Ionisation Mass Spectrometry (TIMS) and Neptuneplus Multicollector-ICPMS, respectively. Precision and accuracy were checked against certified reference material La Jolla (¹⁴³Nd/¹⁴⁴Nd = 0.511859; Saji et al. (2016)), which measured mean values ¹⁴³Nd/¹⁴⁴Nd of 0.511847 and 0.511871 on two separate TIMS run. Results of the analyses are presented in Table 4-4.

4.3 RESULTS

Representative whole-rock geochemical data for the coherent rocks of the Lower and Upper sequences of the Houndé and Boromo greenstone belts are presented in Table 4-1 and Table 4-2. The representative samples in each table are the most primitive compositions, thus having the highest MgO concentrations. The entire whole-rock major and trace element geochemical dataset can be found in Appendix B Table A- 10. Major element concentrations are reported in percent weight oxide and have been recalculated to 100% on an anhydrous volatile-free basis. Total ferrous oxide (FeO) concentration was calculated from the XRF measured Fe₂O₃ concentrations assuming the ratio of Fe²⁺/Fe³⁺ = 0.85, according to Brooks (1976). Trace element concentrations are reported in parts per million (ppm).

4.3.1 Assessing Chemical Alteration and Element Mobility

The petrographic analysis of the samples (Chapter 3) revealed that the rocks under study are not pristine and have undergone at least greenschist facies metamorphism, weathering, and /or hydrothermal alteration. Therefore, it is essential to assess the geochemical data for the potential disturbance of primary igneous signatures before proceeding to make interpretations of the data. The chemical weathering index by Ohta and Arai (2007) is a tool used to determine the extent of chemical alteration due to weathering. The weathering index of Ohta and Arai (2007) is preferred over other formulae because it factors in a wider range of major element concentrations (i.e. SiO₂, TiO₂, Al₂O₃, MgO, Fe₂O₃, CaO, Na₂O, and K₂O). See Appendix B Table A-12 for the formulae and results of the calculations. More than 95% of the analysed coherent volcanic and intrusive rocks of the Lower and Upper sequence of both belts plot on the fresh igneous rock trend (Figure 4-2). Only a few samples follow the trajectory towards the weathering apex (W). The chemical index calculations of Ohta and Arai (2007) demonstrates that although the rocks have undergone post-emplacement alteration, the effects of chemical weathering on the original whole-rock major element chemistry of the selected samples are minor.

Additionally, the isocon method of Grant (2005) was used to further test and quantify the mobility of the major and trace elements. The isocon method quantitatively evaluates changes in each oxide/element concentration during metamorphism/metasonatism. The change in concentration is estimated by comparing each oxide/element of an altered rock with a fresh composition. The most immobile

oxides/elements define a straight line through the origin called the isocon. In this study, the oxides/elements were evaluated against the most immobile trace elements during low-grade metamorphism such as the heavy rare earth elements (Condie, 1976). The calculated isocon line was subsequently compared with the 1:1 to estimate the extent of mobility. Figure 4-3 is the graphical representation of the isocon element mobility test. Statistical results are presented in Table A- 13 of the Appendix.

The results of the isocon analysis reveal that major elements TiO_2 , Al_2O_3 , CaO , MgO , Fe_2O_3 , and SiO_2 have remained mostly immobile compared to the selected immobile elements with slopes between 0.9–1.2. On the other hand, K_2O and Na_2O behave moderately mobile with slopes less than 0.9. Typically, Na_2O falls below the isocon while K_2O above, indicating element loss and gain, respectively. The best-fit isocon lines, based on the slopes of pre-selected immobile elements (Y and REE), have values between 0.98 and 1.03. The most mobile trace elements are Cs, Rb, and Pb and plot away from the isocon line. The compatible trace elements (Ni, Co, Cr and Sc) plot near the best-fit isocon line, indicating they are generally immobile and reliable. In summary, the element mobility analysis demonstrates that most of the major and trace elements are suitable for petrological interpretation. The elements K_2O , Na_2O , Cs, Rb, Ba, Mo, and Pb, are deemed unreliable for further geochemical assessment in this study.

Table 4-1 Major and trace element geochemical data of representative samples of the Houndé belt.
Values are normalised to 100%.

Lithologies	Aphyric Basalt	Feldspar-porphyritic Basalt	Feldspar-megacrystic Basalt	Pyroxene-porphyritic Basalt	Hornblende-plagioclase porphyritic Andesite	Gabbro	Dolerite
Sample ID	GSA080	GSA029	GSA028	GSA011	GS_030	GS_003	GS_048
Major Elements (Wt. %)							
SiO ₂	46.06	49.29	50.07	46.62	56.48	54.54	54.79
Al ₂ O ₃	13.08	13.45	14.44	12.58	14.18	5.26	14.9
TiO ₂	1.50	1.48	0.93	0.81	0.76	0.45	0.89
MgO	7.40	6.10	7.09	15.36	6.16	16.41	6.62
Fe ₂ O ₃	2.94	2.84	2.37	2.43	1.47	1.51	1.68
FeO	14.97	14.45	12.07	12.34	7.51	7.7	8.52
CaO	12.04	9.78	10.99	7.49	7.06	12.76	8.97
Na ₂ O	1.64	1.89	1.72	1.53	3.44	1.06	2.39
K ₂ O	0.04	0.37	0.04	0.55	2.48	0.12	0.88
P ₂ O ₅	0.13	0.12	0.08	0.08	0.33	0.04	0.21
MnO	0.21	0.22	0.19	0.20	0.14	0.16	0.15
Total	100.00	100.00	100.00	100.00	100	100	100
LOI	0.03	2.51	2.56	3.94	5.54	1.86	2.25
Trace Elements (ppm)							
Ni	64.42	73.60	111.23	432.49	82.13	623.7	148.64
Cr	73.73	161.95	253.89	649.81	272.66	1547.41	228.31
Co	58.03	53.88	50.96	82.52	27.56	53.75	38.25
V	402.20	412.49	321.28	172.82	177.4	154.11	190.82
Sc	53.62	54.20	50.98	26.29	28.07	50.54	28.68
Cu	131.90	97.63	149.39	130.20	49.8	27.18	45.31
Zn	108.67	120.41	91.35	86.65	73.09	52.1	232.12
Mo	0.25	0.34	0.21	0.11	1.13	0.2	0.79
Li	6.60	4.77	4.89	15.92	17.12	2.88	18.08
Ba	12.89	42.32	15.20	116.43	725.55	51.8	291.13
Cs	0.08	0.22	0.05	1.00	4.76	0.06	1.12
Rb	0.69	4.22	0.61	13.79	84.37	2.32	22.12
Sr	258.64	106.33	150.72	149.95	566.23	78.71	216.74
Pb	0.29	0.80	1.11	0.89	6.83	0.81	3.03
Ga	19.35	20.31	16.98	13.22	17.23	7.54	15.91
Zr	23.00	39.71	31.40	47.64	144.99	38.95	124.39
Hf	0.84	1.50	0.98	1.44	3.49	1.04	2.89
Nb	4.01	2.70	2.42	3.36	5.76	1.86	7.32
Ta	0.25	0.22	0.18	0.28	0.42	0.15	0.44
Th	0.06	0.33	0.27	0.34	3.34	0.48	1.91
U	0.02	0.09	0.07	0.11	1.08	0.12	0.55
Y	27.22	32.30	19.83	15.97	22.61	10.69	21.99
La	2.84	3.86	3.14	4.57	19.66	5.54	15.41
Ce	8.20	9.54	6.90	9.23	40.27	9.9	35.51
Pr	1.39	1.80	1.26	1.62	4.81	1.61	4.43
Nd	7.70	9.69	6.64	7.95	19.37	7.09	17.73
Sm	2.63	3.44	2.13	2.20	4.11	1.74	3.67
Eu	1.11	1.25	0.84	0.73	1.37	0.6	1.22
Gd	3.81	4.77	2.92	2.67	4.88	2.21	4.34
Tb	0.65	0.85	0.54	0.46	0.61	0.31	0.69
Dy	4.87	5.81	3.55	2.88	3.7	1.97	3.93
Ho	1.02	1.26	0.81	0.61	0.75	0.39	0.81

Table 4-1 continued

Lithologies	Aphyric Basalt	Feldspar-porphyritic Basalt	Feldspar-megacrystic Basalt	Pyroxene-porphyritic Basalt	Hornblende-plagioclase porphyritic Andesite	Dacite	Gabbro	Dolerite
Sample ID	GSA080	GSA029	GSA028	GSA011	GS_030	GS_037	GS_003	GS_048
Er	2.92	3.64	2.39	1.75	2.37	0.73	1.06	2.49
Tm	0.45	0.53	0.36	0.26	0.36	0.09	0.15	0.37
Yb	2.77	3.37	2.32	1.65	2.3	0.54	0.91	2.4
Lu	0.43	0.46	0.34	0.25	0.34	0.07	0.13	0.36
Ti	8612.74	9804.81	6172.43	5337.63	4252.58	2640.32	2574.97	4911.33
W	60.33		0.49		108.47	86.21	196.79	0.18

Table 4-2 Major and trace element geochemical data of representative samples of the Boromo belt.
Values are normalised to 100%

Lithologies	Aphyric Basalt	Feldspar-porphyritic Basalt	Feldspar-megacrystic Basalt	Pyroxene-porphyritic Basalt	Hornblende-plagioclase porphyritic Andesite	Gabbro	Dolerite
Sample ID	GS_086	GSA039	GSA043	GS_083b	GSA062	GS_042	GSA041B
Major Elements (Wt. %)							
SiO ₂	48.64	50.59	50.42	51.83	59.66	45.3	52.5
Al ₂ O ₃	13.60	13.02	14.48	10.34	16.14	5.63	11.04
TiO ₂	0.81	0.78	0.94	0.63	0.62	1.12	0.65
MgO	8.09	6.55	6.99	11.31	3.42	22.18	9.37
Fe ₂ O ₃	2.83	2.64	2.62	2.12	1.45	2.83	2.15
FeO	14.40	13.47	13.36	10.82	7.35	14.45	10.98
CaO	8.82	11.25	8.20	9.50	6.62	8.07	10.3
Na ₂ O	2.47	1.24	2.59	1.24	3.39	0.09	1.72
K ₂ O	0.02	0.19	0.11	1.85	1.05	0.02	0.95
P ₂ O ₅	0.06	0.06	0.07	0.16	0.18	0.1	0.15
MnO	0.26	0.21	0.23	0.19	0.13	0.2	0.19
Total	100.00	100.00	100.00	100.00	100	100	100
LOI	3.15	2.35	3.39	3.50	0.97	4.51	1.94
Trace Elements (ppm)							
Ni	56.47	63.14	119.72	106.15	35.05	1333.16	66.86
Cr		35.19	156.17		67.61	1726.29	523.15
Co	63.67	59.88	61.99	50.01	22.61	119.67	49.95
V		330.42	343.58		123.51	187.18	282.8
Sc	48.63	58.18	57.46	39.14	17.05	23.05	52.93
Cu	137.59	171.09	174.94	92.73	30.78	66.03	73.72
Zn	153.21	97.56	265.57	82.70	83.11	316.26	80.59
Mo	0.30	0.17	0.14	0.33	0.56	0.54	0.11
Li	15.69	7.73	12.34	36.68	9.54	1.15	7.26
Ba	27.23	30.07	115.01	539.52	649.51	19.02	384.81
Cs	0.16	0.16	0.08	0.75	0.27	0.09	0.33
Rb	0.45	3.67	1.77	28.72	24.74	0.51	18.61
Sr	147.05	212.35	144.17	483.95	429.68	17.89	290.12
Pb	1.13	0.57	1.11	2.82	4.44	1.19	2.56
Ga	15.39	17.59	16.18	10.50	17.44	9.38	12.38
Zr	40.04	27.96	22.19	37.48	103.52	68.64	32.42
Hf	1.18	1.02	0.99	1.05	2.58	1.65	1.07
Nb	0.72	0.82	2.71	1.87	5.02	6.53	1.89
Ta	0.04	0.13	0.21	0.11	0.31	0.41	0.15
Th	0.10	0.16	0.38	0.54	2.15	0.8	0.6
U	0.04	0.05	0.10	0.25	0.8	0.22	0.19
Y	21.69	21.13	20.04	16.10	16.9	13.58	14.63
La	1.31	1.51	3.65	6.24	13.6	7.89	5.02
Ce	3.92	3.60	8.24	10.95	30.98	17.95	9.78
Pr	0.71	0.68	1.39	1.90	3.77	2.93	1.58
Nd	4.04	4.17	7.25	8.64	15.08	13.36	7.76
Sm	1.69	1.74	2.26	2.25	3.09	3.29	2.12
Eu	0.69	0.69	0.86	0.71	1.09	1.12	0.71
Gd	2.76	2.58	2.97	2.71	3.58	3.53	2.49
Tb	0.53	0.54	0.53	0.44	0.46	0.54	0.4
Dy	3.66	3.76	3.65	2.73	2.98	2.86	2.71
Ho	0.85	0.84	0.79	0.60	0.58	0.56	0.55

Table 4-2 continued

Lithologies	Aphyric Basalt	Feldspar-porphyritic Basalt	Feldspar-megacrystic Basalt	Pyroxene-porphyritic Basalt	Hornblende-plagioclase porphyritic Andesite	Gabbro	Dolerite
Sample ID	GS_086	GSA039	GSA043	GS_083b	GSA062	GS_042	GSA041B
Er	2.50	2.49	2.30	1.70	1.68	1.54	1.67
Tm	0.39	0.39	0.36	0.26	0.25	0.23	0.24
Yb	2.49	2.49	2.24	1.64	1.62	1.3	1.54
Lu	0.38	0.38	0.33	0.25	0.25	0.21	0.25
Ti	4730.72	5207.55	6225.34	3612.42	3315.57	6082.91	4331.08
W	0.03		0.29	0.35	252.43	0.35	0.17

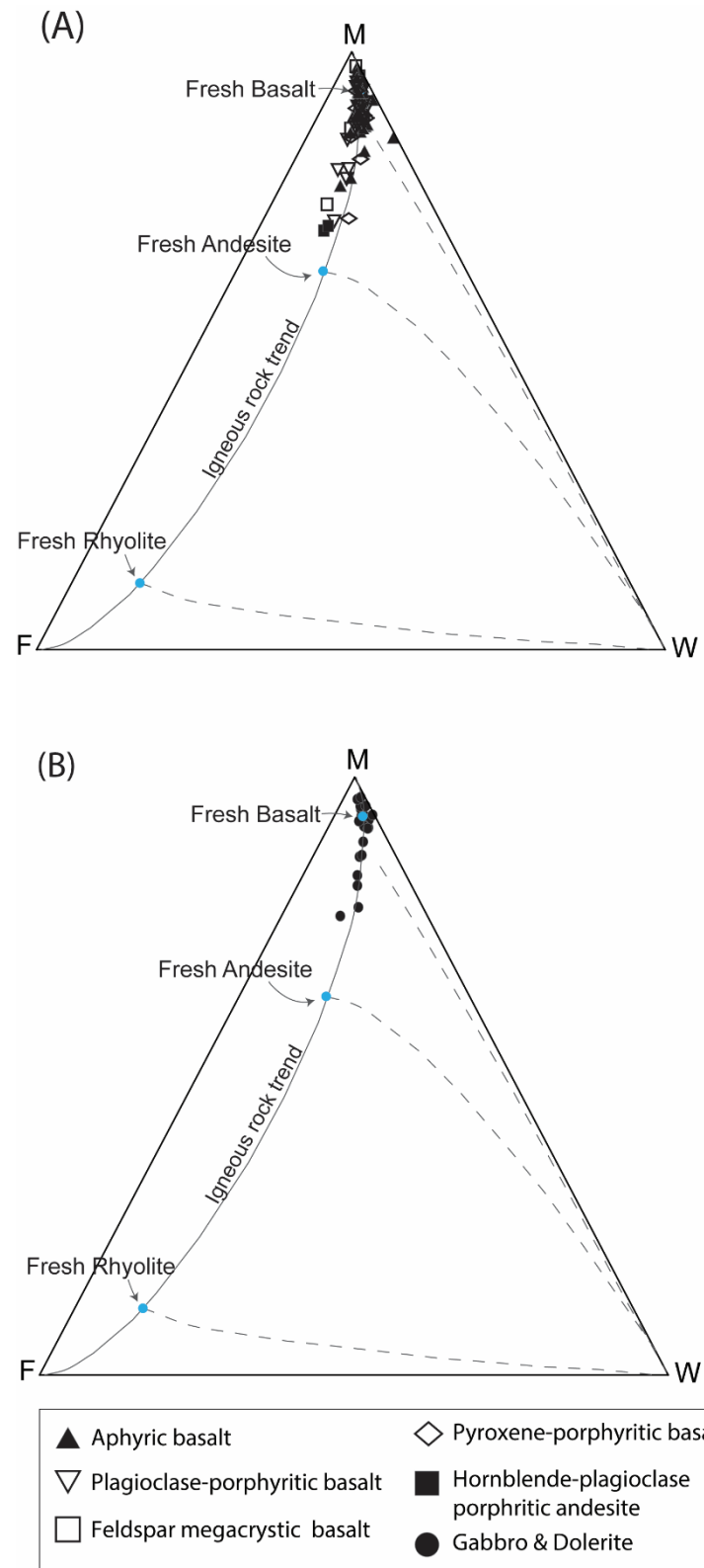


Figure 4-2 Weathering index ternary plots for igneous rocks after Ohta and Arai (2007). (A) corresponds to coherent volcanic lithofacies of the Lower Sequence and Upper sequence and (B) plots for the intrusive lithofacies (Gabbro and Dolerite). Dash lines represent weathering profiles, and the solid line shows the trend of fresh igneous rocks: M-fresh mafic rocks, F-fresh felsic rocks, W-weathered igneous rock. The majority of the rocks fall along the fresh igneous rock trend.

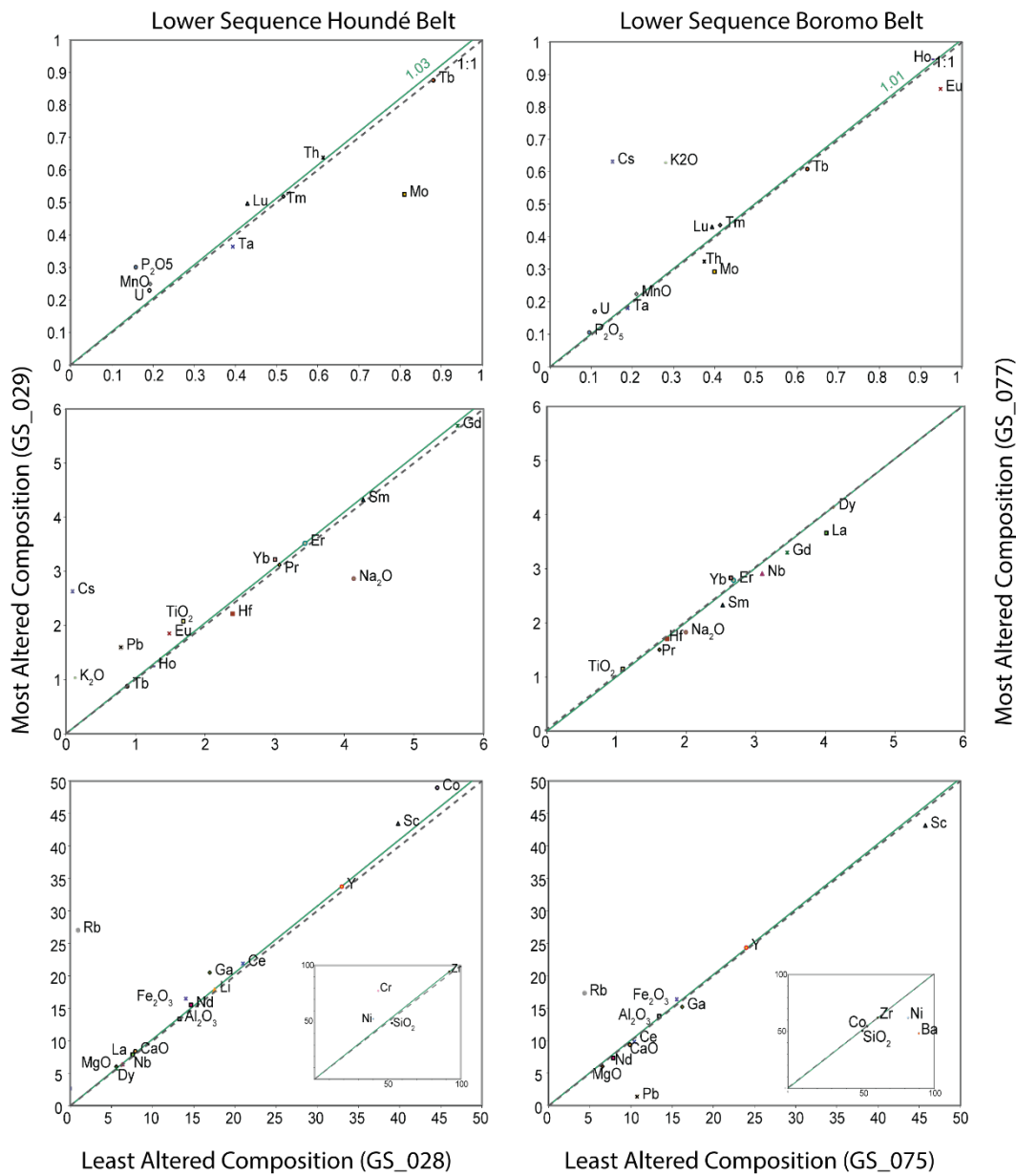


Figure 4-3 Isocon diagram of altered and unaltered compositions from Lower volcanic Sequence of the Boromo and Houndé belts following element mobility method of Grant (1986), (2005). Altered and unaltered compositions were selected based on LOI. Line of best fit isocon defined by pre-selected immobile elements (solid green line). 1:1 isocon line (grey broken line). The analyses were achieved using the MS Excel worksheet designed by López-Moro (2012). Oxides/elements above the isocon line have gained while those below have lost abundance. Oxides and elements concentrations have been scaled to fit the plots following López-Moro (2012). Insets have higher relative abundances compared to the majority of the oxides and elements.

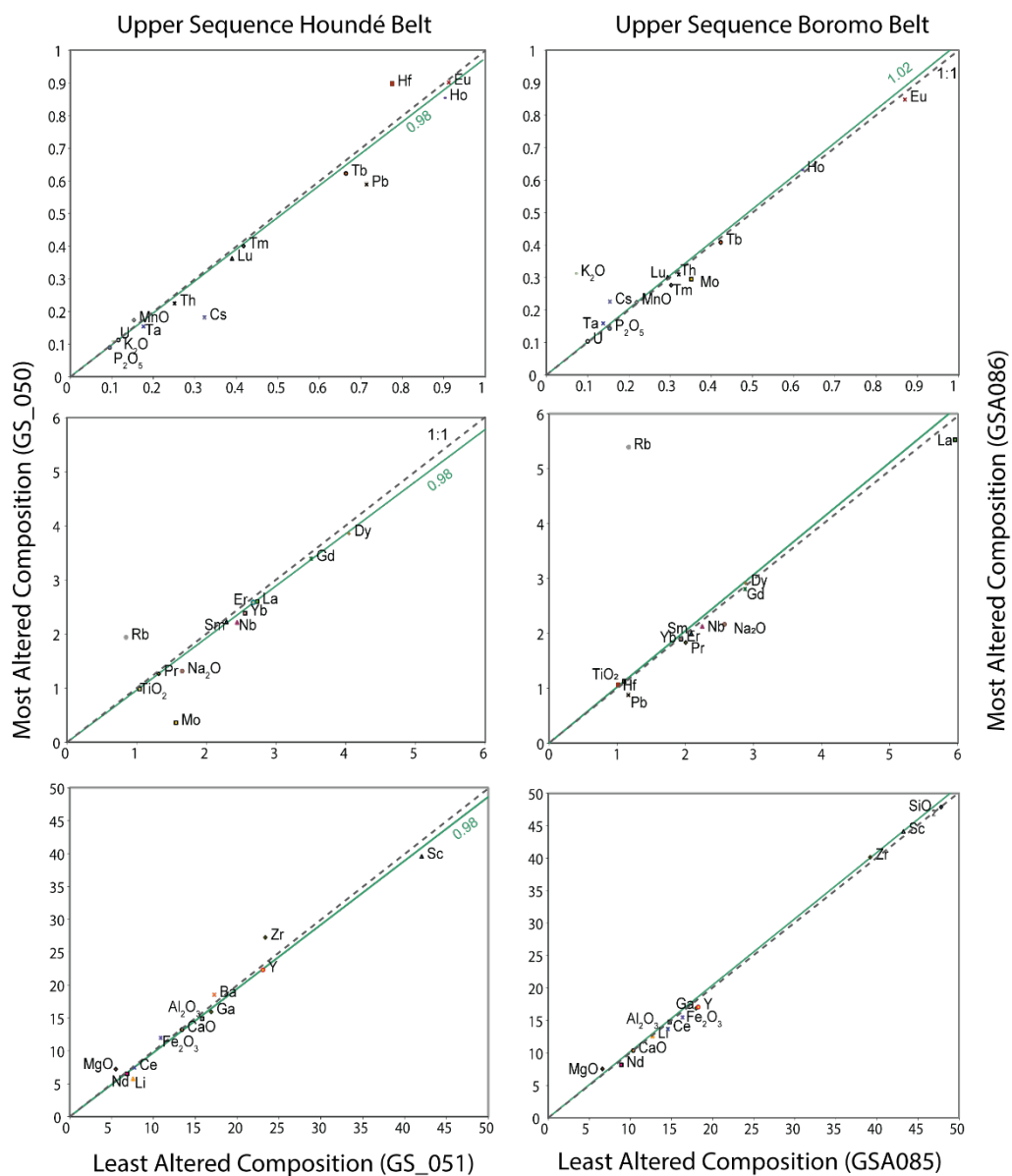


Figure 4-3 continued—Isocon diagram of altered and unaltered compositions from the Upper volcanic sequence of the Houndé and Boromo belts.

4.3.2 Geochemical Classification and Variation

The rocks of the Lower and Upper sequences and the gabbro-dolerite lithofacies of the Houndé and Boromo belts can be categorised into four distinct groups based on key trace element signatures. The four groups were verified using the K-means clustering algorithm to define the boundaries of each group statistically. Details of the K-means analysis is presented in Appendix B. Key characteristics of the four distinct groups named Group 1, Group 2, Group 3, and Group 4 are summarised in Table 4-3 and described below. The alphabets “L” and “U” will be attached to each geochemical group idea to denote Lower and Upper sequence, respectively, based to their stratigraphic position.

Group 1

Group 1 signature is characterised by relatively lower abundances of light rare earth elements (LREE) than heavy rare earth elements (HREE). Their REE pattern is depicted by the downward dip in the LREE and near-flat HREE Chondrite-normalised patterns with $(\text{La}/\text{Sm})_N = 0.5\text{--}1.0$ and $(\text{Gd}/\text{Yb})_N = 0.9\text{--}1.3$ (Figure 4-4). The rocks within this subset do not exhibit pronounced Eu anomalies but rather possess minor positive and negative Eu anomalies ($\text{Eu}/\text{Eu}^* = 0.8\text{--}1.1$). Relative to Primitive Mantle (PM) compositions by Sun and McDonough (1989), Group 1 rocks exhibit minor negative Nb-Ta and Ti anomalies compared to adjacent high field strength elements (HFSE) (Figure 4-5). Two samples GSA080 and GS_026, from the Houndé belt, do not exhibit the characteristic negative Nb-Ta and Ti anomalies. Besides the relative depletion in Nb and Ti, the Group 1 rocks are between 3–10 times the values of PM.

Based on the Jensen cation plot after Jensen (1976), Group 1 rocks are high-Fe tholeiitic basalts except for two samples (Gs_050 and Gs_051) from the Upper sequence of the Houndé belt, which plot near the high-Mg tholeiitic basalt field (Figure 4-8). Gabbros and dolerites with Group 1 signatures also fall within the high-Fe tholeiite field of the Jensen cation plot. Group 1 rocks (both Lower and Upper sequence) are low Th-basalts because of their low Th concentrations relative to TiO_2 ($\text{Th}/\text{TiO}_2 = 0.04\text{--}0.42$) (Figure 4-9). Group 1 rocks have moderately low magnesium numbers ($\text{Mg}^\#_{(\text{molar})} = \text{Mg}^{2+}/(\text{Mg}^{2+} + \text{Fe}^{2+})$) between 35 and 55 (Figure 4-10). Major element compositions of Group 1 rocks are characterised by SiO_2 concentrations of 44.8–52.1 wt. %, MgO of 4.7–8.1 wt. %, Al_2O_3 of 12.0–15.7 wt. %, FeO of 9.7–16.8

wt. %, CaO of 6.7–13.3 wt. % and TiO₂ of 0.8–1.8 wt.%. The concentrations of compatible trace element Ni for Group 1 rocks are moderately low, with values ranging from 42 to 170 ppm. High field strength elements Nb, Th, La, and Y have concentrations in the range of 0.69–4.01 ppm, 0.06–0.41 ppm, 1.26–5.05 ppm, and 18.15–42.34 ppm, respectively.

Figure 4-11 and 12 are binary plots of MgO and selected major and trace elements showing the variations in compositions of the volcanic lithofacies using MgO as an index of magma evolution. In relation to the major elements for Group 1L, TiO₂, SiO₂, and FeO increase while CaO and Al₂O₃ decrease with decreasing MgO. Notably, the FeO concentration increases until about MgO= 5 wt.% and FeO= 15 wt.%, where the concentrations remain fairly constant. For the trace elements, Nb, Th, La, and Y concentrations increase with decreasing MgO while Ni reduces. Only two Group 1U samples are present in this study, hence, a trend could not be established.

Lithologically, Group 1L rocks include abundant massive aphyric basalts, few aphyric pillow basalts, plagioclase-porphyritic basalts, gabbros, and dolerites. Group 1U samples are both aphyric basalts. The majority of the Group 1 rocks were sampled in the Lower sequence of the Boromo belt, with few samples in the Houndé belt. Two samples belong to the Upper sequence of the Houndé belt.

Group 2

Group 2 signatures are characterised by relatively flat Chondrite-normalised REE patterns with $(\text{La}/\text{Sm})_{\text{N}} = 0.9\text{--}1.2$ and $(\text{Gd}/\text{Yb})_{\text{N}} = 1.0\text{--}1.2$ (Figure 4-4). Few Group 2 rocks exhibit minor negative and positive Eu anomalies ($\text{Eu}/\text{Eu}^* = 0.9\text{--}1.2$). The HFSE of Group 2 rocks are about 2–10 times the value of PM and do not exhibit outstanding anomalies in contrast to Group 1 (Figure 4-5).

Group 2 rocks are high-Fe tholeiitic basalts, including a few gabbros and dolerites, which also plot within the high-Fe tholeiite field of the Jensen cation plot (Figure 4-8). Two feldspar megacrystic basalts (GS_070 and GS_097B) plot as calc-alkaline andesites-dacites due to their relatively high aluminium concentrations. Group 2 rocks are low Th-basalts with Th/TiO₂ ratios of 0.21–0.46 and moderately low Mg# values of 33–57 (Figure 4-9 & 10). Major element compositions of Group 2 rocks are characterised by SiO₂ concentrations of 47.5–52.0 wt. %, MgO of 3.2–7.9 wt. %, Al₂O₃ of 11.7–14.8 (outlier 24.5) wt. %, FeO of 6.2–17.1 wt. %, CaO of 5.7–

13.5 wt. % and TiO_2 of 0.4–1.8 wt.%. The concentrations of compatible trace element Ni for Group 2 rocks are moderately low, with values ranging from 62 to 138 ppm. The concentrations of Nb, Th, La, and Y fall within the ranges of 1.06–5.27 ppm, 0.10–0.60 ppm, 1.32–5.82 ppm, and 9.97–36.07 ppm, respectively. The major elements, TiO_2 , SiO_2 , and FeO, increases while CaO and Al_2O_3 decrease with decreasing MgO. The concentrations of Nb, Th, La, and Y increase with decreasing MgO while Ni reduces.

Group 2 rocks are composed of abundant massive and pillow aphyric basalts with minor feldspar megacrystic basalts, gabbros, and dolerites. Group 2 rocks were only sampled in the Lower sequence (thus Group 2L) and are common in the Boromo belt with few samples in the southern part of the Houndé belt, near Kampti.

Group 3

Group 3 rocks are characterised by enriched LREE abundances relative to HREE. This is depicted by the gently sloping REE Chondrite-normalised patterns with $(\text{La}/\text{Sm})\text{N} = 0.9\text{--}1.6$ and $(\text{Gd}/\text{Yb})\text{N} = 1.2\text{--}2.1$ (Figure 4-4). A subset of the Group 3 rocks has relatively low middle REE concentrations (Tb, Dy, and Ho) and exhibit a dip in their REE Chondrite-normalised patterns. Few Group 3 rocks possess minor negative and positive Eu anomalies, but most do not exhibit any Eu anomalies ($\text{Eu}/\text{Eu}^*= 0.8\text{--}1.2$). The HFSE of Group 3 rocks are approximately 2–20 times the abundance of Primitive mantle values and do not exhibit any outstanding anomalies relative to PM (Figure 4-5 to 7).

Group 3L rocks of the Lower sequence are high-Fe tholeiitic basalts, while those of the Upper sequence (Group 3U) fall into the fields of tholeiitic andesites, komatiitic basalts, and calc-alkaline basalts (Figure 4-8). Gabbros and dolerites with Group 3 signatures fall within the komatiitic basalt field due to high magnesium concentrations. All Group 3 rocks have relatively low Th concentrations relative to TiO_2 ($\text{Th}/\text{TiO}_2 = 0.20\text{--}0.76$) (Figure 4-9). Magnesium numbers for Group 3 rocks range from 27 to 71, with rocks of $\text{Mg}^{\#} > 55$ belonging to the Upper sequence and intrusive lithofacies (Figure 4-10). Major element compositions of Group 3 rocks are characterised by SiO_2 concentrations of 45.9–59.0 wt. %, MgO of 2.3–18.5 wt. %, Al_2O_3 of 7.8–16.9 wt. %, FeO of 9.1–18.6 wt. %, CaO of 4.5–15.8 wt. % and TiO_2 of 0.8–2.8 wt.%. The concentrations of compatible trace element Ni for Group 3 rocks range from relatively

low values of 9.7 to very high values of 909 ppm. Trace elements such as Nb, Th, La, and Y have concentrations in the range of 1.11–15.00 ppm, 0.16–1.12 ppm, 1.94–14.63 ppm, and 6.44–45.87 ppm, respectively.

Group 3 rocks of both Lower and Upper sequences exhibit a general increase in concentrations of TiO₂, SiO₂ and a decrease in CaO with decreasing concentrations of MgO. However, in regards to Al₂O₃ and FeO, the rocks of Group 3L exhibit trends of increasing FeO coupled with decrease concentrations of Al₂O₃ with decreasing MgO. In contrast, the Group 3U rocks of the Upper sequence rocks form a trend where FeO concentrations decrease simultaneously with increasing Al₂O₃ as MgO decreases. The trace element concentrations of Nb, Th, La, and Y in both cases increase with decreasing MgO while Ni reduces.

Group 3 rocks are the most abundant sample set and are commonly encountered in the Lower and Upper sequences of the Houndé belt with few samples in the Boromo belt. Group 3L comprises abundant massive and pillow aphyric basalts with minor feldspar megacrystic and plagioclase-porphyritic basalts, while Group 3U is made up of abundant massive and pillow plagioclase-porphyritic basalts, and minor pyroxene-porphyritic basalts, gabbros, and dolerites.

Group 4

Lastly, rocks with Group 4 signature are characterised by relatively more abundant LREE compared to HREE. Chondrite-normalised REE patterns portray steep slopes with $(\text{La}/\text{Sm})_{\text{N}} = 1.4\text{--}5.2$ and $(\text{Gd}/\text{Yb})_{\text{N}} = 1.1\text{--}3.9$ (Figure 4-4). Few rocks within this subset exhibit outstanding negative Eu anomalies ($\text{Eu}/\text{Eu}^* = 0.3$), but most do not display Eu anomalies ($\text{Eu}/\text{Eu}^* = 0.9\text{--}1.1$). Group 4 rocks exhibit pronounced negative Nb-Ta and Ti anomalies compared to adjacent high field strength elements (HFSE) (Figure 4-6 & 7). Besides the relative depletion in Nb, Ta, and Ti, the large ion lithophile and LREE are between 5–100 times and the HREE between 3 to 8 times the value of PM.

Group 4 comprises a wider variety of rock types compared to the other geochemical groups. Based on the Jensen cation plot, Group 4 are high-Fe and high-Mg tholeiitic basalts, calc-alkaline basalts and andesites, and komatiitic basalts (Figure 4-8). The gabbros and dolerites typically plot in the komatiite and high-Mg basalt fields representing their high magnesium compositions. Only a few Group 4 rocks

have low-Th concentrations, with the majority having intermediate to high-Th concentrations relative to TiO_2 ($\text{Th}/\text{TiO}_2 = 0.28\text{--}4.39$) (Figure 4-9). Group 4 rocks have comparatively higher magnesium numbers between 41 and 79 (32 outlier) (Figure 4-10). Major element compositions of Group 4 rocks are characterised by SiO_2 concentrations of 45.3–60.9 wt. %, MgO of 3.0–22.2 wt. %, Al_2O_3 of 5.26–19.6 wt. %, FeO of 6.9–14.6 wt. %, CaO of 5.4–12.9 wt. % and TiO_2 of 0.5–1.6 wt. %. The concentrations of compatible trace element Ni for Group 4 rocks range from as low as 28 ppm to 1333 ppm. Selected HFSE Nb, Th, La, and Y have concentrations in the range of 1.29–14.27 ppm, 0.31–5.47 ppm, 5.02–44.30 ppm, and 10.69–27.66 ppm, respectively. The major element concentrations TiO_2 , SiO_2 , and Al_2O_3 increases while CaO and FeO decrease with decreasing MgO , similar to Group 3 rocks of the Upper sequence. The trace element concentrations of Nb, Th, La, and Y increase with decreasing MgO while Ni reduces.

Group 4 comprises massive aphyric basalts, massive and pillow plagioclase-porphyritic basalts, pyroxene-porphyritic basalts, hornblende-plagioclase porphyritic andesites, gabbros, and dolerites. Group 4 rocks occur as lavas and intrusions in the Upper sequence (Group 4U) and often occur as late intrusives hosted in the Lower sequence of both belts.

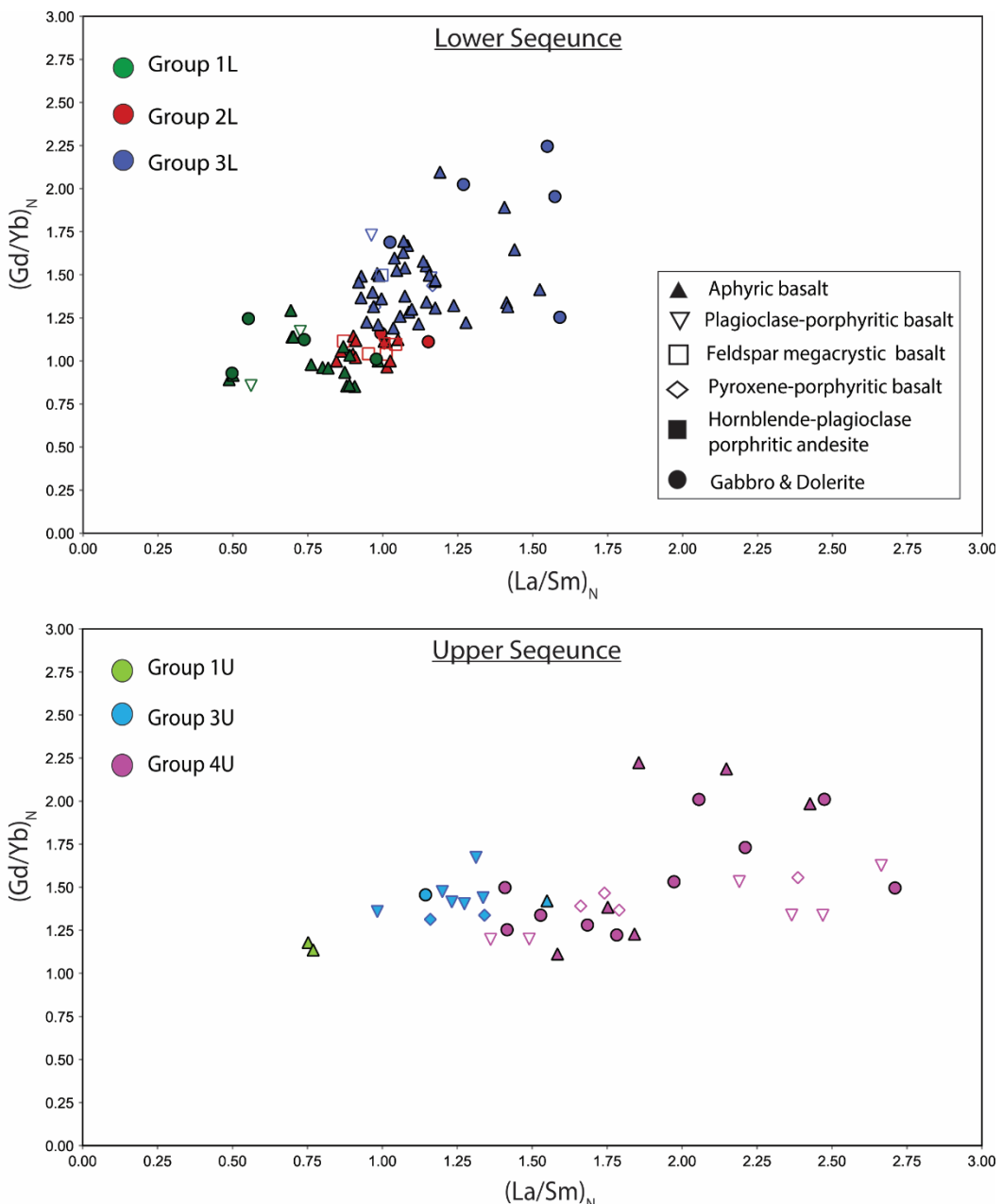


Figure 4-4 Plot of La/Sm against Gd/Yb Chondrite normalised ratios illustrating the range and variation of the four recognised geochemical groups within the study area. Top panel illustrates variations in the Lower sequence while bottom panel shows that of the Upper sequence for both belts. Three outlier samples with $(\text{La}/\text{Sm})_N > 3$ have been omitted from the plot.

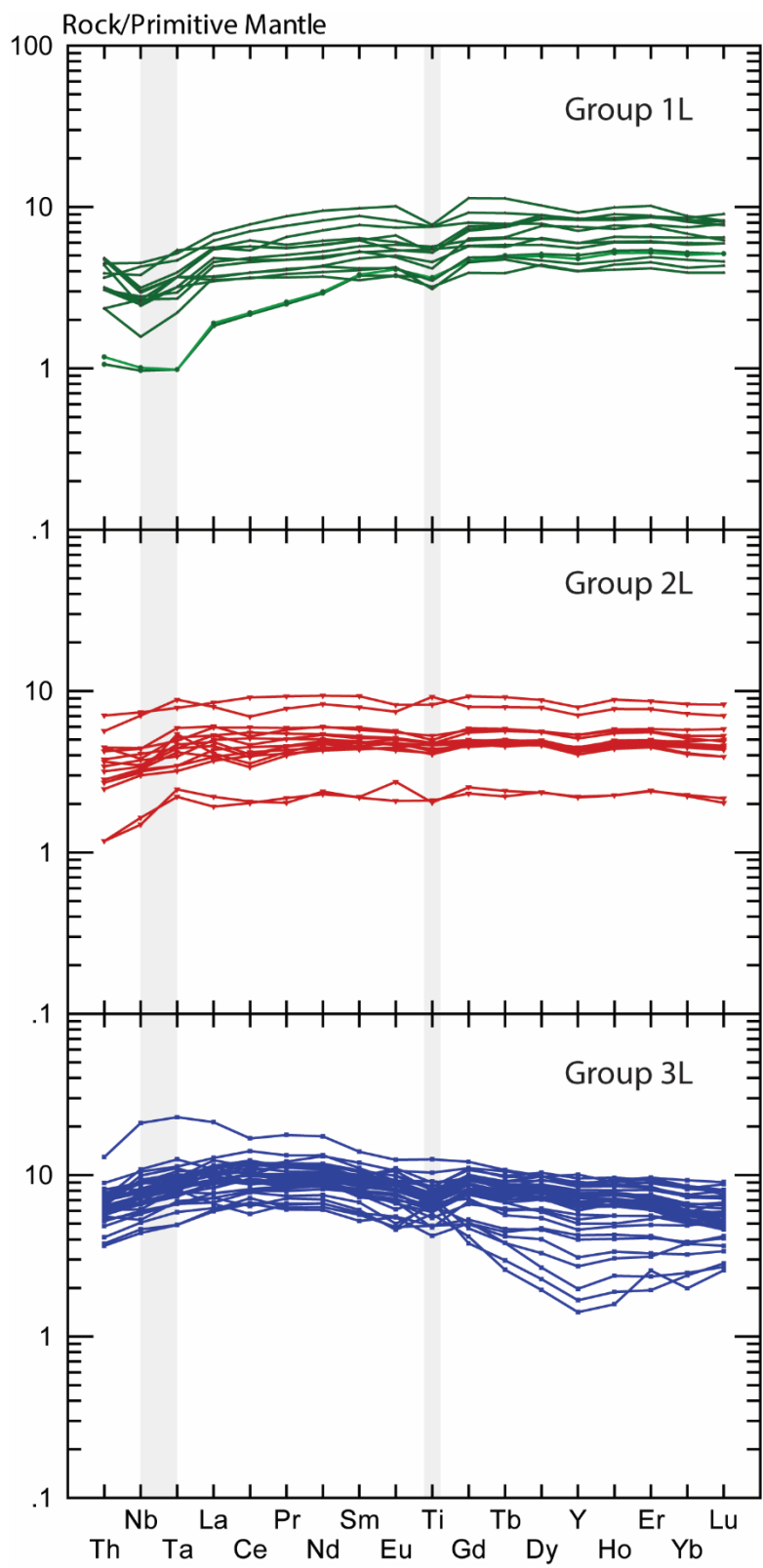


Figure 4-5 Primitive Mantle-normalised multi-element diagrams for rocks of the Lower volcanic sequence of the Houndé and Boromo belts showing the three distinct geochemical groups. Note: Pronounced negative Nb-Ta and Ti anomalies in some of the Group 1L rocks. No Group 4 signatures belong to the Lower sequence Normalising values from Sun and McDonough (1989).

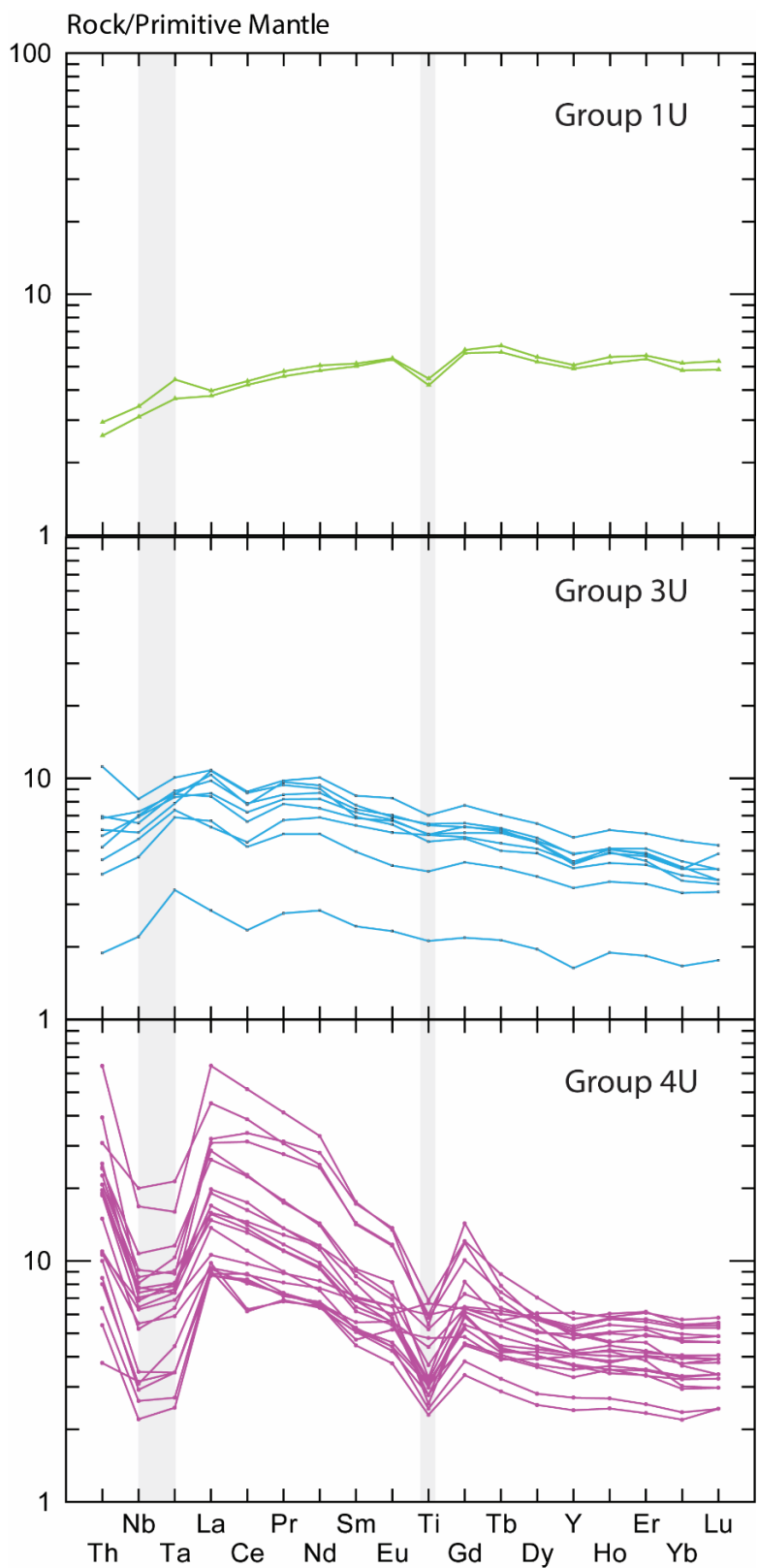


Figure 4-6 Primitive Mantle-normalised multi-element diagrams of rocks of the Upper volcanic sequence of the Houndé and Boromo belts exhibit three distinct geochemical groups. Note: pronounced negative Nb-Ta and Ti anomalies in rocks of Group 1 and Group 4. No Group 2 signatures were sampled in the Upper sequence. Normalising values from Sun and McDonough (1989). Note change in scale on the y-axis from Figure 4-5.

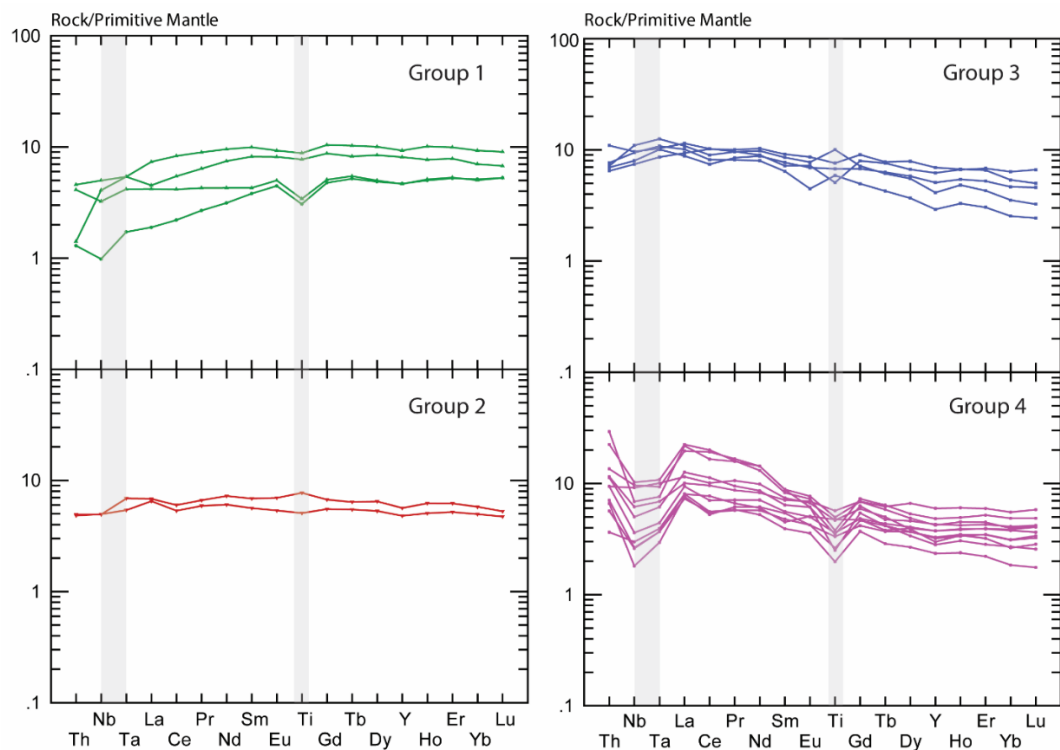


Figure 4-7 Primitive Mantle-normalised multi-element diagrams for the Intrusive units of the Houndé and Boromo belts. The gabbros and dolerites exhibit all four distinct geochemical groups. Note: pronounced negative Nb-Ta and Ti anomalies in some rocks of Group 1 and all Group 4. Normalising values from Sun and McDonough (1989)

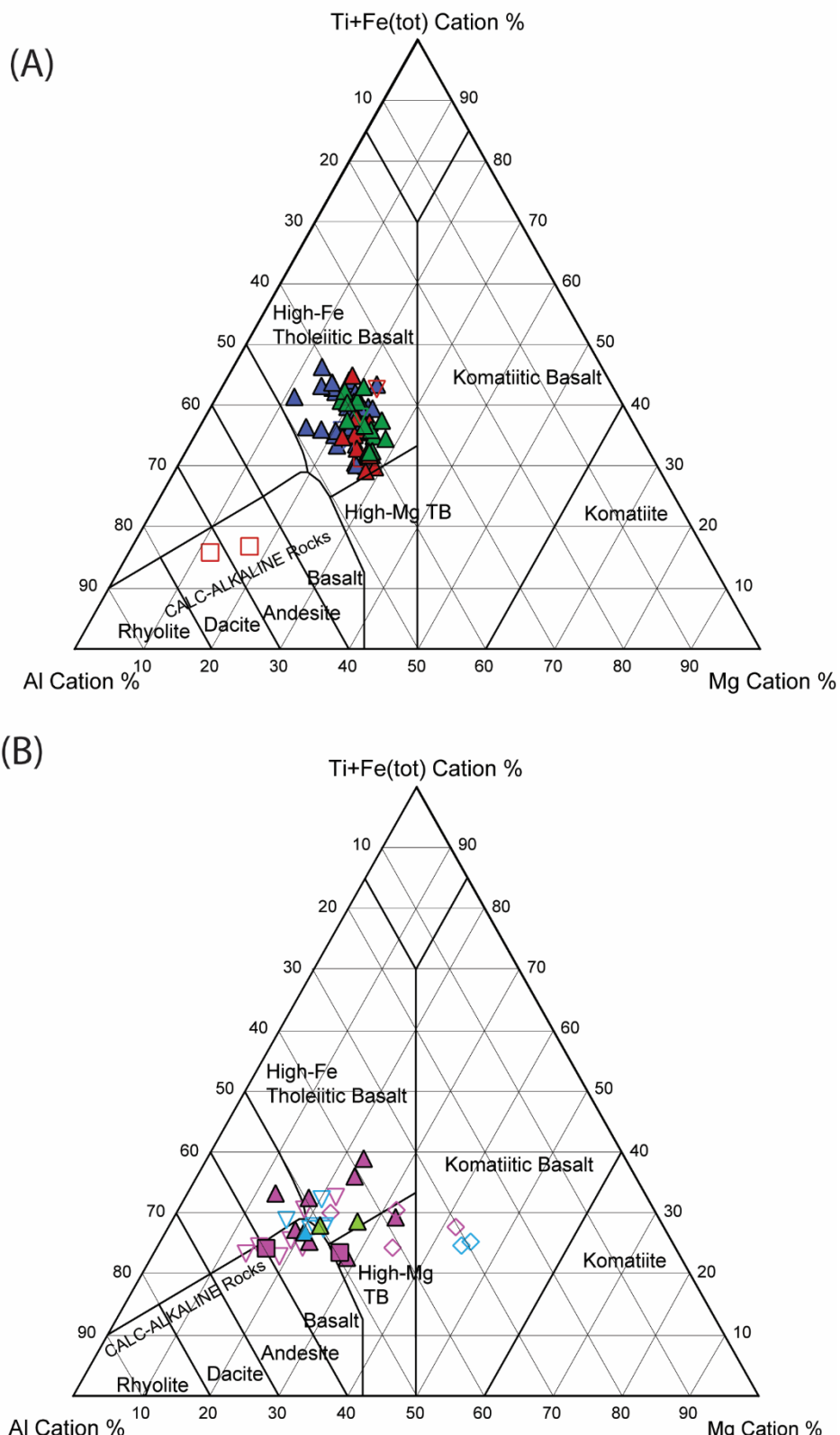


Figure 4-8 Geochemical classification diagrams of Jensen (1976) showing the diversity of rock types in the (A) Lower volcanic sequence; High-Fe tholeiites, (B) Upper volcanic sequence; minor high-Mg and high-Fe tholeiites and calc-alkaline. Legend below.

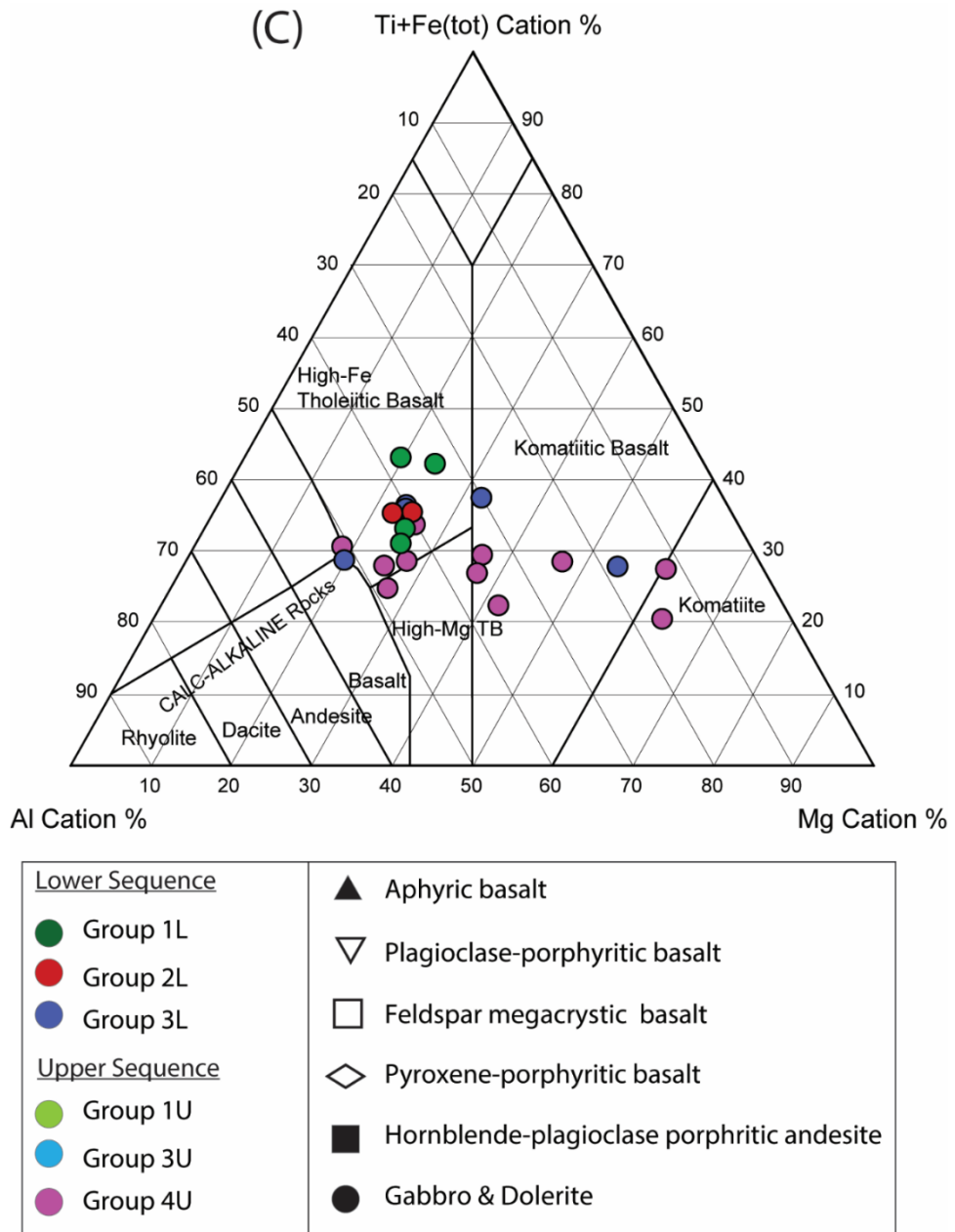


Figure 4-8 continued (C) Geochemical diversity of Gabbro & Dolerite lithofacies which range from high-Mg to high-Fe varieties. Note: Because of the difficulty in assigning the Gabbros and Dolerites to any stratigraphic sequence, they have been coloured as the Lower sequence but do not all necessarily belong to the Lower sequence.

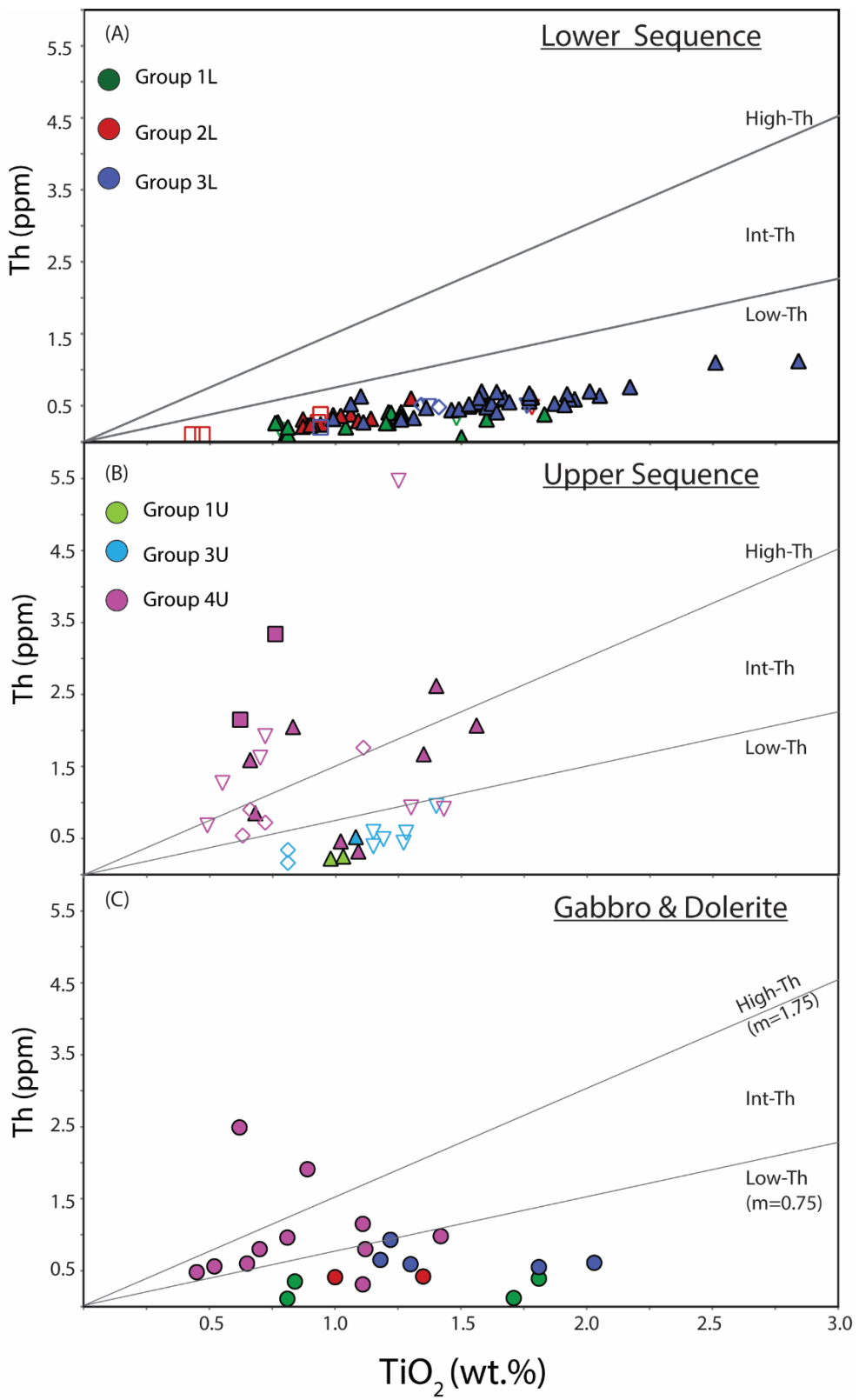


Figure 4-9 Th-TiO₂ classification for rocks of the (A) lower volcanic sequence, (B) Upper volcanic sequence, (C) Gabbros and dolerites of both belts illustrating the abundance of Th relative to TiO₂.

Plot demarcations follow Barnes et al. (2012); Hayman, Thébaud, et al. (2015) where Low-Th = $\text{Th}/\text{TiO}_2 < 0.75$; High-Th = $\text{Th}/\text{TiO}_2 > 1.5$. Rocks of the Lower sequence consistently have Low Th-TiO₂ ratios while the Upper sequence is intermediate to high-Th compositions. Symbol legend same as Figure 4-8.

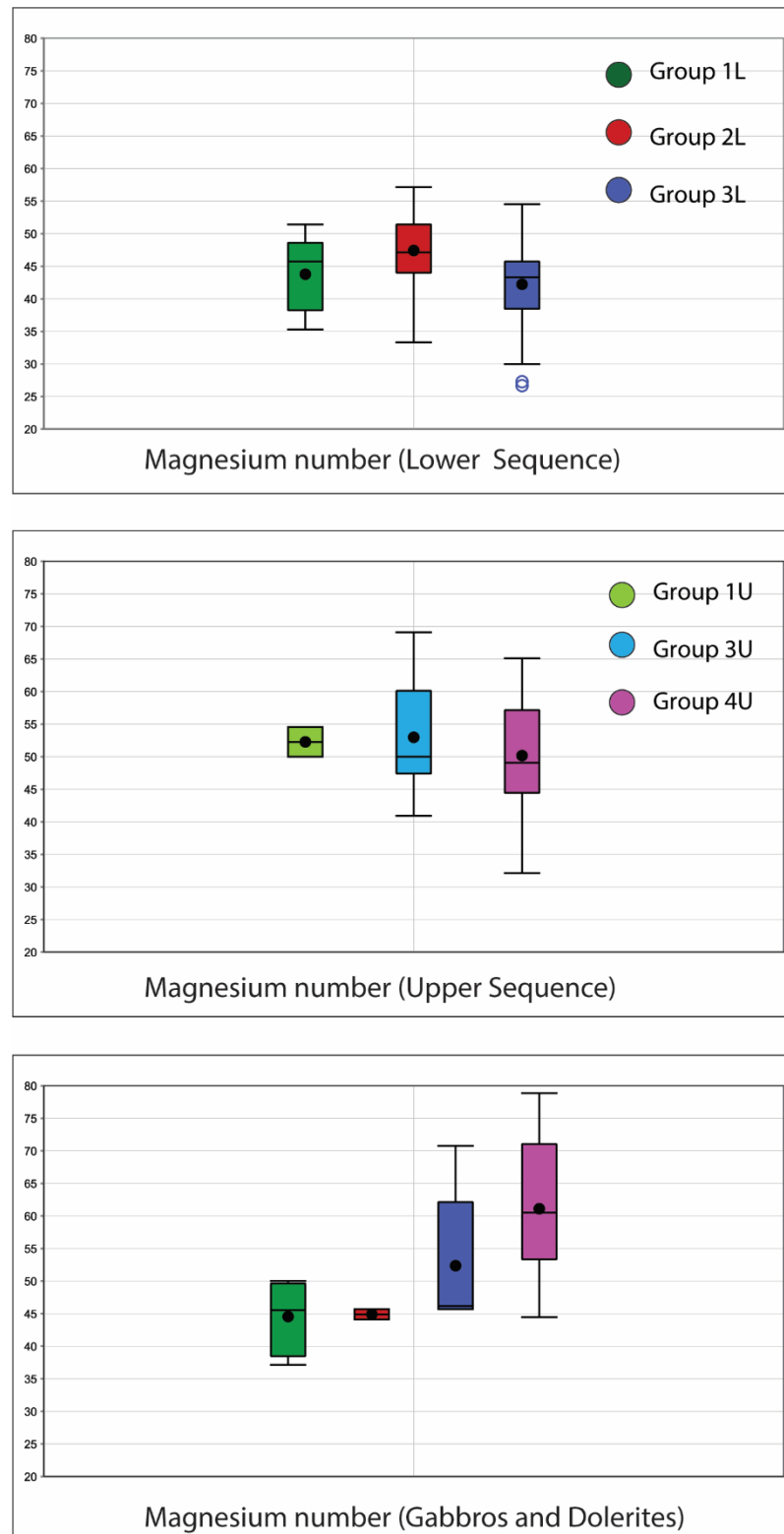


Figure 4-10 Box and whisker plots, showing the range of magnesium numbers (Mg#) for the rocks of the Lower, Upper sequences and the gabbro-dolerite lithofacies. The top and bottom of whiskers represent minimum and maximum values in each subset; the black line is the median value, and the black dot is the mean value. Details of the box and whisker plots are presented in Appendix B Table A-16.

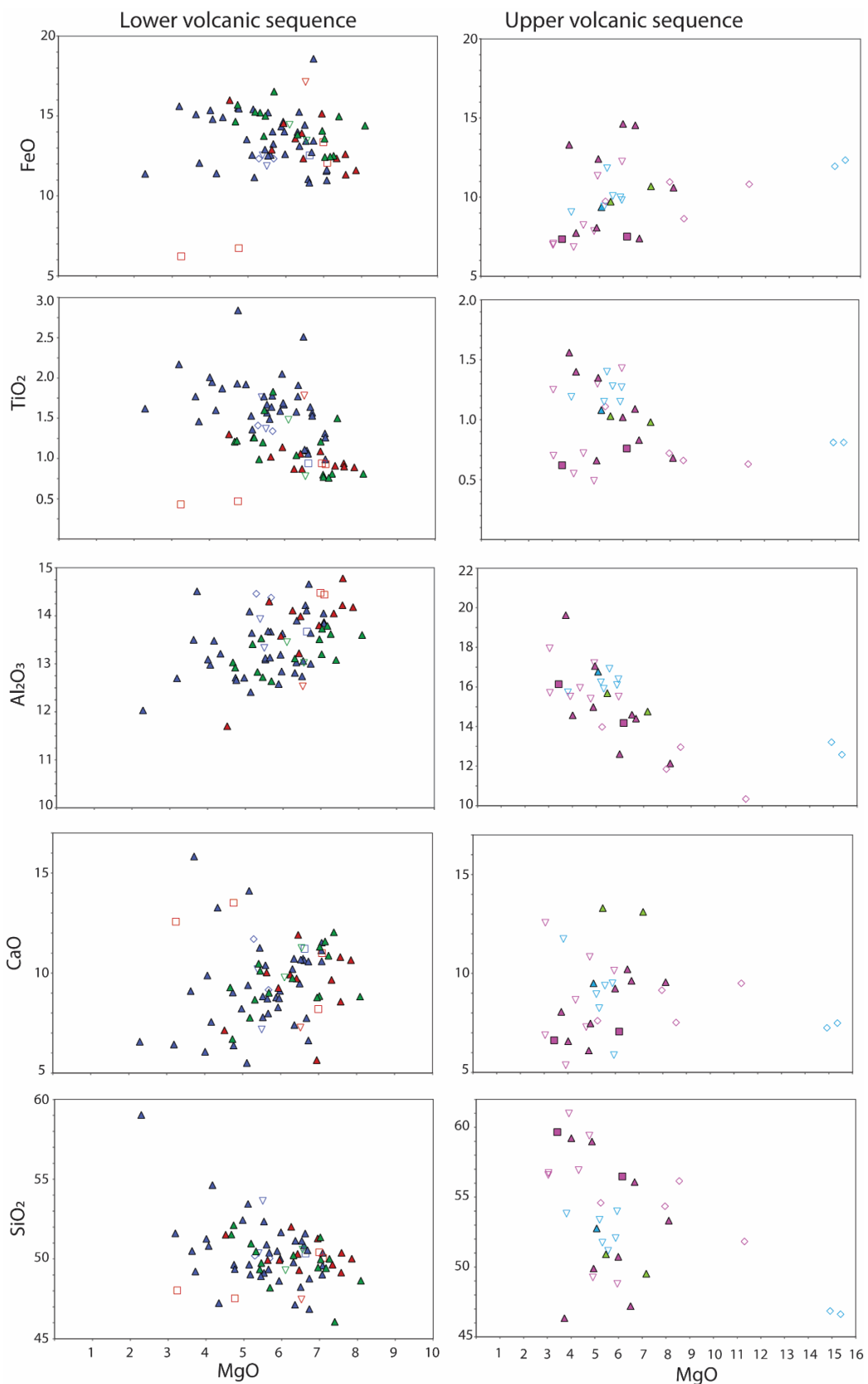


Figure 4-11 Binary plots of selected major elements against MgO for the volcanic rocks showing variation. Two pyroxene-porphyritic basalt samples from the UVS with MgO ~15 wt. % have been omitted to deskew the plot. All gabbros and dolerites have been omitted to enhance comparison between volcanic rocks only.

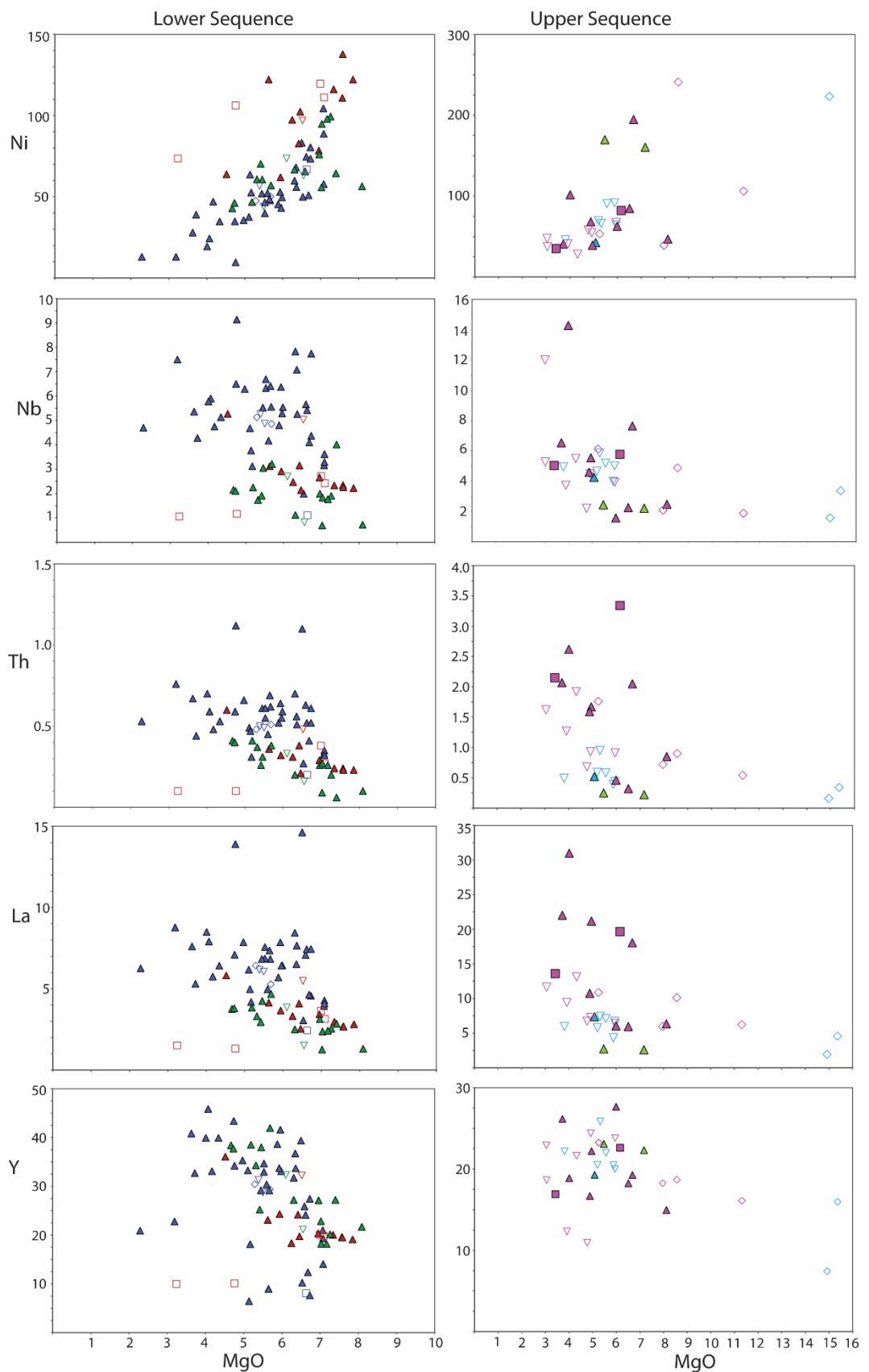


Figure 4-12 Binary plots of selected trace elements against MgO for the volcanic rocks showing variation. Intrusive rocks have excluded to deskew the plots.

Table 4-3 Key geochemical characteristics of the Lower and Upper volcanic Sequence and associated Intrusive lithofacies.

	Lower Sequence			Upper Sequence			Gabbros & Dolerite			
	Group 1L	Group 2L	Group 3L	Group 1U	Group 3U	Group 4U	Group 1	Group 2	Group 3	Group 4
Mg#	35–51	33–57	27–55	50 & 54	41–69	32–65	37–50	44 & 46	46–71	44–79
(La/Sm)_N	0.5–1.0	0.8–1.1	0.9–1.5	0.8	1.0–1.5	1.4–5.2	0.5–1.0	1.0 & 1.2	1.1–1.6	1.4–2.7
(Gd/Yb)_N	0.9–1.3	1.0–1.1	1.2–2.1	1.2	1.3–1.7	1.1–3.9	0.9–1.2	1.1 & 1.2	1.3–2.0	1.2–2.2
Eu/Eu*	0.8–1.1	0.9–1.2	0.8–1.2	1.0	0.9–1.0	0.3–1.1	0.9–1.1	1.0	0.8–1.0	0.8–1.1
Th/TiO₂	0.04–0.4	0.2–0.5	0.2–0.6	0.2	0.2–0.7	0.3–4.4	0.1–0.4	0.3 & 0.4	0.3–0.8	0.3–4.0

Magnesium number Mg# = molar $[\text{Mg}/(\text{Mg} + \text{Fe})] * 100$. N = Chondrite normalised. Eu/Eu* = $(\text{Eu})_{\text{N}} / [(\text{Sm})_{\text{N}} \times (\text{Gd})_{\text{N}}]^{0.5}$

4.3.3 Neodymium isotopes

Whole-rock Sm-Nd isotopic data for the Houndé and Boromo belts are presented in Table 4-4. The dataset from each belt includes four samples from the Lower sequence, one intrusive sample, and one sample from the Upper sequence and covers Groups 1–4 signatures. The $^{147}\text{Sm}/^{144}\text{Nd}$ and $^{143}\text{Nd}/^{144}\text{Nd}$ ratios obtained for samples of the Boromo belt range from 0.1313–0.2534 and 0.511620–0.513623, while those of the Houndé belt range from 0.1187 to 0.2283 and 0.511558 to 0.513092, respectively.

Calculating the initial $^{143}\text{Nd}/^{144}\text{Nd}$ ratios of the dataset is no straightforward task as the precise ages of these rocks are unknown. Due to the lack of precise ages of the rocks in the Lower and Upper sequences, it is assumed that the rocks within each volcanic sequence are co-magmatic and contemporaneous, and their collective ages will be estimated based on this assumption. Thus, the volcanic rocks of the Lower Sequences of each belt were emplaced roughly at about the same timeframe. Figure 4-13 displays the pseudo-isochron diagrams of Group 1L and 2L and Group 1L and 3L rocks of the Boromo and Houndé belts, respectively. Samples from the Boromo belt define a pseudo-isochron line with a slope of 2369 ± 76 Ma (MSWD = 2.2 σ , N = 5), an initial $^{143}\text{Nd}/^{144}\text{Nd}$ ratio of 0.509590 ± 0.000010 and εNd (t=2.3 Ga) value of -1.31. Samples from the Houndé belt yields a slope of 2313 ± 34 Ma (MSWD = 16.2 σ , N = 5), an initial $^{143}\text{Nd}/^{144}\text{Nd}$ ratio of 0.509641 ± 0.000042 and εNd (t=2.3 Ga) value of -0.31. No age could be estimated for the rocks of the Upper sequence because only two samples were analysed. However, the magmatic age of the Upper sequence is estimated at approximately 2200 Ma based on a 2212 ± 31 Ma (Amphibole in rhyolite, K-Ar isotopic system) emplacement age obtained by Castaing et al. (2003) in the western Houndé belt.

Initial $^{143}\text{Nd}/^{144}\text{Nd}$ ratios of each sample have been calculated using the estimated ages to evaluate deviations (εNd) from the Chondritic uniform Earth (CHUR) ratios. Calculated initial $^{143}\text{Nd}/^{144}\text{Nd}$ ratios of the Lower sequence of the Boromo belt vary from 0.509641 to 0.509782 with εNd (t=2.3 Ga) values of -0.32 to +2.45 while that of the Houndé belt range from 0.509619–0.509695 with εNd (t=2.3 Ga) values of -0.74 to +0.74. On the other hand, the initial $^{143}\text{Nd}/^{144}\text{Nd}$ ratios of the Upper sequence rocks are 0.509718 and 0.509837 with εNd (t=2.2 Ga) values of -1.37 and +0.97.

Table 4-4 Whole-rock Sm-Nd isotope data of selected samples from the Lower (LVS), Upper volcanic sequences (UVS), and intrusive lithofacies of the Houndé and Boromo belts.

Stratigraphic sequence	Group	Sample	Lithofacies	Sm (ppm)	Nd (ppm)	$^{147}\text{Sm}/^{144}\text{Nd}$	\pm	$^{143}\text{Nd}/^{144}\text{Nd}$	$\pm 2\text{SD}$	$^{143}\text{Nd}/^{144}\text{Nd}$ initial	
ϵNd (t=2.3Ga)											
<u>Boromo Belt</u>											
LVS	G1	GS_086	Aphyric Basalt	1.9	4.19	0.2534	0.00127	0.513623	0.00009	2.45	0.509782
LVS	G1	GSA063	Aphyric Basalt	2.45	6.12	0.2237	0.00112	0.513031	0.000027	-0.32	0.509641
LVS	G2	GS-076	Aphyric Basalt	2.08	6.16	0.1887	0.00094	0.512523	0.000009	0.11	0.509663
LVS	G2	GSA004	Aphyric Basalt	2.13	6.08	0.1952	0.00098	0.512668	0.000008	1.02	0.509709
Intrusive	G1	GSA073	Gabbro	7.05	16.69	0.2357	0.00118	0.513278	0.00001	0.95	0.509706
<u>Houndé Belt</u>											
LVS	G3	GS_029	Aphyric Basalt	4.94	15.65	0.1760	0.00088	0.512362	0.000013	0.74	0.509695
LVS	G3	GSA022	Aphyric Basalt	5.98	20.25	0.1648	0.00082	0.512165	0.000012	0.20	0.509667
LVS	G3	GSA023	Aphyric Basalt	4.04	12.27	0.1836	0.00092	0.512403	0.000002	-0.74	0.509619
LVS	G1	GSA080	Aphyric Basalt	2.82	7.29	0.2161	0.00108	0.512946	0.000007	0.29	0.509672
Intrusive	G1	GS_026A	Gabbro	3.86	9.45	0.2283	0.00114	0.513092	0.000091	-0.48	0.509632
ϵNd (t=2.2Ga)											
UVS	G4	GSA078	Aphyric Basalt	6.71	31.53	0.1187	0.00059	0.511558	0.000019	0.97	0.509837
UVS	G4	GSA062	Hornblende-plagioclase porphyritic Andesite	3.55	15.08	0.1313	0.00066	0.511620	0.000048	-1.37	0.509718

Error in $^{147}\text{Sm}/^{144}\text{Nd}$ ratio is estimated at 0.5%, error on Nd isotope is internal reproducibility of standard value of La Jolla. ϵNd is calculated at 2.3 Ga and 2.2 Ga based on chondritic uniform reservoir (CHUR); present-day values of $^{143}\text{Nd}/^{144}\text{Nd} = 0.512638$ and $^{147}\text{Sm}/^{144}\text{Nd} = 0.1967$ of DePaolo and Wasserburg (1976).

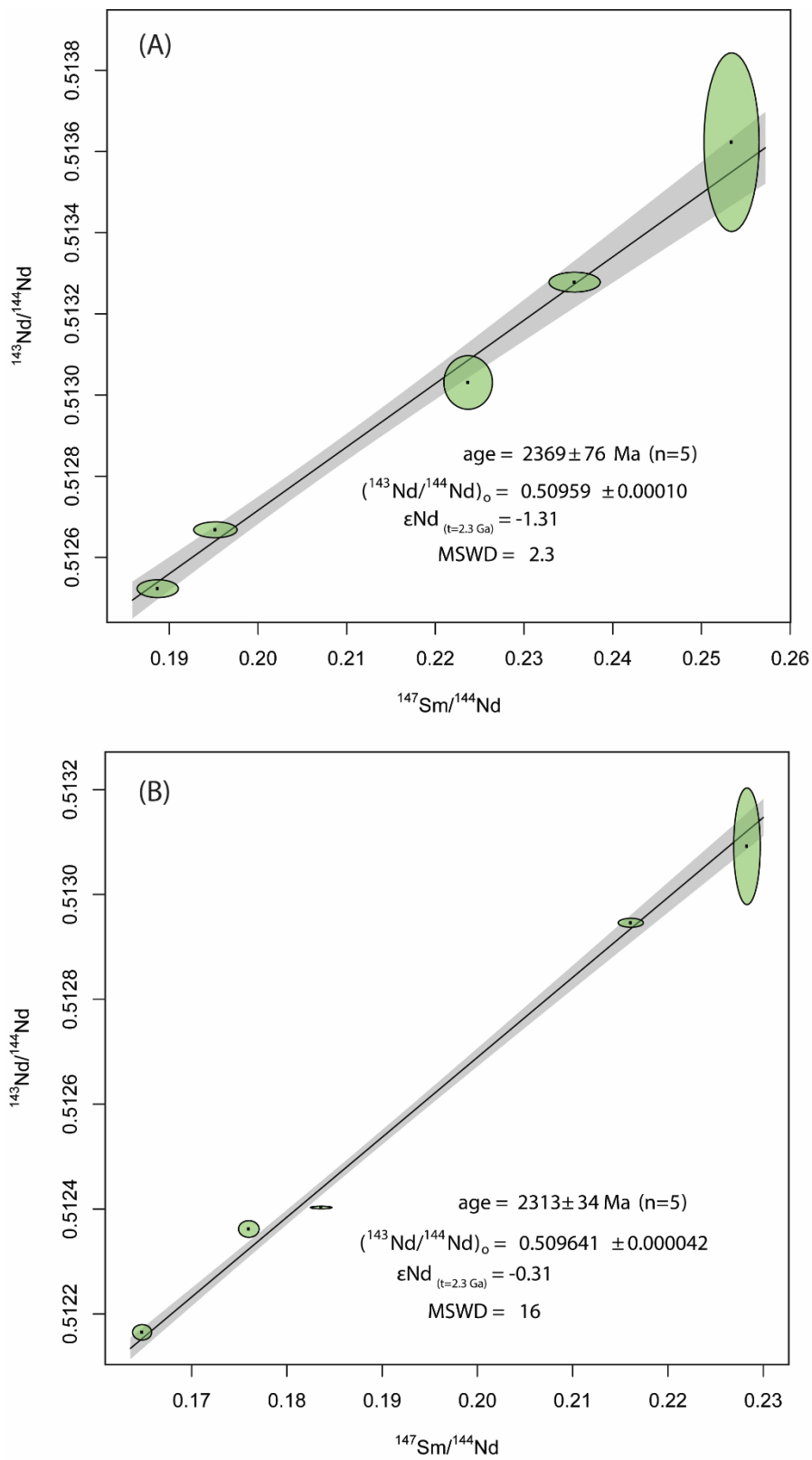


Figure 4-13 $^{143}\text{Nd}/^{144}\text{Nd}$ vs $^{147}\text{Sm}/^{144}\text{Nd}$ pseudo-isochron plots of Lower sequence rocks (A) Select samples from the Boromo belt yielding an age of 2369 ± 76 Ma (MSWD = 2.3) (B) Select samples from the Houndé belt yielding an age of 2313 ± 34 Ma (MSWD = 16). Error margins are 2 sigma standard deviation and expressed by the outline of ellipses. Grey boundaries around the regression line are the error on the isochron. Age calculation was done using the online version of IsoplotR by Vermeesch (2018).

4.3.4 Chemostratigraphy

Here, the geochemical groups are superimposed on the reconstructed volcanic stratigraphy (this study; Chapter 3) to shed light on the spatial and relative temporal distribution of the magmatic systems in the study area. The compilation of geochemistry and stratigraphy has helped to correlate identical volcanic successions and to reaffirm the boundaries of the Lower and Upper sequence of both belts (Figure 4-14).

The Lower sequence of the Houndé belt (eastern margin) is dominated by thick (>5km) successions of evolved low-Th, high-Fe tholeiitic basalts with Group 3L signatures (slightly enriched LREE over HREE). This succession is intercalated with Group 1L (LREE depleted over HREE) near the base and is host to Group 4U (strong LREE enrichment over HREE) Upper sequence intrusions. In the southern part of the belt, the base of the succession comprises Group 1L (flat REE) rocks overlain by Group 3L. The Lower sequence of the southern part of the Houndé belt has a different lithological succession compared to the rest of the belt. The Upper sequence of the Houndé belt is dominated by low to high-Th tholeiitic and calc-alkaline basaltic to andesitic rocks. At the western part of the Houndé belt, the base of the Upper sequence comprises rare lavas with Group 1U signatures, which are overlain by Group 4U rocks. In the southern part of the belt, the Upper sequence comprises Group 3U rocks only.

In contrast, the Lower sequence of the Boromo belt is dominated by evolved low-Th, high-Fe tholeiitic basalts with Group 2L signatures overlain by Group 1L in most places. In the northern part of the Boromo belt, the lowermost successions are characterised by Group 1L rocks and intruded by Group 4U rocks. In the southern part of the Boromo belt, Group 2L is overlain by Group 3L rocks similar to the southern extension of the Houndé belt. The Upper sequence of the Boromo belt comprises low to high-Th tholeiitic and calc-alkaline basaltic to andesitic rocks of Group 4U signatures only.

By comparing the spatial distribution and intrusive relationships of the geochemical groups in both belts, it is apparent that Group 3L rocks dominate the Lower sequence of the Houndé belt while Group 2L rocks dominate the Boromo belt. But in the southern part of both belts, Group 2L lavas are overlain by Group 3L, suggesting Group 2L magmatism pre-dates Group 3L. Concurrently, Group 1L rocks, which are common in the northern part of the Boromo belt, also intrude Group 3L

succession in the Houndé belt suggesting Group 1L probably post-dates Group 3, making Group 1L signatures the youngest in the Lower sequence. There appears to be a south to north relative age progression in the Lower sequence of both belts. Concerning the Upper sequence, Group 4 dominates both belts, but in the southern part of the Houndé belt, Group 3 is the most common. Group 4 rocks, which are lavas in the Upper sequence, also intrude the Lower sequence (all groups) of both belts, suggesting they are significantly younger. The relationship between Groups 1U, 3U, and 4U remains unclear due to the lack of contact relationships between them to interpret their relative age. However, because Group 1U appears at the base of the stratigraphic succession of the Upper sequence in the Houndé belt they might be the oldest.

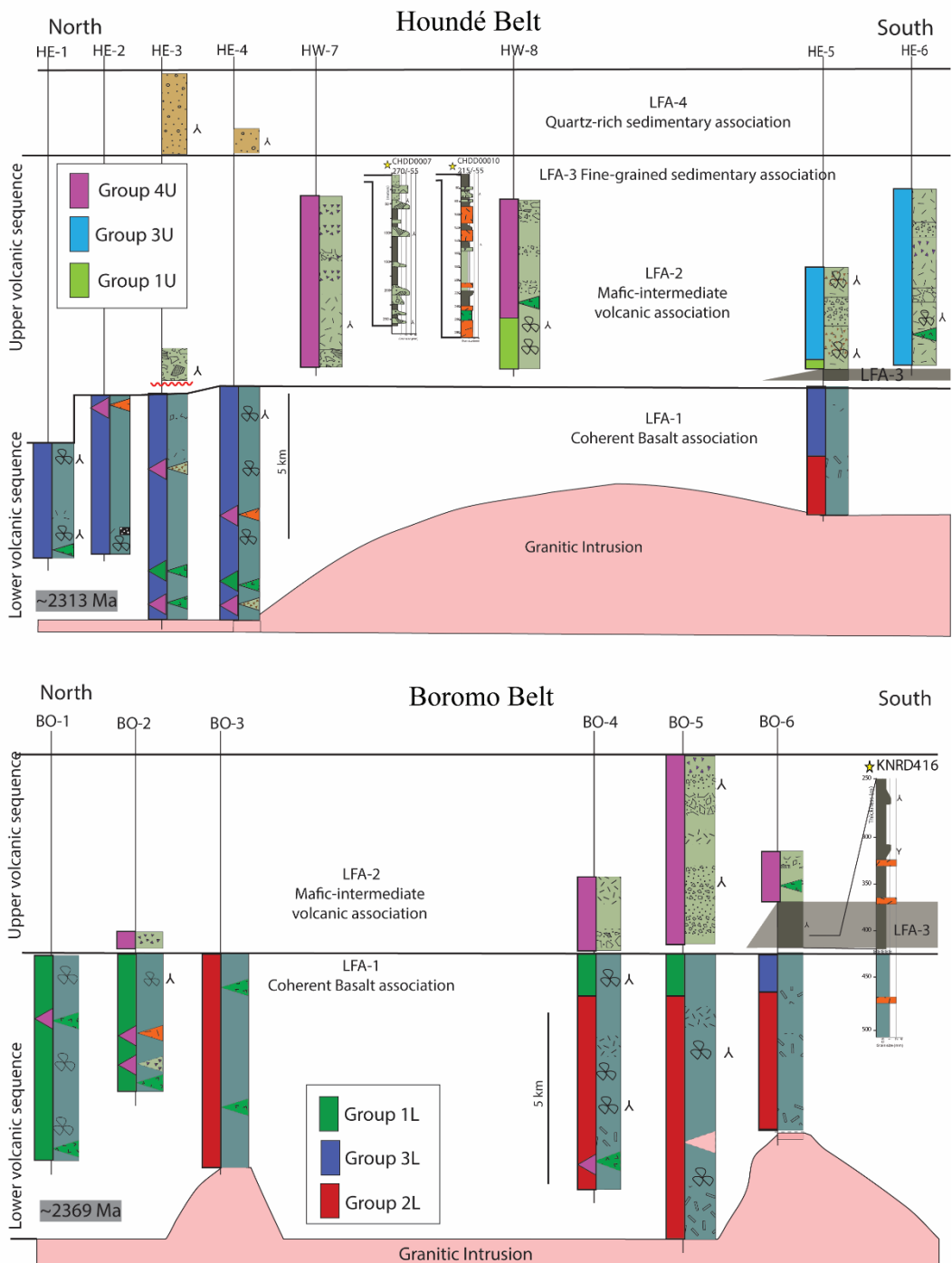


Figure 4-14 Summary of the spatial distribution of geochemical groups within the Houndé and Boromo belts. For the Lower sequence, Group 3L dominates the Houndé belt and is underlain by Group 2L in the south. In contrast, Group 2L dominates the Boromo belt and in places overlain by Group 1L with the south similar to the southern Houndé succession. In the Upper sequence of both belts, Group 4U dominates and is underlain by Group 1U. In the southern part of the Houndé belt, Group 3U of the Upper sequence dominates.

4.4 PETROGENESIS

The major and trace elements concentrations reveal distinguishable signatures within the Lower and Upper sequence rocks, which are critical to understanding their petrogenetic history. Generally, the rocks of the Lower sequence are evolved (low Mg#), low-Th tholeiitic basalts composed of rocks with Group 1L, 2L, and 3L signatures. Group 1L and Group 2L rocks of the Lower sequence typically possess lower absolute concentrations of TiO₂, Nb, Th, La, and higher concentrations of Ni than Group 3L rocks, making them (Group 1L & 2L) collectively more primitive (less evolved) than Group 3L. On the other hand, the rocks of the Upper sequence are moderately evolved, intermediate to high-Th basalts and andesites, exhibiting tholeiitic and calc-alkaline affinities. They are characterised by a few Group 1U, Group 3U, and abundant Group 4U signatures.

In this section, the petrogenetic origin of each geochemical group will be investigated based on their major, trace elements, and Sm-Nd isotope variations to reconstruct the magmatic history of both belts. The intrusive lithofacies will not be investigated further due to the lack of robust stratigraphic constraints.

4.4.1 Fractional Crystallisation

The major and trace elements trends of the Lower and Upper sequence relative to MgO define good near-linear correlation, which corresponds to fractional crystallisation in an evolving magma (Frey et al., 1978) (see Figure 4-11 & 12). All the trace elements and TiO₂, SiO₂, and CaO exhibit similar trends relative to MgO. In contrast, the concentrations of FeO and Al₂O₃ relative to MgO differ between the Lower and Upper sequence rocks as MgO decreases. The concentrations of Al₂O₃ decrease while FeO increases in the rocks of the Lower sequence and vice versa for the Upper sequence (see Figure 4-11). This observation suggests contrasting fractional crystallisation pathways for the Lower and Upper sequence rocks resulting from the physical or chemical state of the evolving magma (e.g. temperature, depth, water content) (Yoder Jr & Tilley, 1962; Till, 2017).

Here, an attempt is made to model the fractional crystallisation pathways to explain the major and trace element variance identified in the Lower and Upper sequence rocks. The models will test the hypothesis that: (1) preferential enrichment in FeO is primarily a function of the water content of the magma; thus, anhydrous

magmas will restrict early crystallisation of magnetite (Fe_3O_4), thereby accumulating iron in the melt (Brooks et al., 1991; Xu et al., 2003), and (2) high-pressure fractionation facilitates clinopyroxene saturation ahead of plagioclase thereby accumulating Al_2O_3 in derivative melts (Albarede, 1992).

Fractional crystallisation model parameters

Primary magmas are unmodified magmas derived from partial melting of a mantle source (Herzberg & Asimow, 2015). Primary magmas are typically characterised by $\text{Mg}\# \geq 70$, high $\text{Ni} > 200$ ppm, and $\text{Cr} > 400$ ppm (Norman & Garcia, 1999; Whattam, 2018). Ideally, to successfully model the differentiation pathway of basalts, it is required to identify the least evolved sample with composition nearest to the potential primary magma composition. However, none of the analysed volcanic rocks of the Lower and Upper sequences has major and trace element compositions close to primary magmas. Therefore, an attempt was made to estimate primary magma compositions from the most primitive aphyric basalts using the formulae of Lee et al. (2009); Herzberg and Asimow (2015). These formulae re-equilibrate the most primitive magma compositions with olivine of forsterite content 90 and assume olivine was the dominant fractionating phase of melt derived from a fertile mantle peridotite (Herzberg & Asimow, 2015). The most primitive volcanic compositions ($\text{MgO} > 7$ wt.%, $\text{Mg}\# > 50$) within the dataset could not be used to estimate primary magma compositions because of the low MgO content relative to CaO . Since the primary magma composition could not be estimated without much error, the most primitive compositions of each geochemical group will be used as the parental magma (starting composition) for the fractional crystallisation models.

The Rhyolite-MELTS thermodynamic modelling software (Gualda et al., 2012) was used to model the fractional crystallisation of each geochemical group. The Rhyolite-MELTS software allows to model magma evolution scenarios under hydrous and anhydrous conditions over a wide range of temperatures (2000–500 °C), pressures (0–2 GPa), and a variety of oxygen fugacity buffers. The fractional crystallisation model aims to replicate the conditions under which the analysed rocks evolved by comparing the results of the model output with the natural rocks. The result of the fractional crystallisation modelling is presented in Table A- 15 of the Appendix. The models were simulated under the following constraints: closed-system fractionation, thus no crustal assimilation, isobaric conditions at each stage of fractionation, redox

condition of quartz-fayalite-magnetite (QFM) buffer, and fractional (Rayleigh) crystallisation equation [$F^{(D-1)} = C_i / C_o$]; where F= fraction of melt remaining, C_i = concentration element in the melt, C_o = initial concentration of that element in the original melt, D = bulk distribution coefficient for element.

Although many scenarios were simulated, only the best fit models are presented here. These are:

Model 1: 1 kbar anhydrous magma condition

Model 2: 5 kbar anhydrous magma condition

Model 3: 1 kbar hydrous magma condition (1% H₂O in starting composition)

Model 4: 5 kbar hydrous magma condition (1% H₂O in starting composition)

Results of Fractional crystallisation modelling

Group 1L- Lower Sequence

The major element trends of the Group 1L rocks of the Lower sequence match well with Model 3 (1 kbar, 1% H₂O) (Figure 4-15). Using sample Gs_086 (MgO = 8.09 wt.%) as the starting composition (parental melt), Model 3 produces a liquid line of descent (LLD) characterised by a gradual increase in FeO until MgO of ~4 wt.% where the concentration of FeO reduces with decreasing MgO and fairly constant Al₂O₃ concentrations which begin to reduce at MgO= ~2 wt.% significantly. Model 3 predicts a liquidus temperature of 1175 °C with olivine of Forsterite content (f_o) = 0.77 being the first solid phase to crystallise from the parental magma composition (GS_086) (Figure 4-17). Subsequently, plagioclase (78% anorthite) crystallises at 1135 °C followed by clinopyroxene at 1095 °C and spinel at 1075 °C. The major element variation of Group 1L rocks matches up to 30% crystal fractionation of LLD of Model 3. A model of the trace element variation was achieved using an estimate of the predicted mineral assemblages of Model 3 and the mineral/melt partitioning coefficient database of Bédard (2001). The incompatible trace element variation of Group 1L rocks generally fits well with the simulated model except for a poor fit for Nb and a relatively higher estimation of HREE abundance. The trace element model accounts for about 50% fractional crystallisation predominantly of clinopyroxene to

achieve the most evolved composition of the Lower Sequence Group 1 rock suite (Figure 4-18).

The major and trace element trends predicted by Model 3 generally align well with Group 1L rocks of the Lower sequence suggesting shallow crustal storage of a hydrous parental melt. Extensive fractional crystallisation of clinopyroxene resulted in the geochemical diversity of this group. The model does not account for the influence of wall rock assimilation, which may have been a significant factor for the natural rocks.

Group 2- Lower Sequence

The major element trends of the Group 2L rocks of the Lower sequence match well with Model 1 (1 kbar, anhydrous) (Figure 4-15). Using sample Gs_096 ($\text{MgO} = 7.58 \text{ wt.\%}$) as the starting composition, Model 1 generates a liquid line of descent (LLD) characterised by an increase in FeO until MgO of $\sim 3.5 \text{ wt.\%}$ where the concentration of FeO reduces with decreasing MgO and consistent reduction in Al_2O_3 . Model 1 of Group 2L rocks predicts a liquidus temperature of 1207°C and olivine ($f_o = 0.79$) is predicted as the first solid phase to crystallise from the parental magma composition (GS_096) (Figure 4-17). Subsequently, plagioclase (67% anorthite) crystallises at 1187°C followed by clinopyroxene at 1167°C and spinel at 1107°C . The major element variation of Group 2L rocks corresponds to about 40% crystal fractionation of LLD of Model 1. Using the predicted mineral assemblages of Model 1, the incompatible trace element variation of Group 2L rocks accounts for more than 50% fractional crystallisation of parent magma to achieve the most evolved composition of the suite (Figure 4-18). The best-fit trace element model is achieved when clinopyroxene is the dominant fractionating solid phase, contrary to the predicted mineral assemblage where plagioclase is the most abundant early crystallising phase. The trace element variation predicted by Model 1 is preferred as it explains the entire geochemical variation observed in Group 2L rocks.

The major and trace element trends predicted by Model 2 suggest Group 2L rocks of the Lower sequence were probably obtained from an anhydrous parental melt composition under shallow crustal storage conditions with extensive crystallisation of clinopyroxene.

Group 3- Lower Sequence

The major element variations of Group 3L rocks of the Lower sequence mostly straddle between Model 1 (1 kbar, anhydrous) and Model 2 (5 kbar, anhydrous) (Figure 4-15). Using sample GSA061 ($\text{MgO} = 7.08 \text{ wt.\%}$) as the starting composition, Model 1 and Model 2 generate LLD characterised by an increase in FeO with inflexions at MgO values of 3.3 and 2.19 wt.%, respectively, where the concentration of FeO reduces with decreasing MgO . Concerning Al_2O_3 trends, Model 1 reduces consistently with decreasing MgO until $\text{MgO} = 3.3 \text{ wt.\%}$ while in Model 2, Al_2O_3 increases until $\text{MgO} = 5.33 \text{ wt.\%}$ as the concentrations begin to decrease. Both models are consistent with trends observed in the major elements trends observed in Group 3L rocks. Model 1 of Group 3L rocks predicts a liquidus temperature of $1198 \text{ }^{\circ}\text{C}$ where plagioclase (75% anorthite) is the first solid phase to crystallise from the parental magma composition (GSA061) (Figure 4-17). Next, clinopyroxene starts to crystallise at $1188 \text{ }^{\circ}\text{C}$, followed by spinel at $1108 \text{ }^{\circ}\text{C}$, and olivine (fayalite = 0.63) is a late phase at $1060 \text{ }^{\circ}\text{C}$. On the other hand, Model 2 of Group 3 rocks predicts a liquidus temperature of $1266 \text{ }^{\circ}\text{C}$ where clinopyroxene is the first solid phase to crystallise from the parental magma composition (GSA061) (Figure 4-17). Plagioclase (67% anorthite) crystallises next at $1226 \text{ }^{\circ}\text{C}$, spinel at $1146 \text{ }^{\circ}\text{C}$ and olivine (Fayalite = 0.74) is a late phase at $1046 \text{ }^{\circ}\text{C}$.

The major element variation of Group 3 rocks correspond to about 40% and 60% crystal fractionation of LLD of Model 1 and Model 2, respectively. Using the predicted mineral assemblages, the incompatible trace element variation of Group 3L rocks accounts for more than 50 % fractional crystallisation of parent magma to achieve the most evolved composition of the suite (Figure 4-18). The best fit trace element model occurs when clinopyroxene is the dominant fractionating solid phase for both Model 1 and Model 2. Model 1 and 2 for Group 3L rocks of the Lower sequence suggest an interaction between shallow and relatively deeper anhydrous magmas at different crustal levels.

Group 3- Upper Sequence

The major element trends of the Group 3U rocks of the Upper sequence best fit with Model 4 (5 kbar, hydrous melt) (Figure 4-16). The liquid line of descent of Model 4 for Group 3U Upper sequence rocks is characterised by an increase in FeO until

MgO of 2.81 wt.%, where FeO concentration reduces with decreasing MgO coupled with only a small increase in Al₂O₃. Model 4 of Group 3U rocks predicts a liquidus temperature of 1185 °C with clinopyroxene as the liquidus phase (Figure 4-17). Subsequently, plagioclase (72 % anorthite) crystallises at 1175 °C, followed by spinel at 1095 °C. The major element variation of the Group 3U rocks matches up to 30% crystal fractionation. The incompatible trace element variation of Group 3U rocks accounts for about 40% fractional crystallisation of parent magma to achieve the most evolved composition of the suite (Figure 4-18). The best-fit trace element model occurs when clinopyroxene is the dominant fractionating solid phase.

The major and trace element trends predicted by Model 3 suggest Group 3U rocks of the Upper sequence were produced by fractionation of clinopyroxene from a hydrous parental melt under relatively deep crustal storage conditions.

Group 4- Upper Sequence

The major element variation of Group 4U rocks of the Upper sequence fit closest to Model 4 (5 kbar, hydrous melt). Using sample GSA085 (MgO = 6.51 wt.%) as the starting composition, the liquid line of descent of Model 4 for Group 4 Upper sequence rocks is characterised by an increase in FeO until MgO of 4.44 wt.% where the concentration of FeO reduces with decreasing MgO while the concentration of Al₂O₃ increases minutely. The concentrations of FeO and Al₂O₃ in the natural rocks are consistently lower and higher, respectively than the modelled concentrations. Model 4 of Group 4U rocks predicts a liquidus temperature of 1186 °C with clinopyroxene as the liquidus phase (Figure 4-17). Subsequently, plagioclase (75% anorthite) crystallises at 1156 °C, followed by spinel at 1126 °C.

The modelled incompatible trace element variation of Group 4U rocks does not fit the variation in the natural rocks. Petrographically, Group 4U comprises abundant pyroxene and hornblende phenocryst; therefore, the model could not account for mineral accumulation during the magma evolution process. Assimilation fractional crystallisation (AFC) model using the composition of the Upper Continental Crust (Rudnick & Gao, 2014) as a contaminant ($r = 0.2$) produces a good prediction of the diversity of Group 4U rocks (Figure 4-18). The AFC model replicated the enrichment in LREE and pronounced negative Nb-Ta anomalies.

The evolution of Group 4U rocks is best explained by assimilation fractional crystallisation of a felsic contaminant similar to the Upper continental crust in a relatively deep crustal magma chamber of a hydrous melt. This interpretation culminates with the relatively high Th content of Group 4U rocks.

Summary

The fractional crystallisation models have been able to replicate the geochemical variations of each geochemical group. For the rocks of the Lower sequence, Group 1L and 2L allude to fractional crystallisation under relatively shallow (~3 km) crustal conditions. In comparison, Group 3L shows possible interaction between melts fractionating at relatively deeper crustal levels (~15 km). Group 2L and 3L rocks fit models for anhydrous melts, while Group 1L rocks suggest they may have been derived from hydrous melts, of at least 1% H₂O. The low-pressure, shallow magma model for Group 1L and 2L rocks shows that olivine is an early fractionating phase. The deficiency in CaO relative to low MgO in these rocks is a testament that perhaps a substantial amount of olivine may have been removed from the melt at an earlier stage before Group 1L and Group 2L melts were derived. This evidence suggests a possible polybaric, multistage fractionation system (Hole, 2018) and explains the consistently low Mg# tholeites of Group 1L and Group 2L. The best fit models for Group 3L rocks suggest clinopyroxene is an early crystallisation phase that is consistent with relatively deeper magma chambers.

Although the variation of Group 1L rocks is best explained by simple fractional crystallisation, they record minor negative Nb and Ti anomalies which may have resulted from assimilation of felsic crust or early fractionation of titanium-bearing phases (Aldanmaz et al., 2000). Concurrently, Group 1L rocks do not show evidence for extensive crustal contamination (e.g. high Sr, Pb, Th, enrichment in LILE and LREE relative to HFSE) (Barley et al., 2008). Therefore, the negative Nb and Ti anomalies could best be explained by fractionating titanium-bearing phases (Heinonen et al., 2019).

On the other hand, the rocks of the Upper volcanic sequence are likely products of fractional crystallisation (Group 3U) and assimilation fractional crystallisation (Group 4U) of hydrous melts stored in relatively deep-seated magma chambers at approximately 15 km equivalent to 5 kbar pressure; around the spinel-plagioclase

lherzolite stability boundary (Perkins & Anthony, 2011). Melts stored in deeper magma storage are more susceptible to the assimilation of crustal material due to higher pressures and temperatures than cooler, low-pressure shallow magma chambers (Heinonen et al., 2019). Group 1U is composed of only two samples, hence could not be modelled.

The fractional crystallisation models produced predict diverse crystallisation pathways common to more than one group. Here intergroup relationships will be explored to determine if one geochemical group could evolve from another via differential crystal fractionation. Figure 4-20 illustrates the fractional crystallisation (dominantly clinopyroxene and minor plagioclase) pathways from the selected parental compositions. The most primitive composition (thus the parental magma) of each geochemical group has distinct Th/Yb and Nb/Yb ratios indicative of distinct parental magma composition. None of the calculated fractional (including assimilation) crystallisation trajectories overlaps. However, some samples of Group 1L and Group 2L, Group 2L and Group 3L overlap suggesting they could share a common starting point. However, the overlapping samples of each group cannot be produced by crystal fractionation of a common parent composition since that would require a higher degree of fractionation ($>50\%$), resulting in the production of geochemically more evolved compositions that are not produced in each geochemical suite. Therefore, this suggests each geochemical group is unique and one group cannot be produced from another without generating more evolved compositions.

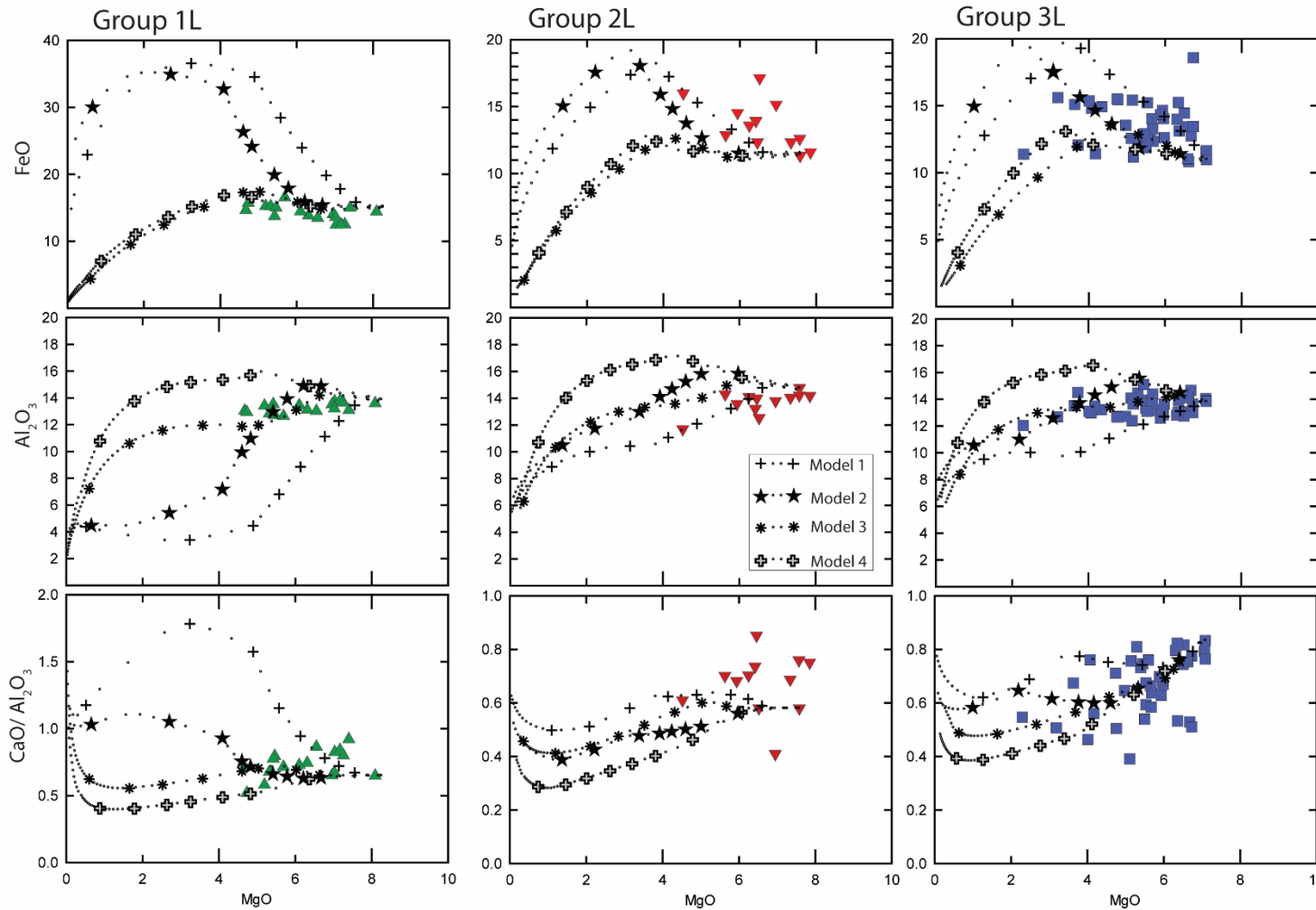


Figure 4-15 Fractional crystallisation modelling results for key major elements. Liquid lines of descent generated at varying pressures and initial H₂O content of starting composition at constant $f\text{O}_2$ indicated by Model 1 to Model 4. The models are compared to Group 1L to Group 3L of the Lower volcanic sequence. Markers indicate 10% increments of fractionation. Model 1: 1 kbar anhydrous magma condition Model 2: 5 kbar anhydrous magma condition Model 3: 1 kbar hydrous magma condition (1% H₂O in starting composition) Model 4: 5 kbar hydrous magma condition (1% H₂O in starting composition)

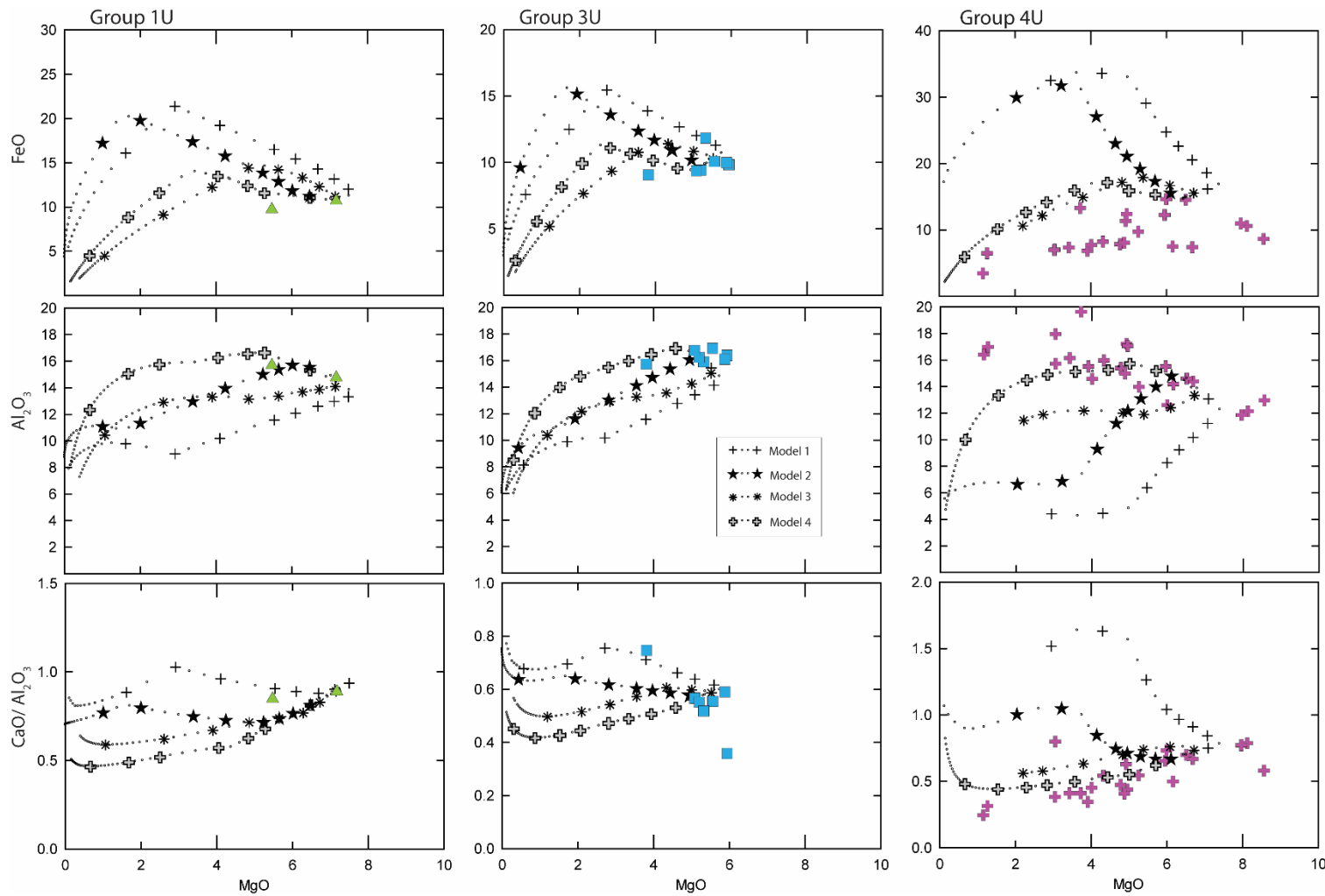


Figure 4-16 Fractional crystallisation modelling results for key major elements. Liquid lines of descent generated at varying pressures and initial H_2O content of starting composition at constant $f\text{O}_2$ indicated by Model 1 to Model 4. The models are compared to Group 1U, Group 3U and Group 4U of the Upper volcanic sequence. Group 1 has too few samples to define a geochemical trend. Markers indicate 10% increments of fractionation.

Lower volcanic sequence.

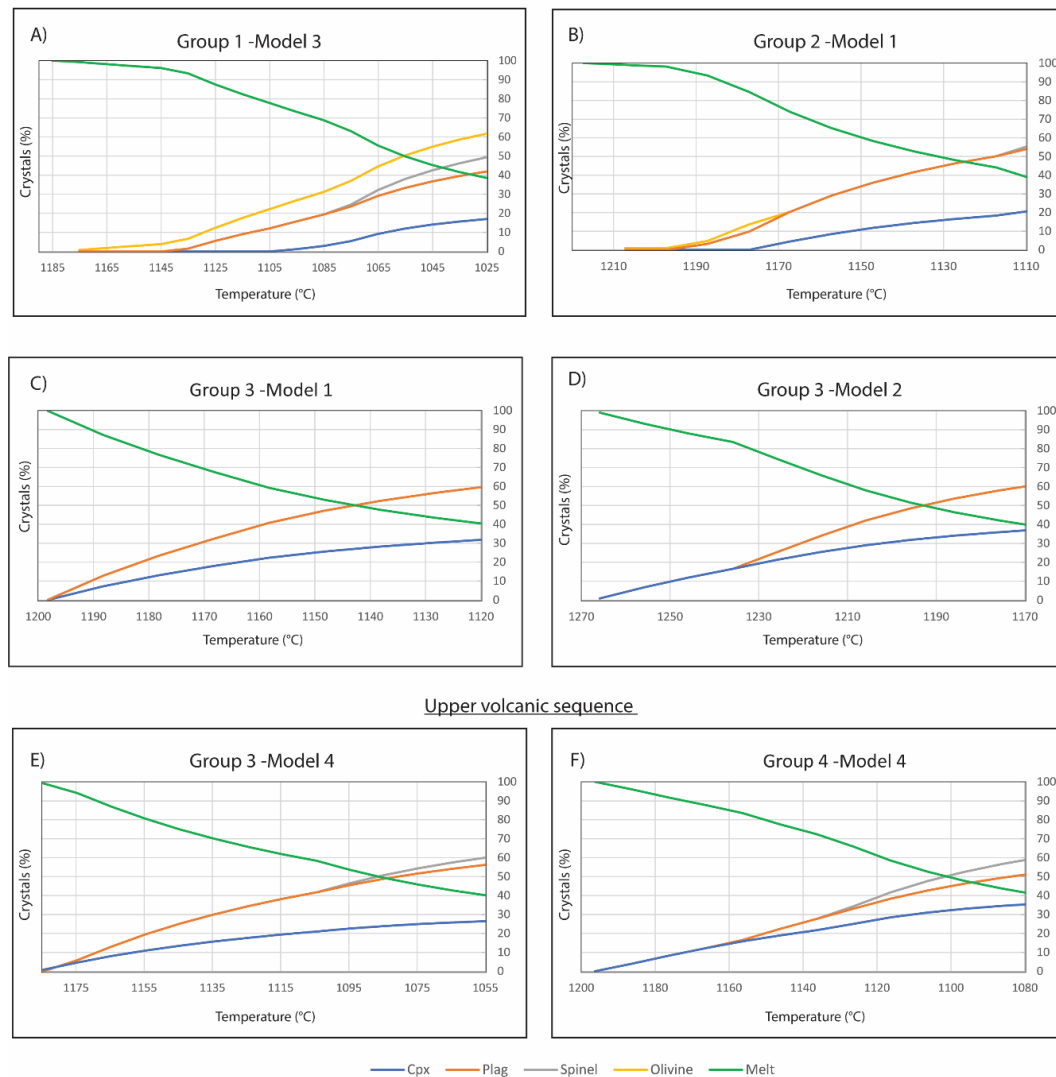


Figure 4-17 Plots of cumulative crystal proportions against the temperature of best-fit MELTS simulated fractional crystallisation models for Groups 1L, 2L & 3L (A, B & C, D) of the Lower sequence and Groups 3U and 4U (E & F) of the Upper sequence. Note: Group 3L of the Lower sequence fits Model 1 and Model 2 fractional crystallisation hence two diagrams. Also, Group 1L of the Upper sequence could not be matched with any model due to a lack of trend. Starting temperatures are calculated liquidus temperature of the parental magma. Crystal label: Cpx-clinopyroxene, Plag-plagioclase.

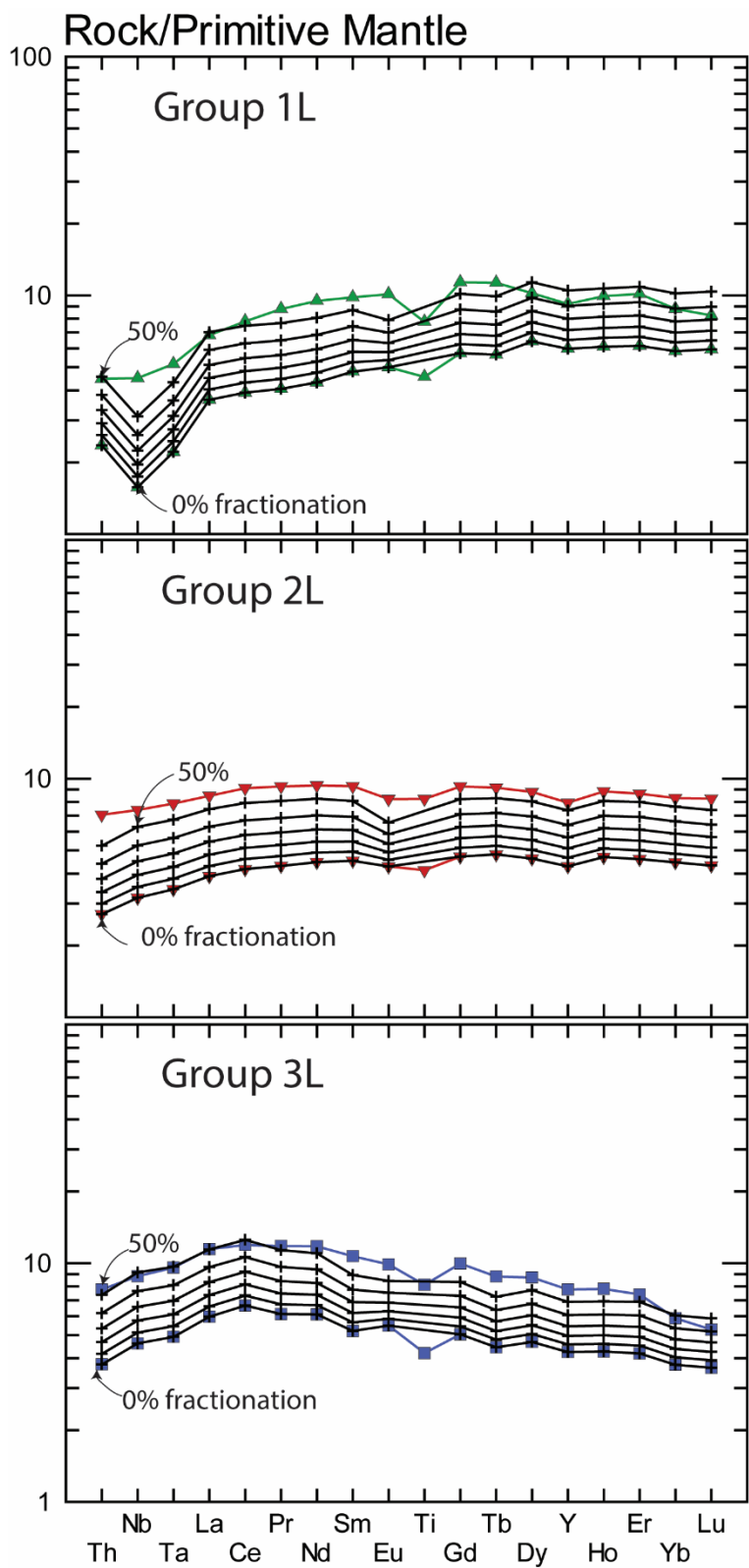


Figure 4-18 Primitive mantle normalised trace element diagrams for Group 1L, 2L, and 3L of the Lower sequence showing calculated liquid line of descent of best fit MELTS generated, fractional crystallisation models. Markers represent 10% incremental crystal fractionation. Note: Ti was not modelled due to a lack of reliable input parameters.

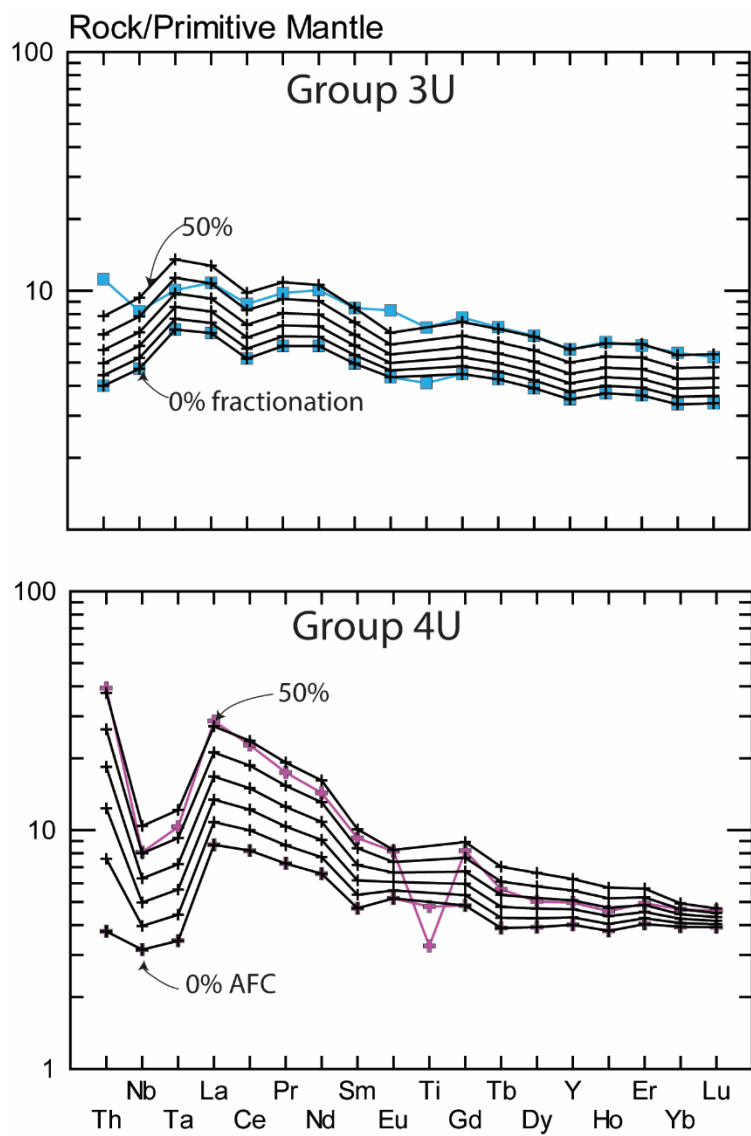


Figure 4-19 Primitive mantle normalised trace element diagrams for Group 3U and 4U of the Upper sequence showing calculated liquid line of descent of best fit MELTS generated fractional and assimilation fractional crystallisation models. Markers represent 10% incremental crystal fractionation. Group 4U was modelled by assimilation of a ratio of $r=0.2$ of the Upper continental crust (Rudnick & Gao, 2014).

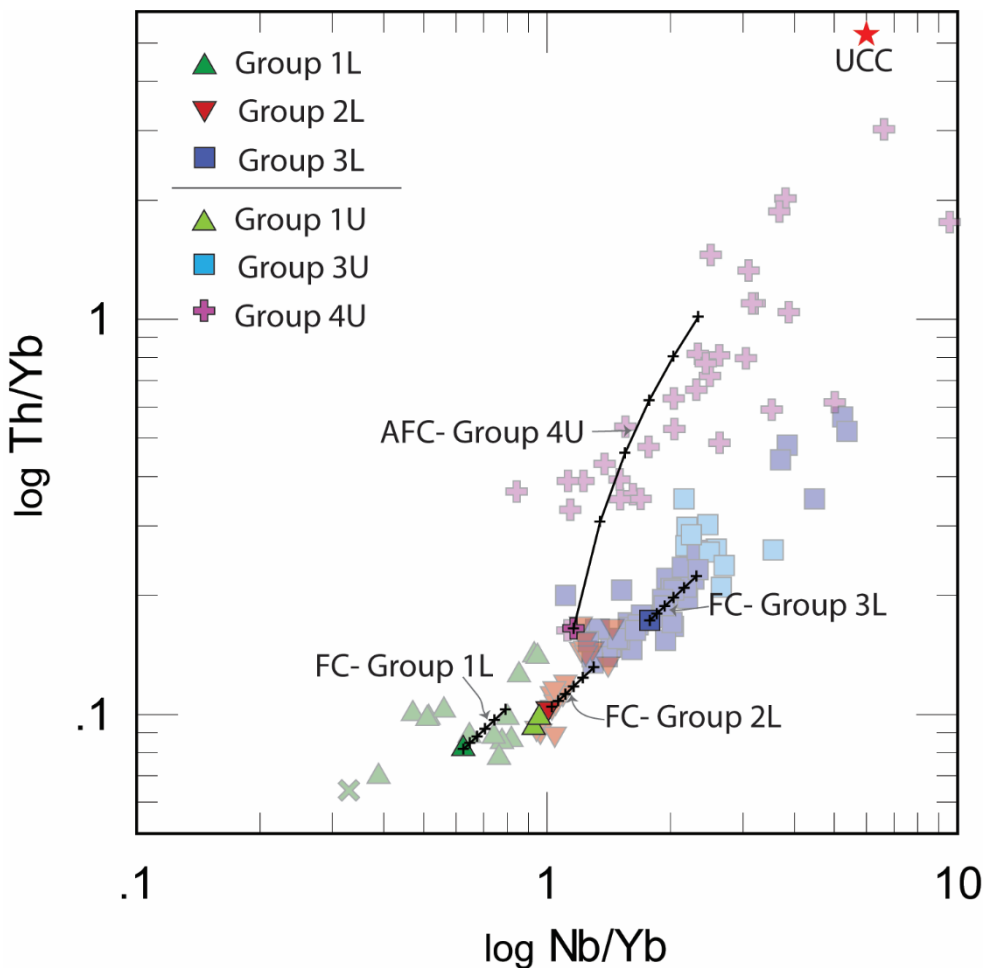


Figure 4-20 Th/Yb against Nb/Yb vector diagram showing the trajectory of calculated fractional crystallisation based on the most primitive composition (parental magma composition) of each geochemical group. The fractional crystallisation pathways of each group demonstrate that it is unlikely to produce the geochemical variation of one group from another through crystal fractionation.

Markers represent 10% fractionation of variable proportions of olivine, clinopyroxene, and plagioclase (see Figure 4-17 for the relative abundance of mineral assemblage). UCC= Upper continental crust by Rudnick and Gao (2014).

4.4.2 Nature of mantle source and origin of rock types

In this section, incompatible trace elements ratios coupled with Nd-isotopes of representative samples will be employed to discuss the nature of the mantle source and origin of Group 1- 4 rocks of the Lower and Upper sequence for both belts.

As previously mentioned, the volcanic rocks of the Lower and Upper sequences are evolved (i.e., relatively low MgO, Ni, and Cr) and do not have compositions comparable with primary magma compositions, which directly reflect the chemistry of the mantle source. Despite the lack of primary mantle compositions, incompatible trace elements ratios (e.g., La/Yb, Th/Ta, La/Nb, Nb/Th) can be used to detect the nature of the mantle source. These incompatible element ratios are not significantly affected by small degrees of fractional crystallisations or partial melting (Condie, 1994; Boyce et al., 2015). Concurrently, mantle-derived rocks inherit the isotopic character of the mantle at the time of melt extraction (DePaolo et al., 1991). Accordingly, the initial ϵ_{Nd} values of mantle-derived melt are consistently positive (high Sm/Nd ratio) as the crust is progressively extracted from the mantle. Therefore, ϵ_{Nd} values of the continental crust with low Sm/Nd ratios would result in negative ϵ_{Nd} values depending on their emplacement ages.

Group 1

Th/Ta and La/Yb ratios of Groups 1-4 rocks have been compared to modern mantle reservoirs; depleted MORB mantle (DMM; Workman and Hart (2005)), primitive mantle (PM), and their derivative basalt compositions to investigate the potential mantle source (Figure 4-21 A). Group 1L and 1U rocks are all characterised by relatively low La/Yb (< 2), signifying depleted mantle sources (Condie, 1994). They generally plot along with the PM–DMM hypothetical mixing line, but closer to PM than to DMM, suggesting that the mantle source was less depleted than the modern DMM. Although they have LREE depleted Chondrite-normalised signatures, their compositions are more enriched than the typical N-MORB. Notably, some of the Group 1L rocks deviate from the PM–DMM line with relatively higher Th-Ta ratios (≤ 2) indicative of source enrichment. These high Th/Ta Group 1L rocks are also characterised by relatively high La/Nb (> 1.4) with low Nb/Th (< 10) ratios (Figure 4-21 B). These features signify mantle source contamination or enrichment either by subduction-derived component (fluid or melt) or recycled crustal material (Stern et al.,

1995; Babechuk & Kamber, 2011). Distinguishing between mantle source modification by subduction-derived metasomatism and recycled material is difficult. Nevertheless, the consistently low Th/TiO₂ of Group 1L rocks precludes mantle source modification by subduction-derived component and more likely by the influence of a mafic recycled component (Sobolev et al., 2007). Group 1U rocks comparatively plot on the PM–DMM hypothetical mixing line with La/Nb <1.4 And Nb/Th ~10 suggesting pristine uncontaminated mantle source composition.

Figure 4-21 C is the modified versions of the Ce/Nb and Th/Nb diagram of Saunders et al. (1988) showing mixing curves between mantle source and end-member components; DMM, slab-derived component (SDC), and eclogitic LILE-depleted residual slab component (RSC). The SDC represents LILE-enriched and Nb-depleted fluid, and RSC is the reconstituted dehydrated slab that produces an Nb-enriched reservoir within the mantle. Compared with modern basalts types, Group 1 rocks generally have relatively higher Ce/Nb and Th/Nb ratios than typical N-MORBs, rather similar to back-arc basin basalts (BABB). Typically, BABB is generated by the interaction between dry melts from the depleted mantle and wet melts derived from subduction metasomatised mantle and can be differentiated from MORBs by the presence of water-rich components, relatively high abundance in LILE and Al₂O₃ coupled with lower TiO₂ and FeO (Bézos et al., 2009). Group 1L rocks correspond to fractional crystallisation LLD of a wet parental melt, although not a significantly high proportion. Together, the trace element ratios coupled with wet parental melt origin for Group 1L rocks suggest extraction from a modified depleted mantle source possibly from slab-derived components and less depleted mantle than the modern DMM.

Concerning their Nd-isotope signatures, the Group 1L rocks have initial ϵ_{Nd} (at 2.3 Ga) values ranging from +2.45 to -0.48. The strongly positive ϵ_{Nd} value of +2.45 is the closest value to the model Paleoproterozoic depleted mantle at 2.3 Ga suggesting Group 1L melts were extracted from a long-lived depleted mantle source (Figure 4-22). On the contrary, the low negative ϵ_{Nd} values may result from recycled crustal material incorporated into the mantle source (Chauvel et al., 1985; Yang et al., 2017). In conjunction with the trace element signatures (e.g., low Th/TiO₂ and LREE-depletion), lower crustal contamination can be ruled out, therefore suggesting deep-seated refertilisation of a depleted mantle source. Group 1U rocks possibly originated from

Group 2

In a similar stance, Group 2L rocks plot at the junction between the PM–DMM line and the PM–Enrichment line (Figure 4-21 A) with relatively low La/Yb (< 2) and Th/Ta (< 2) ratios. Their trace element variation suggests the Group 2 rocks were probably extracted from a PM-like mantle which is chemically less depleted in incompatible elements than DMM. The consistently flat unfractionated REE Chondrite-normalised patterns of Group 2L agree with a PM-like source. This PM-like mantle may be likened to enriched mantle 1 (EM-1) with estimated trace element and $^{207}\text{Pb}/^{204}\text{Pb}$ ratios comparable with PM yet not as highly enriched as the other enriched mantle reservoirs (e.g., EM-2 and HIMU; high $\mu = ^{238}\text{U}/^{204}\text{Pb}$) (Kamber, 2011). Also, Group 2L rocks are characterised by relatively low Nb/Th (6–12) and La/Nb (< 1.3) ratios which suggest they have not been contaminated by continental crust or subduction-derived components (Figure 4-21 B).

The Ce/Nb and Th/Nb diagram (Figure 4-21 C), Group 2 basalts plot in the overlap between ocean island basalt (OIB) and BABB compositions. However, the lack of subduction-zone signatures such as calc-alkaline basalts, negative Nb-Ta anomaly, and marks of wet melts rules out the likelihood of Group 2L basalt being BABB. The preferred origin of Group 2L rocks is from the extraction of deeply generated uncontaminated mantle melts such as plume magmatism. Group 2L rocks do not possess the characteristically high $(\text{Gd}/\text{Yb})_{\text{N}}$ and $(\text{La}/\text{Sm})_{\text{N}}$ ratios of the typical modern OIB, which result from low degrees of partial melting of deep garnet-bearing enriched source (Willbold & Stracke, 2006; Pearce, 2008).

A possible explanation for the lack of typical OIB signatures in Group 2L rocks is that they were extracted from the plume head (Loewen et al., 2013) or relatively shallow mantle reservoirs supplied by the upslope flow of a distal mantle plume towards a progressively thinner lithosphere (Pearce, 2008; Yang et al., 2017). This explanation also further indicates the influence of decompression melting and is supported by the evidence of shallow magma chambers; ~3 km for Group 2 rocks (see Figure 4-15). The low-positive initial ϵNd values (+0.11– +1.02; Figure 4-22) support the lack of crustal contamination or subduction-derived metasomatism and suggest minimal modification of a near-Chondritic mantle composition. The trace element ratios coupled with the flat REE signatures and isotopic variation are consistent with

oceanic flood basalts derived by shallow decompressions melting of a plume (e.g., Ontong Java plateau; Fitton et al. (2004)).

Group 3

Group 3 rocks, unlike Group 1 and 2, have relatively higher La/Yb and consistently low Th/Ta ratios (Figure 4-21). The Group 3L and Group 3U rocks plot along the PM-enriched component line suggesting their parental magmas were possibly obtained from an enriched mantle source. Their Chondrite-normalised REE patterns are similar to E-MORB with average $(La/Sm)_N$ ratios of 1.2 but comparatively lower than the global E-MORB ratio of >1.5 (Gale et al., 2013). Since the Group 3 signatures are compositionally similar to E-MORBs, they may have evolved by similar processes. The origin of E-MORBs is complex and highly debated. Some of the proposed origins of E-MORB include low-degree melting of an enriched garnet-bearing source (Waters et al., 2011) and two-component mixing of a depleted and enriched source (Arevalo & McDonough, 2010). In this case, Group 3 rocks do not exhibit pronounced HREE depletion, which rules out residual garnet in the source (Pearce, 2008). Therefore, the mixing between a depleted source and an enriched component is more likely in this instance. Their relatively higher abundance of Ti than Groups 1 and 2 also supports a relatively more enriched source (see Figure 4-9). Using their La/Nb and Nb/Th ratios, the majority of the samples exhibit relatively low La/Nb and Nb/Th ratios with few outlier samples having relatively higher La/Nb (~1.7) and Nb/Th (~13) (Figure 4-21 B). The observed trend shows that the mantle source of Group 3 rocks has not been significantly contaminated by crustally-derived components, although, not entirely absent.

On the Ce/Nb and Th/Nb diagram (Figure 4-21 C), Group 3L & U basalts plot in the overlap between ocean island basalt (OIB) and BABB compositions similar to Group 2L basalts. Comparable to Group 2L basalts, both Group 3L and Group 3U basalts lack subduction-related signatures hence are unlikely BABB. Also, Group 3 rocks exhibit relatively high $(Gd/Yb)_N$ and $(La/Sm)_N$ ratios typical of small degrees of partial melting of a relatively deeper source (e.g. basalts from Caribbean plateau; Kerr et al. (2000)). This evidence fits the relatively deeper (~15 km) magma residence condition of Group 3 rocks (see Figure 4-15). The initial ϵ_{Nd} values of Group 3L rocks are low positive and negative (-0.74 – +0.74; Figure 4-22), precluding any significant crustal contamination; but rather implies mixing between a minimally depleted source

and enriched component; perhaps deep-seated recycled crustal material (Frey et al., 2000; Sobolev et al., 2007). Overall, the Group 3L & U rocks have signatures comparable to tholeiites extracted from an enriched mantle component.

Group 4

Lastly, Group 4U rocks plot between Arc mantle and Upper continental crust compositions with relatively higher Th/Ta and La/Yb ratios than Group 1-3 (Figure 4-21 A). The observed trend in Figure 4-21 A coupled with mostly high Th/TiO₂ ratios, pronounced negative Nb-Ta and Ti anomalies, as well as relatively high abundances of LILE and LREE suggests they were possibly extracted from a contaminated or metasomatised mantle source. The mentioned characteristics of Group 4 rocks make them similar to modern island arc basalts (IAB). Concurrently, Group 4 rocks display relatively higher La/Nb (> 1.4) with low Nb/Th (<10) ratios signifying effects of either crustal contamination and/or metasomatism of mantle source by subduction-derived component (Condie, 2005; Pearce, 2008)(Figure 4-21 B).

The Ce/Nb and Th/Nb ratios of Group 4U basalts overlap between the BABB and arcs composition and trend towards the composition of subduction-derived component (Figure 4-21 C). The compositional variation within Group 4 rocks, thus low to high Th/TiO₂, tholeiitic to calc-alkaline basalt, and andesites, indicate that variable petrogenetic processes are important to their generation. These variations could have resulted from the complex interplay between the sub-lithospheric crustal contamination and slab-derived component (fluid and melt) modification of parental melts (e.g. Honshu arc Gust et al. (1997)). Therefore, it is suggested that the low-Th tholeiitic basalts of Group 4U, which do not exhibit strong signatures of crustal contamination, may have been the primitive melts in early arc evolution. Initial ϵ_{Nd} of two Group 4 samples (high La/Nb; crustally contaminated with values -1.37 and +0.97 (Figure 4-22) supports the interplay between crustal contamination (negative ϵ_{Nd}) and enriched SDC metasomatised mantle (Zhao & McCulloch, 1993).

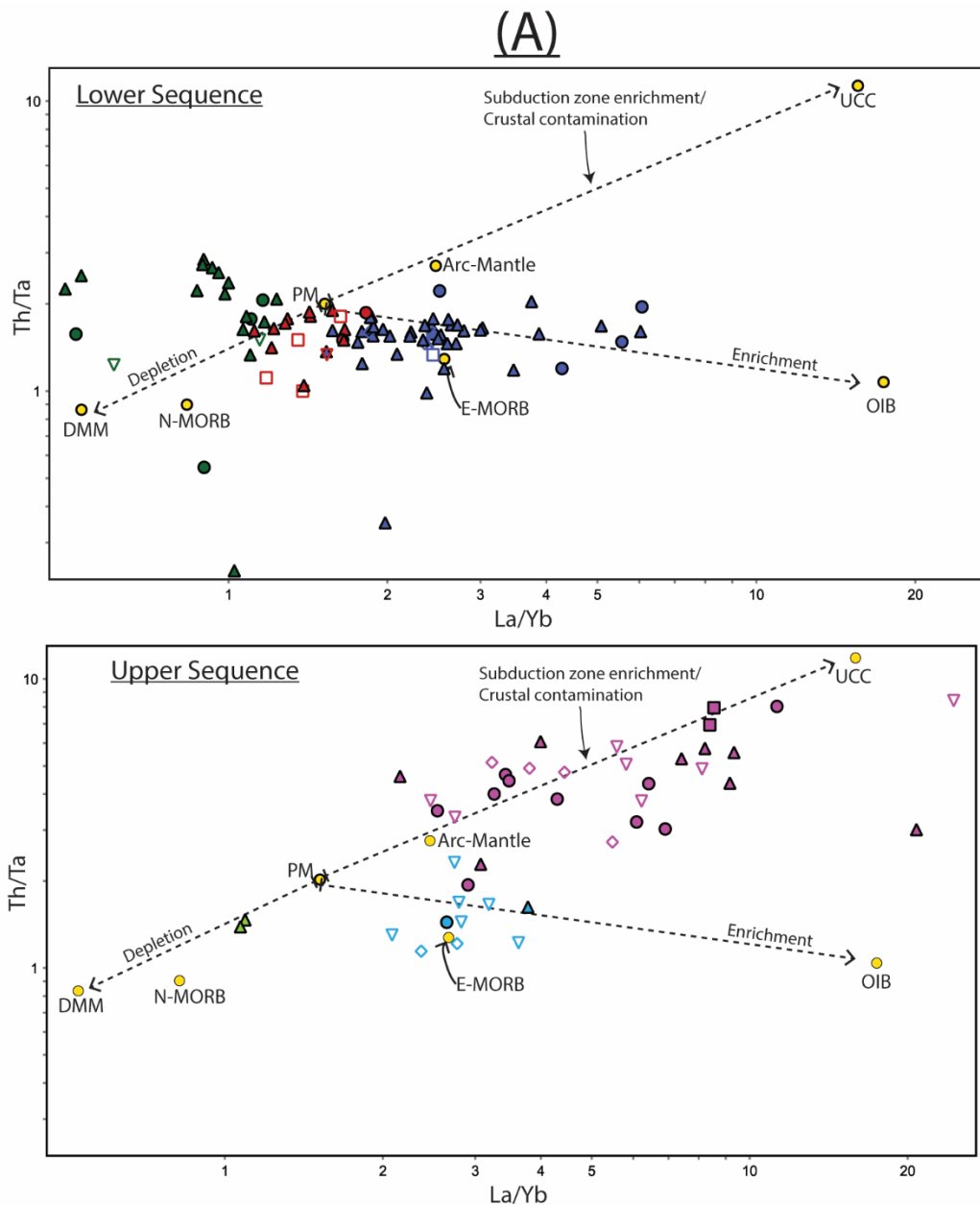


Figure 4-21 Incompatible trace element ratio plots of all geochemical groups in the study illustrating the trace element characteristics of the mantle source from which the rocks were derived characteristics. (A) La/Yb against Th/Ta plot after Condie (1994). Top panel: Samples of the Lower sequence with Groups 2L and 3L & 3U plotting along the PM-Enriched source hypothetical mixing line while Group 1 plots near the PM-DMM source composition. Bottom panels are samples of the Upper sequence with Group 4U plotting along the Arc mantle-UCC line with high Th-Ta ratios indicative of crustal contamination or subduction zone enrichment. Group 3L & 3U plots near the E-MORB composition and trend towards the Arc mantle composition while Group 1 plots on the PM-DMM line indicating a moderately depleted mantle source compared to modern DMM.

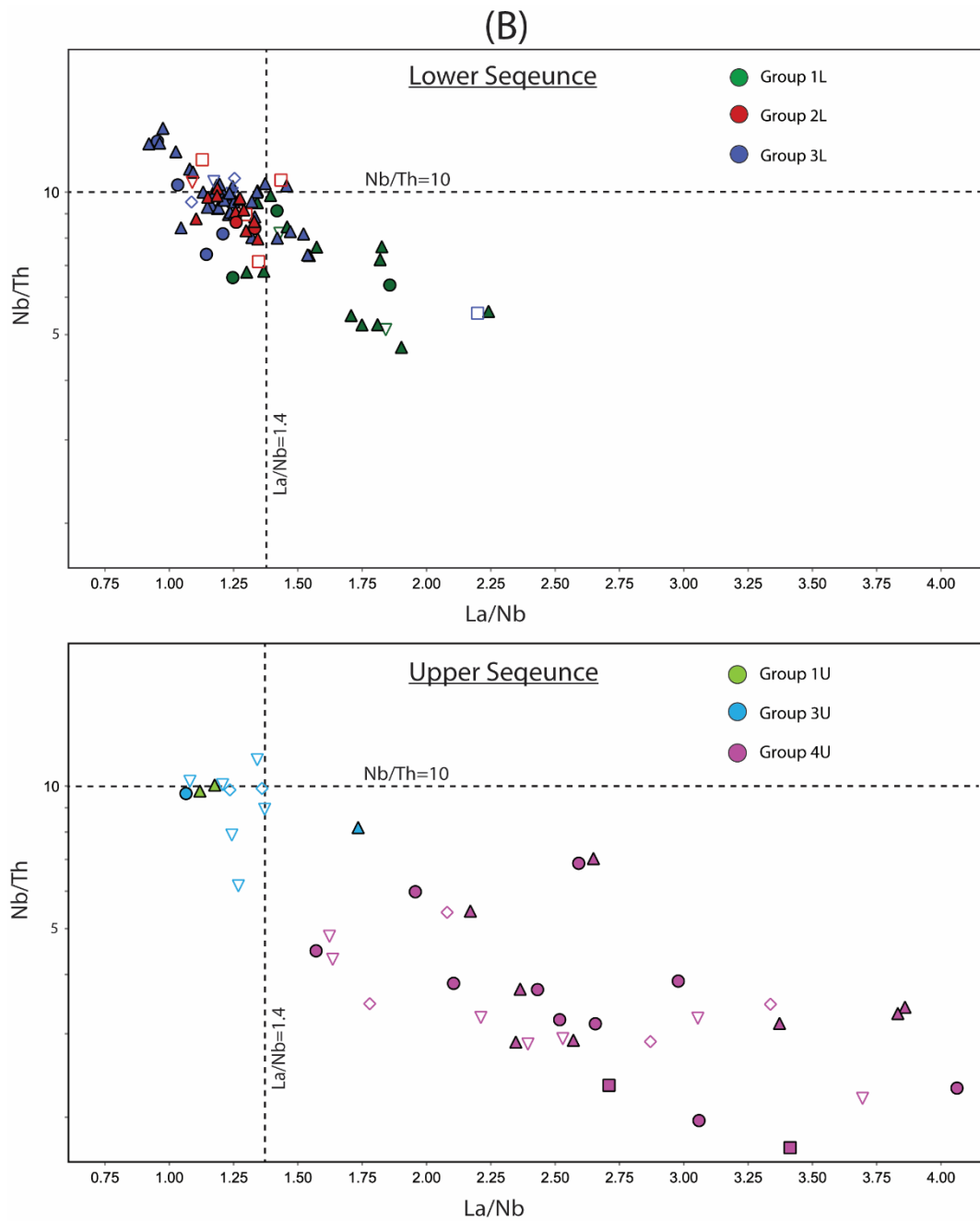


Figure 4-21 (continued) (B) La/Nb against Nb/Th ratio plot modified after Babechuk and Kamber (2011). The top panel shows most of Group 2L and 3L rocks of the Lower sequence have La/Nb ratios less than 1.4 indicating no significant crustal contamination in source while Group 1L rocks have La/Nb ratios greater than 1.4 indicating some amount of source modification. The bottom panel shows evidence for crustal contamination for Group 4U rocks due to $\text{La/Nb} > 1.4$ and $\text{Nb/Th} < 10$.

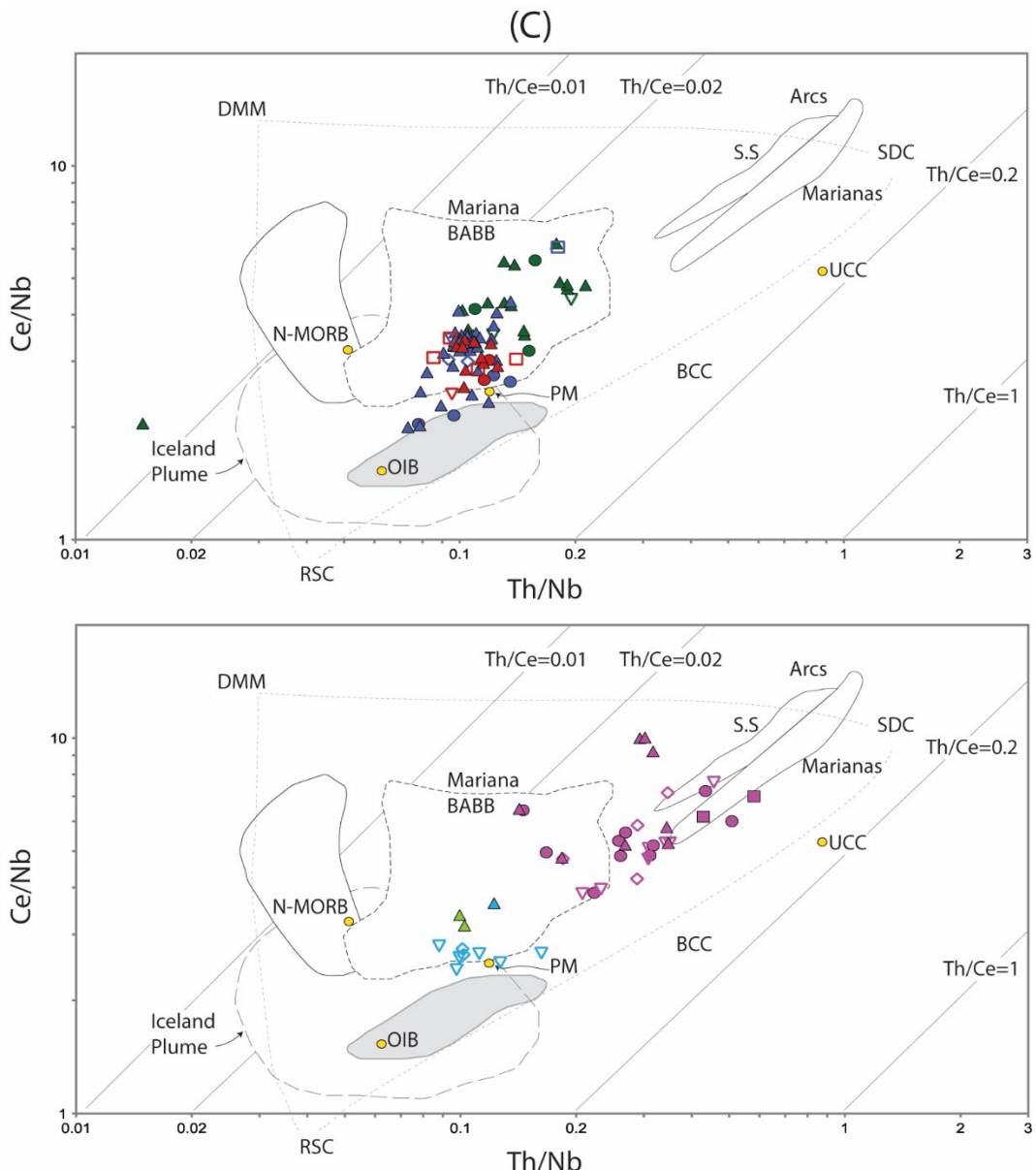


Figure 4-21 (continued) (C) Th/Nb against Ce/Nb diagram modified after Saunders et al. (1988) and basalt fields after Khanna et al. (2015) compared with basalts from this study. Group 2L, 3L, and Group 1L plot within the Mariana back-arc basin basalts (BABB; Pearce et al., 2005) field with an overlap in the Iceland plume and ocean island basalt (OIB). Group 4U plot near the arc basalt field of Mariana Arcs and overlap BABB field. Notably, Group 1 rocks do not plot in the N-MORB field. The dashed line connecting the end-member component is the mixing curve. Depleted MORB mantle (DMM); Workman and Hart (2005), Arc mantle; Kovalenko et al. (2010), Upper continental crust (UCC); Rudnick and Gao (2014), and Primitive mantle (PM), N-MORB, Ocean Island Basalt (OIB); Sun and McDonough (1989), subduction zone component (SDC), residual slab component (RSC).

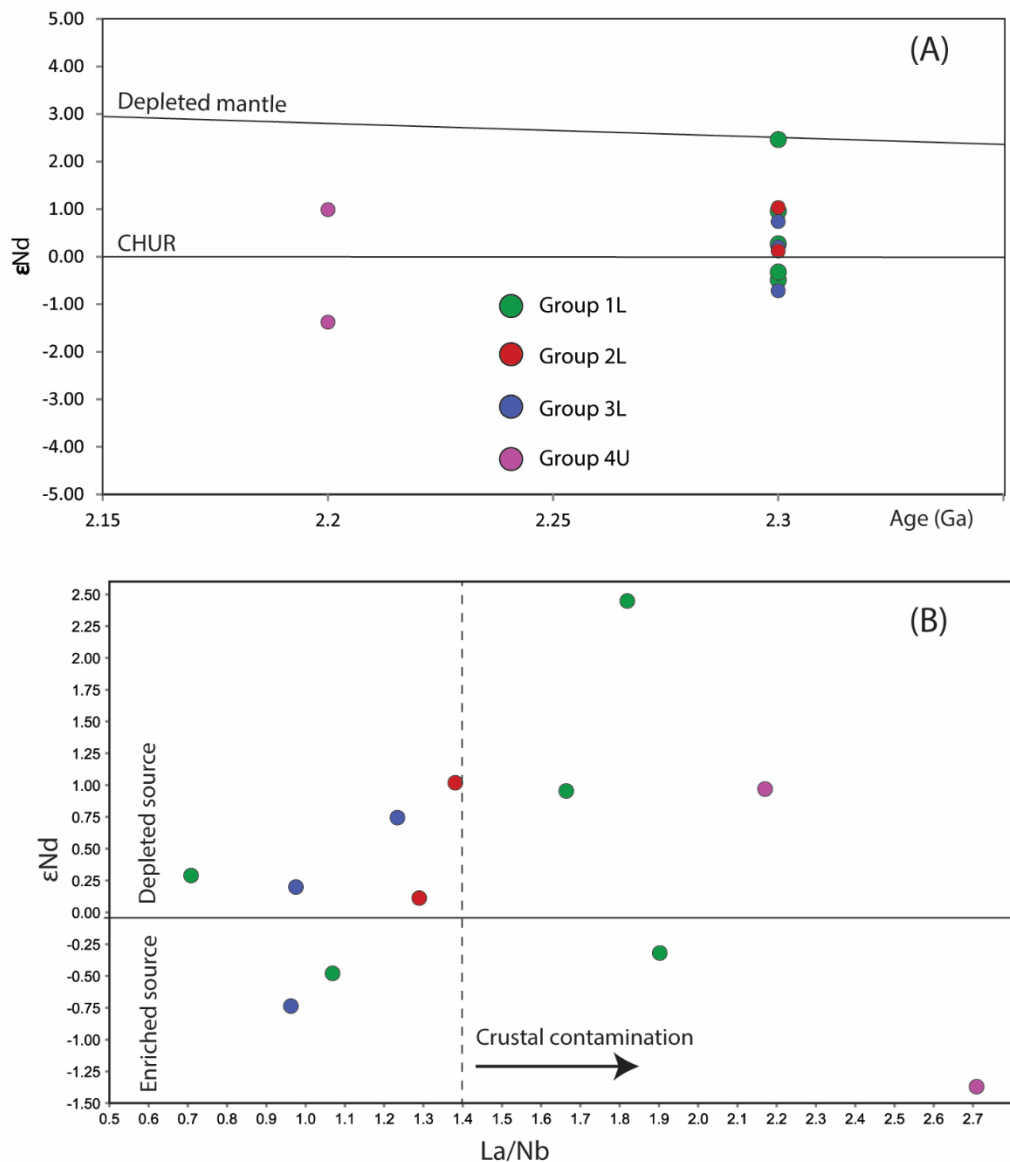


Figure 4-22 ϵ_{Nd} against (A) Time showing the variation of Nd-isotopic ratios with time and (B) La/Nb illustrating mantle source signatures for the select Nd-isotope analysed samples of Group 1-3 of the Lower sequence and Group 4 of the Upper sequence. La/Nb > 1.4 signifies crustal contamination of mantle source. CHUR- Chondritic uniform Earth and Depleted mantle evolution line after DePaolo et al. (1991).

4.5 CONCLUSIONS

The whole-rock major, trace and Nd-isotope geochemistry of coherent volcanic and intrusive lithofacies of the Lower and Upper sequence of the Houndé and Boromo belts demonstrate that:

- Although the rocks have undergone substantial post-emplacement alteration either by weathering, metamorphism and/or hydrothermal alteration, some of the major and most high-field strength elements have generally remained unchanged from their original composition.
- Four distinct geochemical groups have been identified:
 - Group 1 – LREE depleted relative to HREE, minor negative Nb-Ta, and Ti depletion, low Th-TiO₂, high-Fe tholeiitic basalts. These can be found in the Lower (Group 1L) and Upper (Group 1U) sequences.
 - Group 2 – unfractionated REE, no significant incompatible element anomaly, moderately evolved, low Th-TiO₂, high-Fe tholeiitic basalts and can only be found in the Lower sequence (Group 2L).
 - Group 3 – slightly more enriched LREE relative to HREE, often pronounced MREE depletion, low Th-TiO₂, high-Fe, high-Mg tholeiitic basalts. These can be found in the Lower (Group 3L) and Upper (Group 3U) sequences.
 - Group 4 – enriched LREE relative to HREE, pronounced negative Nb-Ta and Ti depletion, low to high Th-TiO₂, high-Mg tholeiitic and calc-alkaline basaltic and andesitic rocks and can only be found in the Upper sequence (Group 4U).
- Sm-Nd isotope defines ages of 2313 ± 34 and 2369 ± 76 Ma for the Houndé and Boromo belts, respectively using Group 1L-3L. Regarding the pseudo-isochron ages obtained for the Houndé and Boromo belts, they are best interpreted as mixing ages rather than distinct crystallisation ages based on the variability of the Nd-isotopic ratios and heterogeneity of the mantle source.
- Spatially, the Lower sequence of the Houndé belt is dominated by Group 3L. In the southern part of the Houndé belt, Group 3L is underlain by Group 2L. Within the Boromo belt, Group 2L dominates and appears to be overlain

by Group 1L. The southern part of the Boromo belt has a succession similar to the Houndé belt suggesting they could be part of the same crustal block. Group 4U rocks dominate the Upper sequence with minor Group 3U and few Group 1U in the Houndé belt.

- The major and trace element variation of Group 1L and 2L (Lower sequence) can be explained by shallow (~3 km) magma fractional crystallisation. Group 1L exhibits evidence for hydrous melts. Group 3L of the Lower sequence shows evidence of relatively deeper (~15 km) anhydrous magma storage conditions. Group 3U and Group 4U rocks of the Upper sequence originate from a deeply seated hydrous melt by fractional crystallisation and assimilation fractional crystallisation.
- Incompatible trace element ratios and Nd-isotope show evidence for compositionally distinct mantle sources:
 - Group 1L originated from a refertilised depleted mantle, Group 2L originated from a Primitive mantle-like source, and Group 3L from an enriched mantle source. The diversity of sources in the Lower sequence implies either the existence of a heterogeneous mantle plume or the progressive evolution and enrichment of a PM-like source. The similarity of Group 2L and Group 3L to oceanic flood basalts suggests mantle plume source.
 - Group 1U originated from a modified depleted mantle source, Group 3U from an enriched source, and Group 4U from a subduction-component modified depleted source. The hydrous melt composition of the Upper sequence rocks suggests the mantle sources of these rocks were influenced by subduction-derived components in an oceanic island arc setting.

Chapter 5: Age constraints on the Eburnean tectonothermal event in the Houndé and Boromo belts

5.1 INTRODUCTION

The metamorphic character of the Paleoproterozoic Birimian domain following magmatic accretion (~2300 to ~2100 Ma) is attributed to the polyphase Eburnean tectonothermal event which occurred between ~2160 to 1980 Ma (Abouchami et al., 1990; Taylor et al., 1992; Feybesse et al., 2006; Ganne et al., 2012). According to Feybesse et al. (2006), the Eburnean event (*sensu lato*), also referred to as the Eburnean orogeny, is marked by three main deformational phases (D1-D3). The Eburnean event led to the extensive emplacement of granitoids, the opening of sedimentary basins, and synchronous regional greenschist facies metamorphism. Also, the Eburnean event led to the stabilisation of the West African craton and the formation of world-class mineralisation (Feybesse et al., 2006; Block et al., 2016; Goldfarb et al., 2017). Across the Birimian domain, regional metamorphism related to the Eburnean event is recorded in two main phases; an early greenschist to amphibolite facies metamorphism from 2160–2120 Ma (Tshibubudze et al., 2015), followed by a younger 2120 to 2060 Ma greenschist to a sub-greenschist metamorphic event (Doumbia et al., 1998).

In western and north-eastern Burkina Faso, the earliest deformational phase (D1) is attributed to E-W compressional tectonism that lasted between 2160 to 2140 Ma syn-emplacement age of the Dori granodiorite (Hein, 2010; Baratoux et al., 2011; Tshibubudze et al., 2015). This deformation phase (D1) is expressed as primary bedding-parallel NNE-NE trending S1 foliation and attributed to a crustal-scale antiform between the Boromo and Houndé belts in western Burkina Faso (Baratoux et al., 2011). In north-eastern Burkina Faso, the D1 phase is defined by N–NW trending dextral shear zones produced during a NE–SW crustal shortening and associated with an early greenschist to amphibolite facies metamorphism. A second deformational phase (D2) operated under the dominant E-W compressional force and subsequently switched to a transcurrent regime (Baratoux et al., 2015). The D2 deformational phase

produced NE trending shear zones that host mineralisation (Le Mignot et al., 2017). In western Burkina Faso, the timing of D2 is constrained by syn-tectonic granitoids emplaced between 2113–2097 (Baratoux et al., 2011) whereas, in northern Ghana, D2 occurred around ~2130 Ma (U-Pb of monazite; Block et al. (2015)). D3 deformation is typically considered the late stage of the Eburnean event, and its structural representation is localised (Baratoux et al., 2011).

One of the critical objectives of this research was to provide an age constraint for emplacement of the Lower sequence rocks in both belts. But after failed attempts to date the age of igneous crystallisation using zircons, this study resulted to metamorphic ages (see Appendix C). This chapter presents an attempt to directly constrain the timing of metamorphism in the rocks of the study area using Titanite. Titanite (CaTiSiO_5) is a common accessory mineral in most igneous rocks and a wide range of metamorphic rocks. Titanite usually captures significant amounts ($10 - < 100$ ppm) of uranium in its crystal lattice, making it useful as a geochronometer (Hayden et al., 2007; Sun et al., 2012). This is particularly beneficial in constraining ages of ultramafic-mafic rocks which do not typically contain radiometric accessory phases such as zircon and monazite. Titanite is estimated to have a minimum U-Pb closure temperature of $600 - 800^\circ\text{C}$ (Cherniak, 1993; Scott & St-Onge, 1995).

In meta-mafic rocks, titanite occurs under various metamorphic conditions (blueschist, greenschist, and amphibolite facies; $< 700^\circ\text{C}$, < 12 kbar) based on the original mineralogy of the host rock (Frost et al., 2001). However, they commonly form under greenschist facies and amphibolite facies conditions (Kohn, 2017). Therefore, metamorphic titanites provide a better constraint on metamorphic ages, unlike the more stable high-temperature accessory phases (e.g. zircon) (Hayden et al., 2007). A complication of titanite geochronology is incorporating significant amounts of common Pb in its crystal lattice during titanite crystallisation. The common Pb component is not produced by radiogenic decay within the closed titanite mineral but rather incorporated from the host rock upon mineral crystallisation (Storey et al., 2006; Kirkland et al., 2018). Nevertheless, as long as the common Pb component is homogenous within the analysed titanites, it is possible to use the Concordia method on a Tera-Wasserburg Concordia to determine the age of titanite crystallisation (e.g. Kohn, 2017; Olierook et al., 2019). Titanites, therefore, have the potential to provide

important insight into metamorphic history (Rubatto & Hermann, 2001; Kirkland et al., 2018).

This study reports the analysis of two samples for U-Pb in titanite using laser ablation inductively coupled mass spectrometry (LA-ICPMS) to provide a constraint on the timing of metamorphism in the Houndé and Boromo belts.

5.2 METHODOLOGY

5.2.1 Scanning electron microscopy (SEM)

The TESCAN Mira3 scanning electron microscope was used identification and characterisation of titanites in polished thin sections at the QUT CARF microscopy laboratories. Before using the SEM, the thin sections were examined using the optical microscope in reflected light mode to obtain photomicrographs of the titanites. Subsequently, the SEM equipped with the ThermoScientific energy dispersive spectroscopy (EDS) system was used for high-resolution backscatter electron imaging and elemental quantification. The EDS analysis was without certified standards. Backscatter images and elemental data for two samples (GS_030 and Gs_041) are presented in Appendix C Table A- 17.

5.2.2 Laser Ablation Inductively Coupled Mass Spectroscopy (LA-ICPMS)

In-situ U-Pb isotope radiometric dating of titanites was done using the 193nm ESI NewWave excimer laser attached to an Agilent 8800 ICP-MS. Single circular laser spots with a diameter of 30 μm were used to ablate the target sample. The elements and isotopes collected in this session are ^{29}Si , ^{55}Mn , ^{202}Hg , ^{204}Pb , ^{206}Pb , ^{207}Pb , ^{208}Pb , ^{232}Th , ^{238}U . Certified and in-house reference materials were introduced after every ten unknown measurements. The reference materials used are two standard titanites TBC-1 and OLT1, one in-house YILT2, and one synthetic glass NIST-610. TBC-1 was used as the primary reference material, whereas instrument optimisation was checked using NIST 610. Data reduction and baseline corrections were performed using Iolite software, while isotope ratios and apparent age for the unknowns and standards were calculated using the Iolite with Igor Pro software. Finally, the $^{206}\text{Pb}/^{238}\text{U}$ age calculation and graphically presentation were done using the IsoplotR free online geochronology plugin designed by Vermeesch (2018). Results of the certified reference materials are presented in Appendix C Table A-18.

5.3 RESULTS

5.3.1 Titanite petrography and microstructures

Sample GS_030 has Group 4U signatures of the Upper sequence and intrudes the Lower sequence of the Houndé belt. Sample GS_030 is hornblende-plagioclase porphyritic andesite with a metamorphic assemblage of actinolite +albite + chlorite + titanite (Figure 5-1 A). The titanite in GS_030 are inclusions in larger relict hornblende crystals and occur as groundmass minerals with sizes ranging from 20 to 80 μm (Figure 5-1 C and E).

Sample GS_041 has Group 1L signatures and belongs to the Lower sequence of the Boromo belt (see Map D, BO-1). GS_041 is a gabbro with a metamorphic assemblage of epidote+albite+chlorite+titanite (Figure 5-1 B). The titanites observed in GS_041 occur as anhedral coronas, typically mantling the rims of ilmenite, and the titanite rims are between 10 and 20 μm thick (Figure 5-1 D & F). The titanites in both samples are anhedral and occur as part of the greenschist facies mineral assemblage indicating they are secondary minerals.

5.3.2 Titanite U-Pb Geochronology

Sample GS_030 yields Th/U ratios of 0.14–1.57 and U concentrations from 12.70 to 83.70 ppm (Figure 5-2). The Th/U ratio range of GS_030 falls within the range for metamorphic titanites for the relatively low U concentration (Th/U =0.05-10, Olierook et al., 2019). Nevertheless, the titanite U-Pb systematics define an excellent Concordia with an intercept age of 2139 ± 23 Ma (MSWD = 1.9) (Figure 5-3 A). The common Pb component that, through mixing with radiogenic derived Pb, defines the $^{207}\text{Pb}/^{206}\text{Pb}$ intercept in the Tera-Wasserburg Concordia plot = 0.96 ± 0.02 is close to expected Pb isotope compositions for the time (Stacey & Kramers, 1975).

Sample GS_041 yields Th/U ratios of 0.34–0.89 and U concentrations from 2.14 to 5.43 ppm (Figure 5-2). The U concentration measured in GS_041 is too low relative to typical igneous titanites (Olierook et al., 2019). The low U and low Pb content of the titanites lead to analyses with high errors, and all $^{238}\text{U}/^{206}\text{Pb}$ analyses have 2σ errors of $> 10\%$. Analyses with 2σ errors of $> 20\%$ were excluded from age determination. All low error analyses are concordant and define a Concordia age of 2432 ± 39 with an MSWD of 53. The high MSWD indicates that the Concordia age has no age

meaning. Following Olierook et al. (2019), the weighted mean is considered to give the best estimate of the age of the titanites at 2437 ± 39 , MSWD = 0.65. Although the weighted mean age calculates lower MSWD, the metamorphic age obtained cannot be explained in this study.

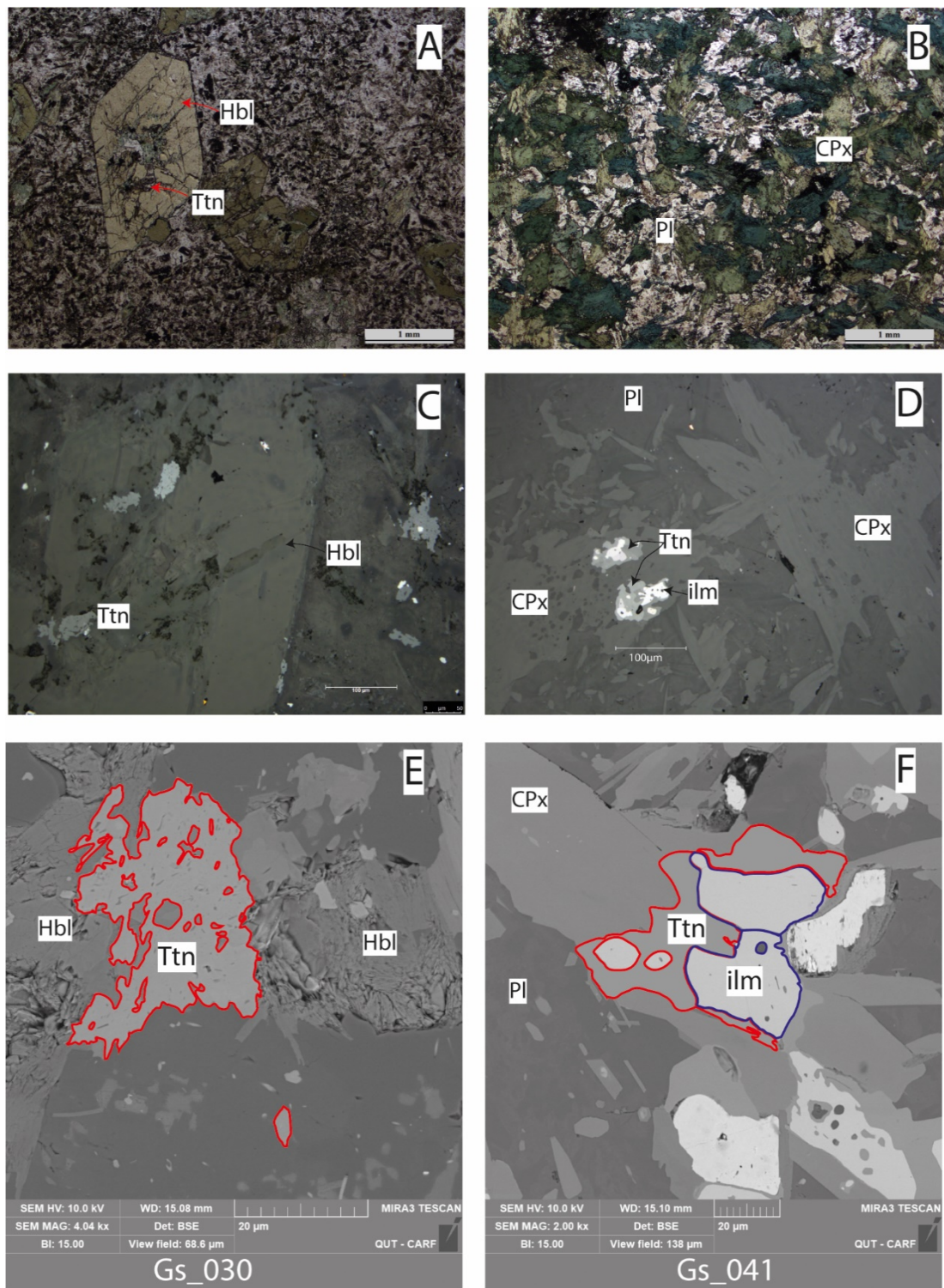


Figure 5-1 Plane polarised light image of (A) GS_030 of the hornblende-plagioclase porphyritic andesite lithofacies from the Houndé belt and (B) Gs_041 Gabbro from the Boromo belt. Representative reflected light image (C) and (D), and SEM BSE (E) and (F) images showing texture and mineral inter-relationship of titanite in samples GS_030 and Gs_041, respectively. The titanites form reaction rims around the primary titanium-bearing minerals ilmenite and hornblende as well as inclusion. Hbl-hornblende, CPx-clinopyroxene, Pl-plagioclase, Ttn-Titanite, ilm- Ilmenite.

Table 5-1 U-Pb isotopic data of titanite spot analyses from GS_030

Analysis number	Th/U (ppm)	Radiogenic Ratios						Apparent ages (Ma)					
		$^{207}\text{Pb}/^{235}\text{U}$	$\pm 2\text{-}\delta$	$^{206}\text{Pb}/^{238}\text{U}$	$\pm 2\text{-}\delta$	Error Correlation	$^{238}\text{U}/^{206}\text{Pb}$	$\pm 2\text{-}\delta$	$^{207}\text{Pb}/^{206}\text{Pb}$	$\pm 2\text{-}\delta$	Error Correlation	$^{206}\text{Pb}/^{238}\text{U}$	$\pm 2\text{-}\delta$
Gs_030_1	0.71	44.10	2.70	0.67	0.03	0.17	1.48	0.07	0.48	0.03	0.47	3320	140
Gs_030_2	0.25	21.70	1.30	0.51	0.02	0.42	1.98	0.07	0.32	0.02	0.19	2630	79
Gs_030_3	0.71	35.50	3.50	0.65	0.05	0.42	1.54	0.12	0.42	0.04	0.50	3180	180
Gs_030_4	0.36	20.00	1.30	0.48	0.02	0.26	2.10	0.09	0.30	0.02	0.41	2504	85
Gs_030_5	0.50	33.70	2.00	0.60	0.02	0.02	1.67	0.06	0.41	0.03	0.51	3014	88
Gs_030_6	0.14	32.90	1.50	0.58	0.02	0.36	1.71	0.06	0.41	0.02	0.34	2957	82
Gs_030_7	0.18	25.30	1.90	0.55	0.03	0.54	1.82	0.09	0.33	0.02	0.26	2820	120
Gs_030_8	1.25	57.50	4.40	0.78	0.04	0.39	1.29	0.06	0.54	0.04	0.36	3700	140
Gs_030_9	0.18	29.00	2.30	0.59	0.03	0.30	1.69	0.07	0.35	0.03	0.26	2980	110
Gs_030_10	0.82	26.80	1.70	0.53	0.03	0.21	1.90	0.09	0.38	0.03	0.44	2710	100
Gs_030_11	0.34	23.90	1.60	0.54	0.03	0.33	1.86	0.09	0.33	0.02	0.27	2780	120
Gs_030_12	0.29	18.20	1.30	0.47	0.03	0.26	2.11	0.11	0.28	0.02	0.47	2490	110
Gs_030_14	0.25	22.70	1.50	0.52	0.02	0.13	1.93	0.07	0.32	0.02	0.45	2678	84
Gs_030_15	0.67	20.60	1.60	0.49	0.02	0.41	2.02	0.09	0.30	0.02	0.24	2594	99
Gs_030_16	0.25	21.10	1.10	0.49	0.02	0.11	2.05	0.07	0.31	0.02	0.48	2557	68
Gs_030_17	0.22	19.10	1.20	0.49	0.02	0.29	2.06	0.09	0.28	0.02	0.44	2538	94

Table 5-1 (continued)

Analysis number	Th/U (ppm)	Radiogenic Ratios								Apparent ages (Ma)			
		$^{207}\text{Pb}/^{235}\text{U}$	$\pm 2\delta$	$^{206}\text{Pb}/^{238}\text{U}$	$\pm 2\delta$	Error Correlation	$^{238}\text{U}/^{206}\text{Pb}$	$\pm 2\delta$	$^{207}\text{Pb}/^{206}\text{Pb}$	$\pm 2\delta$	Error Correlation	$^{206}\text{Pb}/^{238}\text{U}$	$\pm 2\delta$
Gs_030_18	0.32	28.60	1.80	0.58	0.03	0.19	1.71	0.08	0.37	0.03	0.30	2950	110
Gs_030_19	0.26	26.10	1.50	0.54	0.02	0.16	1.84	0.08	0.35	0.02	0.44	2784	97
Gs_030_20	0.35	21.80	1.50	0.49	0.03	0.53	2.06	0.11	0.32	0.02	0.38	2540	110
Gs_030_21	0.36	24.70	1.50	0.52	0.03	0.33	1.94	0.09	0.35	0.03	0.51	2660	110
Gs_030_22	0.20	35.10	2.90	0.64	0.04	0.03	1.56	0.10	0.41	0.04	0.46	3150	160
Gs_030_23	0.36	28.10	1.70	0.57	0.03	0.33	1.75	0.10	0.37	0.03	0.63	2890	130
Gs_030_24	0.41	31.40	2.90	0.60	0.04	0.35	1.68	0.11	0.39	0.04	0.40	3010	160
Gs_030_25	0.80	64.30	6.40	0.81	0.07	0.77	1.24	0.10	0.57	0.04	-0.06	3750	230
Gs_030_26	1.00	47.10	3.50	0.70	0.04	0.41	1.44	0.08	0.51	0.04	0.50	3370	150
Gs_030_27	1.57	26.90	3.20	0.52	0.04	0.20	1.92	0.16	0.37	0.05	0.40	2660	180
Gs_030_28	0.23	23.20	3.20	0.52	0.04	0.20	1.94	0.14	0.35	0.05	0.06	2670	170
Gs_030_29	0.21	20.52	0.88	0.49	0.02	0.21	2.05	0.07	0.31	0.02	0.51	2557	69
Gs_030_30	0.39	70.30	4.20	0.87	0.04	0.59	1.15	0.05	0.58	0.03	0.33	4010	140
Gs_030_31	0.41	49.10	2.60	0.67	0.03	0.31	1.49	0.06	0.53	0.03	0.45	3320	110
Gs_030_32	0.36	72.80	3.30	0.90	0.04	0.36	1.11	0.05	0.58	0.03	0.55	4110	120
Gs_030_33	0.79	73.90	4.40	0.88	0.04	0.51	1.14	0.05	0.61	0.03	0.32	4040	140

Table 5-1 (continued)

Analysis number	Th/U (ppm)	Radiogenic Ratios						Apparent ages (Ma)					
		$^{207}\text{Pb}/^{235}\text{U}$	$\pm 2\text{-}\delta$	$^{206}\text{Pb}/^{238}\text{U}$	$\pm 2\text{-}\delta$	Error Correlation	$^{238}\text{U}/^{206}\text{Pb}$	$\pm 2\text{-}\delta$	$^{207}\text{Pb}/^{206}\text{Pb}$	$\pm 2\text{-}\delta$	Error Correlation	$^{206}\text{Pb}/^{238}\text{U}$	$\pm 2\text{-}\delta$
Gs_030_34	0.33	20.90	1.50	0.51	0.02	0.17	1.98	0.09	0.31	0.02	0.51	2625	97
Gs_030_36	0.37	21.80	1.20	0.51	0.02	0.06	1.96	0.09	0.32	0.02	0.65	2644	98
Gs_030_37	0.49	44.60	2.40	0.70	0.03	0.55	1.43	0.07	0.48	0.03	0.38	3400	130
Gs_030_39	0.27	29.60	1.60	0.54	0.02	0.42	1.86	0.07	0.40	0.02	0.37	2768	88
Gs_030_40	0.46	34.10	2.70	0.59	0.03	0.42	1.69	0.08	0.41	0.03	0.41	3040	140
Gs_030_41	0.31	20.90	1.50	0.49	0.03	0.25	2.04	0.10	0.31	0.03	0.48	2550	110
Gs_030_42	0.33	21.10	1.50	0.52	0.03	0.66	1.94	0.09	0.30	0.02	0.33	2660	110
Gs_030_43	0.78	40.70	3.40	0.66	0.04	0.37	1.52	0.10	0.47	0.04	0.46	3220	170
Gs_030_44	0.64	39.50	2.30	0.64	0.03	0.30	1.57	0.08	0.46	0.03	0.48	3160	120

Table 5-2 U-Pb isotopic data of titanite spot analyses from GS_041

Analysis number	Radiogenic Ratios								Apparent ages (Ma)				
	Th/U (ppm)	$^{207}\text{Pb}/^{235}\text{U}$	$\pm 2\delta$	$^{206}\text{Pb}/^{238}\text{U}$	$\pm 2\delta$	Error Correlation	$^{238}\text{U}/^{206}\text{Pb}$	$\pm 2\delta$	$^{207}\text{Pb}/^{206}\text{Pb}$	$\pm 2\delta$	Error Correlation	$^{206}\text{Pb}/^{238}\text{U}$	$\pm 2\delta$
GS_041_45	0.44	10.2	3.2	0.40	0.07	0.05	2.53	0.47	0.28	0.11	0.15	2020	300
GS_041_46	0.43	12.1	4	0.47	0.06	0.06	2.15	0.30	0.20	0.07	0.27	2410	290
GS_041_47	0.36	13	3.8	0.45	0.06	0.10	2.23	0.30	0.25	0.07	0.45	2340	280
GS_041_48	0.78	9.5	3.9	0.50	0.09	-0.10	1.99	0.34	0.20	0.09	0.03	2460	340
GS_041_49	0.34	13.4	4.7	0.44	0.06	0.14	2.29	0.31	0.31	0.11	0.32	2300	270
GS_041_50	0.41	9.6	2.9	0.45	0.05	0.29	2.23	0.25	0.20	0.06	0.35	2320	220
GS_041_52	0.73	12.6	6.2	0.46	0.08	-0.16	2.18	0.40	0.27	0.14	0.72	2380	380
GS_041_53	0.88	19.3	6.3	0.48	0.08	0.49	2.07	0.34	0.31	0.11	0.61	2390	310
GS_041_55	0.83	14.2	4.6	0.48	0.10	0.40	2.08	0.43	0.20	0.14	0.51	2290	390
GS_041_60	0.70	11.3	5.3	0.44	0.09	0.37	2.26	0.46	0.31	0.14	0.14	2170	370
GS_041_61	0.71	10.9	4.5	0.43	0.09	0.29	2.35	0.48	0.25	0.12	0.79	2110	350
GS_041_62	0.72	15.4	5.9	0.43	0.07	0.61	2.35	0.41	0.20	0.19	0.50	2140	320
GS_041_64	0.78	7.6	4.3	0.48	0.07	-0.19	2.11	0.33	0.22	0.12	0.18	2430	340
GS_041_65	0.57	12	3.7	0.42	0.07	0.06	2.37	0.38	0.35	0.14	0.65	2200	330
GS_041_68	0.89	21.8	7	0.46	0.08	0.12	2.17	0.37	0.31	0.23	0.76	2390	370

GS_041_72	0.55	13.8	6.1	0.47	0.09	-0.09	2.14	0.42	0.39	0.17	0.29	2410	410
GS_041_74	0.67	10	3.7	0.43	0.07	-0.02	2.31	0.39	0.18	0.24	0.73	2190	300
GS_041_81	0.45	11.2	3.4	0.49	0.06	0.02	2.04	0.26	0.26	0.09	0.43	2470	270

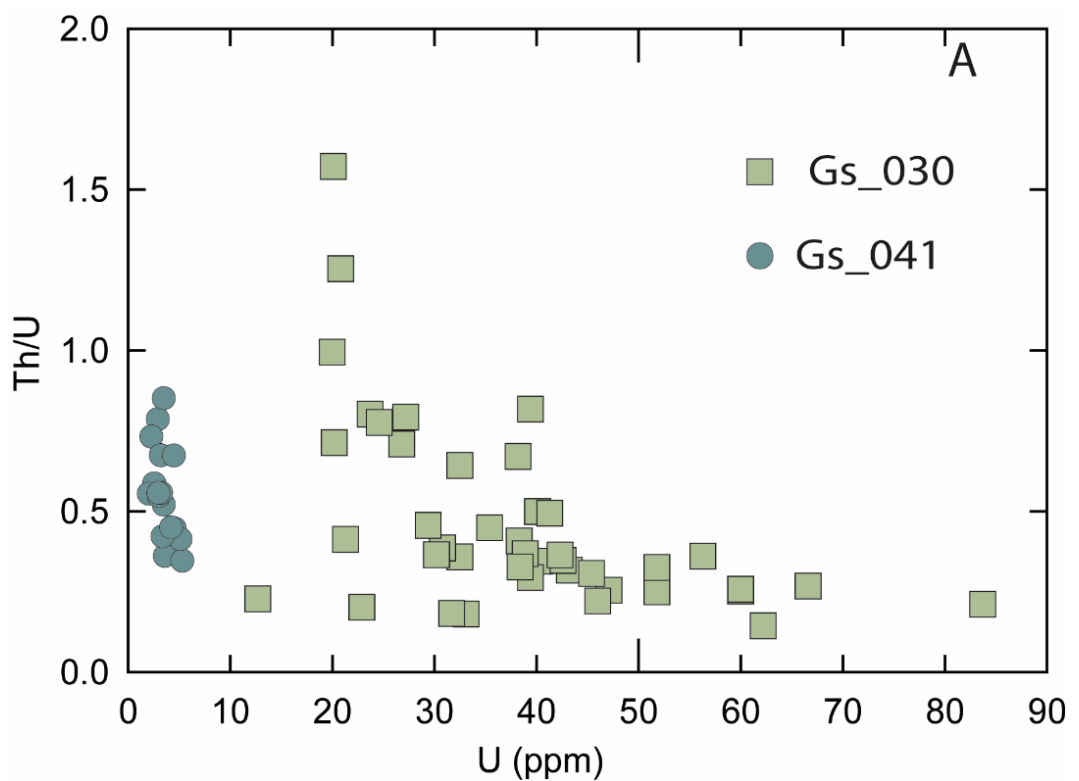


Figure 5-2 Th/U against U plot for spot analysis of sample Gs_030 and Gs_041 showing a relatively lower concentration of U in Gs_041 compared to Gs_030. Th/U ratios are consistent with that for metamorphic titanites (0.05–10) for the given U concentrations, according to Olieroor et al. (2019).

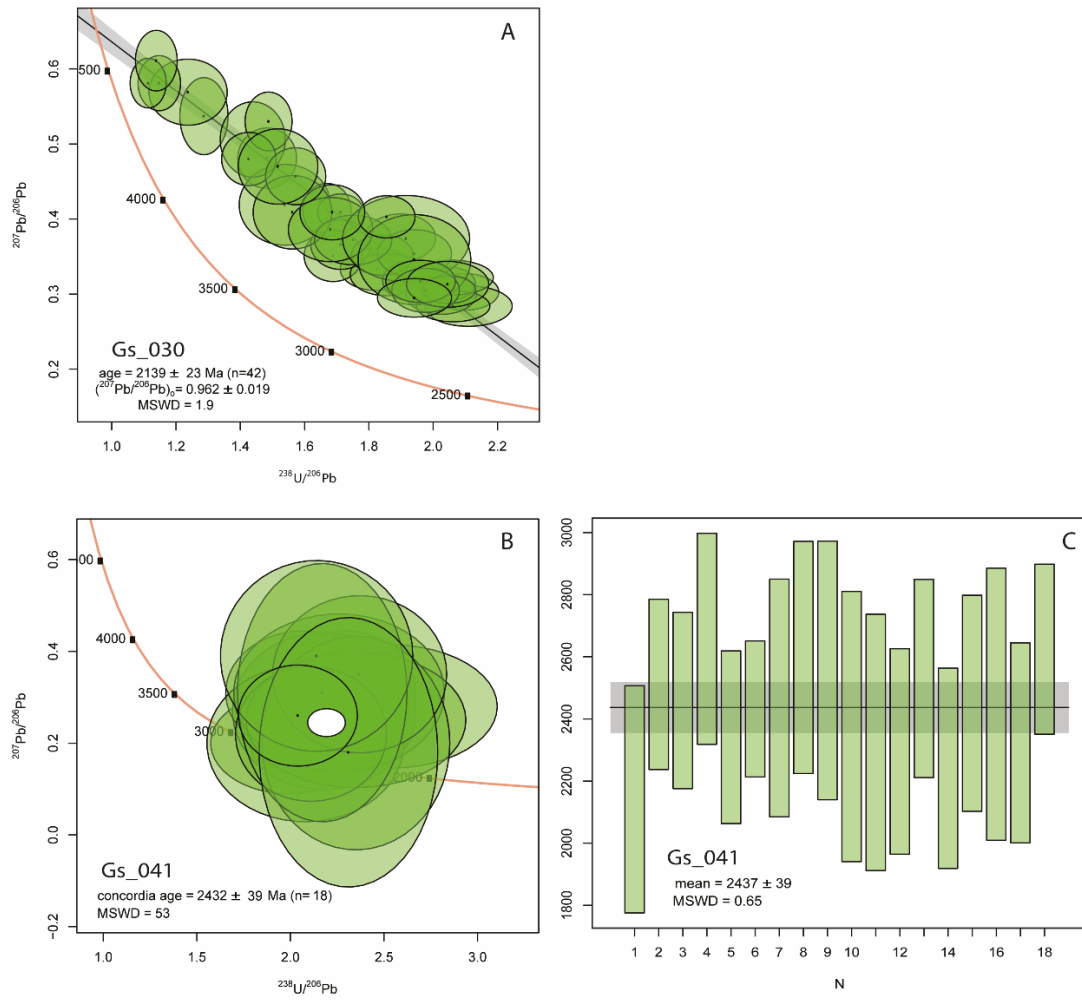


Figure 5-3 U–Pb ages of titanite in (A) Gs_030; hornblende-plagioclase porphyritic andesite from Houndé belts and (B) Gs_041-gabbro from Boromo belt. Left column: Tera-Wasserburg Concordia (A) and (B) Concordia diagrams showing spot analyses of LA-ICPMS; the error of ellipses are 2σ . (C) $^{206}\text{Pb}/^{238}\text{U}$ weighted mean ages; the error bars are 2σ . Diagrams and age calculations achieved using IsoplotR software by Vermeesch (2018)

5.4 DISCUSSION

5.4.1 Origin of secondary Titanite

Secondary titanites are commonly produced by the breakdown of titanium-bearing phases (e.g., ilmenite, Ti-rich hornblende) in igneous rocks during metamorphism or hydrothermal alteration (Corfu & Stone, 1998; Broska et al., 2007). The dated titanite crystals are in textural equilibrium with greenschist facies assemblages suggesting the growth of titanite was achieved at this metamorphic grade. The textural relationship between titanite and its precursor minerals (e.g. plagioclase, clinopyroxene) is indicative of a metamorphic reaction between titanium-bearing and

Ca-rich phases (Scott & St-Onge, 1995; Frost et al., 2001). According to Frost et al. (2001), the growth of titanite on the rims of rutile/ilmenite is typical of decompression textures in high-grade metabasite rocks. This implies the growth of titanite is accompanied by fluid infiltration and the remobilisation of titanium in the protolith (Stearns et al., 2015; Zhang et al., 2018). However, there is no evidence for metamorphic assemblages within the samples investigated that reflect higher metamorphic grade than the titanite bearing assemblages. Therefore, the textural relationship observed in both samples reflects prograde greenschist facies metamorphism.

5.4.2 Insight tectonic history of the study area

Insitu titanite U-Pb dating in this study has obtained new direct constrain on the timing of metamorphism. Titanites in samples Gs_030 yield a U-Pb age of 2139 ± 23 Ma (Figure 5-3 A). Given the micro-textural relationship of the dated titanite crystals and their petrographical implications, the age obtained represent the crystallisation of titanite during a prograde greenschist facies metamorphic event. The titanite age obtained for Gs_030 falls within the age range inferred for early metamorphism event associated with the Eburnean collisional event between 2160–2120 Ma recorded in Burkina Faso and elsewhere in the Birimian Domain (Gueye et al., 2008; Tshibubudze et al., 2015; Grenholm et al., 2019). The older age obtained from Gs_041 is considered not to represent a geologically significant age because of the high errors during the analysis and the lack of independent evidence that the Boromo belt has any components with ages greater than 2400 Ma.

Based on the lithostratigraphy and geochemical characteristics of sample Gs_030, this sample belongs to the Upper Sequence and intrudes the Lower sequence of the Houndé belt. Therefore, titanite age obtain provides a minimum crystallisation age for this lithofacies at ~ 2139 Ma. Although this age does not provide a robust constraint on the timing of magmatic accretion of the volcanic rocks, it offers evidence for the minimum age at which the rocks of the Lower and Upper sequence were within the same tectonic environment or depositional basin.

Previous studies have shown that the early Eburnean tectonothermal event (2160–2120 Ma) attributed to NE-SW and E-W directed compression also affected the rocks of the study area and is responsible for the D1 and D2 deformational phases,

extensive syn-deformational granitoids (Baratoux et al., 2011; Block et al., 2016). This period is also associated with regional greenschist metamorphism, which peaked at about 2160–2130 Ma (Hein, 2010; Baratoux et al., 2011; Tshibubudze et al., 2015). Although the early Eburnean event is mainly attributed to a compressive deformational regime, there is evidence for localised transtensional regime marked by exhumation of lower crustal material and opening of large sedimentary basins at this timeframe (Perrouty et al., 2012; Block et al., 2015; Block et al., 2016). Thermodynamic modelling by Ganne et al. (2012) also reveals a retrogressive thermal regime and extensive hydrothermal alteration attributed to the exhumation of greenstones at about 2150 Ma. Based on the lines of evidence from other studies, the ~2139 Ma titanite crystallisation age, which represents prograde metamorphism, occurred near the end of the early Eburnean event and could be related to crustal thickening resulting from the D1 compressional event recorded in the study area.

5.5 CONCLUSION

The petrographic observations of titanite-bearing rocks of the Houndé and Boromo belts of western Burkina Faso show that secondary titanite crystallisation resulted from prograde greenschist facies metamorphism. This metamorphic reaction is dated at ~2139 Ma. The age of titanite crystallisation and, therefore, metamorphism is consistent with the late stages of the regional D1 deformational event, which resulted from E-W compressional tectonics. Since titanites form within certain temperature pressure regimes, it is inferred that the host rocks must have been subjected to temperatures of at least 550 °C under pressure conditions less than 12 kbar, which is equivalent to about 30 km deep. The age obtained shows that the Lower and Upper sequences must have already been juxtaposed before this time frame since Gs_030 intrudes the Lower sequence. This study has shown that the integration of petrographic analysis and in situ U-Pb geochronology of titanite crystals is vital for directly dating metamorphic events and delineating geological timing mafic volcanic rocks, which are difficult to date.

Chapter 6: Geological synthesis and Conclusions

6.1 RECONSTRUCTION OF THE DEVELOPMENT OF THE HOUNDÉ AND BOROMO GREENSTONE BELTS

The findings of this research demonstrate a complex evolution of the Houndé and Boromo greenstone belts of south-western Burkina Faso. In this section, the physical volcanology, lithostratigraphy, and geochemical implications are combined to reconstruct the magmatic and tectonic history of both belts in four distinct stages. The stages of evolution are sequentially discussed below and summarised in Figure 6-1.

6.1.1 Ocean plateau Stage (ca. 2350–? Ma)

The earliest recognised magmatic event produced mafic lavas of the coherent basalt association (LFA-1) and its associated intrusive complexes, which make up the Lower sequence of both belts. These rocks are the high-Fe tholeiitic, low Th-TiO₂ basalts which exhibit Group 1L (depleted LREE), Group 2L (flat REE), and predominantly Group 3L (slightly enriched LREE) geochemical signatures. This stage represents an extensive and voluminous outpouring of mafic magma (>5 km * >10,000 km²) consistent with large igneous provinces (> 0.1 Mkm²; Bryan and Ernst (2008)).

The geochemical characteristics of Groups 1L, 2L, and 3L rocks constrain the nature of its mantle source. Firstly, the general lack of pronounced HREE depletion suggests no residual garnet in the source, indicative of depths of partial melting above the garnet lherzolite stability zone [< 80 km; Grove et al. (2013)]. A comparison of key trace element ratios (e.g., Th/Ta and La/Yb) with modern mantle source compositions demonstrate: 1) Group 1L rocks were derived from a modified depleted mantle source geochemically different from the modern MORB mantle, 2) Group 2L rocks formed from a mantle source similar to the Primitive mantle, and 3) Group 3L rocks formed from a relatively LREE enriched source compared to Group 2L. The three basalt types appear to have originated from distinct mantle reservoirs at roughly the same time. The best explanation for contemporaneously distinct mantle sources within the same region is a heterogeneous mantle source possibly resulting from slivers

of both depleted and enriched mantle components as has been documented in many large igneous provinces [e.g., Paraná-Etendeka flood basalt province; Ewart et al. (2004) and Kerguelen plateau of the Indian Ocean; Frey et al. (2000)]. A heterogeneous plume-operated mantle source is also supported because magma differentiation processes such as fractional crystallisation cannot account for the geochemical diversity within the Lower sequence.

The melts generated at this stage were mantle-derived melts (primary magmas) which stalled in the crust in magma chambers, where they fractionated and evolved. Petrogenetic models support fractionation of Groups 1L and 2L magmas at ~3 km depths, and Group 3L magmas at ~15 km depths. Plagioclase and clinopyroxene were the dominant fractionating phases of the parental magma based on the positive relationship of CaO and FeO with decreasing MgO. Olivine must have been removed early in the magma differentiation process because of the relatively low MgO and Ni abundances. Crustal contamination was minimal to non-existent based on the low Th-TiO₂ ratios, absence of low negative ϵ_{Nd} values, pronounced depletion in Nb-Ta, or enrichment in Th relative to the other HFSE except for Group 1L rocks, which show minimal depletion in Nb-Ta and Ti.

There is no exposed basement to support a continental (ensialic) or oceanic (ensimatic) emplacement, so one must examine the geochemical and other physical evidence to distinguish between these two possibilities. Evidence for a continental basement is normally exhibited by crustal contamination of mafic magmas (negative Nb anomalies, negative ϵ_{Nd}), presence of xenocrystic zircons, and often interlayered sedimentary rocks, erosional surfaces, and basal conglomeratic beds (Arndt, 1999; Thurston, 2002). It is well documented that basaltic lavas of large igneous provinces which erupt through a continental lithosphere typically inherit strong contamination signatures (Kerr et al., 2000) [e.g., Columbia River basalts; Wolff et al. (2008)] while those erupted through the oceanic crust do not possess such geochemical signatures [e.g., Ontong Java plateau; Fitton et al. (2004)]. The signatures indicative of a continental basement are absent from the basalts of the Lower sequence, strongly indicating that the sequence was not built on continental crust. The absence of sheeted dyke complexes, which are characteristic of ophiolite sequences formed at the mid-oceanic ridge (Dilek & Furnes, 2011), precludes formation at spreading centres, while the absence of subduction-related signatures also points to formation away from plate

margins. Therefore, the preferred interpretation is that the magmas generated at this stage were emplaced onto a pre-existing oceanic crust. The basement was not observed in this study.

The minimum emplacement age for the Lower sequence basalts in both belts is pegged at 2212 Ma based on the crystallisation age of a rhyolite in the western Houndé belt (Castaing et al., 2003), which intrudes rocks of the Upper sequence. However, the stratigraphic position and relationship of this rhyolite unit with the Lower sequence mafic lavas are unclear and show that this is not a good constraint. The best timing constraint for emplacement of these basalts is the average pseudo-isochron whole-rocks Sm-Nd age of 2350 Ma estimated in this study. Although the pseudo-isochron ages were produced from mixing different geochemical groups, the consistency in the ages, overlapping at ~2350 Ma, presents a good approximation of the age of magmatism. This age is consistent with the oldest ages recorded across the West African Craton. For example, the U-Pb 2312 ± 17 Ma of zircon cores from the Dabakala tonalites located in the Ouango-Fetini belt in the Ivory Coast (Gasquet et al., 2003). Similar ages have been recorded by de Kock et al. (2011) in northern Ghana (east of the Boromo belt) as well as by Parra-Avila et al. (2016) in detrital zircons.

The estimated thickness (> 5 km), lateral continuity of geochemically correlatable units over some hundreds of kilometres shows a period of high-flux volcanism within a limited time (~100 m.y.), which is consistent with plume-derived flood basalt provinces. Many flood basalt provinces with thick, geochemically distinguishable basaltic lava successions are traceable over large areal extent consistent with rapid, voluminous lava flows [e.g., the Roza member 1300 km^3 of the Columbia River basalt province; Jerram (2002)]. The paleo-depositional setting was deep-water (> 5000 m) due to abundant pillow lavas, scarce vesicles (Cas & Simmons, 2018), and the apparent lack of carbonate deposits and terrestrial deposits within the plume-derived flood basalts of the Lower sequence [e.g., flood basalts of the Ontong Java oceanic plateau; Greene et al. (2009)]. The eruption rate of the basaltic lavas is interpreted as rapid because of the abundance of massive basalts and the absence of interbedded sediments as well as internal erosional surfaces (Griffiths & Fink, 1992). Additionally, the lack of extra-basinal sedimentary deposits also shows no emergent landmass proximal to the depositional basin. The physical and chemical evidence

deduced from this assemblage suggest oceanic flood basalts similar to modern oceanic plateaus.

To summarise, the earliest event is characterised by the formation of oceanic plateau-like mafic flood basalts province(s) at about 2350 Ma.

6.1.2 Island arc building Stage (~2212–2160 Ma)

This stage is characterised by the emplacement of diverse rock types comprising low to high Th-TiO₂ tholeiitic and calc-alkaline lavas and volcaniclastic deposits of the mafic-intermediate volcanic association (LFA-2), including their associated intrusive complexes and the proximal to distal fine-grained sedimentary association (LFA-3). These lithologies make up the Upper sequence of both belts predominantly composed of geochemical Group 4U and minor proportions of Groups 1U and 3U. The basic-intermediate melts generated in this stage depict magma extraction from a depleted mantle and a subduction-derived metasomatised mantle based on relatively high Th/Ta, La/Yb, Ce/Nb ratios similar to typical island arc rocks. Groups 1U and 3U rocks originated from primitive melts and are probably the earliest forming melt during the onset of this magmatic event. Wet melting was the main mechanism for partial melting and magma generation, evidenced by abundant hydrous minerals (e.g. hornblende) and LILE consistent with the hydration of the mantle wedge from subduction-derived fluids. The relative abundance of the HREEs to other HFSE suggests the mantle source is above the garnet stability zone (> 80 km). The derived melts were stored in relatively deep magma chambers (~15 km) before magma eruption. Petrological modelling reveals fractional crystallisation (Group 3U), and assimilation fractional crystallisation (Group 4U) of felsic material controlled the geochemical variations observed in these rocks. This shows that Group 3U rocks are primitive and perhaps formed at the onset of the subduction-related melting. In contrast, Group 4U formed later as the system evolved to allow for significant crustal assimilation trends.

The magmas were erupted into a deep to shallow water setting, building isolated emergent composite volcanoes and tephra cones. The strongest case for emergence is provided by the rounded clasts in conglomerates, as such rounded forms only develop in tractional environments, such as fluvial or beach settings (Cas & Wright, 1987; Hayman et al., 2020). Clast provenance indicates derivation from a variety of intermediate porphyritic volcanic sources, which is a testament to the building of

diverse volcanic edifices such as stratovolcanoes. The presence of abundant resedimented mass flow deposits depicts collapses of the over steepened flanks of the stratovolcanoes. Turbidites of LFA-3, often interbedded with LFA-2, were formed as mass flows down the flanks of emergent volcanic edifices and deposited proximal to medial deposits while the mudstone-siltstone beds formed in distal basins.

The onset of magmatism is estimated at around 2212 Ma based on the oldest crystallisation age of a rhyodacite unit in the Upper sequence of the Houndé belt (Castaing et al., 2003). Magmatism peaked between 2195–2160 Ma based on abundant volcanic and intrusive units within this time frame. The termination of magmatism is difficult to constrain, but the lack of crystallisation ages of volcanic lithologies after ~2160 Ma coupled with the onset of the D1 compressional deformation suggests volcanic arc magmatism may have ceased at this time. Syn-tectonic granitoids with similar geochemical characteristics as the Upper sequence volcanic rocks in both belts also range in crystallisation age between 2195 ± 4 Ma (Trondhjemite, U-Pb zircon; Bruguier, 2011) to 2162 ± 32 Ma (Gasquet et al., 2003). This age range indicating a roughly 52 m.y. of magmatic history and is consistent with the 40–100 m.y. life span of a typical volcanic arc (Stern, 2002).

Based on the current belt symmetry, it is presumed that the volcanic arc assemblages of the Houndé and Boromo belts belong to distinct volcanic arc terranes (Figure 6-1). Although the Upper sequence of both belts possesses similar geochemical and lithostratigraphic characteristics, the distance between both sequences (compressed width > 100 km) is wider than for typical volcanic arc terranes in modern subduction zones, which are ~45–100 km wide (Ishizuka et al., 2006). There is no unequivocal evidence for the polarity of the subduction zones of the presumed volcanic arc terranes. However, the orientation of both belts (i.e., the outcropping of the Upper sequence on opposite sides of the Lower sequences of both belts) can best be explained by west-ward dipping subduction zones on adjacent sides of the oceanic plateau terrane (Figure 6-1). Subsequent propagation of the subduction front led to the accretion of volcanic arc terranes and the oceanic plateau terrane after failure to subduct the thick, buoyant oceanic plateau.

In summary, this stage can be described as the progressive building of island arcs (including edifice construction and destruction) and deposition of volcaniclastic products in one or more subduction zones.

6.1.3 Terrane accretion and D-1 deformational Stage (2160–2124 Ma)

The third stage represents the collision and deformation of both terranes through subduction accretion processes. This stage was initiated by the accretion and collision of the oceanic plateau and island arc terranes. Subsequently, both distinct terranes were involved in a crustal-scale E-W compressional deformation, leading to major open folds and N-S trending shear zones, as well as regional greenschist facies (and localised amphibolite) metamorphism. The regional greenschist facies metamorphism reflects conditions of burial [4–7 kbar, 400–500 °C; Best (2003)] and is consistent with the formation of metamorphic titanites at ~2139 Ma. The age of this event was not determined in this study. However, according to Baratoux et al. (2011), the major shear zones and crustal folding associated with an E-W compression (D1) occurred between 2160–2124 Ma based on radiometric dating of syn-orogenic granitoids (not evaluated in this study).

This stage involved crustal-scale folding evidenced by large synclines formed within the rocks of the Upper sequence of the Houndé belt. The fine-grained sedimentary lithofacies association within the center of the belt forms the fold hinge zone. Notably, the oceanic plateau assemblages of the Lower sequence in the Houndé belt, although older, do not appear at the synclinorium's outer limbs. Therefore, it is postulated that the island arc assemblages of the Upper sequence were folded on collision with the oceanic plateau of the Lower sequence. The thickness and density of oceanic plateaus result in clogging of the subduction zone or reorientation of the subduction front rather than subducting the plateau into the mantle (Stern & Gerya, 2018). This presumption is also supported by the apparent absence of an erosional unconformity between the Lower and Upper sequence; thus, there are no basal sedimentary deposits in the Upper sequence with clast provenance from the Lower sequence. Therefore, the Lower sequence and the Upper sequence do not form a typical layer-cake stratigraphy as suggested by others [e.g., Baratoux et al. (2011); Le Pape et al. (2017)], but rather were juxtaposed during the D1 E-W compressional terrane accretion event mentioned above. During the accretion, syn-orogenic calc-alkaline intermediate-felsic rocks with similar geochemical signatures as Group 4U

rocks intruded both the Lower and Upper sequence indicating that these stratigraphic successions were accreted at this stage.

In summary, this stage presents compressional deformation of the oceanic plateau terrane and subduction-derived island arc terrane of the Lower and Upper sequences, respectively, emplacement of syn-orogenic granitoids and regional greenschist facies metamorphism. This stage depicts the typical Eburnean tectono-magmatic event recorded in the Birimian domain.

6.1.4 Late D-1 and Successive Basin Stage (ca. 2124 Ma)

The final recognised event is represented by the deposition of the quartz-rich sedimentary lithofacies association (LFA-4), which forms a narrow (1-5 km) N-S sedimentary basin running for about 100 km, and a late D1 granitoid emplacement. The sedimentary basin formed during the waning stages of the E-W compressional (D1) event resulting from the reactivation of major fault zones. The quartz-rich sedimentary deposits, found only in the Houndé belt, texturally and compositionally resemble the rocks of the Tarkwaian Group described by Bossière et al. (1996) in the Houndé belt and by Smith et al. (2016) in the Ashanti belt of Ghana. The timing of deposition of this succession is inferred from the end of the D1 compressional event pegged at about 2124 Ma according to Bossière et al. (1996); Baratoux et al. (2011). The secondary titanite crystallisation age obtained in this current study, which dates peak greenschist metamorphism at ~2139 Ma, provides a constraint on the lower limit of the timing of peak D1 compressional event. The events of the D1 deformation do not imprint in the rocks of the quartz-rich sedimentary lithofacies association. Hence, the quartz-rich sedimentary lithofacies association must have been deposited after ~2139 Ma which supports the timing proposed by Baratoux et al. (2011) and Bossière et al. (1996).

Sediment provenance is mainly from granitic rocks, evidenced by the plutonic quartz crystals, the abundance of granitic clasts, and detrital zircons (Bossière et al., 1996) all of which indicate derivation from the erosion of granitic rocks that were uplifted and eroded. The depositional setting is interpreted as a subaerial fluvial system due to large-scale cross-beds, planar sandstones, and the abundance of texturally mature sedimentary deposits such as the clast-supported conglomerates.

This stage indicates the strengthening of the Birimian crust at the end of the early Eburnean orogenic cycle between 2140-2120 Ma (Block et al., 2016).

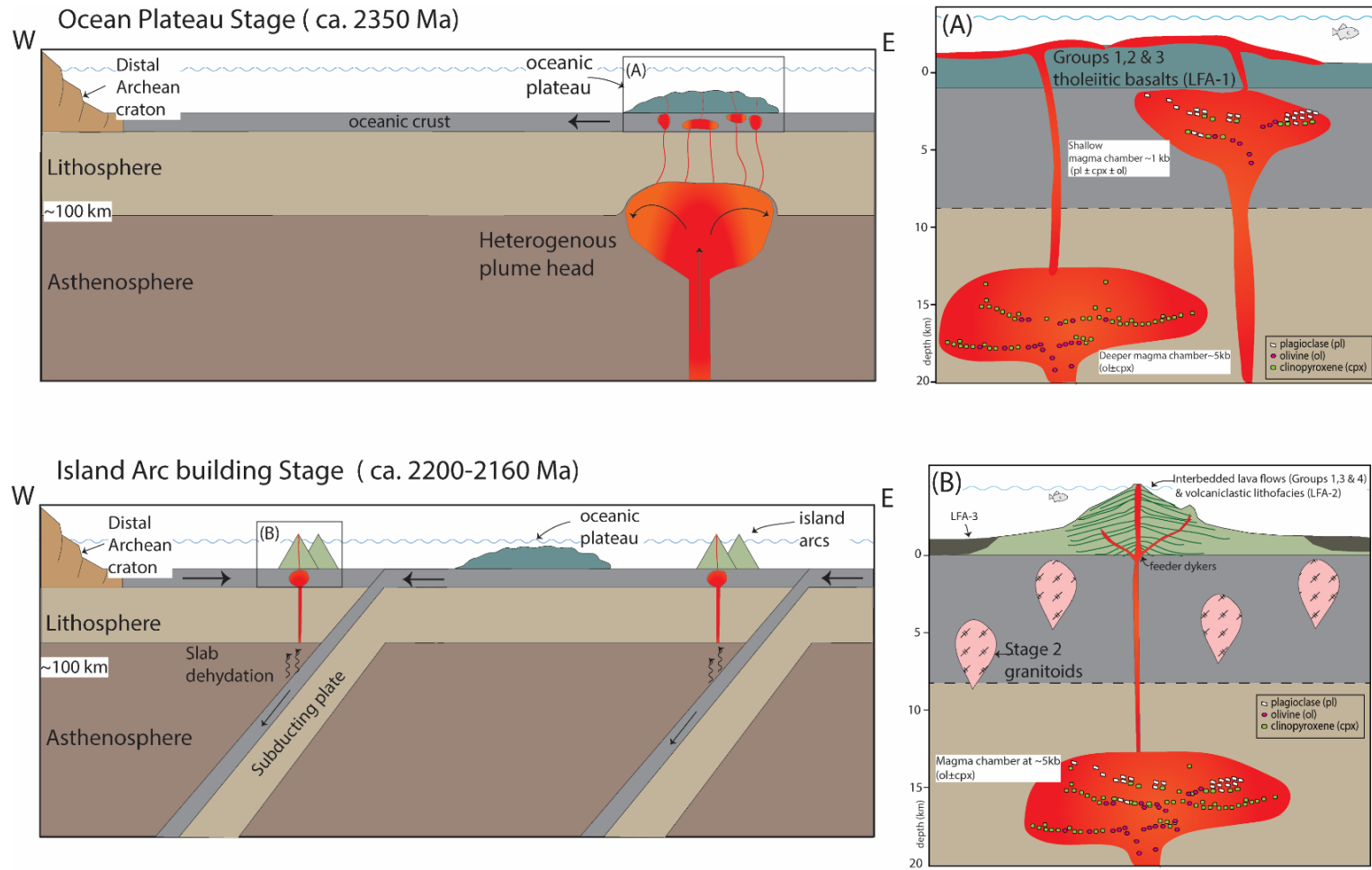


Figure 6-1 Schematic representation of the geodynamic evolution of the Paleoproterozoic Houndé and Boromo greenstone belts in sequential order; Ocean Plateau Stage: Emplacement of abundant tholeiitic flood basalt assemblages of the Lower sequence onto an oceanic crust with magma production by a mantle plume. Island Arc building Stage: Tholeiitic and calc-alkaline subduction-related magmatism in an island arc setting (Upper sequence).

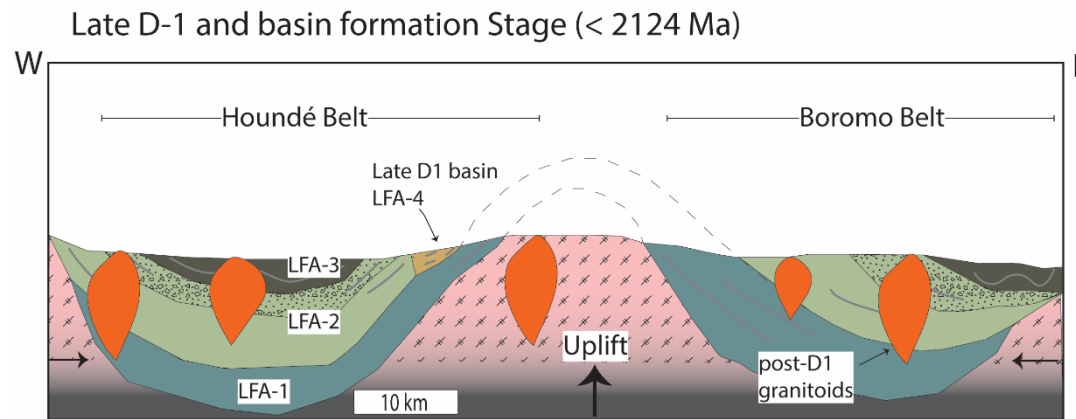
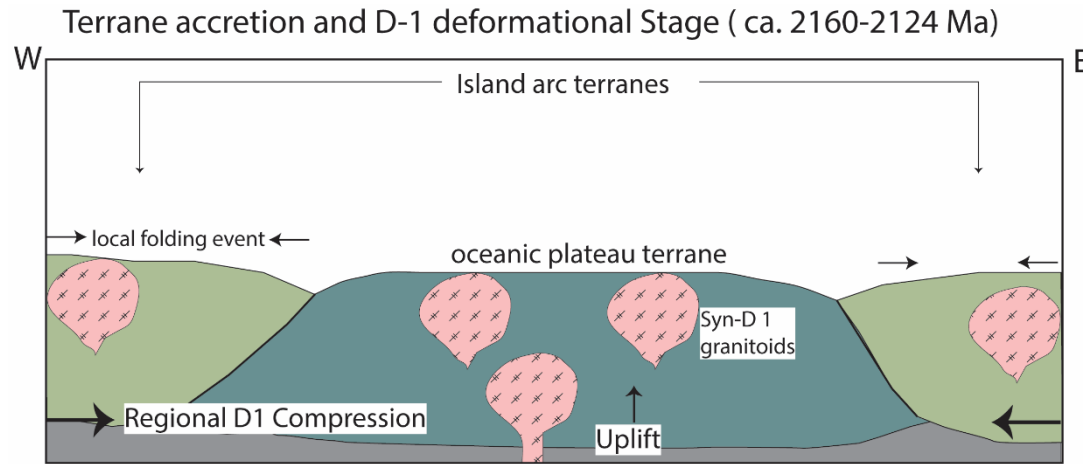


Figure 6-1 (continued) Terrane accretion and D-1 deformational Stage: convergence of island arc terrane with oceanic plateau terrane, compressional deformation and emplacement of syn-deformational granitoids. Late D-1 and basin formation Stage: cessation of arc magmatism resulting from accretion and collision of terranes, late episode deformation, and emplacement of intermediate-felsic granitoids followed by uplift, the opening of late sedimentary basin, and deposition of quartz-rich sedimentary lithofacies association. Note: vertical scale not to scale.

6.2 AUTOCHTHONOUS VS ALLOCHTHONOUS ORIGIN

The lithostratigraphic, structural, and petrogenetic relationship between the Lower and Upper sequences of the Houndé and Boromo belts reveal contrasting geodynamic histories consistent with the allochthonous terrane accretion model. The Lower sequence, which consists of within-plate flood basalt assemblages, represents the oceanic plateau lithotectonic domain. In contrast, the Upper sequence made up of the island arc assemblages represents the subduction-related lithotectonic domain. This suggests that the lithostratigraphic pile composed of the Lower and Upper stratigraphic sequence comprises at least two distinct lithotectonic domains and are not stratigraphically conformable. The allochthonous terrane accretion model proposed presumes an east to west convergence of the oceanic plateau and island arc lithotectonic terranes leading to the growth of the Houndé and Boromo belts sequentially between 2350 Ma–2160 Ma followed by deformation and sedimentary deposition until ~2124 Ma.

The allochthonous accretion model proposed in this study differs from the previously proposed arc-back arc accretion model (Baratoux et al., 2011). This study recognises the accretion of distinct terranes instead of subduction-related magmatism only. This model also diverges from the in-situ oceanic plateau vertical accretion (Lombo, 2009) because of the lack of continuous layer-cake stratigraphic successions between the Lower and Upper sequences and the presence of allochthonous subduction-related terranes. Abouchami et al. (1990) and Béziat et al. (2000) recognised the involvement of two contrasting geodynamic settings; thus, island arc and oceanic plateau in developing the Birimian greenstone belts are similar to the proposed model in this study.

The proposed geodynamic evolution of the Houndé and Boromo greenstone belts is exemplified today in the accreted allochthonous Caribbean oceanic plateau (~95-88 Ma), which is rimmed between the Antilles arcs and the Central American arcs (White et al., 1999; Kerr et al., 2000). In this region, the Caribbean oceanic plateau collided with the Antilles arcs at ca. 85 Ma causing a change in subduction polarity to initiate the eastward dipping Central American subduction zone at ca. 65 Ma (Wright & Wyld, 2011) (Figure 6-2). The polarity and proximity of the subduction zones in the Caribbean region to the continental crust of the North and South American plate do

not represent the model postulated for the evolution of the Houndé and Boromo belt. However, the current symmetry, thus an oceanic plateau rimmed on opposite sides by volcanic arc terranes, resembles the study area's situation and, therefore, a suitable modern analogy.

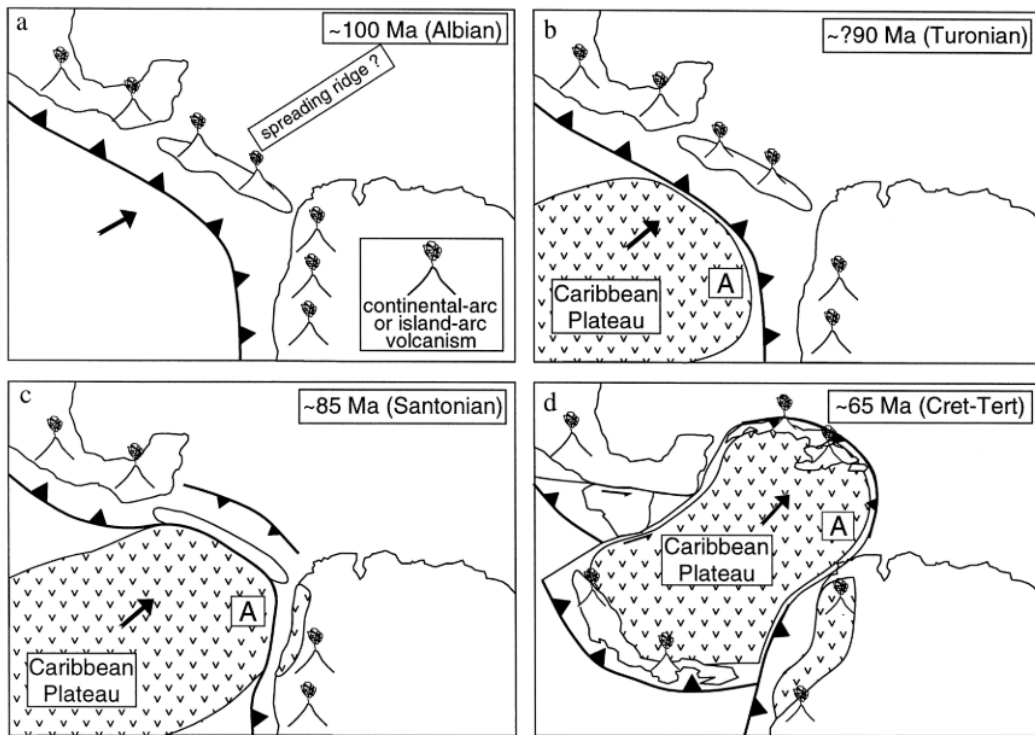


Figure 6-2 Schematic representation of the tectonic evolution of the Caribbean-Colombian Cretaceous igneous province according to White et al. (1999). Here, the Caribbean plateau is rimmed by volcanic arc terranes in a complex subduction accretion setting, similar to the geodynamic model proposed for the Houndé and Boromo belts in this study.

6.3 IMPLICATIONS OF THE PALEOPROTEROZIC EVOLUTION OF THE HOUNDÉ AND BOROMO BELTS

Compared with the geodynamic evolution of other volcano-sedimentary packages, the supracrustal rocks of the Houndé and Boromo belts share many similarities and contrasting styles with both Archean and Phanerozoic packages. For instance, many Archean greenstone belts typically show a conformable layer-cake lithostratigraphic succession from bottom to top. These display a lower ultramafic-mafic group (i.e. komatiitic to tholeiitic basalts) through to a middle greenstone group (i.e. tholeiitic to calc-alkaline coherent and volcaniclastic rocks) capped with an upper sedimentary group accumulated within a relatively short time (<50 m.y.) (Anhaeusser, 2014). Such Archean packages exhibit abundant xenocrystic zircons and progressive up-sequence contamination due to in-situ accretion of each lithostratigraphic succession (e.g., the ~2700 Ma Agnew greenstone belt, Kalgoorlie terrane; Hayman, Thébaud, et al. (2015)). On the contrary, most Phanerozoic orogens are characterised by crustal-scale fault-bounded tectonic packages, usually of different age brackets and geochemical composition juxtaposed during the subduction accretion crust forming events (e.g., the late Neoproterozoic to early Mesozoic Tasmanides of eastern Australia; Doublier et al. (2018)). Hence, in relation to the lithostratigraphic development of the Houndé and Boromo greenstone belts, lack of evidence for a continuous layer-cake stratigraphy and the evidence for the accretions and juxtaposition of distinct non-conformable packages resembles typical Phanerozoic orogens.

The sedimentary package of most Archean greenstone belts is dominated by subaqueous chemical sedimentary rocks and graywacke-shale assemblages and typically capped by minor subaerial clastic deposits (e.g., Abitibi greenstone belt; Thurston et al. (2008)). The proportions of subaerial clastic sedimentary deposits in the Archean succession has been primarily attributed to much of Archean crust submerged below sea level due to dense amphibole-garnet-pyroxenite lithospheric roots (Campbell & Davies, 2017; Hayman et al., 2020). On the contrary, many Paleoproterozoic, as well as Phanerozoic sedimentary packages, comprised of mature, often quartz-rich platform sediments (such as LFA-4 of this study) indicative of stable, rigid, and emergent continental crust (Campbell & Davies, 2017). Additionally, most cratons that preserve Paleoproterozoic magmatism (2.4-2.0 Ga) present evidence for

continental rift and passive margin setting, including the Kaapvaal, Superior and Fennoscandian cratons (Barley et al., 2005). This is in stark contrast to the Houndé and Boromo belts, which rather present evidence for primarily oceanic settings with no significant input from a continental setting.

Komatiites (high magnesium volcanic rocks) have not been encountered in the Houndé and Boromo belts and the question remains if perhaps they are indeed absent, rare, or completely eroded from the rock record. Komatiites are common in the Archean and are postulated to have formed by relatively hotter (> 1500 °C) mantle temperatures (Polat & Kerrich, 2001; Condie, 2016; Campbell & Davies, 2017). Although there are isolated cases of Komatiitic formations in Paleoproterozoic greenstone belts and Phanerozoic formations (e.g., Gorgona Komatiites; Kerr et al. (1996)) their occurrence relative to the Archean is minor (Wyman, 2020). The apparent decline of Komatiitic rocks in the rocks record with time appears to corroborate the progressive evolution of the mantle's chemical and thermal state through time. Therefore, the lack of Komatiites within the Houndé and Boromo rock sequences shows that the mantle source from which these rocks were generated were markedly different (perhaps cooler and chemically more evolved) from those of the typical Archean mantle sources (Shervais, 2006).

In comparison with other Birimian greenstone belts, many studies have also shown ample diversity within the rock assemblages comparable to that observed in the Houndé and Boromo belts. For example, age dating in the Haute Comoé area of the northern Ivory Coast displays two generations of adjacent volcanic assemblages separated by at least 50 m.y. (Hirdes et al., 1996). These distinct volcanic assemblages form the Ouango Fetini and Téhini greenstone belts, respectively, possess contrasting island arc and MORB affinity showing a variable geodynamic history. Similar divergence in geochemical affinities also exists in the southern Ashanti belt of Ghana (Dampare et al., 2009), where rock types exhibiting both island arc and MORB affinities with no evidence for the involvement of continental crust. The identification of chemically and stratigraphically distinct assemblages in other greenstone belts within the Birimian domain attests to the widespread juxtaposition of allochthonous terranes.

6.3.1 Mantle source heterogeneity in the Paleoproterozoic era

It is widely accepted that the progressive melting of the mantle to form the continental crust has left the upper mantle strongly depleted in incompatible trace elements in the earliest part of the Earth's evolution (Campbell & Griffiths, 1993; Hofmann, 1997; White, 2015). With time, the mantle evolved from a primitive mantle state as a result of continuous re-distribution of elements and radiogenic isotope decay (Kimura et al., 2017). Here, the trace element ratios and Nd-isotopic compositions of the mantle-derived uncontaminated basalts of the Lower sequence for the Houndé and Boromo belts provide ample evidence for a heterogeneous mantle source. The distinction in the chemical diversity of the studied basalts cannot be easily explained by fractional crystallisation of a common parental magma or assimilation fractional crystallisation. Instead, the evidence supports an early refertilisation or modification of the mantle source recognised as enriched zones/components of a deep-seated heterogeneous mantle source. This heterogeneous source was tapped by a mantle plume (s) to generate the flood basalts of the Lower sequence of both belts.

The timing of this mantle modification event was not investigated but can be constrained to have occurred prior to the ~2.3 Ga magmatic age estimated for these rocks. According to Gamal El Dien et al. (2020), the timing of the onset of widespread operation of plate tectonics is marked by the refertilisation of the lower and upper mantle at ~3.2 Ga. Their interpretation is based on the dramatic increase in large ion lithophile element ratios in mantle-derived basalts indicative of extensive re-introduction of terrestrial material into the mantle by subduction processes. Assuming this correlation is accurate, the continual operation of subduction processes globally would have facilitated mantle convection events leading to the development of distinct mantle reservoirs post 3.2 Ga era.

The heterogeneous mantle source origin hypothesised for the Lower sequence of the Houndé and Boromo belts in this study, therefore, corroborates with the widespread heterogeneity of the mantle by the early Proterozoic. This provides support for the existence of well-established enriched (OIB-like) mantle reservoirs as far back as 2.3 Ga. This implies that some mechanism similar to the modern subduction regime operated in the early Precambrian. The mechanism facilitated the establishment of heterogeneous mantle reservoirs by the redistribution of crustal material into the

mantle reservoirs. But the resemblance of this mechanism with the modern-style subduction regime remains elusive.

6.4 CONCLUSIONS

The geological history of Houndé and Boromo greenstone belts of the Birimian domain of the West African Craton is characterised by major magmatic and tectonic events spanning more than 200 m.y. from ca. 2350 Ma to 2124 Ma. The earliest preserved magmatic event was initiated at about 2350 Ma by effusive magmatism of tholeiitic basalts and associated mafic intrusives originating from melting a heterogeneous mantle plume in a deep-water oceanic plateau setting. This event was followed by the eruption of dominantly calc-alkaline magmatism of metasomatised mantle in an island arc subduction setting initiated around 2200 Ma and formed discrete subaqueous-emergent composite volcanoes. The peak volcanic period was subsequently followed by lateral accretion of the oceanic plateau and volcanic arc terranes, E-W compressional deformation (D1), and regional greenschist metamorphism between 2160-2124 Ma. The uppermost succession of the stratigraphy was deposited in a subaerial fluvial setting around 2124 Ma towards the end of the deformational event following uplift and erosion of granitic bodies. Critical analysis of the lithostratigraphy and geochemical data show that the oceanic plateaus of the Houndé and Boromo belts share a common geodynamic history, developing as a distinct lithotectonic terrane before amalgamation with the island arc terrane(s). The evolution of both belts cannot be supported by the lateral accretion of island arcs only nor in-situ growth of oceanic plateaus. The preferred model is by allochthonous terrane subduction-related accretion of mantle plume-derived oceanic plateaus and volcanic arcs. The evidence provided in previous chapters supports the postulated model, including distinct lithological packages, discontinuous lithological successions, contrasting petrogenetic histories, and lack of evidence for contamination or inheritance of a continental basement complex. The reconstructed geological history of rocks of the Houndé and Boromo belts suggests the existence of well-established heterogeneous mantle sources at least by the Paleoproterozoic era due to sequestrated crustal materials by earlier subduction-like processes.

6.4.1 Recommendations for future studies

There are some pertinent questions that this research was unable to answer due to the scope and data collected:

- What was the duration of mantle plume magmatism in forming the oceanic plateau assemblage of the Lower sequence? There is currently no convincing constraint on the termination of the mantle plume magmatism. This will help answer whether some assemblages of the Lower sequence (thus Group 1L rocks) formed contemporaneously with the onset of subduction-related magmatism. More robust dating is required, especially for the emplacement of the mafic tholeiitic rocks of the Lower sequence, to help answer this question.
- Are the volcanic arc terranes of the Houndé and Boromo belts truly contemporaneous, or is there a significant time gap between them? Although these two lithotectonic assemblages have been placed within the same time gap, the upper limit of the age of volcanism is constrained by post D1 granitoid intrusions, which occurred after terrane accretion, therefore common to both belts. Extensive age dating of volcanic and granitic rocks within the Upper sequences of both belts will be required to unravel the geological history of the subduction-related rocks in both belts.
- Future studies in other Birimian greenstone belts should consider using the lithofacies approach to unravel the volcanic architecture and geological history of each greenstone belt. This will help identify distinct lithotectonic terranes within the Birimian domain leading to a better understanding of its geodynamic evolution.

Bibliography

- Abbott, D., & Mooney, W. (1995). The Structural and Geochemical Evolution of the Continental Crust: Support for the Oceanic Plateau Model of Continental Growth. *Reviews of Geophysics*, 33(S1), 231-242. doi:10.1029/95RG00551
- Abouchami, W., Boher, M., Michard, A., & Albarede, F. (1990a). A Major 2.1 Ga Event of Mafic Magmatism in West Africa'. An Early Stage of Crustal Accretion. *JOURNAL OF GEOPHYSICAL RESEARCH, VOL. 95*(NO. B I 1), PAGES 17,605-617,629.
- Albarede, F. (1992). How Deep Do Common Basaltic Magmas Form and Differentiate? *Journal of Geophysical Research*, 97(B7). doi:10.1029/91jb02927
- Aldanmaz, E., Pearce, J. A., Thirlwall, M. F., & Mitchell, J. G. (2000). Petrogenetic Evolution of Late Cenozoic, Post-Collision Volcanism in Western Anatolia, Turkey. *Journal of Volcanology and Geothermal Research*, 102(1), 67-95. doi: [https://doi.org/10.1016/S0377-0273\(00\)00182-7](https://doi.org/10.1016/S0377-0273(00)00182-7)
- Anhaeusser, C. R. (2014). Archaean Greenstone Belts and Associated Granitic Rocks – a Review. *Journal of African Earth Sciences*, 100, 684-732. doi:10.1016/j.jafrearsci.2014.07.019
- Anhaeusser, C. R., Mason, R., Viljoen, M. J., & Viljoen, R. P. (1969). A Reappraisal of Some Aspects of Precambrian Shield Geology. *Geological Society of America Bulletin*, 80(11), 2175-2200. doi:10.1130/0016-7606(1969)80[2175:arosao]2.0.co;2
- Arevalo, R. J., & McDonough, W. F. (2010). Chemical Variations and Regional Diversity Observed in Morb. *Chemical Geology*, 271, 70-85.
- Arndt, N. (1999). Why Was Flood Volcanism on Submerged Continental Platforms So Common in the Precambrian? *Precambrian Research*, 97(3-4), 155-164. doi:10.1016/S0301-9268(99)00030-3
- Arndt, N., & Davaille, A. (2013). Episodic Earth Evolution. *Tectonophysics*, 609, 661-674. Retrieved from <http://www.sciencedirect.com/science/article/pii/S0040195113004150>. doi: <http://dx.doi.org/10.1016/j.tecto.2013.07.002>
- Attoh, K. (1982). Structure, Gravity Models and Stratigraphy of an Early Proterozoic Volcanic—Sedimentary Belt in Northeastern Ghana. *Precambrian Research*,

18(3), 275-290. Retrieved from
<http://www.sciencedirect.com/science/article/pii/0301926882900146>. doi:
[http://dx.doi.org/10.1016/0301-9268\(82\)90014-6](http://dx.doi.org/10.1016/0301-9268(82)90014-6)

Attoh, K., Evans, M. J., & Bickford, M. E. (2006). Geochemistry of an Ultramafic-Rodingite Rock Association in the Paleoproterozoic Dixcove Greenstone Belt, Southwestern Ghana. *Journal of African Earth Sciences*, 45(3), 333-346. doi:10.1016/j.jafrearsci.2006.03.010

Augustin, J., & Gaboury, D. (2017). Paleoproterozoic Plume-Related Basaltic Rocks in the Mana Gold District in Western Burkina Faso, West Africa: Implications for Exploration and the Source of Gold in Orogenic Deposits. *Journal of African Earth Sciences*, 129, 17-30. doi:10.1016/j.jafrearsci.2016.12.007

Augustin, J., Gaboury, D., & Crevier, M. (2016). The World-Class Wona-Kona Gold Deposit, Burkina Faso. *Ore Geology Reviews*, 78, 667-672. doi:10.1016/j.oregeorev.2015.10.017

Ayer, J., Amelin, Y., Corfu, F., Kamo, S., Ketchum, J., Kwok, K., & Trowell, N. (2002). Evolution of the Southern Abitibi Greenstone Belt Based on U-Pb Geochronology: Autochthonous Volcanic Construction Followed by Plutonism, Regional Deformation and Sedimentation. *Precambrian Research*, 115(1), 63-95.

Babechuk, M. G., & Kamber, B. S. (2011). An Estimate of 1.9ga Mantle Depletion Using the High-Field-Strength Elements and Nd–Pb Isotopes of Ocean Floor Basalts, Flin Flon Belt, Canada. *Precambrian Research*, 189(1-2), 114-139. doi:10.1016/j.precamres.2011.05.006

Baratoux, L., Metelka, V., Naba, S., Jessell, M. W., Grégoire, M., & Ganne, J. (2011). Juvenile Paleoproterozoic Crust Evolution During the Eburnean Orogeny (~2.2–2.0ga), Western Burkina Faso. *Precambrian Research*, 191(1-2), 18-45. doi:10.1016/j.precamres.2011.08.010

Baratoux, L., Metelka, V., Naba, S., Ouiya, P., Siebenaller, L., Jessell, M. W., . . . Franceschi, G. (2015). Tectonic Evolution of the Gaoua Region, Burkina Faso: Implications for Mineralization. *Journal of African Earth Sciences*, 112, 419-439. doi:10.1016/j.jafrearsci.2015.10.004

Baratoux, L., Söderlund, U., Ernst, R., de Roever, E., Jessell, M., Kamo, S., . . . Yatte, D. (2019). New U–Pb Baddeleyite Ages of Mafic Dyke Swarms of the West African and Amazonian Cratons: Implication for Their Configuration in Supercontinents through Time. In *Dyke Swarms of the World: A Modern Perspective* (pp. 263-314): Springer.

Barley, M., Bekker, A., & Krapez, B. (2005). Late Archean to Early Paleoproterozoic Global Tectonics, Environmental Change and the Rise of Atmospheric Oxygen. *Earth and Planetary Science Letters*, 238(1-2), 156-171. doi:10.1016/j.epsl.2005.06.062

Barley, M. E., Brown, S. J. A., Krapež, B., & Kositcin, N. (2008). Physical Volcanology and Geochemistry of a Late Archaean Volcanic Arc: Kurnalpi and Gindalbie Terranes, Eastern Goldfields Superterrane, Western Australia. *Precambrian Research*, 161(1-2), 53-76. Retrieved from <http://www.sciencedirect.com/science/article/pii/S0301926807002070>. doi: <http://doi.org/10.1016/j.precamres.2007.06.019>

Barnes, S. J., Van Kranendonk, M. J., & Sonntag, I. (2012). Geochemistry and Tectonic Setting of Basalts from the Eastern Goldfields Superterrane. *Australian Journal of Earth Sciences*, 59(5), 707-735. doi: 10.1080/08120099.2012.687398

Bédard, J. H. (2001). Parental Magmas of the Nain Plutonic Suite Anorthosites and Mafic Cumulates: A Trace Element Modelling Approach. *Contributions to Mineralogy and Petrology*, 141(6), 747-771. doi:10.1007/s004100100268

Bédard, J. H. (2013). How Many Arcs Can Dance on the Head of a Plume? *Precambrian Research*, 229, 189-197. doi:10.1016/j.precamres.2012.05.004

Bédard, J. H. (2017). Stagnant Lids and Mantle Overturns: Implications for Archaean Tectonics, Magmagenesis, Crustal Growth, Mantle Evolution, and the Start of Plate Tectonics. *Geoscience Frontiers*. doi:10.1016/j.gsf.2017.01.005

Best, M. G. (2003). *Igneous and Metamorphic Petrology* (2nd ed.): Blackwell Publishing.

Béziat, D., Bourges, F., Debat, P., Lombo, M., Martin, F., & Tollen, F. (2000). A Paleoproterozoic Ultramafic-Mafic Assemblage and Associated Volcanic Rocks of the Boromo Greenstone Belt: Fractionates Originating from Island-Arc Volcanic Activity in the West African Craton *Precambrian research*, 101(1), 25-47. doi: 10.1016/S0301-9268(99)00085-6

Bézos, A., Escrig, S., Langmuir, C. H., Michael, P. J., & Asimow, P. D. (2009). Origins of Chemical Diversity of Back-Arc Basin Basalts: A Segment-Scale Study of the Eastern Lau Spreading Center. *Journal of Geophysical Research*, 114(B6). doi:10.1029/2008jb005924

Block, S., Baratoux, L., Zeh, A., Laurent, O., Bruguier, O., Jessell, M., . . . Bosch, D. (2016). Paleoproterozoic Juvenile Crust Formation and Stabilisation in the South-Eastern West African Craton (Ghana); New Insights from U-Pb-Hf

Zircon Data and Geochemistry. *Precambrian Research*, 287, 1-30.
doi:10.1016/j.precamres.2016.10.011

Block, S., Ganne, J., Baratoux, L., Zeh, A., Parra-Avila, L. A., Jessell, M., . . . Siebenaller, L. (2015). Petrological and Geochronological Constraints on Lower Crust Exhumation During Paleoproterozoic (Eburnean) Orogeny, Nw ghana, West African Craton. *Journal of Metamorphic Geology*, 33(5), 463-494. doi:10.1111/jmg.12129

Boggs, S. (2006). *Principles of Sedimentology and Stratigraphy*.: Pearson Education, Inc.

Boher, M., Abouchami, W., Michard, A., Albarede, F., & Arndt, N. T. (1992). Crustal Growth in West Africa at 2.1 Ga. *Journal of Geophysical Research: Solid Earth*, 97(B1), 345-369. Retrieved from <http://dx.doi.org/10.1029/91JB01640>.
doi:10.1029/91JB01640

Bossière, G., Bonkoungou, I., Peucat, J.-J., & Pupin, J.-P. (1996). Origin and Age of Paleoproterozoic Conglomerates and Sandstones of the Tarkwaian Group in Burkina Faso, West Africa. *Precambrian Research*, 80(3), 153-172. Retrieved from <http://www.sciencedirect.com/science/article/pii/S0301926896000149>.
doi: [http://dx.doi.org/10.1016/S0301-9268\(96\)00014-9](http://dx.doi.org/10.1016/S0301-9268(96)00014-9)

Bouma, A. H. (1962). Sedimentology of Some Flysch Deposits: A Graphic Approach to Facies Interpretation. *Elsevier*, 168.

Boyce, J. A., Nicholls, I. A., Keays, R. R., & Hayman, P. C. (2015). Variation in Parental Magmas of Mt Rouse, a Complex Polymagmatic Monogenetic Volcano in the Basaltic Intraplate Newer Volcanics Province, Southeast Australia. *Contributions to Mineralogy and Petrology*, 169(2).
doi:10.1007/s00410-015-1106-y

Brooks, C. K. (1976). The Fe₂O₃/FeO Ratio of Basalt Analyses: An Appeal for a Standardized Procedure. *Bull. Geol. Soc. Denmark*, 25, 117-120.

Brooks, C. K., Larsen, L. M., & Nielsen, T. F. D. (1991). Importance of Iron-Rich Tholeiitic Magmas at Divergent Plate Margins: A Reappraisal. *Geology*, 19(3), 269-272. doi: [https://doi.org/10.1130/0091-7613\(1991\)019<0269:IOIRTM>2.3.CO;2](https://doi.org/10.1130/0091-7613(1991)019<0269:IOIRTM>2.3.CO;2)

Broska, I., Harlov, D., Tropper, P., & Siman, P. (2007). Formation of Magmatic Titanite and Titanite–Ilmenite Phase Relations During Granite Alteration in the Tribeč Mountains, Western Carpathians, Slovakia. *Lithos*, 95(1-2), 58-71.
doi:10.1016/j.lithos.2006.07.012

- Brown, M. (2010). Geodynamic Regimes and Tectonic Settings for Metamorphism: Relationship to the Supercontinent Cycle. *Indian Journal of Geology*, Vol.80, ,(Nos. 1-4), p.3-21.
- Bryan, S. E., & Ernst, R. E. (2008). Revised Definition of Large Igneous Provinces (Lips). *Earth-Science Reviews*, 86(1-4), 175-202. doi:10.1016/j.earscirev.2007.08.008
- Cagnard, F., Barbey, P., & Gapais, D. (2011). Transition between “Archaeen-Type” and “Modern-Type” Tectonics: Insights from the Finnish Lapland Granulite Belt. *Precambrian Research*, 187(1-2), 127-142. doi:10.1016/j.precamres.2011.02.007
- Campbell, I. H., & Davies, D. R. (2017). Raising the Continental Crust. *Earth and Planetary Science Letters*, 460, 112-122. doi:10.1016/j.epsl.2016.12.011
- Campbell, I. H., & Griffiths, R. W. (1993). The Evolution of the Mantle's Chemical Structure. *Lithos*, 30(3-4), 389-399. doi:[https://doi.org/10.1016/0024-4937\(93\)90047-G](https://doi.org/10.1016/0024-4937(93)90047-G)
- Cas, R. A. F., Allen, R. L., Bull, S. W., Clifford, B. A., & Wright, J. V. (1990). Subaqueous, Rhyolitic Dome-Top Tuff Cones: A Model Based on the Devonian Bunga Beds, Southeastern Australia and a Modern Analogue. *Bulletin of Volcanology*, 52(3), 159-174. doi:10.1007/BF00334802
- Cas, R. A. F., Porritt, L., Pittari, A., & Hayman, P. C. (2009). A Practical Guide to Terminology for Kimberlite Facies: A Systematic Progression from Descriptive to Genetic, Including a Pocket Guide. *Lithos*, 112, 183-190. doi:10.1016/j.lithos.2009.03.051
- Cas, R. A. F., & Simmons, J. M. (2018). Why Deep-Water Eruptions Are So Different from Subaerial Eruptions. *Frontiers in Earth Science*, 6. doi:10.3389/feart.2018.00198
- Cas, R. A. F., & Wright, J. V. (1987). *Volcanic Successions, Modern and Ancient: A Geological Approach to Processes, Products, and Successions*: London; Boston: Allen & Unwin/Chapman & Hall.
- Castaing, C., Bila, M., Milési, J.-P., Thiéblemont, D., Le Metour, J., Egal, E., . . . Zunino, C. (2003). *Notice Explicative De La Carte Géologique Et Minière Du Burkina Faso À 1/1000 000*.

Cawood, P. A., Hawkesworth, C. J., & Dhuime, B. (2013). The Continental Record and the Generation of Continental Crust. *Geological Society of America Bulletin*, 125(1-2), 14-32. doi:10.1130/b30722.1

Cawood, P. A., Kröner, A., & Pisarevsky, S. (2006). Precambrian Plate Tectonics: Criteria and Evidence. *GSA Today*, 16(7), 4. doi:10.1130/gsat01607.1

Cawthorn, R. G., & Ashwal, L. D. (2009). Origin of Anorthosite and Magnetitite Layers in the Bushveld Complex, Constrained by Major Element Compositions of Plagioclase. *Journal of Petrology*, 50(9), 1607-1637.

Chauvel, C., Dupré, B., & Jenner, G. A. (1985). The Sm-Nd Age of Kambalda Volcanics Is 500 Ma Too Old! *Earth and Planetary Science Letters*, 74(4), 315-324. doi:10.1016/S0012-821X(85)80003-0

Cherniak, D. J. (1993). Lead Diffusion in Titanite and Preliminary Results on the Effects of Radiation Damage on Pb Transport. *Chemical geology*, 110(1-3), 177-194. Retrieved from [https://doi.org/10.1016/0009-2541\(93\)90253-F](https://doi.org/10.1016/0009-2541(93)90253-F)

Chorlton, L. B. (2007). *Generalized Geology of the World: Bedrock Domains and Major Faults in Gis Format: A Small-Scale World Geology Map with an Extended Geological Attribute Database*.

Ciborowski, T. J. R., Minifie, M. J., Kerr, A. C., Ernst, R. E., Baragar, B., & Millar, I. L. (2017). A Mantle Plume Origin for the Palaeoproterozoic Circum-Superior Large Igneous Province. *Precambrian Research*, 294, 189-213. doi:10.1016/j.precamres.2017.03.001

Condie, K. (2013). Preservation and Recycling of Crust During Accretionary and Collisional Phases of Proterozoic Orogens: A Bumpy Road from Nuna to Rodinia. *Geosciences*, 3(2), 240-261. doi:10.3390/geosciences3020240

Condie, K. (2015). Changing Tectonic Settings through Time: Indiscriminate Use of Geochemical Discriminant Diagrams. *Precambrian Research*, 266, 587-591. Retrieved from <http://www.sciencedirect.com/science/article/pii/S0301926815001448>

Condie, K. C. (1976). Trace-Element Geochemistry of Archean Greenstone Belts. *Earth-Science Reviews*, 12(4), 393-417. doi:10.1016/0012-8252(76)90012-X

Condie, K. C. (1994). Greenstones through Time. In K. C. Condie (Ed.), *Archean Crustal Evolution*: Elsevier, Amsterdam.

Condie, K. C. (2005). High Field Strength Element Ratios in Archean Basalts: A Window to Evolving Sources of Mantle Plumes? *Lithos*, 79(3-4), 491-504. doi:10.1016/j.lithos.2004.09.014

Condie, K. C. (2016). A Planet in Transition: The Onset of Plate Tectonics on Earth between 3 and 2 Ga? *Geoscience Frontiers*. doi:10.1016/j.gsf.2016.09.001

Condie, K. C., Aster, R. C., & van Hunen, J. (2016). A Great Thermal Divergence in the Mantle Beginning 2.5 Ga: Geochemical Constraints from Greenstone Basalts and Komatiites. *Geoscience Frontiers*, 7(4), 543-553. doi:10.1016/j.gsf.2016.01.006

Condie, K. C., Bickford, M. E., Aster, R. C., Belousova, E., & Scholl, D. W. (2011). Episodic Zircon Ages, Hf Isotopic Composition, and the Preservation Rate of Continental Crust. *Geological Society of America Bulletin*, 123(5-6), 951-957. doi:10.1130/b30344.1

Condie, K. C., & O'Neill, C. (2011). The Archean-Proterozoic Boundary: 500 My of Tectonic Transition in Earth History. *American Journal of Science*, 310(9), 775-790. doi:10.2475/09.2010.01

Condie, K. C., & Shearer, C. K. (2017). Tracking the Evolution of Mantle Sources with Incompatible Element Ratios in Stagnant-Lid and Plate-Tectonic Planets. *Geochimica et Cosmochimica Acta*, 213, 47-62. doi:10.1016/j.gca.2017.06.034

Corfu, F., & Stone, D. (1998). The Significance of Titanite and Apatite U-Pb Ages: Constraints for the Post-Magmatic Thermal-Hydrothermal Evolution of a Batholithic Complex, Berens River Area, Northwestern Superior Province, Canada. *Geochimica et Cosmochimica Acta*, 62(17), 2979-29995. Retrieved from [https://doi.org/10.1016/S0016-7037\(98\)00225-7](https://doi.org/10.1016/S0016-7037(98)00225-7)

Cox, K., Bell, J., & Pankhurst, R. (1979). *The Interpretation of Igneous Rocks*, George Allen and Unwin: London.

Dabo, M., Aïfa, T., Gning, I., Faye, M., Ba, M. F., & Ngom, P. M. (2017). Lithological Architecture and Petrography of the Mako Birimian Greenstone Belt, Kédougou-Kéniéba Inlier, Eastern Senegal. *Journal of African Earth Sciences*, 131, 128-144. doi:10.1016/j.jafrearsci.2017.04.005

Dampare, S. B., Shibata, T., Asiedu, D., Okano, O., Manu, J., & Sakyi, P. (2009). Sr-Nd Isotopic Compositions of Paleoproterozoic Metavolcanic Rocks from the Southern Ashanti Volcanic Belt, Ghana. *Okayama University Earth Science Report*, 16(1), 9-28.

Dampare, S. B., Shibata, T., Asiedu, D. K., Osae, S., & Banoeng-Yakubo, B. (2008). Geochemistry of Paleoproterozoic Metavolcanic Rocks from the Southern Ashanti Volcanic Belt, Ghana: Petrogenetic and Tectonic Setting Implications. *Precambrian Research*, 162(3-4), 403-423. doi:10.1016/j.precamres.2007.10.001

Davies, G. F. (1992). On the Emergence of Plate Tectonics. *Geology*, 20(11), 963-966. Retrieved from <http://geology.gsapubs.org/content/20/11/963.abstract>. doi:10.1130/0091-7613(1992)020<0963:oteopt>2.3.co;2

Davis, D. W., Hirdes, W., Schaltegger, U., & Nunoo, E. A. (1994). U-Pb Age Constraints on Deposition and Provenance of Birimian and Gold-Bearing Tarkwaian Sediments in Ghana, West Africa. *Precambrian Research*, 67(1-2), 89-107. doi:10.1016/0301-9268(94)90006-X

de Kock, G. S., Armstrong, R. A., Siegfried, H. P., & Thomas, E. (2011). Geochronology of the Birim Supergroup of the West African Craton in the Wa-Bolé Region of West-Central Ghana: Implications for the Stratigraphic Framework. *Journal of African Earth Sciences*, 59(1), 1-40. Retrieved from <http://www.sciencedirect.com/science/article/pii/S1464343X10001470>. doi: <https://doi.org/10.1016/j.jafrearsci.2010.08.001>

de Wit, M. J. (2004). Archean Greenstone Belts Do Contain Fragments of Ophiolites. In T. M. Kusky (Ed.), *Precambrian Ophiolites and Related Rocks* (Vol. 13, pp. 599-614.): Elsevier.

de Wit, M. J., & Ashwal, L. D. (1995). Greenstone Belts: What Are They? [Article]. *South African Journal of Geology*, 98(4), 505. Retrieved from <http://gateway.library.qut.edu.au/login?url=http://search.ebscohost.com/login.aspx?direct=true&AuthType=ip,url,uid&db=afh&AN=9709171822&site=ehost-live&scope=site>

DePaolo, D. J., Linn, A. M., & Schubert, G. (1991). The Continental Crustal Age Distribution: Methods of Determining Mantle Separation Ages from Sm-Nd Isotopic Data and Application to the Southwestern United States. *Journal of Geophysical Research*, 96(B2). doi:10.1029/90jb02219

DePaolo, D. J., & Wasserburg, G. J. (1976). Nd Isotopic Variations and Petrogenetic Models. 3(5), 249-252. Retrieved from <https://agupubs.onlinelibrary.wiley.com/doi/abs/10.1029/GL003i005p00249>. doi:10.1029/GL003i005p00249

Dilek, Y., & Furnes, H. (2011). Ophiolite Genesis and Global Tectonics: Geochemical and Tectonic Fingerprinting of Ancient Oceanic Lithosphere. *Geological*

Society of America Bulletin, 123(3-4), 387-411. Retrieved from <http://gsabulletin.gsapubs.org/content/123/3-4/387.abstract>. doi:10.1130/b30446.1

Doublier, M. P., Purdy, D. J., Hegarty, R., Nicoll, M. G., & Zwingmann, H. (2018). Structural Elements of the Southern Thomson Orogen (Australian Tasmanides): A Tale of Megafolds. *Australian Journal of Earth Sciences*, 65(7-8), 943-966. doi:10.1080/08120099.2018.1526213

Doumbia, S., Pouclet, A., Kouamelan, A., Peucat, J. J., Vidal, M., & Delor, C. (1998). Petrogenesis of Juvenile-Type Birimian (Paleoproterozoic) Granitoids in Central Côte-D'Ivoire, West Africa: Geochemistry and Geochronology. *Precambrian Research*, 87(1), 33-63. Retrieved from <http://www.sciencedirect.com/science/article/pii/S0301926897002015>. doi:10.1016/S0301-9268(97)00201-5

Egal, E., Thiéblemont, D., Lahondère, D., Guerrot, C., Costea, C. A., Iliescu, D., . . . Kolié, P. (2002). Late Eburnean Granitization and Tectonics Along the Western and Northwestern Margin of the Archean Kénéma-Man Domain (Guinea, West African Craton). *Precambrian Research*, 117(1-2), 57-84. Retrieved from <http://www.sciencedirect.com/science/article/pii/S0301926802000608> doi:10.1016/S0301-9268(02)00060-8

Ennih, N., & Liégeois, J. P. (2008). *The Boundaries of the West African Craton, with Special Reference to the Basement of the Moroccan Metacratonic Anti-Atlas Belt.* (Vol. 297): Geological Society, London, Special Publications.

Ewart, A., Marsh, J. S., Milner, S. C., Duncan, A. R., Kamber, B. S., & Armstrong, R. A. (2004). Petrology and Geochemistry of Early Cretaceous Bimodal Continental Flood Volcanism of the Nw Etendeka, Namibia. Part 1: Introduction, Mafic Lavas and Re-Evaluation of Mantle Source Components. *Journal of Petrology*, 45(1), 59-105. doi:10.1093/petrology/egg083

Feybesse, J.-L., Billa, M., Guerrot, C., Duguey, E., Lescuyer, J.-L., Milesi, J.-P., & Bouchot, V. (2006). The Paleoproterozoic Ghanaian Province: Geodynamic Model and Ore Controls, Including Regional Stress Modeling. *Precambrian Research*, 149(3-4), 149-196. doi:10.1016/j.precamres.2006.06.003

Fisher, R. V. (1984). Submarine Volcaniclastic Rocks *Geological Society, London, Special Publications*(16), 5-27. doi:10.1144/GSL.SP.1984.016.01.02

Fitton, J. G., Mahoney, J. J., Wallace, P. J., & Saunders, A. D. (2004). Leg 192 Synthesis: Origin and Evolution of the Ontong Java Plateau. In J. G. Fitton, J. J. Mahoney, P. J. Wallace & A. D. Saunders (Eds.), *Proceedings of the Ocean Drilling Program* (Vol. 192, pp. 1-8): Scientific Results.

Folk, R. (1974). Petrology of Sedimentary Rocks: Austin, Texas, Hemphill Pub. Co, 182p.

Frey, F. A., Coffin, M. F., Wallace, P. J., Weis, D., Zhao, X., Wise Jr, S. W., . . . Antretter, M. (2000). Origin and Evolution of a Submarine Large Igneous Province: The Kerguelen Plateau and Broken Ridge, Southern Indian Ocean. *Earth and Planetary Science Letters*, 176(1), 73-89. Retrieved from [https://doi.org/10.1016/S0012-821X\(99\)00315-5](https://doi.org/10.1016/S0012-821X(99)00315-5)

Frey, F. A., Green, D. H., & Roy, S. D. (1978). Integrated Models of Basalt Petrogenesis: A Study of Quartz Tholeiites to Olivine Melilitites from South Eastern Australia Utilizing Geochemical and Experimental Petrological Data. *Journal of Petrology*, 19(3), 463-513. doi:10.1093/petrology/19.3.463

Frost, B. R., Chamberlain, K. R., & Schumacher, J. C. (2001). Sphene (Titanite): Phase Relations and Role as a Geochronometer. *Chemical geology*, 172(1-2). Retrieved from [https://doi.org/10.1016/S0009-2541\(00\)00240-0](https://doi.org/10.1016/S0009-2541(00)00240-0)

Furnes, H., de Wit, M., & Robins, B. (2013). A Review of New Interpretations of the Tectonostratigraphy, Geochemistry and Evolution of the Onverwacht Suite, Barberton Greenstone Belt, South Africa. *Gondwana Research*, 23(2), 403-428. Retrieved from <http://www.sciencedirect.com/science/article/pii/S1342937X12001839>. doi:10.1016/j.gr.2012.05.007

Furnes, H., Dilek, Y., & de Wit, M. (2015). Precambrian Greenstone Sequences Represent Different Ophiolite Types. *Gondwana Research*, 27(2), 649-685. doi:10.1016/j.gr.2013.06.004

Gale, A., Dalton, C. A., Langmuir, C. H., Su, Y., & Schilling, J.-G. (2013). The Mean Composition of Ocean Ridge Basalts. *Geochemistry, Geophysics, Geosystems*, 14(3), 489-518. doi:10.1029/2012gc004334

Gamal El Dien, H., Doucet, L. S., Murphy, J. B., & Li, Z. X. (2020). Geochemical Evidence for a Widespread Mantle Re-Enrichment 3.2 Billion Years Ago: Implications for Global-Scale Plate Tectonics. *Sci Rep*, 10(1), 9461. Retrieved from <https://www.ncbi.nlm.nih.gov/pubmed/32528085>. doi:10.1038/s41598-020-66324-y

Ganne, J., De Andrade, V., Weinberg, R. F., Vidal, O., Dubacq, B., Kagambega, N., . . . Allibon, J. (2011). Modern-Style Plate Subduction Preserved in the Palaeoproterozoic West African Craton. *Nature Geoscience*, 5(1), 60-65. doi:10.1038/ngeo1321

Ganne, J., & Feng, X. (2017). Primary Magmas and Mantle Temperatures through Time. *Geochemistry, Geophysics, Geosystems*, 18(3), 872-888. Retrieved from <http://dx.doi.org/10.1002/2016GC006787>. doi:10.1002/2016GC006787

Gasquet, D., Barbey, P., Adou, M., & Paquette, J. L. (2003). Structure, Sr–Nd Isotope Geochemistry and Zircon U–Pb Geochronology of the Granitoids of the Dabakala Area (Côte D’ivoire): Evidence for a 2.3 Ga Crustal Growth Event in the Palaeoproterozoic of West Africa? *Precambrian Research*, 127(4), 329–354. doi:10.1016/s0301-9268(03)00209-2

Gerya, T. (2014). Precambrian Geodynamics: Concepts and Models. *Gondwana Research*, 25(2), 442-463. doi:10.1016/j.gr.2012.11.008

Gill, R. (2010). *Igneous Rocks and Processes: A Practical Guide.*: John Wiley & Sons.

Gleeson, M. L. M., Stock, M. J., Pyle, D. M., Mather, T. A., Hutchison, W., Yirgu, G., & Wade, J. (2017). Constraining Magma Storage Conditions at a Restless Volcano in the Main Ethiopian Rift Using Phase Equilibria Models. *Journal of Volcanology and Geothermal Research*, 337, 44-61. doi:10.1016/j.jvolgeores.2017.02.026

Goldfarb, R. J., André-Mayer, A.-S., Jowitt, S. M., & Mudd, G. M. (2017). West Africa: The World’s Premier Paleoproterozoic Gold Province. *Economic Geology*, 112(1), 123-143. doi:10.2113/econgeo.112.1.123

Goldfarb, R. J., Groves, D. I., & Gardoll, S. (2001). Orogenic Gold and Geologic Time: A Global Synthesis. *Ore Geology Reviews*, 18(1–2), 1-75. Retrieved from <http://www.sciencedirect.com/science/article/pii/S0169136801000166>. doi:10.1016/S0169-1368(01)00016-6

Grachev, A. F., & Fedorovsky, V. S. (1981). On the Nature of Greenstone Belts in the Precambrian. *Tectonophysics*, 73(1–3), 195-212. Retrieved from <http://www.sciencedirect.com/science/article/pii/0040195181901840>. doi:10.1016/0040-1951(81)90184-0

Grant, J. A. (2005). Isocon Analysis: A Brief Review of the Method and Applications. *Physics and Chemistry of the Earth, Parts A/B/C*, 30(17), 997-1004. Retrieved from <http://www.sciencedirect.com/science/article/pii/S1474706505000458>. doi:10.1016/j.pce.2004.11.003

Greene, A. R., Scoates, J. S., Weis, D., Nixon, G. T., & Kieffer, B. (2009). Melting History and Magmatic Evolution of Basalts and Picrites from the Accreted Wrangellia Oceanic Plateau, Vancouver Island, Canada. *Journal of Petrology*, 50(3), 467-505. doi:10.1093/petrology/egp008

- Grenholm, M., Jessell, M., & Thébaud, N. (2019). A Geodynamic Model for the Paleoproterozoic (Ca. 2.27–1.96 Ga) Birimian Orogen of the Southern West African Craton – Insights into an Evolving Accretionary-Collisional Orogenic System. *Earth-Science Reviews*. doi:10.1016/j.earscirev.2019.02.006
- Griffiths, R. W., & Fink, J. H. (1992). Solidification and Morphology of Submarine Lavas: A Dependence on Extrusion Rate. *Journal of Geophysical Research*, 97(B13). doi:10.1029/92jb01594
- Grove, T. L., Holbig, E. S., Barr, J. A., Till, C. B., & Krawczynski, M. J. (2013). Melts of Garnet Lherzolite: Experiments, Models and Comparison to Melts of Pyroxenite and Carbonated Lherzolite. *Contributions to Mineralogy and Petrology*, 166(3), 887-910. doi:10.1007/s00410-013-0899-9
- Gualda, G. A. R., Ghiorso, M. S., Lemons, R. V., & Carley, T. L. (2012). Rhyolite-Melts: A Modified Calibration of Melts Optimized for Silica-Rich, Fluid-Bearing Magmatic Systems. *Journal of Petrology*, 53(5), 875-890. doi:10.1093/petrology/egr080
- Gueye, M., Ngom, P. M., Diène, M., Thiam, Y., Siegesmund, S., Wemmer, K., & Pawlig, S. (2008). Intrusive Rocks and Tectono-Metamorphic Evolution of the Mako Paleoproterozoic Belt (Eastern Senegal, West Africa). *Journal of African Earth Sciences*, 50(2-4), 88-110. doi:10.1016/j.jafrearsci.2007.09.013
- Gust, D. A., Arculus, R. J., & Kersting, A. B. (1997). Aspects of Magma Sources and Processes in the Honshu Arc. *The Canadian Mineralogist*, 35(2), 347-365.
- Hawkesworth, C., Cawood, P., & Dhuime, B. (2013). Continental Growth and the Crustal Record. *Tectonophysics*, 609, 651-660. doi:10.1016/j.tecto.2013.08.013
- Hawkesworth, C., Cawood, P. A., & Dhuime, B. (2018). Rates of Generation and Growth of the Continental Crust. *Geoscience Frontiers*. doi:10.1016/j.gsf.2018.02.004
- Hawkesworth, C. J., Dhuime, B., Pietranik, A. B., Cawood, P. A., Kemp, A. I. S., & Storey, C. D. (2010). The Generation and Evolution of the Continental Crust. *Journal of the Geological Society*, 167(2), 229-248. doi:10.1144/0016-76492009-072
- Hayden, L. A., Watson, E. B., & Wark, D. A. (2007). A Thermobarometer for Sphene (Titanite). *Contributions to Mineralogy and Petrology*, 155(4), 529-540. doi:10.1007/s00410-007-0256-y

Hayman, P. C., Cas, R. A. F., Squire, R. J., Campbell, I. A., Chen, M., & Doutch, D. (2019). Emplacement Origins of Coarsely-Crystalline Mafic Rocks Hosted in Greenstone Belts: Examples from the 2.7 Ga Yilgarn Craton, Western Australia. *Precambrian Research*, 324, 236-252. doi:10.1016/j.precamres.2019.01.023

Hayman, P. C., Fullard, R., Cas, R. A. F., & Squire, R. J. (2020). Clasts in Archean Conglomerates and Implications for Uplift: Evidence from the 2.7 ga Agnew Greenstone Belt (Western Australia). *Precambrian Research*, 344. doi:10.1016/j.precamres.2020.105758

Hayman, P. C., Hull, S. E., Cas, R. A. F., Summerhayes, E., Amelin, Y., Ivanic, T. J., & Price, D. (2015). A New Period of Volcanogenic Massive Sulfide Formation in the Yilgarn: A Volcanological Study of Theca 2.76 Ga Hollandaire Vms Deposit, Yilgarn Craton, Western Australia. *Australian Journal of Earth Sciences*, 62(2), 189-210. doi:10.1080/08120099.2015.1011399

Hayman, P. C., Thébaud, N., Pawley, M. J., Barnes, S. J., Cas, R. A. F., Amelin, Y., . . . Pegg, I. (2015). Evolution of a ~2.7ga Large Igneous Province: A Volcanological, Geochemical and Geochronological Study of the Agnew Greenstone Belt, and New Regional Correlations for the Kalgoorlie Terrane (Yilgarn Craton, Western Australia). *Precambrian Research*, 270, 334-368. doi:10.1016/j.precamres.2015.09.016

Hein, K. A., Morel, V., Kagoné, O., Kiemde, F., & Mayes, K. (2004). Birimian Lithological Succession and Structural Evolution in the Goren Segment of the Boromo–Goren Greenstone Belt, Burkina Faso. *Journal of African Earth Sciences*, 39(1-2), 1-23. doi:10.1016/j.jafrearsci.2004.05.003

Hein, K. A. A. (2010). Succession of Structural Events in the Goren Greenstone Belt (Burkina Faso): Implications for West African Tectonics. *Journal of African Earth Sciences*, 56(2–3), 83-94. Retrieved from <http://www.sciencedirect.com/science/article/pii/S1464343X09001083>. doi:10.1016/j.jafrearsci.2009.06.002

Hein, K. A. A. (2015). The Bagassi Gold Deposits on the Eastern Margin of the Houndé Greenstone Belt, Burkina Faso. *Ore Geology Reviews*. doi:10.1016/j.oregeorev.2015.10.028

Heinonen, J. S., Luttinen, A. V., Spera, F. J., & Bohrson, W. A. (2019). Deep Open Storage and Shallow Closed Transport System for a Continental Flood Basalt Sequence Revealed with Magma Chamber Simulator. *Contributions to Mineralogy and Petrology*, 174(11). doi:10.1007/s00410-019-1624-0

- Herzberg, C., & Asimow, P. D. (2015). Primelt3 Mega.Xlsm Software for Primary Magma Calculation: Peridotite Primary Magma Mgo Contents from the Liquidus to the Solidus. *Geochemistry, Geophysics, Geosystems*, 16(2), 563-578. doi:10.1002/2014gc005631
- Hickman, A. H. (2004). Two Contrasting Granite–Greenstone Terranes in the Pilbara Craton, Australia: Evidence for Vertical and Horizontal Tectonic Regimes Prior to 2900ma. *Precambrian Research*, 131(3-4), 153-172. doi:10.1016/j.precamres.2003.12.009
- Higgins, M. D., & Chandrasekharam, D. (2007). Nature of Sub-Volcanic Magma Chambers, Deccan Province, India: Evidence from Quantitative Textural Analysis of Plagioclase Megacrysts in the Giant Plagioclase Basalts. *Journal of Petrology*, 48(5), 885-900. doi:10.1093/petrology/egm005
- Hirdes, W., & Davis, D. W. (2002). U–Pb Geochronology of Paleoproterozoic Rocks in the Southern Part of the Kedougou-Kenieba Inlier, Senegal, West Africa: Evidence for Diachronous Accretionary Development of the Eburnean Province. *Precambrian Research*, 118(1), 83-99.
- Hirdes, W., Davis, D. W., Lüdtke, G., & Konan, G. (1996). Two Generations of Birimian (Paleoproterozoic) Volcanic Belts in Northeastern Côte D'ivoire (West Africa): Consequences for the ‘Birimian Controversy’. *Precambrian Research*, 80(3-4), 173-191. Retrieved from [https://doi.org/10.1016/S0301-9268\(96\)00011-3](https://doi.org/10.1016/S0301-9268(96)00011-3)
- Hofmann, A. W. (1997). Mantle Geochemistry: The Message from Oceanic Volcanism. *Nature*, 385(6613), 219-229. doi:10.1038/385219a0
- Hogan, J. P. (1993). Monomineralic Glomerocrysts: Textural Evidence for Mineral Resorption During Crystallization of Igneous Rocks. *The Journal of Geology*, 101(4), 531-540.
- Hole, M. J. (2018). Mineralogical and Geochemical Evidence for Polybaric Fractional Crystallization of Continental Flood Basalts and Implications for Identification of Peridotite and Pyroxenite Source Lithologies. *Earth-Science Reviews*, 176, 51-67. doi:10.1016/j.earscirev.2017.09.014
- Ishizuka, O., Kimura, J., Li, Y., Stern, R., Reagan, M., Taylor, R., . . . Hargroveiii, U. (2006). Early Stages in the Evolution of Izu–Bonin Arc Volcanism: New Age, Chemical, and Isotopic Constraints. *Earth and Planetary Science Letters*, 250(1-2), 385-401. doi:10.1016/j.epsl.2006.08.007

Jensen, L. S. (1976). *A New Cation Plot for Classifying Subalkalic Volcanic Rocks*: Ministry of Natural Resources.

Jerram, D. A. (2002). Volcanology and Facies Architecture of Flood Basalts. In M. A. Menzies, S. L. Klempner, C. J. Ebinger & J. Baker (Eds.), *Volcanic Rifted Margins* (Vol. 362, pp. 119-132).

Jessell, M., Santoul, J., Baratoux, L., Youbi, N., Ernst, R. E., Metelka, V., . . . Perrotouty, S. (2015). An Updated Map of West African Mafic Dykes. *Journal of African Earth Sciences*, 112, 440-450. doi:10.1016/j.jafrearsci.2015.01.007

Jochum, K. P., Weis, U., Schwager, B., Stoll, B., Wilson, S. A., Haug, G. H., . . . Enzweiler, J. (2016). Reference Values Following Iso Guidelines for Frequently Requested Rock Reference Materials. *Geostandards and Geoanalytical Research*, 40(3), 333-350. Retrieved from <https://doi.org/10.1111/j.1751-908X.2015.00392.x>

Kamber, B. S. (2011). Geochemistry and Secular Geochemical Evolution of the Earth's Mantle and Lower Crust,. In R. S. Harmon & A. Parker (Eds.), *Frontiers in Geochemistry* (pp. 1-19). Chichester, UK.: John Wiley & Sons, Ltd.

Kamber, B. S. (2015). The Evolving Nature of Terrestrial Crust from the Hadean, through the Archaean, into the Proterozoic. *Precambrian Research*, 258, 48-82. doi:10.1016/j.precamres.2014.12.007

Kerr, A. C., Marriner, G. F., Arndt, N. T., Tarney, J., Nivia, A., Saunders, A. D., & Duncan, R. A. (1996). The Petrogenesis of Gorgona Komatiites, Picrites and Basalts: New Field, Petrographic and Geochemical Constraints. *Lithos*, 37(2), 245-260. Retrieved from <https://www.sciencedirect.com/science/article/pii/0024493795000399>. doi:10.1016/0024-4937(95)00039-9

Kerr, A. C., White, R. V., & Saunders, A. D. (2000). Lip Reading: Recognizing Oceanic Plateaux in the Geological Record. *Journal of Petrology*, 41(7), 1041–1056. Retrieved from <https://doi.org/10.1093/petrology/41.7.1041>

Kerrich, R., & Polat, A. (2006). Archean Greenstone-Tonalite Duality: Thermochemical Mantle Convection Models or Plate Tectonics in the Early Earth Global Dynamics? *Tectonophysics*, 415(1-4), 141-165. doi:10.1016/j.tecto.2005.12.004

Khanna, T. C., Sesha Sai, V. V., Bizimis, M., & Krishna, A. K. (2015). Petrogenesis of Basalt–High-Mg Andesite–Adakite in the Neoarchean Veligallu Greenstone Terrane: Geochemical Evidence for a Rifted Back-Arc Crust in the Eastern Dharwar Craton, India. *Precambrian Research*, 258, 260-277. doi:10.1016/j.precamres.2015.01.004

- Kimura, J. I., Gill, J. B., van Keken, P. E., Kawabata, H., & Skora, S. (2017). Origin of Geochemical Mantle Components: Role of Spreading Ridges and Thermal Evolution of Mantle. *Geochemistry, Geophysics, Geosystems*, 18(2), 697-734. doi:10.1002/2016gc006696
- Kirkland, C. L., Fougerouse, D., Reddy, S. M., Hollis, J., & Saxe, D. W. (2018). Assessing the Mechanisms of Common Pb Incorporation into Titanite. *Chemical Geology*, 483, 558-566. doi:10.1016/j.chemgeo.2018.03.026
- Klein, E. L., Moura, C. A. V., & Pinheiro, B. L. S. (2005). Paleoproterozoic Crustal Evolution of the São Luís Craton, Brazil: Evidence from Zircon Geochronology and Sm-Nd Isotopes. *Gondwana Research*, 8(2), 177-186. doi:10.1016/s1342-937x(05)71116-3
- Koffi, Y. H., Djro, S. C., & Wenmenga, U. (2017). Lithostructural and Petrochemical Survey of Djarkadougou Gold Prospect (South West Burkina Faso / West Africa). *Earth Science Research*, 6(1), 155. doi:10.5539/esr.v6n1p155
- Koffi, Y. H., Wenmenga, U., & Djro, S. C. (2016). Tarkwaian Deposits of the Birimian Belt of Houndé: Petrological, Structural and Geochemical Study (Burkina-Faso, West Africa). *International Journal of Geosciences*, 07(05), 685-700. doi:10.4236/ijg.2016.75053
- Kohn, M. J. (2017). Titanite Petrochronology. *Reviews in Mineralogy and Geochemistry*, 83(1), 419-441. doi:10.2138/rmg.2017.83.13
- Korenaga, J. (2013). Initiation and Evolution of Plate Tectonics on Earth: Theories and Observations. *Annual Review of Earth and Planetary Sciences*, 41(1), 117-151. doi:10.1146/annurev-earth-050212-124208
- Korenaga, J. (2018). Crustal Evolution and Mantle Dynamics through Earth History. *Philos Trans A Math Phys Eng Sci*, 376(2132). Retrieved from <https://www.ncbi.nlm.nih.gov/pubmed/30275159>. doi:10.1098/rsta.2017.0408
- Kouamelan, A. N., Delor, C., & Peucat, J.-J. (1997). Geochronological Evidence for Reworking of Archean Terrains During the Early Proterozoic (2.1 Ga) in the Western Côte D'Ivoire (Man Rise-West African Craton). *Precambrian Research*, 86, 177-199.
- Kovalenko, V. I., Naumov, V. B., Girnis, A. V., Dorofeeva, V. A., & Yarmolyuk, V. V. (2010). Average Composition of Basic Magmas and Mantle Sources of Island Arcs and Active Continental Margins Estimated from the Data on Melt

Inclusions and Quenched Glasses of Rocks. *Petrology*, 18(1), 1-26.
doi:10.1134/s0869591110010017

Krapež, B., Standing, J. G., Brown, S. J. A., & Barley, M. E. (2008). Late Archaean Synorogenic Basins of the Eastern Goldfields Superterrane, Yilgarn Craton, Western Australia. *Precambrian Research*, 161(1-2), 154-182.
doi:10.1016/j.precamres.2007.06.017

Lange, A. E., Nielsen, R. L., Tepley, F. J., & Kent, A. J. R. (2013). The Petrogenesis of Plagioclase-Phyric Basalts at Mid-Ocean Ridges. *Geochemistry, Geophysics, Geosystems*, 14(8), 3282-3296. doi:10.1002/ggge.20207

Le Maitre, R., Streckeisen, A. L., Zanettin, B., Le Bas, M. J., Bonin, B., & Bateman, P. (2002). *Igneous Rocks: A Classification and Glossary of Terms: Recommendations of the International Union of Geological Sciences Subcommission on the Systematics of Igneous Rocks*. (2 ed.): Cambridge University Press.

Le Mignot, E., Reisberg, L., André-Mayer, A. S., Bourassa, Y., Fontaine, A., & Miller, J., 112(1), 145-168. (2017). Re-Os Geochronological Evidence for Multiple Paleoproterozoic Gold Events at the Scale of the West African Craton. *Economic Geology*, 112(1), 145-168. doi:10.2113/econgeo.112.1.145

Le Mignot, E., Siebenaller, L., Béziat, D., Salvi, S., AndrÉMayer, A.-S., Reisberg, L., . . . Franceschi, G. (2014). The Paleoproterozoic Copper-Gold Deposit of Gaoua, Burkina Faso: Evidence for a Polyphased Mineralization. *Acta Geologica Sinica - English Edition*, 88(s2), 970-972. doi:10.1111/1755-6724.12378_5

Le Pape, F., Jones, A. G., Jessell, M. W., Perrouty, S., Gallardo, L. A., Baratoux, L., . . . Boren, G. (2017). Crustal Structure of Southern Burkina Faso Inferred from Magnetotelluric, Gravity and Magnetic Data. *Precambrian Research*, 300, 261-272. doi:10.1016/j.precamres.2017.08.013

Lebrun, E., Thébaud, N., Miller, J., Ulrich, S., Bourget, J., & Terblanche, O. (2016). Geochronology and Lithostratigraphy of the Siguiri District: Implications for Gold Mineralisation in the Siguiri Basin (Guinea, West Africa). *Precambrian Research*, 274, 136-160. doi:10.1016/j.precamres.2015.10.011

Lee, C.-T. A., Luffi, P., Plank, T., Dalton, H., & Leeman, W. P. (2009). Constraints on the Depths and Temperatures of Basaltic Magma Generation on Earth and Other Terrestrial Planets Using New Thermobarometers for Mafic Magmas. *Earth and Planetary Science Letters*, 279(1-2), 20-33.
doi:10.1016/j.epsl.2008.12.020

- Leube, A., Hirdes, W., Mauer, R., & Kesse, G. O. (1990). The Early Proterozoic Birimian Supergroup of Ghana and Some Aspects of Its Associated Gold Mineralization. *Precambrian Research*, 46(1-2), 139-165.
- Loewen, M. W., Duncan, R. A., Kent, A. J. R., & Krawl, K. (2013). Prolonged Plume Volcanism in the Caribbean Large Igneous Province: New Insights from Curaçao and Haiti. *Geochemistry, Geophysics, Geosystems*, 14(10), 4241-4259. doi:10.1002/ggge.20273
- Lombo, M. (2009). Geodynamic Evolution of the 2.25-2.0 Ga Palaeoproterozoic Magmatic Rocks in the Man-Leo Shield of the West African Craton. A Model of Subsidence of an Oceanic Plateau. *Geological Society, London, Special Publications*, 323(1), 231-254. doi:10.1144/sp323.11
- Lombo, M. (2010). Paleoproterozoic Structural Evolution of the Man-Leo Shield (West Africa). Key Structures for Vertical to Transcurrent Tectonics. *Journal of African Earth Sciences*, 58(1), 19-36. doi:10.1016/j.jafrearsci.2010.01.005
- López-Moro, F. J. (2012). Easygresgrant—a Microsoft Excel Spreadsheet to Quantify Volume Changes and to Perform Mass-Balance Modeling in Metasomatic Systems. *Computers & Geosciences*, 39, 191-196. doi:10.1016/j.cageo.2011.07.014
- MacLean, W., & Barrett, T. (1993). Lithogeochemical Techniques Using Immobile Elements. *Journal of geochemical exploration*, 48(2), 109-133. doi:10.1016/0375-6742(93)90002-4
- Martí, J., Groppelli, G., & Brum da Silveira, A. (2018). Volcanic Stratigraphy: A Review. *Journal of Volcanology and Geothermal Research*, 357, 68-91. Retrieved from <http://www.sciencedirect.com/science/article/pii/S0377027317305577>. doi:10.1016/j.jvolgeores.2018.04.006
- McCuag, T. C., Fougerouse, D., Salvi, S., Siebenaller, L., Parra-Avila, L. A., Seed, R., . . . André-Mayer, A. S. (2016). The Inata Deposit, Belahouro District, Northern Burkina Faso. *Ore Geology Reviews*, 78, 639-644. doi:10.1016/j.oregeorev.2015.11.014
- McFarlane, H. B., Ailleres, L., Betts, P., Ganne, J., Baratoux, L., Jessell, M. W., & Block, S. (2019). Episodic Collisional Orogenesis and Lower Crust Exhumation During the Palaeoproterozoic Eburnean Orogeny: Evidence from the Sefwi Greenstone Belt, West African Craton. *Precambrian Research*, 325, 88-110. doi:10.1016/j.precamres.2019.02.012

McPhie, J., M., D., & R., A. (1993). *Volcanic Textures: A Guide to the Interpretation of Textures in Volcanic Rocks*. Centre for Ore Deposit and Exploration Studies.

Merabet, N.-e., Mahdjoub, Y., Henry, B., Abtout, A., Maouche, S., Kahoui, M., . . . Ayache, M. (2016). Paleoproterozoic Structural Frame of the Yetti Domain (Eglab Shield, Algeria): Emplacement Conditions of the Tinguicht Late Pluton from Magnetic Fabric Study. *Journal of African Earth Sciences*, 114, 158-173. doi:10.1016/j.jafrearsci.2015.11.018

Mériaud, N., Thébaud, N., Masurel, Q., Hayman, P., Jessell, M., Kemp, A., . . . Scott, P. M. (2020). Lithostratigraphic Evolution of the Bandamian Volcanic Cycle in Central Côte D'ivoire: Insights into the Late Eburnean Magmatic Resurgence and Its Geodynamic Implications. *Precambrian Research*, 347. doi:10.1016/j.precamres.2020.105847

Metelka, V., Baratoux, L., Naba, S., & Jessell, M. W. (2011). A Geophysically Constrained Litho-Structural Analysis of the Eburnean Greenstone Belts and Associated Granitoid Domains, Burkina Faso, West Africa. *Precambrian Research*, 190(1-4), 48-69. doi:10.1016/j.precamres.2011.08.002

Milési, J., Feybesse, J., Pinna, P., Deschamps, Y., Kampunzu, H., Muhongo, S., . . . Billa, M. (2004). Geological Map of Africa 1: 10,000,000, Sigafrigue Project. In *20th Conference of African Geology, BRGM, Orléans, France* (pp. 2-7).

Mueller, W., Chown, E. H., & Thurston, P. C. (2000). Processes in Physical Volcanology and Volcaniclastic Sedimentation: Modern and Ancient. *Precambrian Research*, 101(2-4), 81-85. Retrieved from <http://www.sciencedirect.com/science/article/pii/S0301926899000959>. doi:10.1016/S0301-9268(99)00095-9

Mueller, W., & Dimroth, E. (1987). A Terrestrial-Shallow Marine Transition in the Archean Opemisca Group East of Chapais, Quebec. *Precambrian Research*, 37(1), 29-55. Retrieved from [https://doi.org/10.1016/0301-9268\(87\)90038-6](https://doi.org/10.1016/0301-9268(87)90038-6)

Mueller, W. U., Garde, A. A., & Stendal, H. (2000). Shallow-Water, Eruption-Fed, Mafic Pyroclastic Deposits Along a Paleoproterozoic Coastline: Kangerluluk Volcano-Sedimentary Sequence, Southeast Greenland. *Precambrian Research*, 101(2-4), 163-192. Retrieved from <http://www.sciencedirect.com/science/article/pii/S030192689900087X>

Nanema, M., Wenmenga, U., & Ilboudo, H. (2017). Geochemical and Geodynamic Constraint of Tholeiitic Volcanism and Related Intrusions in the Kampti Gold District, Southwest Burkina Faso: Implication for Mineral Exploration. *Earth Science Research*, 7(1), 76. doi:10.5539/esr.v7n1p76

- Norman, M. D., & Garcia, M. O. (1999). Primitive Magmas and Source Characteristics of the Hawaiian Plume: Petrology and Geochemistry of Shield Picrites. *Earth and Planetary Science Letters*, 168, 27-44.
- Ogg, J. G., Ogg, G. M., & Gradstein, F. M. (2016). 3 - Precambrian. In J. G. Ogg, G. M. Ogg & F. M. Gradstein (Eds.), *A Concise Geologic Time Scale* (pp. 19-28): Elsevier.
- Ohta, T., & Arai, H. (2007). Statistical Empirical Index of Chemical Weathering in Igneous Rocks: A New Tool for Evaluating the Degree of Weathering. *Chemical Geology*, 240(3-4), 280-297. doi:10.1016/j.chemgeo.2007.02.017
- Olierook, H. K. H., Taylor, R. J. M., Erickson, T. M., Clark, C., Reddy, S. M., Kirkland, C. L., . . . Barham, M. (2019). Unravelling Complex Geologic Histories Using U-Pb and Trace Element Systematics of Titanite. *Chemical Geology*, 504, 105-122. doi:10.1016/j.chemgeo.2018.11.004
- Parra-Avila, L. A., Belousova, E., Fiorentini, M. L., Baratoux, L., Davis, J., Miller, J., & McCuaig, T. C. (2016). Crustal Evolution of the Paleoproterozoic Birimian Terranes of the Baoulé-Mossi Domain, Southern West African Craton: U-Pb and Hf-Isotope Studies of Detrital Zircons. *Precambrian Research*, 274, 25-60. Retrieved from <http://www.sciencedirect.com/science/article/pii/S0301926815002910>. doi: 10.1016/j.precamres.2015.09.005
- Patchett, J., Kouvo, O., Hedge, C. E., & Tatsumoto, M. (1982). Evolution of Continental Crust and Mantle Heterogeneity: Evidence from Hf Isotopes. *Contributions to Mineralogy and Petrology*, 78(3), 279-297. Retrieved from <https://doi.org/10.1007/BF00398923>. doi:10.1007/BF00398923
- Pawligr, S., Gueye, M., Klischies, R., Schwarz, S., Wemmer, K., & Siegfried, S. (2006). Geochemical and Sr-Nd Isotopic Data on the Birimian of the Kedougou-Kenieba Inlier (Eastern Senegal): Implications on the Palaeoproterozoic Evolution of the West African Craton. *SOUTH AFRICAN JOURNAL OF GEOLOGY, VOLUME 109, PAGE 411-427*.
- Pearce, J. A. (2008). Geochemical Fingerprinting of Oceanic Basalts with Applications to Ophiolite Classification and the Search for Archean Oceanic Crust. *Lithos*, 100(1-4), 14-48. doi:10.1016/j.lithos.2007.06.016
- Perkins, D., & Anthony, E. Y. (2011). The Evolution of Spinel Lherzolite Xenoliths and the Nature of the Mantle at Kilbourne Hole, New Mexico. *Contributions to Mineralogy and Petrology*, 162(6), 1139-1157. doi:10.1007/s00410-011-0644-1

Perrouty, S., Aillères, L., Jessell, M. W., Baratoux, L., Bourassa, Y., & Crawford, B. (2012). Revised Eburnean Geodynamic Evolution of the Gold-Rich Southern Ashanti Belt, Ghana, with New Field and Geophysical Evidence of Pre-Tarkwaian Deformations. *Precambrian Research*, 204-205, 12-39. doi:10.1016/j.precamres.2012.01.003

Petersson, A., Scherstén, A., & Gerdes, A. (2018). Extensive Reworking of Archaean Crust within the Birimian Terrane in Ghana as Revealed by Combined Zircon U-Pb and Lu-Hf Isotopes. *Geoscience Frontiers*, 9(1), 173-189. Retrieved from <http://www.sciencedirect.com/science/article/pii/S167498711730035X>. doi:10.1016/j.gsf.2017.02.006

Pigois, J.-P., Groves, D. I., Fletcher, I. R., McNaughton, N. J., & Snee, L. W. (2003). Age Constraints on Tarkwaian Palaeoplacer and Lode-Gold Formation in the Tarkwa-Damang District, SW Ghana. *Mineralium Deposita*, 38(6), 695-714. doi:10.1007/s00126-003-0360-5

Pin, C., & Zalduogui, S. F. J. (1997). Sequential Separation of Light Rare-Earth Elements, Thorium and Uranium by Miniaturized Extraction Chromatography: Application to Isotopic Analyses of Silicate Rocks. *Analytica Chimica Acta*, 339(1-2), 79-89.

Pohl, D., & Carlson, C. (1993). A Plate Tectonic Re-Interpretation of the 2.2–2.0 Ga Birimian Province, Tarkwaian System and Metallogenesis in West Africa. *Regional Trends in African Geology, Geol. Soc. Africa*, 378-381.

Polat, A., & Kerrich, R. (2001). Geodynamic Processes, Continental Growth, and Mantle Evolution Recorded in Late Archean Greenstone Belts of the Southern Superior Province, Canada. *Precambrian Research*, 112(1–2), 5-25. Retrieved from <http://www.sciencedirect.com/science/article/pii/S0301926801001681>. doi:10.1016/S0301-9268(01)00168-1

Polat, A., Wang, L., & Appel, P. W. U. (2015). A Review of Structural Patterns and Melting Processes in the Archean Craton of West Greenland: Evidence for Crustal Growth at Convergent Plate Margins as Opposed to Non-Uniformitarian Models. *Tectonophysics*, 662, 67-94. doi:10.1016/j.tecto.2015.04.006

Pouclet, A., Doumbia, S., & Vidal, M. (2006). Geodynamic Setting of the Birimian Volcanism in Central Ivory Coast (Western Africa) and Its Place in the Palaeoproterozoic Evolution of the Man Shield. *Bulletin de la Société Géologique de France*, 177(2), 105-121. Retrieved from <http://bsgf.geoscienceworld.org/content/gssgbull/177/2/105.full.pdf>. doi:10.2113/gssgbull.177.2.105

Reading, H. G. (1996). *Sedimentary Environments: Processes, Facies and Stratigraphy* (3rd ed.): Blackwell Science.

Reddy, S. M., & Evans, D. A. D. (2009). Palaeoproterozoic Supercontinents and Global Evolution: Correlations from Core to Atmosphere. *Geological Society, London, Special Publications*, 323(1), 1-26. doi:10.1144/sp323.1

Reimink, J. R., Davies, J. H. F. L., Chacko, T., Stern, R. A., Heaman, L. M., Sarkar, C., . . . Pearson, D. G. (2016). No Evidence for Hadean Continental Crust within Earth's Oldest Evolved Rock Unit. *Nature Geoscience*, 9(10), 777-780. Retrieved from <https://doi.org/10.1038/ngeo2786>. doi:10.1038/ngeo2786

Rey, P. F., Philippot, P., & Thébaud, N. (2003). Contribution of Mantle Plumes, Crustal Thickening and Greenstone Blanketing to the 2.75–2.65ga Global Crisis. *Precambrian Research*, 127(1-3), 43-60. doi:10.1016/s0301-9268(03)00179-7

Roddaz, M., Debat, P., & Nikiema, S. (2007). Geochemistry of Upper Birimian Sediments (Major and Trace Elements and Nd–Sr Isotopes) and Implications for Weathering and Tectonic Setting of the Late Paleoproterozoic Crust. *Precambrian Research*, 159(3-4), 197-211. doi:10.1016/j.precamres.2007.06.008

Rogers, R., Ross, P.-S., Goutier, J., & Mercier-Langevin, P. (2014). Using Physical Volcanology, Chemical Stratigraphy, and Pyrite Geochemistry for Volcanogenic Massive Sulfide Exploration: An Example from the Blake River Group, Abitibi Greenstone Belt. *Economic Geology*, 109(1), 61-88. doi: 10.2113/econgeo.109.1.61

Rosa, C. J. P., McPhie, J., Relvas, J. M. R. S., Pereira, Z., Oliveira, T., & Pacheco, N. (2008). Facies Analyses and Volcanic Setting of the Giant Neves Corvo Massive Sulfide Deposit, Iberian Pyrite Belt, Portugal. *Mineralium Deposita*, 43(4), 449-466. doi:10.1007/s00126-008-0176-4

Rubatto, D., & Hermann, J. (2001). Exhumation as Fast as Subduction? *Geology*, 29(1), 3-6.

Rudnick, R. L., & Gao, S. (2014). Composition of the Continental Crust. 1-51. doi:10.1016/b978-0-08-095975-7.00301-6

Sager, W. W., Sano, T., & Geldmacher, J. (2011). How Do Oceanic Plateaus Form? Clues from Drilling at Shatsky Rise. *Transactions American Geophysical Union*, 92(5), 37-44. doi:10.1029/2011EO050001

Saji, N. S., Wielandt, D., Paton, C., & Bizzarro, M. (2016). Ultra-High-Precision Nd-Isotope Measurements of Geological Materials by Mc-Icpms. *J Anal At Spectrom*, 31(7), 1490-1504. Retrieved from <https://www.ncbi.nlm.nih.gov/pubmed/27429505>. doi:10.1039/C6JA00064A

Sakyi, P. A., Su, B.-X., Anum, S., Kwayisi, D., Dampare, S. B., Anani, C. Y., & Nude, P. M. (2014). New Zircon U–Pb Ages for Erratic Emplacement of 2213–2130ma Paleoproterozoic Calc-Alkaline I-Type Granitoid Rocks in the Lawra Volcanic Belt of Northwestern Ghana, West Africa. *Precambrian Research*, 254, 149-168. doi:10.1016/j.precamres.2014.08.009

Saunders, A. D., Norry, M. J., & Tarney, J. (1988). Origin of Morb and Chemically-Depleted Mantle Reservoirs: Trace Element Constraints. *Journal of Petrology*, Volume Special_Volume(1), 415-445. doi:10.1093/petrology/Special_Volume.1.415

Schwartz, M. O., & Melcher, F. (2003). The Perkoa Zinc Deposit, Burkina Faso. *Economic Geology*, 98(7), 1463-1485. doi:10.2113/gsecongeo.98.7.1463

Scott, D. J., & St-Onge, M. R. (1995). Constraints on Pb Closure Temperature in Titanite Based on Rocks from the Ungava Orogen, Canada: Implications for U-Pb Geochronology and P-T-T Path Determinations. *Geology* 23(12), 1123-1126. Retrieved from [https://doi.org/10.1130/0091-7613\(1995\)023<1123:COPCTI>2.3.CO;2](https://doi.org/10.1130/0091-7613(1995)023<1123:COPCTI>2.3.CO;2)

Self, S., Thordarson, T., Keszthelyi, L., Walker, G. P. L., Hon, K., Murphy, M. T., . . . Finnemore, S. (1996). A New Model for the Emplacement of Columbia River Basalts as Large, Inflated Pahoehoe Lava Flow Fields. *Geophysical Research Letters*, 23(19), 2689-2692. doi:10.1029/96gl02450

Senyah, G. A., Dampare, S. B., & Asiedu, D. K. (2016). Geochemistry and Tectonic Setting of the Paleoproterozoic Metavolcanic Rocks from the Chirano Gold District, Sefwi Belt, Ghana. *Journal of African Earth Sciences*, 122, 32-46. doi:10.1016/j.jafrearsci.2015.07.022

Shanmugam, G. (1997). The Bouma Sequence and the Turbidite Mind Set. *Earth-Science Reviews*, 42(4), 201-229. Retrieved from [https://doi.org/10.1016/S0012-8252\(97\)81858-2](https://doi.org/10.1016/S0012-8252(97)81858-2)

Shervais, J. W. (2006). The Significance of Subduction-Related Accretionary Complexes in Early Earth Processes. *Geological Society of America Special Papers*, 405(173-192). doi:10.1130/2006.2405(10)

Sheth, H. (2016). Giant Plagioclase Basalts: Continental Flood Basalt–Induced Remobilization of Anorthositic Mushes in a Deep Crustal Sill Complex.

Smith, A. J. B., Henry, G., & Frost-Killian, S. (2016). A Review of the Birimian Supergroup- and Tarkwaian Group-Hosted Gold Deposits of Ghana. *Episodes*, 39(2), 177. doi:10.18814/epiugs/2016/v39i2/95775

Smithies, R. H., Champion, D. C., Van Kranendonk, M. J., Howard, H. M., & Hickman, A. H. (2005). Modern-Style Subduction Processes in the Mesoarchaean: Geochemical Evidence from the 3.12 Ga Whundo Intra-Oceanic Arc. *Earth and Planetary Science Letters*, 231(3-4), 221-237. doi:10.1016/j.epsl.2004.12.026

Smithies, R. H., Lu, Y., Kirkland, C. L., Johnson, T. E., Mole, D. R., Champion, D. C., . . . Johnson, S. P. (2021). Oxygen Isotopes Trace the Origins of Earth's Earliest Continental Crust. *Nature*, 592(7852), 70-75. Retrieved from <https://www.ncbi.nlm.nih.gov/pubmed/33790444>. doi:10.1038/s41586-021-03337-1

Sobolev, A. V., Hofmann, A. W., Kuzmin, D. V., Yaxley, G. M., Arndt, N. T., Chung, S. L., . . . Teklay, M. (2007). The Amount of Recycled Crust in Sources of Mantle-Derived Melts. *Science*, 316(5823), 412-417.

Stacey, J. S., & Kramers, J. D. (1975). Approximation of Terrestrial Lead Isotope Evolution by a Two-Stage Model. *Earth and Planetary Science Letters*, 26(2), 207-221. Retrieved from [https://doi.org/10.1016/0012-821X\(75\)90088-6](https://doi.org/10.1016/0012-821X(75)90088-6)

Stearns, M. A., Hacker, B. R., Ratschbacher, L., Rutte, D., & Kylander-Clark, A. R. C. (2015). Titanite Petrochronology of the Pamir Gneiss Domes: Implications for Middle to Deep Crust Exhumation and Titanite Closure to Pb and Zr Diffusion. *Tectonics*, 34(4), 784-802. doi:10.1002/2014tc003774

Stern, R. A., Syme, E. C., & Lucas, S. B. (1995). Geochemistry of 1.9 Ga Morb- and Oib-Like Basalts from the Amisk Collage, Flin Flon Belt, Canada: Evidence for an Intra-Oceanic Origin. *Geochemica et Cosmochimica Acta*, 59(15), 3131-3154. Retrieved from [https://doi.org/10.1016/0016-7037\(95\)00202-B](https://doi.org/10.1016/0016-7037(95)00202-B)

Stern, R. J. (2002). Subduction Zones. *Reviews of Geophysics*, 40(4). doi:10.1029/2001rg000108

Stern, R. J. (2005). Evidence from Ophiolites, Blueschists, and Ultrahigh-Pressure Metamorphic Terranes That the Modern Episode of Subduction Tectonics Began in Neoproterozoic Time. *Geology*, 33(7), 557. doi:10.1130/g21365.1

Stern, R. J., & Gerya, T. (2018). Subduction Initiation in Nature and Models: A Review. *Tectonophysics*, 746, 173-198. doi:10.1016/j.tecto.2017.10.014

Stewart, A. L., & McPhie, J. (2006). Facies Architecture and Late Pliocene - Pleistocene Evolution of a Felsic Volcanic Island, Milos, Greece. *Bulletin of Volcanology*, 68(7-8), 703-726. Retrieved from ProQuest Central. doi: 10.1007/s00445-005-0045-2

Storey, C. D., Jeffries, T. E., & Smith, M. (2006). Common Lead-Corrected Laser Ablation Icp-Ms U-Pb Systematics and Geochronology of Titanite. *Chemical Geology*, 227(1-2), 37-52. doi:10.1016/j.chemgeo.2005.09.003

Stracke, A. (2016). Mantle Geochemistry. In: White W. (Eds) Encyclopedia of Geochemistry. In *Encyclopedia of Earth Sciences* (pp. 1-12).

Stracke, A., Hofmann, A. W., & Hart, S. R. (2005). Fozo, Himu, and the Rest of the Mantle Zoo. *Geochemistry, Geophysics, Geosystems*, 6(5). doi:10.1029/2004gc000824

Sun, J., Yang, J., Wu, F., Xie, L., Yang, Y., Liu, Z., & Li, X. (2012). In Situ U-Pb Dating of Titanite by La-Icpms. *Chinese Science Bulletin*, 57(20), 2506-2516. doi:10.1007/s11434-012-5177-0

Sun, S. s., & McDonough, W. F. (1989). Chemical and Isotopic Systematics of Oceanic Basalts: Implications for Mantle Composition and Processes. *Geological Society, London, Special Publications*, 42(1), 313-345. doi:10.1144/gsl.sp.1989.042.01.19

Swager, C. P. (1997). Tectono-Stratigraphy of Late Archaean Greenstone Terranes in the Southern Eastern Goldfields, Western Australia. *Precambrian Research*, 83(1), 11-42. Retrieved from <http://www.sciencedirect.com/science/article/pii/S030192689700003X>. doi: 10.1016/S0301-9268(97)00003-X

Sylvester, P. J., & Attoh, K. (1992). Lithostratigraphy and Composition of 2.1 Ga Greenstone Belts of the West African Craton and Their Bearing on Crustal Evolution and the Archean-Proterozoic Boundary. *The Journal of Geology*, 100(4), 377-393. doi:<http://www.jstor.org/stable/30065738>

Tapsoba, B., Lo, C. H., Jahn, B. M., Chung, S. L., Wenmenga, U., & Izuka, Y. (2013). Chemical and Sr-Nd Isotopic Compositions and Zircon U-Pb Ages of the Birimian Granitoids from Ne Burkina Faso, West African Craton: Implications on the Geodynamic Setting and Crustal Evolution. *Precambrian Research*, 224, 364-396.

- Taylor, P. N., Moorbath, S., Leube, A., & Hirdes, W. (1992). Early Proterozoic Crustal Evolution in the Birimian of Ghana: Constraints from Geochronology and Isotope Geochemistry. *Precambrian Research*, 56(1), 97-111. Retrieved from <http://www.sciencedirect.com/science/article/pii/0301926892900864>. doi:[https://doi.org/10.1016/0301-9268\(92\)90086-4](https://doi.org/10.1016/0301-9268(92)90086-4)
- Thurston, P. C. (2002). Autochthonous Development of Superior Province Greenstone Belts? *Precambrian Research*, 115(1-4), 11-36. doi:10.1016/s0301-9268(02)00004-9
- Thurston, P. C. (2015). Igneous Rock Associations 19. Greenstone Belts and Granite-Greenstone Terranes: Constraints on the Nature of the Archean World. *Geoscience Canada*, 42(4), 437. doi:10.12789/geocanj.2015.42.081
- Thurston, P. C., Ayer, J. A., Goutier, J., & Hamilton, M. A. (2008). Depositional Gaps in Abitibi Greenstone Belt Stratigraphy: A Key to Exploration for Syngenetic Mineralization. *Economic Geology*, 103(6), 1097-1134. doi:<https://doi.org/10.2113/gsecongeo.103.6.1097>
- Till, C. B. (2017). A Review and Update of Mantle Thermobarometry for Primitive Arc Magmas. *American Mineralogist*. doi:10.2138/am-2017-5783
- Tshibubudze, A., Hein, K. A. A., & McCuaig, T. C. (2015). The Relative and Absolute Chronology of Strato-Tectonic Events in the Gorom-Gorom Granitoid Terrane and Oudalan-Gorouol Belt, Northeast Burkina Faso. *Journal of African Earth Sciences*, 112, 382-418. doi:10.1016/j.jafrearsci.2015.04.008
- Valer, M., Bachèlery, P., & Schiano, P. (2017). The Petrogenesis of Plagioclase-Ultraphyric Basalts from La Réunion Island. *Journal of Petrology*, 58(4), 675-698. doi:10.1093/petrology/egx030
- van Hunen, J., van Keken, P. E., Hynes, A., & Davies, G. F. (2008). Tectonics of Early Earth: Some Geodynamic Considerations. In K. C. Condie & V. Pease (Eds.), *When Did Plate Tectonics Begin on Planet Earth?* (Vol. 440, pp. 157–171): The Geological Society of America.
- Van Kranendonk, M. J. (2007). Chapter 8.6 Tectonics of Early Earth. *Developments in Precambrian Geology*, 15, 1105-1116. doi:10.1016/s0166-2635(07)15086-6
- Van Kranendonk, M. J. (2011). Onset of Plate Tectonics. *Science*, 333(6041), 413-414. Retrieved from <http://www.jstor.org.ezp01.library.qut.edu.au/stable/27978276>

Van Kranendonk, M. J., Ivanic, T. J., Wingate, M. T. D., Kirkland, C. L., & Wyche, S. (2013). Long-Lived, Autochthonous Development of the Archean Murchison Domain, and Implications for Yilgarn Craton Tectonics. *Precambrian Research*, 229, 49-92. doi:10.1016/j.precamres.2012.08.009

Van Kranendonk, M. J., Smithies, R. H., Griffin, W. L., Huston, D. L., Hickman, A. H., Champion, D. C., . . . Pirajno, F. (2014). Making It Thick: A Volcanic Plateau Origin of Palaeoarchean Continental Lithosphere of the Pilbara and Kaapvaal Cratons. *Geological Society, London, Special Publications*, 389(1), 83-111. doi:10.1144/sp389.12

Vanderhaeghe, O., Ledru, P., Thiéblemont, D., Egal, E., Cocherie, A., Tegyey, M., & Milési, J.-P. (1998). Contrasting Mechanism of Crustal Growth Geodynamic Evolution of the Paleoproterozoic Granite–Greenstone Belts of French Guiana. *Precambrian Research* 92, 165–193.

Vearncombe, J. R., Barton Jr, J. M., Van Reenen, D. D., Phillips, G. N., & Wilson, A. H. (1986). Greenstone Belts: Their Components and Structure. In *Workshop on Tectonic Evolution of Greenstone Belts*, 214-220.

Vermeesch, P. (2018). Isoplotr: A Free and Open Toolbox for Geochronology. *Geoscience Frontiers*, 9(5), 1479-1493. doi:10.1016/j.gsf.2018.04.001

Vidal, M., & Alric, G. (1994). The Palaeoproterozoic (Birimian) of Haute-Comoé in the West African Craton, Ivory Coast: A Transtensional Back-Arc Basin. *Precambrian Research*, 65(1), 207-229.

Vidal, M., Gumiaux, C., Cagnard, F., Pouclet, A., Ouattara, G., & Pichon, M. (2009). Evolution of a Paleoproterozoic “Weak Type” Orogeny in the West African Craton (Ivory Coast). *Tectonophysics*, 477(3-4), 145-159. doi:10.1016/j.tecto.2009.02.010

Villiger, S. (2004). The Liquid Line of Descent of Anhydrous, Mantle-Derived, Tholeiitic Liquids by Fractional and Equilibrium Crystallization--an Experimental Study at 1.0 Gpa. *Journal of Petrology*, 45(12), 2369-2388. doi:10.1093/petrology/egh042

Vogel, T. A., Hidalgo, P. J., Patino, L., Tefend, K. S., & Ehrlich, R. (2008). Evaluation of Magma Mixing and Fractional Crystallization Using Whole-Rock Chemical Analyses: Polytopic Vector Analyses. *Geochemistry, Geophysics, Geosystems*, 9(4), n/a-n/a. doi:10.1029/2007gc001790

Wane, O., Liégeois, J.-P., Thébaud, N., Miller, J., Metelka, V., & Jessell, M. (2018). The Onset of the Eburnean Collision with the Kenema-Man Craton Evidenced by Plutonic and Volcanosedimentary Rock Record of the Masssigui Region,

- Waters, C. L., Sims, K. W. W., Perfit, M. R., Blichert-Toft, J., & Blusztajn, J. (2011). Perspective on the Genesis of E-MORB from Chemical and Isotopic Heterogeneity at 9–10°N East Pacific Rise. *Journal of Petrology*, 52(3), 565–602. doi:10.1093/petrology/egq091
- Whattam, S. A. (2018). Primitive Magmas in the Early Central American Volcanic Arc System Generated by Plume-Induced Subduction Initiation. *Frontiers in Earth Science*, 6. doi:10.3389/feart.2018.00114
- White, R. V., Tarney, J., Kerr, A. C., Saunders, A. D., Kempton, P. D., Pringle, M. S., & Klaver, G. T. (1999). Modification of an Oceanic Plateau, Aruba, Dutch Caribbean: Implications for the Generation of Continental Crust. *Lithos*, 46(1), 43–68. Retrieved from [https://doi.org/10.1016/S0024-4937\(98\)00061-9](https://doi.org/10.1016/S0024-4937(98)00061-9)
- White, W. M. (2015). Probing the Earth's Deep Interior through Geochemistry. *Geochemical Perspectives*, 4(2), 95–96. Retrieved from <http://perspectives.geoscienceworld.org/gsgp/4/2/95.full.pdf>
- Willbold, M., & Stracke, A. (2006). Trace Element Composition of Mantle End-Members: Implications for Recycling of Oceanic and Upper and Lower Continental Crust. *Geochemistry, Geophysics, Geosystems*, 7(4). doi:10.1029/2005gc001005
- Wilson, J. T. (1969). Aspects of the Different Mechanics of Ocean Floors and Continents. *Tectonophysics*, 8(4), 281–284.
- Windley, B. F. (1984). The Archaean-Proterozoic Boundary. *Tectonophysics*, 105(1), 43–53. Retrieved from <http://www.sciencedirect.com/science/article/pii/0040195184901938>. doi: 10.1016/0040-1951(84)90193-8
- Windley, B. F. (2003). Continental Growth in the Proterozoic: A Global Perspective. *Geological Society, London, Special Publications*, 206(1), 23–33. doi:10.1144/gsl.sp.2003.206.01.03
- Wolff, J. A., Ramos, F. C., Hart, G. L., Patterson, J. D., & Brandon, A. D. (2008). Columbia River Flood Basalts from a Centralized Crustal Magmatic System. *Nature Geoscience*, 1(3), 177–180. doi:10.1038/ngeo124

Workman, R. K., & Hart, S. R. (2005). Major and Trace Element Composition of the Depleted Morb Mantle (Dmm). *Earth and Planetary Science Letters*, 231(1-2), 53-72. doi:10.1016/j.epsl.2004.12.005

Wright, J. E., & Wyld, S. J. (2011). Late Cretaceous Subduction Initiation on the Eastern Margin of the Caribbean-Colombian Oceanic Plateau: One Great Arc of the Caribbean (?). *Geosphere*, 7(2), 468-493. doi:10.1130/ges00577.1

Wyman, D. (2020). Komatiites from Mantle Transition Zone Plumes. *Frontiers in Earth Science*, 8. doi:10.3389/feart.2020.540744

Xu, Y., Mei, H., Xu, J., Huang, X., Wang, Y., & Chung, S.-L. (2003). Origin of Two Differentiation Trends in the Emeishan Flood Basalts. *Chinese Science Bulletin*, 48, 390-394. doi:10.1007/bf03183236

Yan, J., Ballmer, M. D., & Tackley, P. J. (2020). The Evolution and Distribution of Recycled Oceanic Crust in the Earth's Mantle: Insight from Geodynamic Models. *Earth and Planetary Science Letters*, 537. doi:10.1016/j.epsl.2020.116171

Yang, A. Y., Zhao, T. P., Zhou, M. F., & Deng, X. G. (2017). Isotopically Enriched N-MORB: A New Geochemical Signature of Off-Axis Plume-Ridge Interaction-a Case Study at 50°28'E, Southwest Indian Ridge. *Journal of Geophysical Research: Solid Earth*, 122(1), 191-213. doi:10.1002/2016jb013284

Yoder Jr, H. S., & Tilley, C. E. (1962). Origin of Basalt Magmas: An Experimental Study of Natural and Synthetic Rock Systems. . *Journal of Petrology*, 3(3), 342-532.

Zhang, L., Chu, X., Zhang, L., Fu, B., Bader, T., Du, J., & Li, X. (2018). The Early Exhumation History of the Western Tianshan Uhp Metamorphic Belt, China: New Constraints from Titanite U-Pb Geochronology and Thermobarometry. *Journal of Metamorphic Geology*, 36(5), 631-651. doi:10.1111/jmg.12422

Zhao, G., Sun, M., Wilde, S. A., Li, S., & Zhang, J. (2006). Some Key Issues in Reconstructions of Proterozoic Supercontinents. *Journal of Asian Earth Sciences*, 28(1), 3-19. doi:10.1016/j.jseaes.2004.06.010

Zhao, J.-x., & McCulloch, M. T. (1993). Sm-Nd Mineral Isochron Ages of Late Proterozoic Dyke Swarms in Australia: Evidence for Two Distinctive Events of Mafic Magmatism and Crustal Extension. *Chemical geology*, 109(1-4), 341-354.

Appendices

Appendix A: Chapter 3

Table A- 1 Sample and outcrop lithological classification and location

Field site	Sample ID	Lithology	Eastern	Northing
1	GS_001	Gabbro	439772	1235597
3	GS_002	Micaceous Schist	455349	1226289
4		Micaceous Schist	455026	1226460
5	GS_003	Gabbro	455335	1226307
6	GS_004	Ultramafic Lithofacies	454739	1228921
7	GS_005	Aphyric Basalt	454742	1231152
8	GS_006	Aphyric Basalt	454497	1231131
9		Aphyric Basalt	454421	1231136
10	GS_007	Plagioclase-Porphyritic Basalt	454174	1231085
11	GS_008	Aphyric Basalt	453660	1230958
12	GS_009	Aphyric Basalt	453794	1233066
14	GS_010	Aphyric Basalt	453794	1233067
15	GS_011	Aphyric Basalt	452941	1233016
16	GS_012	Aphyric Basalt	452683	1233052
17	GS_013	Aphyric Basalt	453365	1236536
18	GS_014	Aphyric Basalt	453120	1236676
18	GS_015	Plagioclase-Porphyritic Basalt	453120	1236676
19		Aphyric Basalt	452696	1236859
20	GS_016	Aphyric Basalt	452669	1236836
21		Aphyric Basalt	452419	1236993
22	GS_017	Plagioclase-Porphyritic Basalt	452324	1237332
23	GS_018	Mafic Aphyric Intrusive	452321	1237371
24		Aphyric Basalt	452349	1237457
25	GS_019	Plagioclase-Porphyritic Basalt	452209	1237567
26	GS_020	Aphyric Basalt	452171	1238007
26b	GS_022	Aphyric Basalt	453537	1241201
27	GS_021	Aphyric Basalt	451694	1238382
28	GS_023	Aphyric Basalt	453340	1241235
29		Micaceous Schist	452971	1241489
30	GS_024	Plagioclase-Porphyritic Basalt	452967	1241479
31	GS_025	Aphyric Basalt	451387	1226720
32	GS_026	Ultramafic Lithofacies	451430	1226250
33	GS_027	Aphyric Basalt	451352	1226597
34	GS_028	Aphyric Basalt	450884	1227490
35	GS_029	Aphyric Basalt	450884	1227490
36	GS_030	Hornblende-Feldspar Porphyritic Andesite	450878	1227765
37		Aphyric Basalt	450867	1227829
38	GS_031	Plagioclase-Porphyritic Basalt	450352	1228077
39	GS_032	Aphyric Basalt	447402	1228028
40	GS_033	Mafic Monomictic Breccia	447398	1228000
41	GS_034	Aphyric Basalt	447007	1228143
42	GS_035	Quartz-Rich Sandstone	446532	1228123
42	GS_036	Quartz-Rich Sandstone	446532	1228123
43		Aphyric Basalt	450795	1234370
44	GS_037	Quartz-feldspar Dacite	450423	1234344
45	GS_038	Polymictic Conglomerate	442994	1228410
45	GS_039	Polymictic Conglomerate	442994	1228410
46	GS_041	Dolerite	478715	1235136
47	GS_042	Ultramafic Lithofacies	478242	1234610
48	GS_043	Aphyric Basalt	477989	1234218
49	GS_044	Aphyric Basalt	478265	1234348
50	GS_045	Plagioclase-Porphyritic Basalt	409842	1222181
50	GS_046	Wavy-Planar Bedded Tuff	409842	1222181
50	GS_048	Dolerite	409884	1222170
50	GS_047	Polymictic Breccia	409842	1222181
51		Polymictic Conglomerate	409825	1220056
52		Polymictic Conglomerate	410216	1219004
53		Polymictic Conglomerate	418741	1208413
54	GS_049	Massive Tuff-Lapilli Sandstone	413296	1207465
55		Polymictic Breccia	409798	1205557
56	GS_050	Aphyric Basalt	408779	1207306
57	GS_051	Aphyric Basalt	408564	1208185
58	GS_052	Gabbro	408592	1208268
59		Aphyric Basalt	408624	1208284
60		Aphyric Basalt	408544	1208291
61		Gabbro	408489	1208143
62		Aphyric Basalt	408185	1207415
63	GS_053	Monomictic Breccia	408329	1207521
64		Planar Bedded Mudstone-Siltstone	419158	1240333

Table A-1 continued

Field site	Sample ID	Lithology	Eastern	Northing
65	GS_062	Aphyric Basalt	419188	1240343
66		Plagioclase-Porphyritic Basalt	419163	1239460
67		Pyroxene-Porphyritic Basalt	418823	1236350
68	GS_063	Pyroxene-Porphyritic Basalt	417219	1235591
69	GS_064	Monomictic Breccia	417284	1236194
70	GS_065	Diorite	416899	1236345
71		Polymictic Breccia	416795	1236318
72	GS_066	Pyroxene-Porphyritic Basalt	416584	1236413
73		Plagioclase-Porphyritic Basalt	417345	1239936
74		Polymictic Breccia/Conglomerate	414226	1236768
75	GS_067	Monomictic Breccia	414451	1236777
76	GS_068	Plagioclase-Porphyritic Basalt	414820	1236698
77	GS_069	Plagioclase-Porphyritic Basalt	415015	1236762
78	GS_070	Feldspar Megacrystic Basalt	488011	1138058
79	GS_071	Aphyric Basalt	488034	1138003
80	GS_072	Dolerite	491542	1133923
80	GS_073	Aphyric Basalt	491553	1133895
81	GS_074	Aphyric Basalt	491808	1133814
82	GS_075	Aphyric Basalt	492452	1133645
83		Aphyric Basalt		
84	GS_076	Aphyric Basalt	493953	1133625
84	GS_077	Aphyric Basalt	493928	1133635
85		Plagioclase-Porphyritic Basalt	495304	1133092
86	GS_078	Aphyric Basalt	496034	1132882
87	GS_079	Massive Tuff-Lapilli Sandstone	496484	1132651
88	GS_080a	Polymictic Breccia/Conglomerate	498198	1131563
88	GS_080b	Massive Tuff-Lapilli Sandstone	498198	1131563
89	GS_081	Massive Tuff-Lapilli Sandstone	498686	1131147
90	GS_082b	Plagioclase-Porphyritic Basalt	500013	1130135
90	GS_082a	Plagioclase-Porphyritic Basalt	500013	1130135
91		Monomictic Breccia	501856	1129623
92	GS_083b	Pyroxene-Porphyritic Basalt	502196	1129684
92	GS_083a	Massive Tuff-Lapilli Sandstone	502196	1129684
93	GS_084	Monomictic Breccia	502140	1130731
94		Aphyric Basalt	496223	1131549
95		Aphyric Basalt	491251	1136008
96	GS_085	Aphyric Basalt	494210	1141766
97		Aphyric Basalt	497413	1142149
98	GS_086	Aphyric Basalt	498270	1142063
99		Aphyric Basalt	498660	1141912
100	GS_087	Quartz Reef	477659	1140539
101		Micaceous Schist	477419	1139011
102	GS_088	Dolerite	477449	1138461
103	GS_089	Dolerite	477304	1137607
104		Aphyric Basalt	476887	1136097
105	GS_090b	Aphyric Basalt	476965	1135357
105	GS_090a	Micaceous Schist	476965	1135357
106	GS_091	Aphyric Basalt	477002	1135168
107	GS_092	Quartz Reef	477223	1135141
108	GS_093	Dolerite	477515	1135249
109		Dolerite	477295	1134038
110	GS_094	Aphyric Basalt	477493	1132666
111		Micaceous Schist	475996	1140422
112	GS_095a	Aphyric Basalt	475620	1140334
112	GS_095b	Quartz-Feldspar Porphyritic Intrusion	475620	1140334
113		Aphyric Basalt	475094	1139327
114	GS_096	Aphyric Basalt	479388	1142242
115	GS_097a	Aphyric Basalt	479149	1142288
115	GS_097b	Feldspar Megacrystic Basalt	479149	1142288
116		Feldspar Megacrystic Basalt	477248	1142372
117	GS_113	Monomictic Breccia	549418	1368807
118		Feldspar Megacrystic Basalt	492610	1088396
119	GSA001	Aphyric Basalt	492454	1088202
120		Aphyric Basalt	492372	1088166
121	GSA002	Feldspar Megacrystic Basalt	492339	1088155
122		Granite	492412	1088004
123	GSA003	Aphyric Basalt	492467	1087998
124	GSA004	Aphyric Basalt	493113	1088484
125	GSA005	Feldspar Megacrystic Basalt	493220	1088577
126		Aphyric Basalt	493288	1088941
127	GSA006	Aphyric Basalt	453933	1110431
128	GSA007	Plagioclase-Porphyritic Basalt	452990	1110833
129	GSA008	Dolerite	452606	1111019
130		Plagioclase-Porphyritic Basalt	450958	1110923
131	GSA009	Massive Tuff-Lapilli Sandstone	450855	1110935
131	GSA010	Massive Tuff-Lapilli Sandstone	450855	1110935
131	GSA011	Hornblende-Feldspar Porphyritic Andesite	450966	1110888
132	GSA012	Hornblende-Feldspar Porphyritic Andesite	450966	1110888
133	GSA013	Plagioclase-Porphyritic Basalt	449369	1111157
134	GSA014	Plagioclase-Porphyritic Basalt	452089	1111759
135	GSA015	Plagioclase-Porphyritic Basalt	451939	1111701
136	GSA016	Monomictic Breccia	451786	1111734

Table A-1 continued

Field site	Sample ID	Lithology	Eastern	Northing
137	GSA017	Plagioclase-Porphyritic Basalt	451674	1111697
138		Polyimitic Breccia/Conglomerate	495680	1089264
139		Aphyric Basalt	495609	1089006
140	GSA018	Gabbro	495581	1088921
141		Carbonaceous Mud-Siltstone	495535	1088554
142		Polyimitic Breccia/Conglomerate	494802	1088212
142		Planar Bedded Mudstone-Siltstone	494802	1088212
143	GSA022	Aphyric Basalt	447053	1119763
144		Aphyric Basalt	447045	1119658
145		Aphyric Basalt	447037	1119643
146	GSA023	Aphyric Basalt	447010	1119607
147	GSA024	Quartz Reef	446928	1119558
148		Aphyric Basalt	446860	1119460
149	GSA025	Aphyric Basalt	446743	1119328
150	GSA026	Aphyric Basalt	446388	1119186
151		Aphyric Basalt	445630	1119501
152	GSA027	Aphyric Basalt	445733	1120016
153		Feldspar Megacrystic Basalt	445780	1120024
154	GSA028	Feldspar Megacrystic Basalt	445747	1120062
155	GSA029	Feldspar Megacrystic Basalt	445452	1118192
156	GSA030	Aphyric Basalt	445169	1117696
157		Siltstone	444090	1116504
158	GSA031	Dolerite	443645	1116254
159	GSA032	Plagioclase-Porphyritic Basalt	443371	1116263
160		Plagioclase-Porphyritic Basalt	442706	1116103
161	GSA033	Plagioclase-Porphyritic Basalt	442542	1116148
162	GSA034	Monomictic Breccia	442654	1115929
163		Monomictic Breccia	442429	1115538
164		Plagioclase-Porphyritic Basalt	442517	1115175
165	GSA035	Plagioclase-Porphyritic Basalt	442536	1115143
166	GSA036	Aphyric Basalt	450820	1116572
168	GSA037	Hornblende-Feldspar Porphyritic Andesite	500351	1142219
169	GSA038	Polyimitic Breccia/Conglomerate	499706	1141971
170	GSA039	Plagioclase-Porphyritic Basalt	496866	1142266
171	GSA040A	Plagioclase-Porphyritic Basalt	496104	1142209
171	GSA040B	Rhyolite	496104	1142209
172		Feldspar Megacrystic Basalt	493369	1143391
173	GSA041B	Dolerite	492366	1144099
174		Aphyric Basalt	493035	1140387
175		Aphyric Basalt	492716	1140443
176	GSA042	Gabbro	492534	1140459
177	GSA043	Feldspar Megacrystic Basalt	492534	1140459
178	GSA044	Aphyric Basalt	492494	1140442
179	GSA045	Quartz-Rich Conglomerate	445086	1223766
180		Granite	444985	1220536
181	GSA046	Quartz Porphyritic Rhyolite	445085	1220554
182	GSA047	Aphyric Basalt	445259	1219663
183	GSA048	Aphyric Basalt	445497	1219828
184	GSA049	Aphyric Basalt	449233	1214625
185	GSA050	Quartz Reef	449950	1214923
186		Diorite	470441	1212788
187	GSA055	Dolerite	469326	1213406
188	GSA056	Dolerite	467141	1215206
189	GSA057	Aphyric Basalt	466267	1215421
190	GSA058	Dolerite	462277	1216421
191	GSA059	Aphyric Basalt	438963	1204833
192	GSA060	Aphyric Basalt	438871	1204838
193	GSA061	Aphyric Basalt	438773	1204815
194		Quartz Reef	472034	1226274
195	GSA062	Pyroxene-Porphyritic Basalt	473343	1227576
196	GSA063	Aphyric Basalt	473458	1227508
197		Aphyric Basalt	473518	1227645
198	GSA064	Dolerite	473481	1227849
199		Mafic Aphyric Intrusive	475330	1228448
200	GSA065	Aphyric Basalt	475436	1228735
201	GSA066	Aphyric Basalt	475741	1228505
202	GSA067	Aphyric Basalt	477113	1228760
203	GSA068	Pyroxene-Porphyritic Basalt	477203	1228672
204	GSA069	Aphyric Basalt	477512	1228791
205	GSA070	Aphyric Basalt	480510	1231480
206		Mafic Aphyric Intrusive	480484	1231918
207	GSA071	Aphyric Basalt	480373	1232072
208		Aphyric Basalt	480320	1232027
209	GSA072	Gabbro	480737	1233035
210	GSA073	Gabbro	480944	1233428
211	GSA074	Aphyric Basalt	479316	1234423
212	GSA075	Aphyric Basalt	445861	1221931
213	GSA076	Aphyric Basalt	446464	1221215
214	GSA077	Aphyric Basalt	447684	1220914
215	GSA078	Aphyric Basalt	447896	1220891
216	GSA079	Aphyric Basalt	448087	1220688
217	GSA080	Aphyric Basalt	448667	1220412

Table A-1 continued

Field site	Sample ID	Lithology	Eastern	Northing
218		Tonalite	448864	1220353
219	GSA081	Aphyric Basalt	451170	1220070
220	GSA082	Dolerite	451443	1220130
221	GSA083	Hornblende-Feldspar Porphyritic Andesite	452512	1219633
222	GSA084	Micaceous Schist	452512	1219633
223		Aphyric Basalt	459683	1250285
224		Ultramafic Lithofacies	528023	1290682
225	GSA085	Aphyric Basalt	527947	1290588
226	GSA086	Dolerite	527892	1290494
227	GSA087	Pyroxene-Porphyritic Basalt	527641	1290311
228		Pyroxene-Porphyritic Basalt	527506	1290298
Drill core	Sample ID	Lithology	Eastern	Northing
CHDD00007	GS_057	Plagioclase-Porphyritic Basalt	409915	1222184
CHDD00007	GS_054	Monomictic Breccia	409915	1222184
CHDD00007	GS_055	Wavy-Planar Bedded Tuff	409915	1222184
CHDD00007	GS_061	Massive Tuff-Lapilli Sandstone	409915	1222184
CHDD00007	GS_056	Polymictic Conglomerate	409915	1222184
CHDD00007	GS_059	Polymictic Conglomerate	409915	1222184
CHDD00007	GS_058	Planar Bedded Mudstone-Siltstone	409915	1222184
CHDD00007	GS_060	Planar Bedded Mudstone-Siltstone	409915	1222184
GHDD063	GSA051	Aphyric Basalt	451771	1237777.82
GHDD118	GSA052	Gabbro	453379	1236112.79
GHDD119	GSA053	Aphyric Basalt	453392	1236058.81
GHDD173	GSA054	Gabbro	453402	1236175.59
KMRD047	GSA019	Aphyric Basalt	496143	1087125
KMRD047	GSA020	Aphyric Basalt	496143	1087125
KMRD047	GSA021	Aphyric Basalt	496143	1087125
KNRD416		Planar Bedded Mudstone-Siltstone	494389	1088420
P5200	GS_098	Aphyric Basalt	N/A	N/A
P5200	GS_099	Aphyric Basalt	N/A	N/A
P5200	GS_102	Rhyolite	N/A	N/A
P5200	GS_104	Rhyolite	N/A	N/A
P5200	GS_105	Rhyolite	N/A	N/A
P5200	GS_106	Aphyric Basalt	N/A	N/A
P5200	GS_107	Rhyolite	N/A	N/A
P5200	GS_108	Rhyolite	N/A	N/A
P5200	GS_100	Polymictic Conglomerate	N/A	N/A
P5200	GS_101	Polymictic Conglomerate	N/A	N/A
P5200	GS_103	Silt-Mudstone	N/A	N/A
P5200	GS_109	Diorite	N/A	N/A
P5300	GS_112	Rhyolite	N/A	N/A
P5301	GS_110	Aphyric Basalt	N/A	N/A
P5301	GS_111	Aphyric Basalt	N/A	N/A
TKD004	GS_040	Aphyric Basalt	452392	1227587

Table A- 2 Results of the Rietveld refinement of selected lithofacies of the Houndé and Boromo belts

Sample ID	Lithology	Albite± Andesine	Actinolite	Augite	Chlorite± Clinochlore	Epidote± Clinzoisite	Calcite± Dolomite	Illite ± Sericite	Quartz	Talc	Non-diffracting	R_wp	GOF
GS_014	Aphyric basalt	28.7			34.1		15.3		21.8		5.12	9.8	4.3
GS_034	Aphyric basalt	42.2			21.2			17.7	18.8		10.68	6.6	3.1
GS_079	Aphyric basalt						18.6	32.6	48.9		22.56	7.5	2.8
GS_075	Aphyric basalt	22.5	35.7		14.2	17.0			10.5		2.52	10.4	4.8
GS_043	Aphyric basalt	23.2	72.5						4.4		1.93	12.3	5.4
GS_076	Aphyric basalt	25.7			24.3		21.5		28.5		16.75	7.7	3.7
GSA025	Aphyric basalt	19.3	51.3		7.8	13.3			8.3		10.2	10.1	4.6
GSA001	Aphyric basalt	18.0	75.5						6.5		2.25	19	8
GSA055	Aphyric basalt	17.2	55.7		4.9	12.3			9.9		4.93	13.3	6.1
GS_017	Aphyric basalt	18.2	36.9		11.0	22.1			11.8		0.95	13.6	6.1
GS_016	Aphyric basalt	27.5	4.1		23.5		19.3	3.5	22.1		16.5	10.8	4.7
GS_086	Aphyric basalt	24.8	20.5	16.1	19.2	12.0			7.4		15.59	8.8	4.1
GS_012	Aphyric Basalts	0.0	46.5		7.5	46.0					4.28	16.5	6.9
GSA064	Dolerite	35.5			4.0		32.7		27.8		14.33	5.1	2.4
GS_070	Feldspar Megacrystic basalts	32.2			14.0	37.3		5.8	10.7		36.07	13.6	5.2
GS_097B	Feldspar Megacrystic basalts	21.5	8.3		19.8	42.7			7.8		6.79	13.1	5.1
GS_042	Gabbro		77.3		22.7						8.34	16.5	7.8
GS_004	Ultramafic lithofacies		39.1		17.4			43.5		8.8	19	9	
GS_013	Pyroxene-phyric basalt	28.7	42.0		15.1			14.2		10.86	13.4	6.1	

The modal proportion of mineral phases are presented in volume %, R_wp = weighted residual error, GOF = goodness of fit

Table A- 3 Descriptions and interpretations of major lithofacies

Lithofacies	Description	Interpretation
Massive and pillow aphyric phryic basalt	Geometry/Structure: Usually <10m thick units, pillow rims are mostly smooth (chilled margins) or may exhibit radial joints. In places, pillows are flattened. Pillow diameter ranges from 20-40cm across. Vesicles commonly occur 1cm away from the rims of the pillows. Inter-pillow spaces are mafic monomictic breccia. Components: aphanitic	Subaqueous basalt lava flow.
Massive and pillow plagioclase-porphyritic basalt	Geometry/Structure: Pale green, massive and pillow. Thickness >10m. Components: 30-50%, 2-5 mm relict plagioclase phenocrysts in microcrystalline groundmass	Subaqueous basalt lava flow.
Massive feldspar megacrystic basalt	Geometry/Structure: Massive, overall thicknesses on the order of >500 m; Components: large (megacrysts) of equant, euhedral feldspars (7-10 cm) make up ~15-70% of the volume; groundmass is fine-grained and dark green.	Subaqueous basaltic lava flows sourced magma chambers rich in feldspar mush (Sheth (2016))
Massive pyroxene-porphyritic basalt	Geometry/Structure: Massive, pale green. Thickness ~10m. Components: pyroxene phenocrysts and glomerocrysts (~30%, 1-5 mm) in a fine-grained groundmass	Sheet lava flow
Gabbro	Geometry/Structure: generally massive, thickness 10-20m; contacts not observed Components: coarse-grained equigranular ~3-5mm, 30-50% pyroxene and 40% plagioclase	Mafic intrusion (sills?)
Dolerite	Geometry/Structure: Massive, thickness ~1m Components: phaneritic, 2-3 mm, 40% pyroxene or 30% hornblende and 30-40% plagioclase.	Mafic intrusion (sill?)
Ultramafic lithofacies	Geometry/Structure: Thickness and geometry unclear, contacts not observed, massive, Components: orthocumulate texture of ~20% relict olivine altered to talc, chlorite and reddish-brown iron-oxide minerals, very weathered, strongly foliated and magnetic.	Cumulate base of layered mafic intrusion
Massive hornblende-plagioclase porphyritic andesite	Geometry/Structure: Contacts and geometry unclear, massive, thickness > 1m. Components: phenocrysts of equant hornblende (~20% and 3 mm), and tabular plagioclase (~30% and 5mm)	lava flow and sub-volcanic intrusions
Massive quartz-feldspar porphyritic dacite	Geometry/Structure: massive, thickness < 1m, typically sharp and discordant contact with host. Components: Several varieties based on abundance and size of quartz and feldspar, most contain phenocrysts of feldspar and quartz 2-3mm in a siliceous groundmass.	Intermediate to acidic intrusions (sills/dykes/blobs) that post-date host lithification.

Lithofacies	Description	Interpretation
Planar bedded mudstone-siltstone	Geometry/Structure: Planar bedded, cm-scale thicknesses. Overall thickness of continuous sequences may exceed 10m. Dark grey to black colouration and strongly deformed; symmetrical ripples absent. Components: Intercalated layers of silt and mud (sometimes carbonaceous); Coarser intervals are made up feldspar crystals and minor lithic clast; quartz absent.	Hemipelagic deposit
Massive to graded siltstone	Geometry/Structure: Typically massive (often well sorted) to normally graded. Thickness: ~5cm Components: Sand-sized fine-grained clasts (basalt?) and ~1mm feldspar crystals in a grey matrix; no quartz crystals observed	Turbiditic mass flow
Wavy to planar-bedded tuff	Geometry/Structure: Roughly 1 meter thick, bedded on mm-scale, planar, wavy and low-angle (anti-dunes) cross-beds. Components: ash-sized particles	Pyroclastic surge?
Massive tuff-lapilli sandstone	Geometry/Structure: massive, dark grey, poorly-sorted, matrix-supported, thickness of about 50cm Components: angular to sub-rounded clasts of (20-40%, ~5 mm) feldspar-porphyritic and minor aphyric amygdaloidal volcanic clasts and feldspar crystals (2-5mm)	Epiclastic mass flow
Massive monomictic breccia	Geometry/Structure: Massive, poorly sorted, >1m thick, matrix-supported. Components: blocks of pyroxene-porphyritic basalt (<7cm) in light green pyroxene-rich (~30%) matrix	Debris flow and debris avalanche deposits
Graded volcanic breccia/conglomerates	Geometry/Structure: thick (1-10m) graded beds. Some monomictic others polymictic, matrix to clast-supported. Lower contact truncates wavy-to planar bedded tuff, top contact gradation to massive to graded siltstone. Components: (1) 1-10 cm angular to cuspatate shaped fine volcanic clasts (2) sub-rounded porphyritic volcanic clasts. Matrix of both gray and crystal-free	Subaqueous mass flows of autobreccia and hyaloclastite
Massive polymictic conglomerate	Geometry/Structure: Massive, dominantly matrix-supported, polymodal poorly sorted. Thickness of unit 50cm. Components: The clasts are dominantly <10cm round to sub-rounded feldspar-porphyritic andesite, minor aphanitic mafic volcanic (basalt), aphanitic flow banded felsic (rhyolite?). The matrix is pale green crystal-free	Debris flow
Quartz-rich sandstone	Geometry/Structure: Light gray, massive to planar bedded sandstone (cm-scale, characterised by alternating light and dark bands). Overall thickness <10m thick; Components: Matrix dominated by quartz (50% 1–2mm), rare mud rip-up clast (<5%)	Fluvial sediments, upper-flow regime (planar beds) and lower-flow regime (high-angle cross-beds)
Quartz-rich polymictic conglomerate	Geometry/Structure: Approximately 1m thick, massive, poorly sorted, matrix-supported. Components: include well-rounded granite clasts, polycrystalline quartz. The matrix is quartz-rich.	Fluvial deposit

Appendix B: Chapter 4

Table A- 4 Detection limit for major element analysis

Oxide	Limit of Detection (%)
PbO	0.004
HfO ₂	0.007
ZnO	0.001
CuO	0.002
NiO	0.002
Fe ₂ O ₃	0.004
Mn ₃ O ₄	0.004
Cr ₂ O ₃	0.004
V ₂ O ₅	0.005
BaO	0.009
TiO ₂	0.005
CaO	0.005
K ₂ O	0.004
SO ₃	0.005
ZrO ₂	0.009
P ₂ O ₅	0.007
SrO	0.007
SiO ₂	0.009
Al ₂ O ₃	0.006
MgO	0.009
Na ₂ O	0.014

Table A- 5 Recovery of trace elements for BHVO-2 from Trinity College Dublin. Acid digestion ICP-MS method

Element (ppb)	Certified value (Jochum et al., 2016)	This work	BHVO-2 Experiment/reference
7Li	4500	4548	1.01
9Be	1076	1036	0.96
31P	1172000	1346913	1.15
45Sc	31830	32167	1.01
49Ti	16373000	16646719	1.02
59Co	44890	45207	1.01
60Ni	119800	117150	0.98
65Cu	129300	120785	0.93
66Zn	103900	95998	0.92
71Ga	21370	21189	0.99
75As	700	1381	1.97
85Rb	9261	9120	0.98
86Sr	394100	395561	1.00
89Y	24910	24194	0.97
91Zr	171200	162912	0.95
93Nb	18100	18262	1.01
98Mo	4070	4077	1.00
111Cd	152	119	0.78
115In	117	86	0.73
120Sn	1776	1957	1.10
121Sb	103	99	0.95
133Cs	100	101	1.01
135Ba	130900	131205	1.00
139La	15200	15107	0.99
140Ce	37530	37497	1.00
141Pr	5339	5354	1.00
146Nd	24270	24341	1.00
149Sm	6023	6042	1.00
151Eu	2043	2049	1.00
159Tb	939	923	0.98
160Gd	6207	6177	1.00
161Dy	5280	5232	0.99
165Ho	989	992	1.00
167Er	2511	2495	0.99
169Tm	335	339	1.01
172Yb	1994	1959	0.98
175Lu	275	274	1.00
178Hf	4470	4202	0.94
181Ta	1154	1148	1.00
184W	251	216	0.86
204Pb	1653	1638	0.99
205Tl	22	20	0.91
206Pb	1653	1609	0.97
207Pb	1653	1589	0.96
208Pb	1653	1638	0.99
Total Pb (calc)	1653	1620	0.98
232Th	1224	1182	0.97
238U	412	418	1.02

Table A- 6 Recovery of trace elements for JA-2 from Trinity College Dublin. Acid digestion ICP-MS method

Element (ppb)	Certified value (Jochum et al., 2016)	This work	Experiment/reference
7Li	29180	28698	0.98
9Be	2260	2059	0.91
31P	663000	748520	1.13
45Sc	18930	19021	1.00
49Ti	4014000	3889260	0.97
59Co	28330	29529	1.04
60Ni	136000	138226	1.02
65Cu	29000	26601	0.92
66Zn	64500	75517	1.17
71Ga	16850	16268	0.97
75As	710	1000	1.41
85Rb	69800	69602	1.00
86Sr	245800	241381	0.98
89Y	16890	15722	0.93
91Zr	108500	104060	0.96
93Nb	9300	9068	0.98
98Mo	581	572	0.98
111Cd	69	73	1.06
115In	37	44	1.18
120Sn	1690	1755	1.04
121Sb	150	154	1.03
133Cs	4780	4676	0.98
135Ba	308400	308683	1.00
139La	15460	15404	1.00
140Ce	32860	32517	0.99
141Pr	3691	3655	0.99
146Nd	14040	13877	0.99
149Sm	3032	2996	0.99
151Eu	893	864	0.97
159Tb	479	473	0.99
160Gd	3013	2936	0.97
161Dy	2851	2885	1.01
165Ho	591	596	1.01
167Er	1676	1667	0.99
169Tm	255	256	1.00
172Yb	1645	1609	0.98
175Lu	255	240	0.94
178Hf	2838	2660	0.94
181Ta	652	637	0.98
184W	1150	1271	1.10
204Pb	18800	17950	0.95
205Tl	330	335	1.02
206Pb	18800	17802	0.95
207Pb	18800	17866	0.95
208Pb	18800	18243	0.97
Total Pb (calc)		18050	
232Th	4800	4700	0.98
238U	2182	2216	1.02

Table A- 7 Recovery of trace elements for W2 CARF QUT. Acid digestion ICP-MS method

Element (ppb)	Certified value	This work	Experiment/reference (%)
7 Li [No Gas]	9210	9035	98
9 Be [No Gas]	672	581	86
45 Sc [He]	35860	34078	95
47 Ti [He]	6354611	5952986	94
51 V [O2]	265800	264837	100
52 Cr [No Gas]	92000	91710	100
59 Co [O2]	44370	43877	99
60 Ni [O2]	72000	70204	98
63 Cu [No Gas]	105900	104750	99
66 Zn [No Gas]	77700	74599	96
71 Ga [No Gas]	17880	18168	102
85 Rb [He]	20230	20074	99
88 Sr [He]	195400	202026	103
89 Y [No Gas]	21820	21148	97
90 Zr [He]	99300	91073	92
93 Nb [No Gas]	7510	7228	96
95 Mo [No Gas]	465	451	97
107 Ag [O2]	46	40	88
111 Cd [He]	77	72	94
121 Sb [He]	809	807	100
133 Cs [He]	915	900	98
138 Ba [He]	172800	181171	105
139 La [He]	10630	10126	95
139 La [No Gas]	10630	10183	96
140 Ce [He]	23210	23675	102
141 Pr [No Gas]	3018	3163	105
146 Nd [No Gas]	13090	13578	104
147 Sm [No Gas]	3300	3317	101
153 Eu [He]	1091	1080	99
157 Gd [No Gas]	3713	3895	105
159 Tb [He]	627	573	91
163 Dy [No Gas]	3806	3992	105
165 Ho [No Gas]	791	773	98
166 Er [He]	2209	2178	99
169 Tm [O2]	331.5	329	99
172 Yb [No Gas]	2054	2095	102
175 Lu [No Gas]	309	293	95
178 Hf [He]	2444	2360	97
181 Ta [No Gas]	489	483	99
182 W [O2]	290	289	100
204 Pb [No Gas]	7930	7719	97
208 Pb [No Gas]	7930	7693	97
232 Th [No Gas]	2179	2176	100
238 U [He]	505	499	99

Table A- 8 Recovery of trace elements for AGV-2 CARF QUT

Element (ppb)	Certified value	This work	Experiment/reference (%)
7 Li [No Gas]	10800	10825	100
9 Be [No Gas]	2209	1998	90
45 Sc [He]	13110	12995	99
47 Ti [He]	6293785	5825590	93
51 V [O2]	118500	118505	100
52 Cr [No Gas]	16220	16857	104
59 Co [O2]	15460	15707	102
60 Ni [O2]	18870	18260	97
63 Cu [No Gas]	51510	51850	101
66 Zn [No Gas]	86700	90278	104
71 Ga [No Gas]	20420	21405	105
85 Rb [He]	67790	69713	103
88 Sr [He]	659500	673866	102
89 Y [No Gas]	19140	19016	99
90 Zr [He]	232000	241029	104
93 Nb [No Gas]	14120	13906	98
95 Mo [No Gas]	2000	1962	98
107 Ag [O2]	90	88	98
111 Cd [He]	184	168	92
121 Sb [He]	458	451	98
133 Cs [He]	1173	1160	99
138 Ba [He]	1134000	1201881	106
139 La [He]	38210	38493	101
139 La [No Gas]	38210	37447	98
140 Ce [He]	69430	69791	101
141 Pr [No Gas]	8165	8533	105
146 Nd [No Gas]	30500	31809	104
147 Sm [No Gas]	5509	5672	103
153 Eu [He]	1553	1739	112
157 Gd [No Gas]	4678	5160	110
159 Tb [He]	651	650	100
163 Dy [No Gas]	3549	3619	102
165 Ho [No Gas]	682	656	96
166 Er [He]	1825	1829	100
169 Tm [O2]	262	250	96
172 Yb [No Gas]	1653	1615	98
175 Lu [No Gas]	251	250	100
178 Hf [He]	5137	5220	102
181 Ta [No Gas]	865	916	106
182 W [O2]	553	547	99
204 Pb [No Gas]	13140	13398	102
208 Pb [No Gas]	13140	13260	101
232 Th [No Gas]	6174	6196	100
238 U [He]	1885	1886	100

Table A- 9 Acid digestion ICP-MS trace element detection limits

Tune Mode	Element	Detection Limit (ppb)	Tune Mode	Element	Detection Limit (ppb)	Tune Mode	Element	Detection Limit (ppb)
He	Li	0.054043719	No Gas	Sr	0.003605147	He	Ce	0.001797
No Gas	Li	0.004412266	He	Sr	0.000716454	No Gas	Ce	0.000513
No Gas	Be	0.002199122	O2	Sr	0.004585052	O2	Ce	0.00615
O2	Sc	0.177172418	He	Y	0.001187925	No Gas	Pr	0.000129
He	Sc	1.809923626	No Gas	Y	0.000967965	He	Pr	0.000139
No Gas	Sc	0.022301963	O2	Y	0.000599297	No Gas	Nd	0.000226
O2	Sc	0.001622496	O2	Y	0.013673572	He	Sm	0.000464
No Gas	Ti	0.044344309	He	Zr	0.000435306	No Gas	Sm	0.000269
He	Ti	0.129121569	No Gas	Zr	0.000929929	He	Eu	0.000171
O2	Ti	0.028246574	O2	Zr	0.005046716	No Gas	Eu	0.000394
No Gas	V	0.014997422	No Gas	Nb	0.000541943	O2	Eu	0.000103
O2	V	0.15265641	He	Nb	0.000729311	He	Gd	0.000638
He	V	0.007551378	O2	Nb	0.010148593	No Gas	Gd	0.000673
O2	V	0.001464822	O2	Nb	0.001287762	O2	Gd	0.015493
O2	V	0.017117835	He	Mo	0.00182824	He	Tb	4.4E-05
O2	Cr	0.010114375	No Gas	Mo	0.000399713	He	Dy	0.000144
No Gas	Cr	0.023598962	O2	Mo	0.005957606	No Gas	Ho	0.000116
He	Cr	0.024326249	O2	Ag	0.000426256	He	Ho	1.72E-05
O2	Cr	0.080192995	He	Ag	0.00016495	No Gas	Tm	0.000123
He	Co	0.00046368	No Gas	Ag	0.000132244	He	Tm	2.99E-05
No Gas	Co	0.005257175	No Gas	Cd	0.000490479	No Gas	Yb	0.000556
O2	Co	0.005101503	O2	Cd	0.000315908	O2	Lu	0.003911
O2	Co	0.012029437	He	Cd	6.52126E-05	He	Lu	7.17E-05
He	Ni	0.034668232	No Gas	Sn	0.003906427	No Gas	Hf	0.000419
No Gas	Ni	0.002032423	O2	Sn	0.006369117	He	Hf	6.76E-05
O2	Ni	0.02923169	He	Sn	0.001094856	O2	Hf	0.002065
O2	Ni	0.066441611	O2	Sn	0.035525481	No Gas	Ta	0.001098
O2	Cu	0.010941987	O2	Sb	0.002534043	He	Ta	0.000164
He	Cu	0.003390787	He	Sb	0.002831474	O2	Ta	0.008182
No Gas	Cu	0.005508957	O2	Sb	0.007698456	O2	Ta	0.000905
O2	Zn	0.116876327	He	Cs	0.000496938	No Gas	W	0.000657
No Gas	Zn	0.07233502	O2	Cs	0.003965162	He	W	0.00116
He	Zn	0.028179789	No Gas	Cs	0.000425907	O2	W	0.034977
O2	Ga	0.000552144	He	Ba	0.001462844	O2	W	0.001166
No Gas	Ga	0.001404069	No Gas	Ba	0.00524793	No Gas	Tl	0.000979
He	Ga	0.001934554	He	La	0.000382235	He	Tl	0.003097
No Gas	Rb	0.002074767	No Gas	La	0.000206747	O2	Tl	0.008824
He	Rb	0.002090091	O2	La	0.000220731	No Gas	Pb	0.005348
O2	Rb	0.000787289				He	Pb	0.00579
						O2	Pb	0.020707
						He	Th	0.000167
						No Gas	Th	5.21E-06
						He	U	8.92E-05

Table A- 9B Values of Zr and Hf for Laser and Acid solution ICP-MS methods of duplicate samples and comparison of both values to verify their relative difference

Sample ID	Laser		Sample ID	Acid solution		Laser/Acid Comparison	
	Zr (ppm)	Hf (ppm)		Zr (ppm)	Hf (ppm)	Zr (ppm)	Hf (ppm)
GS_001	74.73	2.23	GS_001	80.16	2.17	0.9	1.0
GS_003	41.31	0.98	GS_003	38.95	1.04	1.1	0.9
GS_005	80.02	2.43	GS_005	102.01	2.71	0.8	0.9
GS_006	128.53	3.51	GS_006	59.87	1.67	2.1	2.1
GS_007	110.98	3.15	GS_007	39.62	1.27	2.8	2.5
GS_008	113.14	3.31	GS_008	70.45	2.03	1.6	1.6
GS_009	120.76	3.47	GS_009	53.3	1.64	2.3	2.1
GS_010	117.53	3.37	GS_010	69.24	1.9	1.7	1.8
GS_011	81.95	2.38	GS_011	29.95	1.03	2.7	2.3
GS_012	93.79	2.44	GS_012	51.84	1.62	1.8	1.5
GS_013	96.70	2.98	GS_013	52.31	1.47	1.8	2.0
GS_014	61.82	1.83	GS_014	29.51	1.01	2.1	1.8
GS_016	55.14	1.61	GS_016	49.06	1.28	1.1	1.3
GS_017	96.22	2.76	GS_017	62.43	1.72	1.5	1.6
GS_019	77.24	2.28	GS_019	83.32	2.18	0.9	1.0
GS_020	129.83	3.70	GS_020	71.64	1.98	1.8	1.9
GS_021	84.69	2.49	GS_021	90.83	2.33	0.9	1.1
GS_022	166.85	4.59	GS_022	173.52	4.4	1.0	1.0
GS_023	111.80	3.13	GS_023	78.99	2.17	1.4	1.4
GS_025	122.95	3.45	GS_025	120.71	3.19	1.0	1.1
GS_026A	54.64	1.72	GS_026a	25.98	1.06	2.1	1.6
GS_028	130.20	3.44	GS_028	92.17	2.4	1.4	1.4
GS_029	106.01	2.75	GS_029	94.53	2.21	1.1	1.2
GS_030	139.81	2.94	GS_030	144.99	3.49	1.0	0.8
GS_031	75.95	2.28	GS_031	53.86	1.42	1.4	1.6
GS_032	105.20	3.07	GS_032	96.42	2.59	1.1	1.2
GS_033	126.64	3.44	GS_033	124.17	3.14	1.0	1.1
GS_034	138.96	3.70	GS_034	123.19	2.89	1.1	1.3
GS_037	132.78	3.72	GS_037	137.4	3.47	1.0	1.1
GS_040	116.37	3.19	GS_040	103.3	2.8	1.1	1.1
GS_041	37.18	1.20	GS_041	12.34	0.49	3.0	2.5
GS_042	61.14	1.71	GS_042	68.64	1.65	0.9	1.0
GS_043	35.71	1.08	GS_043	12.04	0.57	3.0	1.9
GS_044	39.36	1.06	GS_044	13.49	0.56	2.9	1.9
GS_048	145.12	3.08	GS_048	124.39	2.89	1.2	1.1
GS_050	46.38	1.40	GS_050	27.25	0.9	1.7	1.6
GS_051	47.55	1.38	GS_051	23.37	0.78	2.0	1.8
GS_052	81.08	2.29	GS_052	82.85	1.93	1.0	1.2
GS_062	133.87	3.19	GS_062	123.02	2.94	1.1	1.1
GS_063	85.04	2.30	GS_063	98.52	2.55	0.9	0.9
GS_068	68.76	2.22	GS_068	77.01	2.12	0.9	1.0
GS_069	61.68	1.78	GS_069	70.67	1.99	0.9	0.9
GS_070	23.02	0.37	GS_070	21.21	0.58	1.1	0.6
GS_071	41.08	1.23	GS_071	32.38	1.05	1.3	1.2
GS_073	49.49	1.57	GS_073	30.39	0.98	1.6	1.6

Table A- 9B (continued) Values of Zr and Hf for Laser and Acid solution ICP-MS methods of duplicate samples and comparison of both values to verify their relative difference

Sample ID	Laser		Sample ID	Acid solution		Laser/Acid Comparison	
	Zr (ppm)	Hf (ppm)		Zr (ppm)	Hf (ppm)	Zr (ppm)	Hf (ppm)
GS_075	57.58	1.81	GS_075	59.58	1.7	1.0	1.1
GS_076	49.41	1.47	GS_076	55.58	1.54	0.9	1.0
GS_077	55.57	1.78	GS_077	62.01	1.71	0.9	1.0
GS_078	50.20	1.58	GS_078	57.02	1.62	0.9	1.0
GS_079	57.67	1.76	GS_079	54.36	1.33	1.1	1.3
GS_081	77.89	1.93	GS_081	81.65	2.13	1.0	0.9
GS_082a	84.66	2.31	GS_082a	90.74	2.35	0.9	1.0
GS_082b	89.34	2.81	GS_082b	97.53	2.52	0.9	1.1
GS_083a	41.27	1.22	GS_083a	48.97	1.34	0.8	0.9
GS_083b	32.15	0.86	GS_083b	37.48	1.05	0.9	0.8
GS_084	68.98	1.86	GS_084	61.59	1.56	1.1	1.2
GS_085A	69.84	1.99	GS_085a	107.59	3	0.6	0.7
GS_085B	49.92	1.52	GS_085b	61.64	1.76	0.8	0.9
GS_086	34.87	1.10	GS_086	40.04	1.18	0.9	0.9
GS_088	51.39	1.38	GS_088	27.7	0.8	1.9	1.7
GS_089	95.26	2.64	GS_089	58.2	1.56	1.6	1.7
GS_093	100.83	2.70	GS_093	90.08	2.55	1.1	1.1
GS_094	90.70	2.72	GS_094	77.51	2.24	1.2	1.2
GS_095A	125.67	3.45	GS_095A	16.98	0.65	7.4	5.3
GS_096	42.32	1.20	GS_096	40.39	1.2	1.0	1.0
GS_097a	45.20	1.27	GS_097a	45.78	1.3	1.0	1.0
GS_097B	28.45	0.61	GS_097B	11.35	0.34	2.5	1.8
GS_098	114.33	3.03	GS_098	92.44	2.39	1.2	1.3
GS_099	112.61	3.01	GS_099	98.44	2.21	1.1	1.4
GS_112	76.66	2.69	GS_112	53.96	2.05	1.4	1.3

Table A- 10 Whole-rock major and trace geochemical data for the Houndé and Boromo greenstone belts

Stratigraphic sequence	Lower Seq													
Lithology	APHYRIC													
Eastern	BASALT													
Northing	454742	454497	453660	453794	453794	452941	452683	453365	453120	452669	452324	452171	451694	453537
Sample ID	1231152	1231131	1230958	123066	123067	123016	123052	1236536	1236676	1236836	1237332	1238007	1238382	1241201
GS_005	GS_006	GS_008	GS_009	GS_010	GS_011	GS_012	GS_013	GS_014	GS_016	GS_017	GS_020	GS_021	GS_022	
Major Element (wt. %)														
SiO ₂	46.36	51.98	49.37	47.16	47.78	50.49	48.91	50.88	44.32	43.3	49.72	50.34	51.99	49.06
Al ₂ O ₃	13.45	12.6	12.64	13.19	12.99	13.57	14.42	13.42	12.7	12.11	14.32	12.86	13.71	12.07
TiO ₂	1.5	1.9	1.92	1.87	1.78	1.48	1.45	1.64	1.18	1.1	1.4	1.93	1.49	2.06
MgO	6.13	4.93	4.71	4.33	5.94	5.55	3.7	5.89	6.39	6.18	5.24	4.03	4.97	3.03
Fe ₂ O ₃	2.29	2.63	3.03	2.92	2.4	2.44	2.35	2.44	2.05	1.99	2.4	2.87	2.4	2.91
FeO	11.68	13.41	15.44	14.9	12.26	12.46	11.98	12.42	10.45	10.17	12.21	14.66	12.22	14.84
CaO	7.11	8.15	8.98	13.25	6.91	10.31	15.73	8.97	10.07	9.25	11.59	9.79	5.36	6.11
Na ₂ O	2.85	2.75	2.57	1.62	2.95	2.37	0.42	2.3	1.89	2.45	1.75	2.07	4.47	4.45
K ₂ O	0.04	0.38	0.36	0.18	0.06	0.18	0.09	0.17	1.1	0.54	0.09	0.07	0.32	0.02
P ₂ O ₅	0.14	0.19	0.19	0.18	0.18	0.13	0.14	0.16	0.11	0.09	0.13	0.23	0.15	0.26
MnO	0.17	0.2	0.25	0.24	0.18	0.21	0.18	0.18	0.15	0.16	0.2	0.23	0.19	0.25
LOI	9.12	2.22	1.76	1.62	7.9	1.37	1.48	2.57	10.33	10.99	2.27	2.31	3.21	6.05
Total_hydrous	100.82	101.33	101.2	101.46	101.33	100.57	100.86	101.03	100.74	98.32	101.33	101.37	100.46	101.1
Trace Elements (ppm)														
Ni	50.97	35.6	34.88	34.86	55.91	52.26	39.01	49.65	104.41	57.84	47.52	24.31	37.58	13.04
Cr	61.43	46.73	34.05	63.75	81.22	75.01	73.96	50.97	192.75	101.72	82.18	28.98	30.96	18.51
Co	39.51	38.98	49.76	43.82	45.65	43.73	38.27	43.03	42.22	39.25	42.39	46.89	42.15	37.74
V	340.96	359.74	409.71	410.27	326.32	345.65	349.35	336.61	294.64	270	315.83	401.85	345.53	294.82
Sc	43	37.09	43.69	41.62	39.53	42.57	39.47	40.9	38.93	38.69	41.63	41.29	37.97	36.38
Cu	146.76	143.67	123.14	95.29	116.15	115.72	104.22	157.13	98.11	105.01	128.5	167.86	169.66	151.28
Zn	108.29	116.46	132.85	105.11	113.27	103.39	69.97	100.36	74.64	84.29	94.95	121.32	103.16	134.2
Mo	0.15	0.46	0.7	0.63	0.21	2.22	0.83	0.33	0.33	0.36	0.76	0.77	0.3	0.54
Li	22.23	7.63	9.67	2.69	25.51	8.66	2.38	18.1	46.61	39.01	17.66	17.47	12.44	10.01
Ba	10.33	93.08	49.96	141.37	40.14	34.53	12.88	46.07	33.11	64.24	54.27	54.62	69.55	16.73
Cs	0.07	0.09	0.29	0.05	0.3	0.1	0.03	0.06	3.59	1.45	0.21	0.04	0.38	0.04
Rb	0.86	8.61	9.82	1.84	2.07	2.08	0.82	2.36	43.44	18.73	1.27	0.24	4.71	0.15
Sr	179.19	175.16	177.52	291.47	145.74	112.75	460.96	201.45	190.21	244.63	214.13	183.79	113.98	155.98
Pb	1.12	1.07	1.24	1.71	0.61	1.11	1.49	1.3	2.96	1.27	0.87	1.33	0.74	1.63
Ga	19.07	20.16	20.74	26.06	16.1	18.34	26	20.73	19.84	16.01	19.59	20.61	16.03	22.05
Zr	102.01	59.87	70.45	53.3	69.24	29.95	51.84	52.31	29.51	49.06	62.43	71.64	90.83	173.52
Hf	2.71	1.67	2.03	1.64	1.9	1.03	1.62	1.47	1.01	1.28	1.72	1.98	2.33	4.4
Nb	4.1	6.29	6.5	5.13	5.26	4.17	4.28	5.54	3.16	3.62	5.13	5.9	4.68	7.5
Ta	0.27	0.39	0.4	0.33	0.35	0.27	0.27	0.35	0.94	0.24	0.33	0.38	0.3	0.46
Th	0.41	0.66	0.59	0.53	0.51	0.45	0.44	0.59	0.33	0.35	0.48	0.59	0.49	0.76
U	0.13	0.21	0.19	0.17	0.17	0.13	0.15	0.17	0.1	0.11	0.18	0.23	0.22	0.26
Y	12.38	35.32	43.41	39.92	33.69	30.39	32.7	33.11	21	14.06	30.43	45.87	33.27	22.79
La	4.64	7.87	7.1	6.42	7.66	4.97	5.31	6.45	3.94	4.29	6.43	7.91	6.18	8.78
Ce	13.87	21.17	20.57	18.05	17.87	14.16	14.53	17.82	11.27	11.94	15.54	18.93	16.39	25.02
Pr	2.05	3.26	3.09	2.8	3.19	2.2	2.28	2.75	1.75	1.84	2.5	3.11	2.4	3.66
Nd	10.19	15.94	15.38	14.17	15.63	11.07	11.62	13.52	8.79	9.04	12.31	15.5	11.91	17.99
Sm	3.01	4.75	4.73	4.47	4.63	3.49	3.55	4.01	2.74	2.58	3.56	4.7	3.64	4.91
Eu	0.84	1.66	1.66	1.78	1.52	1.25	1.58	1.44	1.08	0.93	1.29	1.67	1.45	1.55
Gd	3.06	5.94	6.42	5.93	5.81	4.65	4.82	5.29	3.59	2.96	4.74	6.53	4.95	5.25
Tb	0.41	0.95	1.07	0.99	0.92	0.78	0.79	0.85	0.59	0.45	0.76	1.05	0.82	0.73
Dy	2.42	6.42	7.64	7.23	6.34	5.78	5.74	5.98	4.13	2.95	5.35	7.22	5.41	4.36
Ho	0.5	1.28	1.58	1.44	1.23	1.14	1.14	1.17	0.81	0.55	1.07	1.48	1.13	0.82
Er	1.5	3.55	4.49	4.07	3.41	3.09	3.2	3.28	2.2	1.57	3.07	4.61	3.4	2.57
Tm	0.25	0.51	0.68	0.58	0.5	0.45	0.46	0.5	0.33	0.23	0.45	0.68	0.53	0.41
Yb	1.86	2.9	4.04	3.59	2.95	2.64	2.85	2.74	1.99	1.59	2.73	4.21	3.15	2.9

Lu	0.31	0.39	0.59	0.53	0.42	0.37	0.41	0.39	0.29	0.25	0.41	0.56	0.46	0.5
Ti	8398.75	10555.08	11032.56	10369.44	9950.53	8355.38	8088.19	9432.81	6701.85	6313.12	7951.19	11012.89	8715.7	11895.13
Be	390.48	686.09	609.47	534.26	491.32	471.02	315.6	494.09	802.22	678.63	473.57	647.64	694.3	736.51
Ag	47.9	47.83	31.36	25.83	35.61	19.53	27.08	30.73	14.09	19.51	57.11	37.91	46.62	76.52
Cd	88.89	51.22	78.41	65.05	71.94	47.46	54.17	55.66	39.54	49.3	70.17	75.94	83.97	147.25
Sn														
Sb	474.12	54.44	256.67	924.22	1013.49	58.29	215.96	1128.77	6161.44	9957.78	652.33	893.68	1759.61	1154.57
W	232.37	252.02	227.08	200.38	313.58	128.35	171.04	223.04	219.69	8824.05	821.17	192.73	140.76	378.09
Tl	28.46	47.66	66.99	33.51	31.61	32.28	27.75	36.51	268.4	99.47	25.68	16.67	31.57	19.57

Stratigraphic sequence	Lower Seq	Upper Seq	Upper Seq	Upper Seq	Upper Seq	Lower Seq	Lower Seq							
Lithology	APHYRIC													
Eastern	BASALT													
Northing	453340	451387	450884	450884	447402	447007	452392	477989	478265	408779	408564	419188	488034	491553
Sample ID	GS_023	GS_025	GS_028	GS_029	GS_032	GS_034	GS_040	GS_043	GS_044	GS_050	GS_051	GS_062	GS_071	GS_073
Major Element (wt. %)														
SiO ₂	54.26	50.37	52.26	47.7	50.75	47.22	51.12	49.02	49.93	48.65	50.76	56.04	48.66	50.09
Al ₂ O ₃	13.39	12.93	13.1	12.94	13.57	12.11	12.73	13.68	13.6	14.5	15.64	14.39	13.81	12.87
TiO ₂	1.59	1.7	1.67	2.01	1.78	2.72	1.61	0.75	0.81	0.96	1.03	0.83	0.86	0.78
MgO	4.14	6	5.52	5.82	3.65	4.55	5.95	7.11	7.25	7.04	5.45	6.67	6.38	6.85
Fe ₂ O ₃	2.22	2.77	2.45	2.82	2.98	2.9	2.85	2.42	2.45	2.06	1.9	1.45	2.39	2.6
FeO	11.33	14.13	12.49	14.37	15.18	14.79	14.53	12.36	12.49	10.5	9.69	7.38	12.18	13.25
CaO	7.51	8.8	7.78	8.13	9.15	6.1	8.89	11.48	10.85	12.88	13.26	9.62	11.76	8.63
Na ₂ O	4.19	3.05	4.08	2.77	2.47	4.06	2.87	1.91	2.05	1.28	1.63	2.6	2.19	2.11
K ₂ O	0.38	0.54	0.12	1	0.44	0.29	0.27	0.17	0.14	0.11	0.1	0.57	0.21	0.07
P ₂ O ₅	0.14	0.16	0.16	0.29	0.2	0.7	0.16	0.05	0.07	0.09	0.09	0.24	0.07	0.06
MnO	0.17	0.23	0.19	0.24	0.33	0.23	0.25	0.22	0.21	0.17	0.15	0.13	0.2	0.21
LOI	1.81	0.79	1.33	2.76	0.55	5.65	0.4	0.63	0.82	1.99	0.86	1	1.11	2.15
Total_hydrous	101.13	101.45	101.13	100.85	101.04	101.31	101.62	99.8	100.67	100.23	100.56	100.92	99.82	99.66
Trace Elements (ppm)														
Ni	46.98	43.11	39.85	53	27.97	9.67	45.35	97.89	99.4	160.43	169.87	194.73	102.39	55.77
Cr	47.62	45.99	43.48	77.77	12.63	17.29	53.11	127.14	138.53	367.54	410.41			
Co	43.2	54.74	44.56	48.96	46.68	32.42	54.38	57.96	57.69	51.82	55.33	32.53	53.37	57.94
V	370.47	389.36	343.22	387.05	388.42	251.82	377	267.82	292.55	268.68	287.86			
Sc	39.96	45.26	39.81	43.44	41.19	38.65	46.85	45.67	47.11	39.56	42.04	25.17	44.09	50.09
Cu	170.74	135.81	149.19	69.02	123.34	5.19	116.37	115.46	125.94	97.4	9.8	7.32	134.11	155.37
Zn	96.78	124.59	107.18	132.26	127.52	148.72	108.96	300.79	97.61	382.49	394.19	70.38	97.94	104.11
Mo	0.26	0.61	0.81	0.52	2.26	0.41	0.54	0.67	0.33	0.36	1.56	0.93	0.91	0.28
Li	5.23	5.97	17.52	17.84	5.81	29.88	3.13	4.48	5.25	5.75	7.58	9.89	5.93	16.34
Ba	137.96	112.49	88.48	475.11	97.78	115.1	39.01	30.41	26.93	18.54	17.27	312.79	34.91	9.93
Cs	0.27	0.92	0.1	2.63	0.23	4.13	0.14	0.14	0.22	0.18	0.32	0.89	0.18	0.07
Rb	5.75	11.56	0.95	27.03	7.84	8.46	3.52	1.81	1.81	1.94	0.85	16.97	2.93	0.63
Sr	89.3	122.84	239.25	241.49	190.54	165.86	116.33	80.88	84.51	100.58	117.48	275.34	86	69.12
Pb	0.61	0.98	0.79	1.6	1.67	1.72	1	0.63	0.4	0.59	0.71	3.13	0.49	0.52
Ga	18.26	18.74	16.94	20.49	22.26	21.13	18.5	14.03	14.88	15.93	16.91	14.83	16.09	14.72
Zr	78.99	120.71	92.17	94.53	96.42	123.19	103.3	12.04	13.49	27.25	23.37	123.02	32.38	30.39
Hf	2.17	3.19	2.4	2.21	2.59	2.89	2.8	0.57	0.56	0.9	0.78	2.94	1.05	0.98
Nb	4.75	5.29	6.33	6.37	5.36	9.14	4.8	1.77	1.9	2.21	2.44	7.64	2.14	0.69
Ta	0.31	0.34	0.39	0.36	0.37	0.55	0.38	0.15	0.15	0.15	0.18	0.47	0.13	0.04
Th	0.48	0.55	0.61	0.64	0.67	1.12	0.52	0.26	0.2	0.22	0.25	2.05	0.21	0.09
U	0.34	0.18	0.19	0.23	0.36	0.4	0.16	0.1	0.06	0.11	0.12	0.63	0.07	0.04
Y	33.1	41.61	32.97	33.73	40.83	34.22	38.64	18.15	20.16	22.32	23.09	19.26	19.73	22.84
La	5.76	6.42	7.57	7.86	7.61	13.91	5.7	2.42	2.55	2.6	2.73	18.06	2.54	1.26
Ce	16.74	17.79	20.98	21.88	21.73	34.17	16.92	6.42	6.94	7.46	7.73	39.72	7.04	3.83
Pr	2.48	2.67	3.07	3.12	3.06	4.99	2.48	1.06	1.14	1.26	1.32	4.91	1.13	0.69

Nd	12.47	13.44	14.65	15.51	15.13	23.9	12.56	5.34	5.78	6.52	6.85	19.01	5.8	3.96	8.07	
Sm	3.79	4.21	4.27	4.32	4.39	6.24	3.89	1.8	1.85	2.23	2.29	3.83	1.94	1.67	2.63	
Eu	1.45	1.55	1.49	1.85	1.54	2.18	1.38	0.71	0.7	0.9	0.91	1.16	0.75	0.63	0.95	
Gd	5.19	5.97	5.63	5.69	5.99	7.38	5.51	2.71	2.9	3.39	3.5	3.66	2.74	2.77	3.5	
Tb	0.84	0.99	0.88	0.88	0.98	1.07	0.91	0.51	0.53	0.62	0.66	0.58	0.5	0.54	0.63	
Dy	5.65	6.8	6.22	6.23	7.29	6.32	6.92	3.17	3.43	3.86	4.04	3.46	3.39	3.76	4.14	
Ho	1.11	1.41	1.25	1.24	1.5	1.24	1.4	0.72	0.76	0.85	0.9	0.73	0.77	0.88	0.93	
Er	3.32	4.34	3.43	3.52	4.28	3.82	4	2.18	2.35	2.58	2.67	2.03	2.27	2.59	2.69	
Tm	0.48	0.67	0.52	0.52	0.68	0.64	0.62	0.34	0.36	0.4	0.42	0.31	0.35	0.4	0.41	
Yb	2.85	4.08	3	3.22	4.08	3.71	3.72	2.07	2.32	2.38	2.55	1.97	2.27	2.57	2.6	
Lu	0.39	0.6	0.43	0.5	0.65	0.56	0.59	0.32	0.34	0.36	0.39	0.29	0.34	0.38	0.39	
Ti	9020.77	9862.27	9774.83	11703.65	10030.1	15673.75	9072.15	4032.6	4532.38	5447.8	5792.95	4804.52	5269.21	4751.27	6461.2	
Be	461.61	501.2	638.07	556.52	534.57	755.05	432.34	0.46	0.27	0.37	0.5	0.73	0.24	0.16	0.27	
Ag	43.68	61.13	45.38	43.76	44.12	51.97	49.01							0.09	0.09	0.11
Cd	70.06	103.76	86.16	78.24	93.56	121.73	91.62							0.6	0.43	0.82
Sn								0.21	0.28	0.29	0.31	1.11				
Sb	113.25	300.62	421.36	4209.75	134.38	1330.95	358.88	0.09	0.05	0.04	0.12	0.13	0.02	0.11	0.2	
W	242.59	731.76	174.82	214.27	280.91	185.39	283.88	0.11	0.07	0.06	0.83	0.22	0.04	0.03	0.09	
Tl	40.45	84.16	22.86	140.71	38.54	90.46	36.25	0.08	0.05	0.08	0.06	0.1	0.02	0.01	0.03	

Stratigraphic sequence	Lower Seq	Lower Seq	Lower Seq	Upper Seq	Lower Seq	Upper Seq	Upper Seq	Lower Seq	Lower Seq						
Lithology	APHYRIC														
Eastern	BASALT														
Northring	493953	493928	496034	502196	496223	494210	498270	477493	475620	479388	479149				
Sample ID	GS 076	GS 077	GS 078	GS 083a	GS 085a	GS 085b	GS 086	GS 094	GS 095A	GS 096	GS 097a	GS 098	GS 099	GSA001	GSA003
Major Element (wt. %)															
SiO ₂	45.83	44.18	45.96	51.86	50.8	48.05	47.48	48.87	47.92	49.6	48.77	46.27	49.94	49.91	49.16
Al ₂ O ₃	12.33	12.02	12.6	11.81	11.54	13.12	13.28	12.5	12.57	14.55	13.8	19.6	17.08	14.15	14.22
TiO ₂	0.97	1.01	1.12	0.66	1.28	1.18	0.79	1.57	1.82	0.89	0.89	1.56	1.35	0.89	0.94
MgO	6.21	5.26	5.05	7.9	4.46	6.76	7.9	5.36	5.66	7.46	7.21	3.72	4.96	7.83	7.57
Fe ₂ O ₃	2.66	2.52	2.51	2.02	3.09	2.68	2.76	2.89	3.22	2.19	2.38	2.61	2.44	2.27	2.47
FeO	13.54	12.87	12.8	10.31	15.77	13.67	14.06	14.75	16.43	11.15	12.13	13.29	12.42	11.57	12.61
CaO	5.05	8.19	9.75	9.3	7.04	8.53	8.61	9.93	8.97	8.44	9.49	8.05	7.48	10.63	10.8
Na ₂ O	2.42	1.6	2.97	2.53	3.93	2.79	2.41	1.86	2.25	3.41	3.12	3.72	3.61	2.05	1.84
K ₂ O	0.09	0.55	0.06	0.51	0.38	0.04	0.02	0.13	0.15	0.46	0.17	0.37	0.31	0.22	0.14
P ₂ O ₅	0.08	0.09	0.11	0.19	0.12	0.11	0.06	0.15	0.18	0.08	0.08	0.48	0.38	0.07	0.08
MnO	0.18	0.2	0.21	0.18	0.2	0.2	0.25	0.23	0.24	0.2	0.19	0.2	0.14	0.19	0.2
LOI	10.57	11.47	7.16	2.56	1.81	3	3.15	2.32	2.12	2	1.86	1.84	1.46	1.29	1.61
Total hydrous	99.93	99.95	100.31	99.83	100.41	100.14	100.77	100.56	101.54	100.43	100.11	101.71	101.56	101.06	101.64
Trace Elements (ppm)															
Ni	78.46	62	70.26	46.71	63.86	76.05	56.47	60.63	56.97	137.78	116.13	40.66	39.18	122.1	110.83
Cr									88.34			23.08	32.41	250.56	242.41
Co	58.15	54.48	50.65	42.81	79.07	56.43	63.67	54.42	56.18	52.45	52.61	61.66	52.79	50.77	49.29
V									401.3			301.82	262.85	317.72	316.76
Sc	43.33	43.12	43.94	40.98	54.98	46.27	48.63	44.24	49.14	41.69	42.57	32.33	26.94	51.21	48.22
Cu	157.26	150.93	118.08	93.62	156.27	135.38	137.59	105.76	112.72	110.15	126.54	10.75	19.12	103.72	119.57
Zn	122.63	109.59	113.15	85.51	163.87	95.78	153.21	124.38	380.32	93.78	101.38	141.25	113.04	91.33	93.33
Mo	0.35	0.29	0.25	0.31	0.34	0.26	0.3	0.54	0.26	0.21	0.33	0.46	1.41	0.17	0.24
Li	131.59	113.09	20.09	25.06	5.11	19.32	15.69	8.3	9.59	8.77	5.08	29.29	21.67	5.08	5.16
Ba	119.74	48.2	34.75	190.4	87.33	18.7	27.23	19.13	14.22	81.67	61.61	363.92	208.51	110.44	27.06
Cs	0.65	0.63	0.21	0.27	0.43	1.24	0.16	0.1	0.13	0.29	0.11	3.02	1.96	0.09	0.11
Rb	2.21	17.31	1.38	6.93	7.19	0.7	0.45	1.37	1	11.58	2.45	10.57	8.46	2.32	2
Sr	85.67	73.03	78.12	470.04	65.36	93.85	147.05	243.79	116.64	70.2	101.48	356.31	418.42	122.77	75.57
Pb	1.6	1.36	0.34	4.21	0.87	0.26	1.13	0.84	0.91	0.36	12.61	4.39	4.39	0.47	0.49
Ga	15.16	15.2	15.58	12.53	17.41	17.3	15.39	19.13	18.18	13.14	15.41	21.46	18.67	16.78	15.9
Zr	55.58	62.01	57.02	48.97	107.59	61.64	40.04	77.51	16.98	40.39	45.78	92.44	98.44	4.75	10.3
Hf	1.54	1.71	1.62	1.34	3	1.76	1.18	2.24	0.65	1.2	1.3	2.39	2.21	0.37	0.51

Nb	2.66	2.91	1.91	2.47	5.27	1.99	0.72	3.05	3.21	2.26	2.33	6.53	5.53	2.22	2.34
Ta	0.16	0.18	0.11	0.14	0.32	0.12	0.04	0.19	0.21	0.14	0.14	0.36	0.3	0.22	0.17
Th	0.29	0.32	0.26	0.85	0.6	0.26	0.1	0.31	0.38	0.23	0.24	2.07	1.67	0.23	0.24
U	0.09	0.17	0.08	0.45	0.3	0.08	0.04	0.1	0.15	0.07	0.08	0.36	0.57	0.05	0.05
Y	20.35	24.31	25.23	14.96	36.07	27.13	21.69	38.01	41.94	19.53	20.04	26.16	22.2	19.12	19.61
La	3.43	3.66	2.95	6.35	5.82	3.13	1.31	4.25	4.68	2.68	2.97	22.02	21.19	2.82	2.69
Ce	9.03	9.82	8.09	14.3	16.2	8.58	3.92	12.54	13.83	7.42	7.99	60.15	55.43	6.31	5.99
Pr	1.39	1.5	1.3	2.01	2.56	1.39	0.71	2.11	2.42	1.19	1.26	8.63	7.64	1.16	1.1
Nd	6.81	7.32	6.7	8.93	12.68	7.17	4.04	11.17	12.85	6.05	6.38	38.03	32.98	6.35	6.01
Sm	2.16	2.33	2.33	2.34	4.13	2.53	1.69	3.91	4.36	2.01	2.11	7.66	6.37	2.02	1.93
Eu	0.78	0.86	0.9	0.74	1.38	0.98	0.69	1.38	1.7	0.72	0.8	2.3	1.96	0.8	0.75
Gd	2.9	3.3	3.42	2.66	5.53	3.7	2.76	5.5	6.77	2.81	2.86	7.2	6	2.81	2.8
Tb	0.53	0.61	0.63	0.43	0.99	0.69	0.53	0.99	1.22	0.52	0.52	0.95	0.8	0.49	0.49
Dy	3.53	4.14	4.29	2.67	6.48	4.66	3.66	6.58	7.53	3.41	3.48	5.19	4.36	3.43	3.51
Ho	0.8	0.95	0.99	0.58	1.45	1.07	0.85	1.48	1.63	0.77	0.79	0.99	0.83	0.74	0.76
Er	2.35	2.79	2.9	1.6	4.15	3.12	2.5	4.24	4.87	2.21	2.3	2.95	2.49	2.2	2.25
Tm	0.37	0.44	0.45	0.24	0.64	0.49	0.39	0.64	0.74	0.34	0.35	0.41	0.35	0.33	0.34
Yb	2.4	2.83	2.95	1.59	4.09	3.18	2.49	3.99	4.33	2.2	2.32	2.68	2.27	2.03	2.23
Lu	0.37	0.43	0.44	0.24	0.61	0.48	0.38	0.57	0.61	0.32	0.34	0.41	0.34	0.29	0.32
Ti	6036.56	6142.28	7106.06	3951.41	10690.19	7395.03	4730.72	9842.49	10078.14	5373.58	5510.1	8900.28	7530.11	5996.42	6129.38
Be	0.32	0.26	0.28	0.7	0.67	0.28	0.13	0.42	0.7	0.32	0.28	0.97	0.75	0.1	0.08
Ag													0.02	0.02	
Cd	0.1	0.09	0.14	0.06	0.12	0.08	0.06	0.14		0.09	0.09			0.05	0.05
Sn	0.71	0.74	0.43	0.71	1.26	0.69	0.47	1.01	0.51	0.59	0.67	0.98	0.91	2.2	1.86
Sb	3.81	1.56	0.3	9.03	0	0.11	0.48	0.11	0.16	0.02	0.08	1.41	1.16	0.08	0.08
W	2.84	1.84	0.04	0.45	0.09	0.05	0.03	0.06	0.54	0.08	0.26	0.1	0.09	0.01	
TI	0.01	0.07	0.01	0.05	0.03	0	0	0.02	0.06	0.08	0.02	0.17	0.11		

Stratigraphic sequence	Lower Seq	Upper Seq	Lower Seq													
Lithology	APHYRIC															
Eastern	BASALT															
Northing	493113	453933	496143	496143	447053	447010	446743	446388	445169	492494	445259	453391.6	466267	438963	438871	438773
Sample ID	GSA004	GSA006	GSA019	GSA021	GSA022	GSA023	GSA025	GSA026	GSA030	GSA044	GSA047	GSA053	GSA057	GSA059	GSA060	GSA061
Major Element (wt. %)																
SiO ₂	45.63	52.61	43.18	42.88	47.88	48.26	49.38	43.43	33.38	49.5	49.89	46.82	45.85	50.99	47.08	46.1
Al ₂ O ₃	11.66	16.72	10.79	11.9	12.64	13.5	12.7	11.55	12.53	13.43	12.74	12.7	13.13	13.94	13.16	12.66
TiO ₂	0.99	1.08	1.18	1.4	2.49	1.55	1.57	1.44	1.73	0.83	1.96	1.65	0.94	1.05	1.02	0.91
MgO	5.83	5.07	4.47	6.16	6.45	6.66	6.26	4.97	5.23	5.95	3.9	5.27	5.17	6.54	6.1	6.48
Fe ₂ O ₃	2.35	1.83	2.63	3.33	2.81	2.61	2.72	2.42	2.98	2.54	2.93	2.41	2.32	2.1	2.01	1.97
FeO	11.99	9.34	13.41	17	14.33	13.31	13.89	12.34	15.17	12.94	14.95	12.31	11.84	10.7	10.23	10.05
CaO	9.52	9.47	8.17	6.07	9.41	10.47	10.12	7.67	9.66	9.44	5.91	7.41	9.21	10.51	9.92	10.54
Na ₂ O	0.97	2.98	2.05	2.36	2.32	2.1	1.87	3.69	2.86	0.18	4.34	2.52	2.73	2.32	2.29	
K ₂ O	0.03	0.34	0.81	0.07	0.31	0.13	0.28	0.15	1.27	0.08	0.23	1.46	0.36	0.32	0.43	0.32
P ₂ O ₅	0.08	0.12	0.1	0.14	0.38	0.15	0.17	0.15	0.16	0.07	0.23	0.16	0.09	0.14	0.14	0.1
MnO	0.2	0.15	0.18	0.2	0.23	0.22	0.22	0.19	0.24	0.19	0.24	0.19	0.19	0.2	0.19	0.17
LOI	11.79	1.04	13.57	9.65	1.63	1.93	1.97	12.55	15.45	5.47	2.42	7.87	1.79	0.81	1.31	1.99
Total_hydro	101.04	100.75	100.53	101.17	100.89	100.9	101.16	100.54	100.66	100.6	99.73	100.77	93.62	99.61	93.88	93.46
Trace Elements (ppm)																
Ni	49.94	42.44	63.66	73.44	83.24	80.45	59.86	48.55	56.13	97.35	19.45	47.82	122.17	74.61	65.67	88.79
Cr	69.79	72.74	35.97	44.29	203.43	151.64	78.66	65.62	74.82	139	2.07	43.15	133.37	126.08	103.31	186.23
Co	44.89	34.63	58.77	73.57	52.56	47.76	54.77	48.14	53.55	55.22	47.6	45.74	71.06	48.79	45.28	53.12
V	289.4	231.75	352.72	414.89	388.17	369.73	380.67	342.13	426.28	319.56	397.41	388.67	351.14	303.88	278.22	276.32
Sc	42.79	33.39	44.94	49.8	48.94	55.35	53.93	46.42	51.87	52.9	50.67	45.97	59.62	52.33	43.2	45.37

Cu	114.35	113.94	141.85	195.53	57.52	94.01	94.91	84.8	97.46	134.2	108.87	165.54	112.19	101	85.6	112.66
Zn	93.29	79.96	112.34	153.29	131.4	122.6	116.38	105.7	144.52	89.68	140.84	99.77	112.25	94.04	92.7	79.97
Mo	0.17	0.24	0.41	0.29	0.71	0.31	0.47	0.32	0.32	0.23	0.4	0.39	0.11	0.86	1.01	0.25
Li	19.74	11.07	20.12	25.73	5.61	5.29	3.46	12.3	10.16	23.22	10.06	18.75	13.47	2.16	3.28	2.46
Ba	12.34	96.47	75.07	12.41	106.86	48.95	74.59	38.62	121.91	6.29	69.1	137.99	126.72	49.52	101.95	74.94
Cs	0.06	0.35	0.89	3.61	0.27	0.1	0.22	0.13	0.62	0.08	0.93	2.96	0.13	0.19	0.19	0.13
Rb	0.82	9.56	18.16	2.54	8.3	1.95	7.42	3.76	22.69	2.15	4.89	32.04	7.83	5.76	9.94	7.03
Sr	74.02	253.46	133.38	104.5	172.89	209.74	141.15	165.48	223.79	187.38	176.85	144.41	111.36	184.46	219.5	174.94
Pb	0.62	1.27	1.77	1.65	1.86	1.09	1.06	1.16	2.14	1.02	1.44	0.94	0.77	1.25	1.2	0.73
Ga	15.82	19.39	15.53	18.29	20.26	19.22	19.22	17.1	20.45	16.77	22.15	20.52	16.62	17.84	17.64	15.75
Zr	44.05	50.45	59.91	44.03	98.5	50.27	78.28	60.07	67.45	20.51	126.95	40.77	16.98	51.5	80.42	36.7
Hf	1.1	1.47	1.93	1.58	2.86	1.7	2.48	2.08	2.29	0.76	3.43	1.34	0.71	1.68	2.1	1.17
Nb	1.99	4.25	3.77	4.37	15	7.74	7.83	6.41	2.87	2.47	5.78	5.56	3.12	5.42	5.66	3.29
Ta	0.18	0.32	0.28	0.33	0.93	0.51	0.71	0.43	0.24	0.19	0.39	0.37	0.24	0.32	0.39	0.2
Th	0.27	0.52	0.47	0.52	1.1	0.61	0.7	0.69	0.35	0.31	0.7	0.62	0.36	0.52	0.63	0.32
U	0.07	0.17	0.14	0.2	0.27	0.15	0.18	0.18	0.15	0.08	0.27	0.18	0.1	0.17	0.2	0.1
Y	10.24	19.28	6.44	7.64	39.37	27.43	31.74	8.98	8.44	18.37	39.93	29.15	23.11	24.14	25.87	19.32
La	3.06	7.37	4.98	4.57	14.63	7.45	8.45	7.36	4.73	3.32	8.5	6.84	4.15	7.44	7.09	4.1
Ce	8.63	15.43	11.4	10.2	29.99	15.63	17.89	15.65	11.4	7.19	19.94	15.74	9.26	15.81	18.58	11.8
Pr	1.25	2.59	1.98	1.81	4.9	2.7	3	2.6	2.08	1.25	3.35	2.72	1.59	2.64	2.64	1.69
Nd	6.37	12.26	9.58	9.01	23.54	13.27	15.02	12.86	11.03	6.41	17.73	14.28	8.16	12.77	12.29	8.26
Sm	2	3.07	2.7	2.6	6.2	3.89	4.27	3.38	3.17	2.12	5.3	4.22	2.55	3.39	3.24	2.31
Eu	0.54	1.08	0.77	0.79	2.09	1.36	1.42	1.03	0.87	0.78	1.79	1.53	0.93	1.14	1.15	0.92
Gd	2.37	3.35	2.48	2.25	7.21	4.65	5.26	2.79	2.63	2.69	6.59	5.2	3.41	3.94	4.11	3
Tb	0.3	0.54	0.28	0.32	1.16	0.81	0.94	0.41	0.45	0.5	1.14	0.87	0.61	0.67	0.65	0.48
Dy	1.95	3.6	1.43	1.67	7.3	5.29	6.04	1.97	1.92	3.39	7.28	5.77	4.1	4.46	4.56	3.45
Ho	0.39	0.73	0.26	0.31	1.54	1.09	1.27	0.39	0.49	0.72	1.54	1.15	0.9	0.92	0.92	0.7
Er	1.15	2.1	1.23	0.93	4.47	3.19	3.7	1.13	1.16	2.15	4.63	3.28	2.67	2.68	2.69	2.01
Tm	0.19	0.3	0.14	0.17	0.65	0.48	0.55	0.18	0.22	0.32	0.72	0.45	0.38	0.39	0.42	0.29
Yb	1.31	1.95	0.98	1.18	4.22	2.91	3.56	1.22	1.61	2	4.58	2.82	2.51	2.48	2.54	1.85
Lu	0.22	0.28	0.19	0.21	0.6	0.43	0.52	0.2	0.3	0.29	0.67	0.36	0.36	0.35	0.39	0.27
Ti	3543.18	7091.89	7459.25	8905.14	16299.96	10305.08	10642.38	9469.26	11673.77	5693.39	13453.95	11150.78	6860.86	7054.23	6149.16	5462.99
Be	191.54	0.34	0.88	0.36	0.57	0.51	0.32	0.25	0.24	0.32	0.71	0.71	0.36	0.69	461.53	291.31
Ag	19.53	0.04	0.04	0.05	0.07	0.03	0.06	0.04	0.05	0.02	0.07	0.03	0.01	0.04	31.76	25.37
Cd	51.28	0.08	0.08	0.08	0.1	0.07	0.09	0.07	0.09	0.05	0.08	0.07	0.07	0.1	70.91	52.07
Sn	0.78	0.44	0.52	0.87	0.66	1.99	2.07	1.95	0.32	0.66	0.53	0.39	0.46			
Sb	103.96	0.04	1.04	1.2	0.28	0.71	0.31	0.66	0.39	0.55	0.49	2.26	0.08	0.11	209.29	86.13
W	730.45	0.02	7.13	2.9	0.72	0.36	0.08	1.74	2.67	0.16	0.06	0.65	0.04	0	209.23	77.73
Tl	49.32		0.05		0.03	0.04	0.01		0.01			0.14		64.4	67.73	

Stratigraphic sequence	Lower Seq	Lower Seq	Upper Seq	Lower Seq												
Lithology	APHYRIC															
Eastern	BASALT															
Northing	473458	475436	475741	477113	477512	480510	480373	479316	445861	446464	447684	447896	448087	448667		
Sample ID	GSA063	GSA065	GSA066	GSA067	GSA069	GSA070	GSA071	GSA074	GSA075	GSA076	GSA077	GSA078	GSA079	GSA080		
Major Element (wt. %)																
SiO ₂	49.89	51.52	57.98	51.47	51.6	50.58	50.9	50.27	55.51	43.06	49.56	58.49	47.43	47.03		
Al ₂ O ₃	12.68	12.77	14.73	13.54	13.05	13.2	12.65	13.81	11.31	11.98	13.2	14.39	13.11	13.36		
TiO ₂	0.98	1.21	0.65	1.27	1.21	1.05	1.02	0.77	1.52	1.11	1.58	1.38	1.78	1.53		
MgO	5.26	4.68	4.8	5.24	4.68	6.35	6.01	7.07	2.15	4.54	5.58	3.96	6.39	7.56		
FeO	2.95	3.04	1.55	3.02	2.88	2.73	2.88	2.45	2.1	1.92	3.01	1.5	3.01	3		
CaO	15.03	15.52	7.93	15.4	14.67	13.93	14.68	12.5	10.7	9.8	15.35	7.64	15.35	15.29		
Na ₂ O	2.95	3	3.62	2.66	2.2	2.62	2.51	1.93	4.22	1.85	2.94	3.4	2.08	1.67		
K ₂ O	0.2	0.16	0.79	0.16	0.23	0.15	0.18	0.14	0.05	0.87	0.37	1.01	0.29	0.04		
P ₂ O ₅	0.09	0.11	0.12	0.14	0.12	0.08	0.08	0.07	0.17	0.11	0.17	0.39	0.17	0.13		
MnO	0.23	0.22	0.13	0.24	0.21	0.19	0.15	0.21	0.13	0.19	0.2	0.11	0.24	0.21		
LOI	1.84	2.41	2.23	0.55	1.25	0.6	0.97	0.81	6.31	12.62	0.53	1.24	0.73	0.03		
Total_hydrous	100.66	101.26	100.53	101.53	101.38	101.29	101.28	101.4	100.35	100.43	101.38	100	101.36	102.12		
Trace Elements (ppm)																
Ni	60.73	46.21	68.12	46.75	42.82	66.68	62.67	94.84	13.02	52.66	46.59	101.58	68.09	64.42		
Cr	27.08	19.87	144.23	18.65	19.67	104.48	99.03	113.01	14.55	40.33	88.08	96.11	122.22	73.73		

Co	53.27	53.42	30.61	53.86	46.01	40.2	37.23	54.91	17.93	36.69	45.3	28.16	55.68	58.03
V	341.89	390.86	159.34	404.36	381.37	341.93	374.81	255.68	350.05	282.5	346.26	153.57	372.92	402.2
Sc	47.24	48.51	22.17	49.19	47.37	49.45	46.43	43.13	33.13	37.61	47	15.24	47.2	53.62
Cu	150.54	120.99	92.58	158.06	40.51	162.73	33.38	131.81	112.82	129.75	101.52	69.77	89.13	131.9
Zn	116.7	127.21	95.77	141.61	113.53	100.21	132.47	96.3	109.36	83.59	116.94	84.96	114.44	108.67
Mo	0.18	0.18	0.4	0.39	0.34	11.8	6.53	0.32	0.33	0.4	0.46	0.78	0.67	0.25
Li	5	4.69	13.77	5.91	12.42	1.74	4.06	4.73	11.06	27.66	5.26	13	6.7	6.6
Ba	60.66	34.09	379.72	32.34	28.95	24.94	109.52	40.14	22.86	67.17	64.34	228.44	95.42	12.89
Cs	0.2	0.13	0.15	0.23	0.34	0.07	0.13	0.05	0.04	0.39	0.34	1.39	0.25	0.08
Rb	4.27	1.66	17.57	2.6	6.24	1.54	3.42	1.22	1.15	30.43	8.84	20.23	6.17	0.69
Sr	105.11	56.8	285.18	118.18	80.05	99.66	129.01	97.15	214.14	90.11	140.82	606.56	124.68	258.64
Pb	0.55	0.63	3.14	0.92	0.75	0.98	2.64	0.41	1.84	0.5	0.76	2.77	1.8	0.29
Ga	17.36	17.95	17.22	19.51	18.54	17.89	19.81	14.6	16.72	15.86	18.03	21.26	18.2	19.35
Zr	54.51	58.15	87.53	63.95	70.49	23.48	37.25	14.63	103.05	60	46.05	233.85	32.31	23
Hf	1.65	1.75	2.29	1.9	1.99	0.85	1.19	0.65	2.79	1.61	1.58	5.29	1.37	0.84
Nb	1.74	2.1	4.58	2.25	2.15	1.12	1.57	1.83	4.7	3.12	6.69	14.27	7.08	4.01
Ta	0.13	0.15	0.3	0.16	0.15	0.09	0.1	0.13	0.3	0.2	0.41	0.87	0.45	0.25
Th	0.37	0.4	1.59	0.41	0.41	0.2	0.46	0.27	0.53	0.31	0.55	2.62	0.56	0.06
U	0.12	0.12	0.61	0.15	0.12	0.19	0.74	0.07	0.21	0.14	0.13	0.85	0.13	0.02
Y	34.3	37.72	16.68	38.52	38.41	27.21	27.66	18.23	20.88	18.13	34.68	18.87	36.74	27.22
La	3.31	3.8	10.75	3.84	3.76	2.51	6.06	2.38	6.26	4.19	6.86	30.97	6.52	2.84
Ce	8.34	10.11	24.06	11	10.1	6.95	15.68	6.47	16.33	12.8	18.76	68.55	17.62	8.2
Pr	1.3	1.54	3.05	1.61	1.53	1.12	2.03	1.01	2.49	1.74	2.6	8.47	2.6	1.39
Nd	6.52	7.86	12.77	8.36	7.92	5.85	8.99	5.02	12.22	8.59	12.65	33.88	12.93	7.7
Sm	2.36	2.76	2.86	2.84	2.76	2.13	2.47	1.56	3.44	2.52	3.77	6.29	3.98	2.63
Eu	0.82	0.91	0.94	1.02	1.12	0.84	0.94	0.63	1.16	0.8	1.34	1.94	1.37	1.11
Gd	3.8	4.24	3.48	4.53	4.35	3.41	3.78	2.33	4.26	3.16	5.2	7.08	5.54	3.81
Tb	0.7	0.81	0.47	0.83	0.81	0.61	0.61	0.42	0.61	0.5	0.85	0.75	0.9	0.65
Dy	5.62	6.3	2.97	6.55	6.22	4.73	4.47	3.23	3.99	3.38	6.13	4	6.45	4.87
Ho	1.2	1.36	0.56	1.4	1.37	1	0.96	0.67	0.79	0.66	1.24	0.69	1.32	1.02
Er	3.73	4.14	1.61	4.19	4.19	2.95	2.92	2	2.36	1.96	3.63	1.85	3.89	2.92
Tm	0.59	0.63	0.23	0.61	0.64	0.43	0.46	0.29	0.36	0.29	0.54	0.24	0.58	0.45
Yb	3.69	4.08	1.45	4.01	4.21	2.88	2.81	1.93	2.4	1.9	3.29	1.49	3.64	2.77
Lu	0.58	0.61	0.22	0.6	0.67	0.44	0.43	0.29	0.38	0.3	0.48	0.22	0.55	0.43
Ti	5412.2	6788.37	3604.88	7136.2	6770.66	5923.93	5697.67	4161.35	8737.61	6308.57	8752.58	7785.1	9768.75	8612.74
Be	245.86	304.37	670.32	305.78	338.53	201.22	323.34	209.08	511.15	325.58	465.59	1099.55	463.94	400.6
Ag	25.63	26.39	38.68	34.23	22.18	69.28	21.23	17.68	45.63	27.64	20.75	76.93	20.34	18.24
Cd	61.5	57.08	73.16	79.5	67.74	36.47	39.18	26.02	96.49	66.67	57.88	178.93	53.65	32.93
Sn														
Sb	82.97	85.59	104.58	93.3	150.19	431.1	323.72	74.61	143.98	189.88	251.87	185.36	161.53	25.32
W	105.96	109.31	226.96	108.44	630.47	925.11	1048.89	108.4	217.05	69.94	134.13	228.4	252.24	60.33
Tl	60.92	47.97	95.99	55.49	61.67	60.17	61.13	50.63	34.66	109.52	69.04	160.06	86.42	29.09

Stratigraphic sequence	Lower Seq	Upper Seq	Lower Seq	Upper Seq	Lower Seq	Upper Seq	Lower Seq	Upper Seq	Lower Seq	Upper Seq	Lower Seq	Upper Seq	Lower Seq	Upper Seq
Lithology	APHYRIC BASALT	APHYRIC BASALT	DOLERITE											
Eastern	451170	527947	478715	409884	477449	477515	452606	492366	492534	469326	467141	462277	473481	451443
Northing	1220070	1290588	1235136	1222170	1138461	1135249	1111019	1144099	1140459	1213406	1215206	1216421	1227849	527892
Sample ID	GSA081	GSA085	GS_041	GS_048	GS_088	GS_093	GSA008	GSA041B	GSA042	GSA055	GSA056	GSA058	GSA064	GSA086
Major Element (wt. %)														
SiO ₂	48.22	46.77	49.36	54.26	49.21	48.46	52.17	52.02	53.7	45.37	45.22	49.52	47.78	48.79
Al ₂ O ₃	14.88	14.47	14.26	14.76	14.5	12.44	16.43	10.94	13.42	12.24	13.41	10.49	9.75	13.46
TiO ₂	1.74	1.08	0.81	0.88	0.83	1.8	1.3	0.64	0.68	0.91	1.26	0.57	1.05	1.78

MgO	5.37	6.45	6.76	6.56	6.76	5.15	4.96	9.28	6.66	6.03	5.62	9.82	1.47	6.27	7.37	
Fe2O3	2.49	2.83	2.54	1.66	2.32	3.11	1.96	2.13	1.96	2.43	2.45	1.47	3.24	2.62	2.68	
FeO	12.71	14.41	12.94	8.44	11.82	15.84	9.99	10.88	9.97	12.39	12.48	7.49	16.52	13.36	13.65	
CaO	11.1	10.12	11.31	8.88	11.41	9.37	9.76	10.21	7.31	10.09	10	7.23	7.81	10.39	10.13	
Na2O	1.54	2.52	2.1	2.37	2.06	2.4	2.56	1.7	2.07	1.16	2.19	2.32	3.26	1.35	2.12	
K2O	0.14	0.07	0.16	0.87	0.1	0.19	0.37	0.94	1.4	0.22	0.21	2.33	0.35	0.17	0.31	
P2O5	0.16	0.15	0.07	0.21	0.07	0.19	0.13	0.15	0.18	0.08	0.08	0.32	0.19	0.17	0.14	
MnO	0.21	0.21	0.22	0.15	0.21	0.25	0.16	0.19	0.18	0.2	0.19	0.13	0.3	0.21	0.22	
LOI	2.39	2.02	0.61	2.25	2.02	1.15	1.31	1.94	3.2	1.45	0.71	1.51	9.5	2.75	2.19	
Total_hydrous	100.94	101.1	101.13	101.27	101.31	100.34	101.1	101.03	100.72	92.56	93.82	93.2	101.19	101.32	101.16	
Trace Elements (ppm)																
Ni	51.94	84.68	79.45	148.64	65.7	48.18	58.71	66.86	39.65	122.32	77.89	264.27	1.31	63.78	93.59	
Cr	49.47	135.85	110.16	228.31	81.69	121.32	523.15	269.33	136.06	88.01	910.11	3.26	97.91	172.52		
Co	42.76	52.74	53.76	38.25	57.79	51.29	36.94	49.95	38	64.05	58.53	48.33	37.88	48.26	58.15	
V	339.66	300.26	254.57	190.82	259.13		274.89	282.8	273.12	352.06	554.58	142.64	89.56	354.09	300.78	
Sc	34.24	43.22	43.07	28.68	50	47.48	34.93	52.93	45.17	57.12	61.81	32.26	29.03	39.87	44.09	
Cu	170.09	81.45	155.56	45.31	151.32	97.75	89.28	73.72	126.36	199.9	214.96	59.96	18.48	125.12	110.64	
Zn	101.61	129.06	294.56	232.12	303.57	150.45	105.25	80.59	108.57	104.42	111.53	57.75	129.57	103.4	106.19	
Mo	0.48	0.35	0.27	0.79	0.26	0.44	0.31	0.11	0.37	0.24	0.32	0.14	0.34	0.39	0.3	
Li	8.15	12.71	10.06	18.08	8.73	9.59	4.85	7.26	11.04	11.24	3.1	51.1	5.54	10.16	12.63	
Ba	22.99	71.91	15.5	291.13	36.49	34.83	99.05	384.81	606.18	46.05	146.89	651.27	126.71	45.02	173.88	
Cs	0.09	0.15	0.12	1.12	0.09	0.31	0.17	0.33	0.45	0.2	0.08	1.25	0.3	0.06	0.23	
Rb	2.97	1.17	1.44	22.12	0.97	2.53	6.78	18.61	29.77	4.77	3.61	90.31	4.88	3.74	5.39	
Sr	292.87	243.48	79.33	216.74	100.8	105.92	253.91	290.12	348.36	126	169.14	300.6	112.49	197.04	142.13	
Pb	1.2	1.17	0.76	3.03	0.67	0.82	1.14	2.56	2.73	0.98	1.18	9.24	0.49	1	0.88	
Ga	22.1	18	14.63	15.91	15.26	19.84	20.53	12.38	14.64	17.72	21.53	13.94	18.34	20.67	16.88	
Zr	87.25	39.18	12.34	124.39	27.7	90.08	45.11	32.42	47.74	34.55	18.75	87.51	101.53	69.92	40.14	
Hf	2.53	1.01	0.49	2.89	0.8	2.55	1.48	1.07	1.42	1.2	0.84	2.64	2.76	2.1	1.06	
Nb	5.53	2.25	0.7	7.32	2.31	3.56	5.69	1.89	2.57	3.54	3.52	4.9	3.02	5.29	2.13	
Ta	0.36	0.14	0.07	0.44	0.17	0.22	0.41	0.15	0.18	0.22	0.28	0.31	0.2	0.35	0.16	
Th	0.61	0.32	0.11	1.91	0.35	0.39	0.59	0.6	0.8	0.41	0.42	2.49	0.63	0.55	0.31	
U	0.19	0.1	0.07	0.55	0.13	0.12	0.2	0.19	0.32	0.11	0.11	1.03	0.22	0.16	0.1	
Y	29.18	18.25	21.31	21.99	21.14	42.34	23.13	14.63	17	21.85	25.69	12.81	29.17	31.52	17.06	
La	6.84	5.96	1.3	15.41	2.88	5.05	6.06	5.02	6.47	4.46	4.69	14.99	6.34	6.44	5.52	
Ce	19.77	14.57	3.91	35.51	7.39	14.74	13.17	9.78	12.51	9.46	10.64	29.42	17.01	18.03	13.68	
Pr	2.91	2	0.74	4.43	1.18	2.47	2.34	1.58	1.96	1.63	1.83	4.36	2.34	2.77	1.83	
Nd	14.18	8.89	4.25	17.73	5.8	12.92	11.91	7.76	9.61	8.19	9.8	19.39	11.81	13.93	8.16	
Sm	4.08	2.09	1.69	3.67	1.9	4.42	3.42	2.12	2.48	2.5	3.05	3.91	3.7	4.06	2	
Eu	1.56	0.87	0.75	1.22	0.84	1.56	1.16	0.71	0.84	0.9	1.17	1.03	1.22	1.45	0.85	
Gd	5.23	2.88	2.84	4.34	3.03	6.22	4.03	2.49	2.88	3.29	4	3.23	4.64	5.39	2.81	
Tb	0.81	0.42	0.56	0.69	0.59	1.11	0.68	0.4	0.47	0.59	0.69	0.45	0.7	0.84	0.41	
Dy	5.45	2.89	3.59	3.93	3.68	7.41	4.27	2.71	2.99	3.91	4.77	2.49	4.88	5.82	2.91	
Ho	1.07	0.62	0.82	0.81	0.84	1.66	0.89	0.55	0.64	0.83	1.02	0.5	1.04	1.1	0.63	
Er	2.97	1.94	2.51	2.49	2.55	4.77	2.51	1.67	1.87	2.49	2.98	1.36	3.25	3.15	1.89	
Tm	0.4	0.3	0.41	0.37	0.4	0.72	0.36	0.24	0.28	0.36	0.42	0.21	0.5	0.45	0.28	
Yb	2.59	1.94	2.53	2.4	2.48	4.58	2.29	1.54	1.86	2.45	2.85	1.33	3.31	2.64	1.9	
Lu	0.39	0.29	0.39	0.36	0.39	0.67	0.34	0.25	0.27	0.35	0.39	0.19	0.51	0.37	0.3	
Ti	9777.1	6216.52	3983.91	4911.33	4440.71	11451.22	8786.13	4331.08	4676.02	6602.97	10049.67	3255.37	5874.03	9869.64	6157.18	
Be	562.93	284.67	0.31	1.04	0.54	0.49	0.49	0.58	0.53	0.32	0.29	2.28	539.24	581.34	241.6	
Ag	44.24	22.99						0.04	0.02	0.03	0.03	0.02	0.05	39.33	34.52	20.79
Cd	84.52	49.67					0.16	0.06	0.05	0.06	0.07	0.08	0.05	102.24	76.64	50.37
Sn		0.19	0.43	0.23	1.31	0.5	0.31	0.36	0.4	0.58	0.56					
Sb	103.54	195.95	0.06	0.2	0.76	0.13	0.09	0.18	0.61	0.26	0.05	0.62	335.3	78.65	117.85	
W	127.46	128.01	0.14	0.18	0.44	0.09	0.06	0.17	0.11	0.02	0.19	85.81	103.24	124.21		
Tl	55.1	32.94	0.09	0.2	0.06	0.01	0.01	0.06	0.13	0.01	0.41	74.78	41.33	69.07		

Stratigraphic sequence	Lower Seq	Lower Seq	Upper Seq												
------------------------	-----------	-----------	-----------	-----------	-----------	-----------	-----------	-----------	-----------	-----------	-----------	-----------	-----------	-----------	-----------

Lithology	FELDSPA R-PYRIC																
Eastern	BASALT																
Northing	454174	450352	414820	415015	498686	500013	500013	452990	452089	451939	451674	445452	442542	442536	500351		
Sample ID	GS_007	GS_031	GS_068	GS_069	GS_081	GS_082a	GS_082b	GSA007	GSA014	GSA015	GSA017	GSA029	GSA033	GSA035	GSA037		
Major Element (wt. %)																	
SiO ₂	50.45	52.59	48.16	47.93	59	56.81	54.74	51.13	53.13	52.11	51.53	48.66	52.84	49.36	56.86		
Al ₂ O ₃	13.95	13.07	16.83	15.24	15.01	15.73	15.35	16.91	16.16	16.11	15.85	13.28	16.04	14.43	14.74		
TiO ₂	1.76	1.34	1.27	1.4	0.53	0.7	0.69	1.28	1.14	1.15	1.39	1.46	1.24	1.09	0.47		
MgO	5.4	5.39	4.81	5.85	3.78	3.05	4.15	5.56	5.18	5.88	5.3	6.02	5.81	3.49	4.57		
Fe ₂ O ₃	2.47	2.28	2.18	2.36	1.3	1.39	1.55	1.97	1.84	1.96	2.31	2.8	1.89	1.63	1.48		
FeO	12.57	11.64	11.1	12.03	6.63	7.07	7.92	10.06	9.37	9.99	11.78	14.27	9.61	8.31	7.52		
CaO	10.21	7.04	10.6	9.96	5.18	12.58	8.33	9.38	8.91	9.51	8.21	9.66	5.75	10.77	6.98		
Na ₂ O	2.8	4.31	2.04	2.82	4.75	2.2	2.42	2.91	3.1	2.86	2.55	1.87	4.38	2.33	2.36		
K ₂ O	0.18	0.06	0.5	0.34	0.31	0.36	0.66	0.46	0.43	0.23	0.35	0.37	0.03	0.06	0.55		
P ₂ O ₅	0.16	0.14	0.13	0.12	0.13	0.15	0.21	0.12	0.11	0.1	0.15	0.12	0.14	0.12	0.08		
MnO	0.2	0.18	0.17	0.19	0.11	0.1	0.13	0.17	0.16	0.17	0.18	0.22	0.16	0.12	0.12		
LOI	1.25	1.63	2.89	2.68	2.86	3.51	3.57	1.16	1.01	0.7	1.47	2.51	2.99	2.79	5.22		
Total_hydro_us	101.4	99.67	100.69	100.91	99.6	103.64	99.72	101.1	100.55	100.77	101.06	101.24	100.87	94.5	100.95		
Trace Elements (ppm)																	
Ni	56.72	43.97	54.52	67.4	40.69	37.31	28.12	90.68	69.34	91.65	66.24	73.6	64.23	45.78	58.01		
Cr	92.34	56.41						161.37	134.91	178.72	27.33	161.95	124.74	74.05	166.09		
Co	43.83	41.44	40.55	47.11	24.38	24.96	26.52	39.13	34.91	40.54	44.35	53.88	36.03	29.06	31.49		
V	349.4	318.4						237.56	245.4	232.2	257.88	412.49	250.53	196.3	130.94		
Sc	39.14	40.68	30.75	35.77	19.65	21.43	25.08	34.79	33.8	34.77	28.71	54.2	34.83	25.34	26.69		
Cu	140.21	126.63	115.38	112.41	61.6	150.05	87.59	6.63	35.11	3.66	25.03	97.63	98.7	52.97	19.26		
Zn	98.12	94.12	100.33	106.97	77.32	67.77	83.96	96.76	84.69	75.33	116.59	120.41	112.38	86.15	55.84		
Mo	0.6	0.82	0.51	0.61	0.35	0.83	1.2	0.36	0.27	0.2	0.42	0.34	0.53	0.7	0.29		
Li	8.41	3.12	10.23	9.16	15.11	20.9	35.21	8.51	2.62	1.45	3.34	4.77	3.15	2.64	17.88		
Ba	37.87	26.83	147.64	222.83	241.89	159.72	283.21	76.06	79.19	37.71	103.65	42.32	42.49	30.5	211.61		
Cs	0.23	0.05	0.51	0.33	0.18	0.32	0.33	0.25	0.26	0.13	0.27	0.22	0.1	0.07	0.76		
Rb	4.04	0.69	15.08	6.32	4.69	5.41	11.45	8.47	8.86	2.94	6.94	4.22	0.62	0.98	7.05		
Sr	247.42	82.61	218.34	190.36	165.44	143.39	129.52	253.8	255.33	240.4	243.55	106.33	288.08	319.77	395.13		
Pb	0.94	0.77	2.01	1.7	3.12	5.64	4.36	1.16	1.34	1.18	1.42	0.8	0.95	1.83	1.53		
Ga	19	16.19	19.45	17.69	15.12	17.69	15.28	19.47	19.64	17.62	20.33	20.31	14.93	21.78	16.84		
Zr	39.62	53.86	77.01	70.67	81.65	90.74	97.53	51.31	51.07	39.53	76.65	39.71	35.23	43.58	54.53		
Hf	1.27	1.42	2.12	1.99	2.13	2.35	2.52	2.59	1.61	1.36	2.31	1.5	1.25	1.55	1.62		
Nb	5.26	4.87	4.48	3.92	3.72	5.26	5.48	5.18	4.65	3.99	5.85	2.7	5	4.93	2.2		
Ta	0.34	0.31	0.28	0.24	0.26	0.32	0.33	0.35	0.35	0.3	0.41	0.22	0.36	0.34	0.18		
Th	0.5	0.49	0.93	0.91	1.27	1.62	1.92	0.58	0.59	0.39	0.95	0.33	0.44	0.49	0.68		
U	0.16	0.16	0.29	0.29	0.58	0.82	1.01	0.14	0.17	0.09	0.26	0.09	0.15	0.17	0.42		
Y	31.29	28.7	24.39	23.79	12.31	18.63	21.62	21.99	20.51	20.46	25.85	32.3	19.99	22.17	10.91		
La	6.17	6.06	7.27	6.41	9.41	11.63	13.12	7.1	5.78	4.31	7.42	3.86	6.71	5.95	6.72		
Ce	18.1	16.11	17.25	15.52	19.54	25.04	28.81	13.8	11.72	9.64	15.64	9.54	13.97	12.83	11.18		
Pr	2.74	2.34	2.45	2.24	2.49	3.23	3.77	2.66	2.16	1.85	2.7	1.8	2.36	2.26	1.87		
Nd	13.84	11.48	11.17	10.42	10.19	13.28	15.66	12.66	10.16	9.3	13.62	9.69	11.78	11.12	8.8		
Sm	4.14	3.37	3.15	3.04	2.28	3.04	3.58	3.43	3.03	2.83	3.76	3.44	3.3	3.2	1.98		
Eu	1.46	1.2	1.09	1.01	0.74	0.93	0.97	1.16	1.12	1	1.39	1.25	1.18	1.13	0.63		
Gd	5.31	4.51	3.84	3.76	2.28	3.23	3.8	3.88	3.54	3.4	4.6	4.77	3.74	3.76	2		
Tb	0.85	0.73	0.67	0.65	0.35	0.52	0.61	0.67	0.64	0.58	0.76	0.85	0.66	0.65	0.31		
Dy	5.94	5.2	4.3	4.25	2.07	3.25	3.77	4.17	4	3.76	4.78	5.81	3.98	4.05	1.86		
Ho	1.13	1.05	0.95	0.94	0.44	0.7	0.82	0.84	0.83	0.8	1	1.26	0.81	0.83	0.4		
Er	3.16	2.92	2.75	2.68	1.22	1.99	2.34	2.45	2.32	2.28	2.83	3.64	2.18	2.35	1.12		
Tm	0.44	0.43	0.41	0.41	0.18	0.31	0.36	0.35	0.36	0.42	0.53	0.32	0.34	0.18			
Yb	2.54	2.52	2.65	2.6	1.16	2	2.35	2.23	2.07	2.71	3.37	1.85	2.11	1.08			
Lu	0.34	0.36	0.4	0.39	0.18	0.3	0.36	0.31	0.36	0.31	0.39	0.46	0.27	0.28	0.18		
Ti	9800.4	7860.57	7749.99	8673.11	3166.43	4055.69	4161.56	8402.72	7629.61	7556.3	9127.74	9804.81	8293.96	7594.55	2984.55		

Be	590.55	510.28	0.54	0.49	0.55	0.91	0.88	0.4	0.44	0.33	0.52	0.29	0.41	0.44	0.59
Ag	25.2	33.74						0.03	0.04	0.02	0.04	0.03	0.03	0.03	0.03
Cd	51.32	47.57	0.1	0.07	0.07	0.09	0.09	0.06	0.05	0.03	0.06	0.08	0.1	0.1	0.04
Sn		0.93	0.92	0.65	1.44	1.05	0.58	0.55	0.61	0.67	0.41	0.46	0.57	0.57	0.26
Sb	266.63	111.69	0.07	0.15	0.22	2.19	1.26	0.14	0.13	0.11	0.11	0.09	0.68	0.38	0.51
W	196.85	101.29	0.13	0.17	0.11	0.6	0.78	0.05	0.02	0.02	0.07	0.08	0.04	0.04	0.01
Tl	40.29	18.73	0.09	0.06	0.04	0.08	0.1		0.03		0.01				

Stratigraphic sequence	Lower Seq	Lower Seq	Upper Seq	Upper Seq	Lower Seq	Lower Seq	Upper Seq	Upper Seq	Lower Seq	Lower Seq	Upper Seq	Lower Seq	Upper Seq	HBL-PYRIC	HBL-PYRIC
Lithology	FELDSPA	FELDSPA	FELDSPA	GABBRO	BASALT	BASALT									
Eastern	496866	496104	452512	439772	455335	451430	478242	408592	495581	453378.5	453402.2	480737	480944	450878	473343
Northing	1142266	1142209	1219633	1235597	1226307	1226250	1234610	1208268	1088921	1236113	1236176	1233035	1233428	1227765	1227576
Sample ID	GSA039	GSA040A	GSA083	GS_001	GS_003	GS_026a	GS_042	GS_052	GSA018	GSA052	GSA054	GSA072	GSA073	GS_030	GSA062
Major Element (wt. %)															
SiO ₂	50.08	46.99	54.79	50.21	54.21	45.26	43.78	48.45	51.36	44.65	42	51.39	55.6	54.38	54.06
Al ₂ O ₃	12.89	12.4	17.38	16.37	5.23	12.14	5.44	12.86	8.02	7.54	9.54	15.05	12.02	13.65	14.62
TiO ₂	0.77	1.76	1.21	1.41	0.45	1.73	1.08	1.1	0.52	1.15	1.8	0.8	1.6	0.73	0.56
MgO	6.48	6.45	2.94	4.7	16.31	6.94	21.44	10.51	12.15	18	8.12	6.35	1.25	5.93	3.1
Fe ₂ O ₃	2.61	3.33	1.33	2.11	1.5	3.34	2.74	2.1	2.12	2.58	2.52	1.99	3.41	1.42	1.31
FeO	13.33	16.96	6.76	10.74	7.65	17.02	13.97	10.72	10.79	13.15	12.85	10.13	17.37	7.23	6.66
CaO	11.14	7.2	6.66	9.96	12.68	12.42	7.8	10.35	12.94	9.08	9.36	9.34	5.54	6.8	6
Na ₂ O	1.23	3.37	3.93	2.73	1.05	1.79	0.09	1.82	1.31	0.64	1.53	2.19	3.61	3.31	3.07
K ₂ O	0.19	0.18	1.33	0.67	0.12	0.06	0.02	0.4	0.44	0.1	0.62	1.2	0.23	2.39	0.95
P ₂ O ₅	0.06	0.13	0.42	0.12	0.04	0.12	0.1	0.25	0.09	0.11	0.1	0.22	0.29	0.32	0.16
MnO	0.21	0.23	0.09	0.18	0.16	0.24	0.19	0.17	0.24	0.19	0.2	0.18	0.31	0.13	0.12
LOI	2.35	2.52	3.33	2.2	1.86	0.01	4.51	2.09	1.51	3.19	7.87	1.91	0.27	5.54	0.97
Total_hydro	101.33	101.52	100.16	101.4	101.27	101.07	101.15	100.83	101.49	100.36	96.5	100.74	101.51	101.82	91.57
Trace Elements (ppm)															
Ni	63.14	96.91	47.5	32.25	623.7	43.94	1333.16	253.7	64.52	909.07	185.43	34.97	3.02	82.13	35.05
Cr	35.19	100.42	54.77	123.75	1547.41	30.7	1726.29	640.71	581.63	2235.9	909.85	151.62	8.9	272.66	67.61
Co	59.88	67.85	22.25	32.4	53.75	55.09	119.67	59.03	49.21	101.07	58.83	35.33	24.55	27.56	22.61
V	330.42	462.12	185.96	311.5	154.11	443.61	187.18	195.78	276.97	259.32	454.84	236.46	2.13	177.4	123.51
Sc	58.18	54.8	12.22	36.98	50.54	50.24	23.05	34.39	90.34	36.09	56.38	33.96	30.48	28.07	17.05
Cu	171.09	146.45	106.52	108.74	27.18	63.72	66.03	125.14	43.29	82.79	123.46	92.81	6.25	49.8	30.78
Zn	97.56	144.89	72.68	86.77	52.1	122.82	316.26	180.4	70.09	82.22	106.25	90.35	176.81	73.09	83.11
Mo	0.17	0.28	0.31	0.4	0.2	0.49	0.54	0.49	0.14	0.17	0.26	0.45	0.6	1.13	0.56
Li	7.73	9.32	9.03	6.68	2.88	7.31	1.15	22.04	0.44	4.75	18.92	14.26	4.24	17.12	9.54
Ba	30.07	73.92	570.42	305.26	51.8	16.43	19.02	262.54	194.29	17.62	40.98	391.82	49.02	725.55	649.51
Cs	0.16	0.21	0.2	0.59	0.06	0.31	0.09	5.65	0.27	0.11	4.72	0.8	0.14	4.76	0.27
Rb	3.67	2.27	30.5	16.61	2.32	1.96	0.51	13.37	7.54	1	25.36	32.5	3.32	84.37	24.74
Sr	212.35	84.3	780.53	226.49	78.71	97.45	17.89	270.35	225.15	65.57	168.42	438.05	99.98	566.23	429.68
Pb	0.57	0.62	4.19	1.98	0.81	0.39	1.19	2.16	2.64	0.79	1.3	2.3	3.48	6.83	4.44
Ga	17.59	18.84	22.94	19.82	7.54	23	9.38	13.63	10.14	12.91	17.9	15.97	25.28	17.23	17.44
Zr	27.96	61.41	195.8	80.16	38.95	25.98	68.64	82.85	20.06	66.78	62.6	65.71	130.65	144.99	103.52
Hf	1.02	2.1	4.31	2.17	1.04	1.06	1.65	1.93	0.73	1.95	1.96	1.75	3.75	3.49	2.58
Nb	0.82	5.03	11.99	4.4	1.86	2.91	6.53	6.88	1.29	6.73	7.81	3.57	3.45	5.76	5.02
Ta	0.13	0.36	0.65	0.28	0.15	0.22	0.41	0.38	0.12	0.44	0.51	0.25	0.22	0.42	0.31
Th	0.16	0.48	5.47	0.98	0.48	0.12	0.8	1.15	0.56	0.65	0.61	0.96	0.49	3.34	2.15
U	0.05	0.13	1.57	0.28	0.12	0.04	0.22	0.39	0.34	0.16	0.15	0.38	0.16	1.08	0.8
Y	21.13	32.21	22.93	27.21	10.69	36.9	13.58	19.2	14.92	13.26	18.76	19.52	84.68	22.61	16.9
La	1.51	5.48	44.3	6.91	5.54	3.11	7.89	13.46	5.24	6.95	7.45	8.68	5.74	19.66	13.6
Ce	3.6	12.33	91.41	17.03	9.9	9.68	17.95	34.12	9.32	14.46	15.92	20	17.4	40.27	30.98
Pr	0.68	2.15	11.39	2.4	1.61	1.76	2.93	4.6	1.7	2.24	2.65	2.62	3.08	4.81	3.77
Nd	4.17	11.24	44.58	11.18	7.09	10.1	13.36	19.38	8.32	10.8	13.26	11.65	17.68	19.37	15.08

Sm	1.74	3.52	7.78	3.15	1.74	3.64	3.29	3.93	2.4	2.85	3.79	2.84	6.69	4.11	3.09
Eu	0.69	1.25	2.26	1.16	0.6	1.37	1.12	1.29	0.71	0.75	1.3	1.03	2.38	1.37	1.09
Gd	2.58	4.75	8.53	4.12	2.21	5.21	3.53	4.08	2.77	2.95	4.26	3.74	10.22	4.88	3.58
Tb	0.54	0.86	0.85	0.67	0.31	0.89	0.54	0.63	0.45	0.46	0.66	0.51	1.86	0.61	0.46
Dy	3.76	5.82	4.19	4.88	1.97	6.22	2.86	3.59	2.71	2.71	4.06	3.39	14.2	3.7	2.98
Ho	0.84	1.27	0.76	0.99	0.39	1.26	0.56	0.74	0.57	0.54	0.79	0.69	3.02	0.75	0.58
Er	2.49	3.71	2.2	2.86	1.06	3.77	1.54	2.15	1.66	1.46	2.06	2.05	9.03	2.37	1.68
Tm	0.39	0.55	0.29	0.45	0.15	0.56	0.23	0.31	0.25	0.21	0.27	0.3	1.36	0.36	0.25
Yb	2.49	3.57	1.81	2.72	0.91	3.46	1.3	1.95	1.53	1.25	1.74	2.02	8.65	2.3	1.62
Lu	0.38	0.52	0.25	0.43	0.13	0.5	0.21	0.3	0.24	0.18	0.24	0.31	1.34	0.34	0.25
Ti	5207.55	11963.13	7042.25	7400.51	2574.97	10046.4	6082.91	6453.09	3412.15	7654.59	13052.17	4547	8856.27	4252.58	3315.57
Be	0.1	0.3	1117.46	549.34	193.86	351.59	1.39	0.99	0.4	0.56	0.64	625.19	607.77	1141.46	711.11
Ag	0.02	0.04	90.25	37.02	18.62	14.8			0.01	0.04	0.04	33.03	49.9	65.82	42.12
Cd	0.07	0.09	131.91	65.16	42.87	50.54			0.05	0.07	0.09	65.36	112.91	108.47	75.45
Sn	0.3	0.36					0.4	0.35	0.4	1.57	0.45				
Sb	0.09	0.31	133.81	152.08	214.5	77.15	0.2	0.17	1.07	0.39	1.6	59.91	150.76	270	80.89
W			331.7	338.99	196.79	112.07	0.35	0.15	0.11	0.02	0.13	171.77	224.2	519.37	252.43
Tl			101.96	87.75	23.67	25.82	0.06	0.09	0.01	0.08	138.91	66.32	450.83	112.21	

Stratigraphic sequence	Lower Seq	Lower Seq	Upper Seq	Upper Seq	Lower Seq	Upper Seq									
Lithology	MG-BASALT	MG-BASALT	MG-BASALT	MG-BASALT	PX-PYRIC BASALT										
Eastern	488011	479149	493220	445747	492534	452209	417219	502196	477304	450966	450966	477203	527641		
Northing	1138058	1142288	1088577	1120062	1140459	1237567	1235591	1129684	1137607	1110888	1110888	1228672	1290311		
Sample ID	GS_070	GS_097B	GSA005	GSA028	GSA043	GS_019	GS_063	GS_083b	GS_089	GSA011	GSA012	GSA068	GSA087		
Major Element (wt. %)															
SiO ₂	46.71	46.47	44.87	49.48	49.13	49.51	53.86	50.07	48.9	45.36	45.61	54.42	55.2		
Al ₂ O ₃	24.29	22.74	12.18	14.27	14.11	14.23	13.79	9.99	13.85	12.24	12.86	11.86	12.74		
TiO ₂	0.42	0.46	0.84	0.92	0.92	1.33	1.1	0.61	1.21	0.79	0.79	0.72	0.65		
MgO	3.15	4.65	5.91	7.01	6.81	5.62	5.18	10.93	6.45	14.95	14.52	7.97	8.41		
Fe ₂ O ₃	1.19	1.29	2.19	2.34	2.55	2.39	1.88	2.05	2.72	2.36	2.28	2.15	1.67		
FeO	6.05	6.58	11.18	11.93	13.02	12.2	9.61	10.45	13.89	12.01	11.63	10.97	8.49		
CaO	12.22	13.21	10	10.86	7.99	9.06	7.51	9.18	8.29	7.29	7.06	9.16	7.39		
Na ₂ O	2.27	1.96	1.7	1.7	2.52	3.83	2.37	1.2	3.67	1.49	1.86	2.36	2.86		
K ₂ O	0.79	0.27	0.01	0.04	0.11	0.42	2.93	1.79	0.09	0.54	0.49	0.13	0.58		
P ₂ O ₅	0.04	0.04	0.07	0.08	0.07	0.13	0.29	0.15	0.13	0.08	0.07	0.18	0.16		
MnO	0.12	0.11	0.18	0.19	0.22	0.22	0.15	0.18	0.22	0.19	0.18	0.2	0.14		
LOI	3.37	3.01	11.94	2.56	3.39	2.11	1.65	3.5	2.12	3.94	4.13	1.14	2.4		
Total hydrous	100.59	100.78	101.06	101.38	100.85	101.06	100.33	100.09	101.54	101.23	101.48	101.26	100.69		
Trace Elements (ppm)															
Ni	73.59	106.21	66.88	111.23	119.72	50.2	53.33	106.15	65.23	432.49	223.37	39.04	241.06		
Cr	165.07	140.11	100.36	253.89	156.17	71.72			67.52	649.81	349.33	297.31	502.12		
Co	29.43	30.19	44.73	50.96	61.99	43.86	33.71	50.01	58.27	82.52	42.54	44.47	44.62		
V	149.9	140.49	255.02	321.28	343.58	320.85			313.88	172.82	71.08	255.71	169.78		
Sc	23.31	21.48	39.83	50.98	57.46	41.66	26.99	39.14	48.53	26.29	14.1	40.33	28.63		
Cu	60.9	70.01	122.44	149.39	174.94	80.84	148.02	92.73	100.72	130.2	73.13	138.76	54.85		
Zn	47.91	52.43	92.22	91.35	265.57	101.13	94.09	82.7	396.82	86.65	43.6	109.67	83.67		
Mo	2.78	0.15	0.17	0.21	0.14	0.45	0.66	0.33	0.18	0.11	0.15	0.52	0.31		
Li	24.78	9.77	18.27	4.89	12.34	12.77	9.56	36.68	9.51	15.92	8.4	6.57	13.82		
Ba	239.29	49.58	20.42	15.2	115.01	111.91	781.55	539.52	43.92	116.43	67.96	70.62	197.48		
Cs	1.23	0.19	0.02	0.05	0.08	0.53	1.69	0.75	0.13	1	0.45	0.1	0.32		
Rb	24.21	8.28	0.31	0.61	1.77	7.85	88.09	28.72	0.93	13.79	5.88	3.03	11.07		
Sr	179.49	121.36	33.43	150.72	144.17	199.98	430	483.95	50.85	149.95	109.4	310.73	201.65		
Pb	1.18	0.25	0.51	1.11	1.11	1.57	4.9	2.82	0.74	0.89	0.55	2.39	1.76		
Ga	17.76	15.86	14.78	16.98	16.18	17.06	15.04	10.5	16.03	13.22	7.08	13.38	15.13		
Zr	21.21	11.35	26.43	31.4	22.19	83.32	98.52	37.48	58.2	47.64	23.39	45.54	67.8		
Hf	0.58	0.34	0.79	0.98	0.99	2.18	2.55	1.05	1.56	1.44	0.74	1.29	1.65		

Nb	1.06	1.17	1.11	2.42	2.71	4.86	6.11	1.87	6.87	3.36	1.57	2.08	4.87
Ta	0.1	0.09	0.15	0.18	0.21	0.32	0.37	0.11	0.42	0.28	0.14	0.14	0.33
Th	0.1	0.1	0.2	0.27	0.38	0.51	1.76	0.54	0.93	0.34	0.16	0.72	0.9
U	0.07	0.03	0.04	0.07	0.1	0.16	0.62	0.25	0.28	0.11	0.05	0.36	0.32
Y	9.97	10.08	8.07	19.83	20.04	29.38	23.25	16.1	28.2	15.97	7.42	18.26	18.69
La	1.52	1.32	2.44	3.14	3.65	5.28	10.87	6.24	7.86	4.57	1.94	5.97	10.13
Ce	3.67	3.59	6.73	6.9	8.24	14.56	25.77	10.95	18.16	9.23	4.16	14.87	23.23
Pr	0.56	0.6	1.01	1.26	1.39	2.36	3.54	1.9	2.67	1.62	0.76	1.97	3.03
Nd	3.23	3.11	5.22	6.64	7.25	11.63	15.55	8.64	12.17	7.95	3.83	9.15	12.53
Sm	0.97	0.98	1.58	2.13	2.26	3.5	4.03	2.25	3.19	2.2	1.08	2.32	2.74
Eu	0.35	0.46	0.56	0.84	0.86	1.12	1.21	0.71	1.21	0.73	0.39	0.77	0.91
Gd	1.38	1.51	1.81	2.92	2.97	4.54	4.34	2.71	4.74	2.67	1.3	3.11	3.48
Tb	0.24	0.26	0.23	0.54	0.53	0.76	0.69	0.44	0.82	0.46	0.23	0.45	0.48
Dy	1.74	1.73	1.44	3.55	3.65	5.37	4.2	2.73	4.91	2.88	1.44	3.09	3.17
Ho	0.37	0.37	0.28	0.81	0.79	1.08	0.89	0.6	1.09	0.61	0.31	0.63	0.66
Er	1.16	1.15	0.91	2.39	2.3	3.07	2.54	1.7	3.27	1.75	0.88	1.92	1.93
Tm	0.15	0.17	0.14	0.36	0.36	0.45	0.38	0.26	0.51	0.26	0.14	0.28	0.28
Yb	1.1	1.12	1	2.32	2.24	2.86	2.45	1.64	3.13	1.65	0.82	1.85	1.85
Lu	0.15	0.16	0.17	0.34	0.33	0.44	0.36	0.25	0.49	0.25	0.13	0.29	0.28
Ti	2729.79	2648.1	2643.01	6172.43	6225.34	7681.43	6753.79	3612.42	6609.7	5337.63	2749.78	4049.4	3874.31
Be	0.38	0.18	137.44	0.31	0.22	528.41	1.34	0.5	0.84	0.26	0.08	783.65	448.71
Ag	0.03		23.81	0.02	0.02	36.51				0.03	0.02	28.44	32.48
Cd	0.05		41.76	0.07	0.06	70.6	0.09	0.07		0.07	0.04	51.64	63.67
Sn	0.63	0.77		0.43	0.39		1.19	0.56	0.33	0.39	0.71		
Sb	0.11	0.22	182.02	1	0.35	2952.9	0.05	6.52	0.25	0.07	0.04	103.58	181.26
W	0.2	0.18	379.86	0.49	0.29	639.62	0.35	0.35	0.6			154.22	119.98
Tl	0.15	0.05	45.78			56.52	0.41	0.2	0.08	0.06	0.01	49.16	101.69

Table A- 11 Formulae for calculating chemical weathering vertices after Ohta and Arai (2007)

STEP 1
M=
$-0.395 \times \ln(\text{SiO}_2) + 0.206 \times \ln(\text{TiO}_2) - 0.316 \times \ln(\text{Al}_2\text{O}_3) + 0.160 \times \ln(\text{Fe}_2\text{O}_3) + 0.246 \times \ln(\text{MgO}) + 0.368 \times \ln(\text{CaO}) + 0.073 \times \ln(\text{Na}_2\text{O}) - 0.342 \times \ln(\text{K}_2\text{O}) + 2.266$
F=
$0.191 \times \ln(\text{SiO}_2) - 0.397 \times \ln(\text{TiO}_2) + 0.020 \times \ln(\text{Al}_2\text{O}_3) - 0.375 \times \ln(\text{Fe}_2\text{O}_3) - 0.243 \times \ln(\text{MgO}) + 0.079 \times \ln(\text{CaO}) + 0.392 \times \ln(\text{Na}_2\text{O}) + 0.333 \times \ln(\text{K}_2\text{O}) - 0.892$
W=
$0.203 \times \ln(\text{SiO}_2) + 0.191 \times \ln(\text{TiO}_2) + 0.296 \times \ln(\text{Al}_2\text{O}_3) + 0.215 \times \ln(\text{Fe}_2\text{O}_3) - 0.002 \times \ln(\text{MgO}) - 0.448 \times \ln(\text{CaO}) - 0.464 \times \ln(\text{Na}_2\text{O}) + 0.008 \times \ln(\text{K}_2\text{O}) - 1.374$
STEP 2
Closure operation a: C100 [exp(M), exp(F), exp(W)]

Table A- 12 Results of Chemical weathering calculations. Where F=felsic, M=mafic and W=weathered.

Sample ID	Lower Sequence			Sample ID	M	F	W
	M	F	W				
GS_005	95.99	0.66	3.35	GSA021	94.70	0.73	4.57
GS_006	90.57	2.52	6.91	GSA022	92.86	1.41	5.73
GS_007	93.80	1.57	4.63	GSA023	94.61	1.05	4.34
GS_008	91.37	2.14	6.49	GSA025	92.32	1.66	6.02
GS_009	93.90	1.13	4.97	GSA026	94.35	1.69	3.96
GS_010	95.34	0.79	3.87	GSA028	96.06	0.65	3.29
GS_011	93.49	1.61	4.90	GSA029	90.89	2.11	7.00
GS_012	91.75	0.64	7.61	GSA039	92.12	1.70	6.18
GS_013	93.19	1.46	5.35	GSA040A	93.84	1.33	4.84
GS_014	86.56	5.06	8.39	GSA043	93.74	1.49	4.76
GS_016	90.09	3.79	6.13	GSA044	85.39	0.51	14.10
GS_017	94.70	0.97	4.33	GSA047	91.42	2.35	6.23
GS_019	90.80	3.62	5.58	GSA053	83.33	5.99	10.68
GS_020	95.03	0.75	4.22	GSA057	90.65	3.53	5.82
GS_021	89.08	3.63	7.28	GSA059	91.42	2.87	5.71
GS_022	96.75	0.51	2.74	GSA060	90.29	3.54	6.17
GS_023	89.51	4.06	6.43	GSA061	91.83	2.92	5.25
GS_025	90.37	3.02	6.61	GSA063	92.64	2.24	5.11
GS_028	94.47	1.50	4.03	GSA065	92.01	1.94	6.05
GS_029	87.45	3.87	8.68	GSA067	92.63	1.69	5.68
GS_031	95.41	1.20	3.39	GSA069	91.69	2.11	6.20
GS_032	89.33	2.93	7.74	GSA070	93.99	1.62	4.39
GS_033	87.91	2.58	9.51	GSA071	93.22	1.83	4.95
GS_034	91.89	1.95	6.16	GSA074	93.90	1.64	4.45
GS_040	92.59	1.94	5.46	GSA075	94.22	1.61	4.17
GS_043	93.51	1.86	4.63	GSA076	88.06	5.03	6.91
GS_044	93.99	1.61	4.40	GSA077	91.51	2.41	6.08
GS_070	75.06	15.90	9.04	GSA079	93.04	1.49	5.47
GS_071	93.19	2.16	4.65	GSA080	96.84	0.37	2.79
GS_073	94.83	1.10	4.07	GSA081	93.42	1.06	5.52
GS_075	91.71	2.16	6.13				
GS_076	92.77	1.33	5.91				
GS_077	87.72	3.42	8.86				
GS_078	96.07	0.97	2.96				
GS_085a	90.32	3.45	6.23				
GS_085b	96.45	0.64	2.92				
GS_086	97.16	0.44	2.40				
GS_094	94.06	1.04	4.90				
GS_095A	93.99	1.05	4.96				
GS_096	89.55	4.38	6.07				
GS_097a	93.77	2.08	4.15				
GS_097B	87.48	6.11	6.41				
GSA001	92.75	2.09	5.16				
GSA003	93.91	1.40	4.70				
GSA004	95.64	0.43	3.93				
GSA005	97.75	0.28	1.97				
GSA019	87.12	4.38	8.50				

Table A-12 continued

Sample ID	Upper Sequence			Sample ID	Intrusive lithofacies		
	M	F	W		M	F	W
GS_050	94.24	1.14	4.62	GS_001	87.08	4.95	7.97
GS_051	94.27	1.36	4.37	GS_003	96.38	1.09	2.53
GS_062	86.58	6.35	7.07	GS_026a	96.68	0.43	2.90
GS_063	72.72	13.42	13.86	GS_030	70.85	18.24	10.91
GS_068	88.23	3.75	8.02	GS_037	37.33	51.10	11.57
GS_069	91.55	2.68	5.76	GS_041	93.64	1.79	4.56
GS_079	56.54	24.11	19.36	GS_042	93.66	0.06	6.28
GS_081	81.21	10.96	7.83	GS_048	83.76	7.28	8.96
GS_082a	86.17	7.02	6.80	GS_052	91.86	2.27	5.87
GS_082b	81.33	9.19	9.49	GS_088	94.70	1.36	3.94
GS_083a	89.15	4.80	6.05	GS_093	93.56	1.33	5.11
GS_083b	82.53	6.75	10.72	GS_112	61.19	20.35	18.46
GS_084	81.76	8.79	9.44	GSA008	89.30	3.65	7.05
GS_089	95.20	1.23	3.57	GSA018	92.73	2.65	4.61
GS_098	88.66	3.77	7.56	GSA041B	86.86	5.41	7.72
GS_099	89.69	3.36	6.94	GSA042	78.46	9.73	11.82
GSA006	89.25	4.23	6.52	GSA052	95.20	0.37	4.44
GSA007	88.68	4.19	7.13	GSA054	91.48	1.88	6.64
GSA010	84.71	5.34	9.95	GSA055	91.62	1.70	6.69
GSA011	89.31	2.57	8.12	GSA056	93.09	1.79	5.12
GSA012	89.77	2.75	7.48	GSA058	77.12	13.20	9.68
GSA014	88.16	4.79	7.05	GSA062	71.59	17.18	11.23
GSA015	91.62	2.79	5.59	GSA064	88.08	5.01	6.91
GSA017	89.24	3.08	7.68	GSA072	82.07	8.11	9.82
GSA033	95.59	0.96	3.45	GSA073	86.48	4.05	9.47
GSA035	94.83	1.44	3.72	GSA082	92.90	1.02	6.08
GSA037	79.67	10.35	9.98	GSA086	91.98	2.15	5.87
GSA066	77.86	12.22	9.92				
GSA068	93.86	1.86	4.28				
GSA078	79.12	9.96	10.92				
GSA083	72.70	15.71	11.59				
GSA085	95.66	0.91	3.43				
GSA087	86.18	6.50	7.32				

Table A- 13 Slope defined by each major and trace element concentration of selected altered and unaltered rock for the lower and upper stratigraphic sequences for each belt. Calculations were performed using a Microsoft Excel spreadsheet by López-Moro (2012).

Element	Values of slopes			
	Houndé Lower Sequence	Houndé Upper Sequence	Boromo Lower Sequence	Boromo Upper Sequence
	Slope	Slope	Slope	Slope
Al ₂ O ₃	1.01	0.94	1.02	1.00
Ba	5.37	1.07	0.54	2.42
CaO	1.06	0.99	0.95	1.00
Ce	1.04	0.97	0.94	0.94
Co	1.10	0.94	1.01	1.10
Cr	1.79	0.90		
Cs	27.44	0.56	4.16	1.47
Cu	0.46	9.94	0.93	1.36
Dy	1.00	0.95	1.01	1.01
Er	1.02	0.97	1.04	0.98
Eu	1.25	0.99	0.90	0.98
Fe ₂ O ₃	1.17	1.10	1.05	0.95
Ga	1.21	0.94	0.94	0.94
Gd	1.01	0.97	0.96	0.98
Hf	0.92	1.16	0.99	1.05
Ho	0.99	0.95	1.02	1.02
K ₂ O	8.53	1.07	2.25	4.42
La	1.04	0.95	0.91	0.93
Li	1.02	0.76	6.37	0.99
Lu	1.16	0.93	1.09	1.02
MgO	1.08	1.31	0.92	1.14
MnO	1.29	1.13	1.07	1.03
Mo	0.65	0.23	0.73	0.84
Na ₂ O	0.69	0.80	0.92	0.84
Nb	1.01	0.91	0.94	0.95
Nd	1.06	0.95	0.93	0.92
Ni	1.33	0.94	0.75	1.11
P ₂ O ₅	1.90	0.94	1.11	0.93
Pb	2.02	0.83	0.13	0.75
Pr	1.02	0.96	0.93	0.91
Rb	28.50	2.29	3.98	4.61
Sc	1.09	0.94	0.94	1.02
SiO ₂	0.93	0.97	0.99	1.00
Sm	1.01	0.97	0.92	0.96
Sr	1.01	0.86	0.59	0.58
Ta	0.92	0.87	0.95	1.15
Tb	0.99	0.94	0.97	0.97
Th	1.04	0.89	0.86	0.96
Ti	1.20	0.94	0.96	0.99
TiO ₂	1.23	0.94	1.06	1.02
Tm	1.00	0.96	1.06	0.92
U	1.19	0.97	1.57	1.03
V	1.13	0.93		
Y	1.02	0.97	1.01	0.93
Yb	1.07	0.93	1.07	0.98
Zn	1.23	0.97	0.98	0.82
Zr	1.03	1.17	1.01	1.02

K-means clustering analysis

K-means clustering algorithm in ioGAS 7.0 software was used to define the boundaries of the four types of rocks identified. K-means clustering is an unsupervised data classification method that reduces a dataset into K number of sub-groups. The objective of K-means clustering algorithm is to minimise variations within a sub-group, thereby maximising the variation between subgroups by computing the Euclidean distances within a cluster away from a centroid. The appropriate K-number of clusters/sub-groups within a population can be assessed by computing the total sum of squares (S.S) of distances. The difference between the total sum of squares (Delta) helps predict the effective K-number. For this study, La/Sm and Gd/Yb were the selected variables. Four clusters were achieved from the algorithm and correspond well with the observed distinct Chondrite-normalised REE patterns.

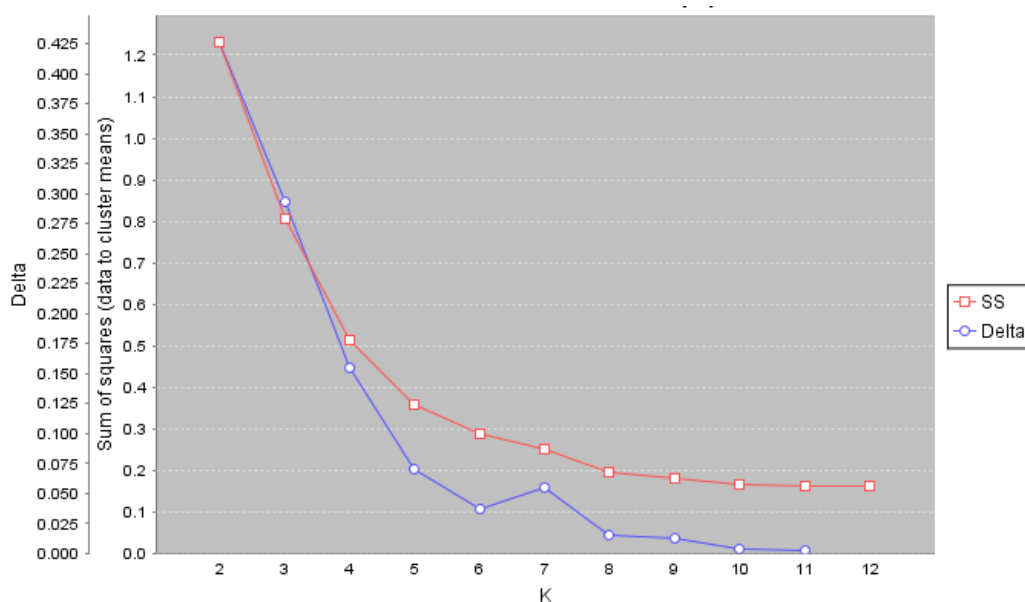


Figure A- 1 A graph of the sum of squares (S.S) and Delta against the number of potential clusters (K-numbers). The most considerable variation of S.S and Delta values is achieved at 4 clusters; thus defining the four groups recognised for the volcanic and intrusive rocks of the Houndé and Boromo greenstone belts.

Table A- 14 Box and Whisker Tukey Outlier Report for Magnesium numbers

	Group 1	Group 2	Group 3	Group 4
Lower volcanic sequence				
Group size	n=17	n=16	n=42	n=0
Min whisker	35	33	30	
Median	45	47	43	
Max whisker	51	57	54	
Mean	43	47	42	
Upper volcanic sequence				
Group size	n=2	n=0	n=9	n=21
Min whisker	50		41	32
Median	52		50	48
Max whisker	55		60	65
Mean	52		53	50
Gabbro and Dolerite				
Group size	n=4	n=2	n=5	n=11
Min whisker	37	44	46	44
Median	46	45	46	61
Max whisker	50	46	70	79
Mean	45	45	52	61

Table A- 15 Results of Fractional crystallisation modelling-Liquid line of descent and crystal-Melt proportion.

Lower sequence - Group 1 Model 3													Crystal-Melt proportion						
Index	T (°C)	SiO ₂	TiO ₂	Al ₂ O ₃	Fe ₂ O ₃	FeO	MnO	MgO	CaO	Na ₂ O	K ₂ O	P ₂ O ₅	H ₂ O	Cpx	Plag	Spinel	Olivine	Melt	
1	1185	47.13	0.82	13.74	2.48	14.89	0.26	8.18	8.91	2.50	0.02	0.06	1.00				100		
2	1175	47.20	0.83	13.85	2.50	14.86	0.26	7.92	8.98	2.52	0.02	0.06	1.01				0.79	99	
3	1165	47.29	0.83	14.00	2.51	14.80	0.26	7.59	9.07	2.54	0.02	0.06	1.02				1.03	98	
4	1155	47.38	0.84	14.14	2.52	14.74	0.26	7.26	9.16	2.57	0.02	0.06	1.03				1.01	97	
5	1145	47.48	0.85	14.29	2.54	14.67	0.26	6.95	9.25	2.60	0.02	0.06	1.04				0.99	96	
6	1135	47.59	0.88	14.19	2.58	14.81	0.26	6.63	9.27	2.63	0.02	0.07	1.07		1.49		1.30	93	
7	1125	47.74	0.93	13.63	2.69	15.35	0.26	6.32	9.16	2.69	0.02	0.07	1.14		3.99		1.79	88	
8	1115	47.88	0.99	13.09	2.79	15.85	0.27	6.02	9.06	2.74	0.02	0.07	1.21		3.51		1.63	82	
9	1105	48.03	1.05	12.56	2.89	16.32	0.27	5.73	8.97	2.79	0.03	0.08	1.28		3.12		1.49	78	
10	1095	48.11	1.11	12.22	2.98	16.84	0.28	5.39	8.73	2.87	0.03	0.08	1.37		1.23	2.40		1.03	73
11	1085	48.16	1.16	11.96	3.06	17.37	0.29	5.04	8.42	2.96	0.03	0.09	1.45		1.66	1.96		0.80	69
12	1075	48.86	1.08	11.87	3.07	17.28	0.31	4.60	8.09	3.13	0.03	0.10	1.59		2.51	1.75		0.94	63
13	1065	50.56	0.82	11.96	2.97	16.14	0.35	4.04	7.77	3.44	0.04	0.11	1.80		3.81	1.67		2.12	56
14	1055	52.10	0.63	11.95	2.87	15.11	0.39	3.57	7.48	3.72	0.04	0.12	2.01		2.78	1.48		1.54	50
15	1045	53.53	0.48	11.88	2.78	14.16	0.43	3.17	7.21	3.98	0.04	0.13	2.21		2.09	1.32		1.16	45
16	1035	54.87	0.37	11.74	2.69	13.27	0.47	2.82	6.95	4.22	0.05	0.15	2.40		1.63	1.18		0.91	42
17	1025	56.14	0.28	11.57	2.59	12.44	0.51	2.52	6.71	4.43	0.05	0.16	2.59		1.29	1.07		0.74	39

Table A-15 continued

Index	T (°C)	Lower sequence - Group 2 Model 1												Crystal-Melt proportion			
		SiO ₂	TiO ₂	Al ₂ O ₃	Fe ₂ O ₃	FeO	MnO	MgO	CaO	Na ₂ O	K ₂ O	P ₂ O ₅	Cpx	Plag	Spinel	Olivine	Melt
1	1217	50.41	0.90	14.78	2.09	11.45	0.20	7.58	8.57	3.46	0.47	0.08					100
2	1207	50.51	0.91	14.92	2.10	11.39	0.20	7.27	8.65	3.49	0.47	0.08				0.92	99
3	1197	50.62	0.92	15.06	2.11	11.33	0.20	6.95	8.73	3.53	0.48	0.08				0.93	98
4	1187	50.80	0.96	14.78	2.18	11.61	0.20	6.60	8.70	3.58	0.50	0.09			3.17	1.62	93
5	1177	51.05	1.06	13.94	2.32	12.32	0.20	6.24	8.57	3.65	0.55	0.09			6.53	2.26	85
6	1167	50.86	1.21	13.23	2.51	13.30	0.23	5.78	8.33	3.82	0.62	0.11	4.51	6.18			74
7	1157	50.63	1.36	12.61	2.70	14.29	0.27	5.33	8.03	3.98	0.69	0.12	3.88	4.75			65
8	1147	50.39	1.51	12.09	2.87	15.30	0.30	4.89	7.62	4.15	0.76	0.14	3.33	3.61			58
9	1137	50.12	1.65	11.58	3.03	16.28	0.33	4.50	7.24	4.29	0.83	0.15	2.65	2.97			53
10	1127	49.82	1.80	11.06	3.19	17.24	0.36	4.14	6.90	4.41	0.90	0.17	2.16	2.51			48
11	1117	49.49	1.94	10.55	3.35	18.20	0.39	3.82	6.59	4.52	0.96	0.18	1.79	2.15			44
12	1107	51.34	1.57	10.41	3.33	17.38	0.47	3.14	6.04	4.99	1.12	0.22	3.05	2.19	1.79		37

Table A-15 continued

Lower sequence – Group 3 Model 1													Crystal-Melt proportion		
Index	T (°C)	SiO ₂	TiO ₂	Al ₂ O ₃	Fe ₂ O ₃	FeO	MnO	MgO	CaO	Na ₂ O	K ₂ O	P ₂ O ₅	Cpx	Plag	Melt
1	1198	50.40	0.99	13.82	2.15	11.00	0.19	7.09	11.52	2.39	0.35	0.11	0.11	5.52	100
2	1188	50.35	1.12	13.47	2.29	12.06	0.22	6.76	10.68	2.53	0.40	0.13	7.24	4.57	87
3	1178	50.26	1.25	13.12	2.43	13.12	0.25	6.40	9.93	2.65	0.45	0.14	5.84	4.57	77
4	1168	50.11	1.40	12.71	2.58	14.19	0.28	5.98	9.32	2.77	0.50	0.16	4.94	4.13	68
5	1158	49.88	1.58	12.13	2.75	15.29	0.32	5.44	8.99	2.87	0.57	0.19	4.28	4.15	59
6	1148	49.64	1.76	11.60	2.91	16.34	0.36	4.97	8.64	2.95	0.63	0.21	3.26	3.12	53
7	1138	49.37	1.94	11.07	3.06	17.35	0.40	4.54	8.33	3.02	0.69	0.23	2.62	2.55	48
8	1128	49.09	2.11	10.56	3.20	18.33	0.44	4.15	8.05	3.07	0.74	0.25	2.15	2.13	43
9	1118	48.79	2.29	10.06	3.34	19.29	0.48	3.79	7.79	3.10	0.80	0.28	1.81	1.81	40

Lower sequence – Group 3 Model 2													Crystal-Melt proportion		
Index	T (°C)	SiO ₂	TiO ₂	Al ₂ O ₃	Fe ₂ O ₃	FeO	MnO	MgO	CaO	Na ₂ O	K ₂ O	P ₂ O ₅	Cpx	Plag	Melt
1	1266	50.39	1.00	13.94	2.02	11.15	0.19	6.99	11.45	2.41	0.35	0.11	0.98		99
2	1256	50.36	1.05	14.50	2.04	11.39	0.20	6.40	11.02	2.55	0.38	0.12	5.85		93
3	1246	50.35	1.09	15.04	2.05	11.61	0.22	5.85	10.59	2.68	0.40	0.13	5.15		88
4	1236	50.37	1.14	15.55	2.06	11.81	0.23	5.33	10.17	2.81	0.42	0.13	4.57		83
5	1226	50.36	1.25	15.32	2.16	12.64	0.25	4.97	9.51	2.92	0.47	0.15	4.80	4.08	75
6	1216	50.28	1.40	14.90	2.28	13.63	0.29	4.60	8.92	3.02	0.52	0.17	4.19	4.49	66
7	1206	50.12	1.58	14.31	2.42	14.64	0.33	4.17	8.57	3.09	0.58	0.19	3.52	4.48	58
8	1196	49.93	1.76	13.72	2.56	15.63	0.37	3.77	8.26	3.15	0.64	0.21	2.77	3.60	52
9	1186	49.71	1.94	13.15	2.69	16.59	0.41	3.40	7.98	3.18	0.71	0.24	2.24	2.94	46
10	1176	49.47	2.13	12.59	2.82	17.52	0.45	3.07	7.73	3.20	0.77	0.26	1.85	2.45	42
11	1166	49.20	2.32	12.04	2.94	18.43	0.49	2.76	7.50	3.21	0.82	0.29	1.57	2.07	38

Table A-15 continued

Index	T (°C)	Upper sequence – Group 3 Model 4												Crystal-Melt proportion			
		SiO ₂	TiO ₂	Al ₂ O ₃	Fe ₂ O ₃	FeO	MnO	MgO	CaO	Na ₂ O	K ₂ O	P ₂ O ₅	H ₂ O	Cpx	Plag	Spinel	Melt
1	1185	52.26	1.07	16.69	1.69	9.40	0.15	4.94	9.34	2.98	0.34	0.12	1.01	0.81			99
2	1175	52.40	1.11	16.91	1.70	9.54	0.16	4.58	8.96	3.09	0.36	0.13	1.06	3.81	1.27		94
3	1165	52.58	1.19	16.70	1.76	9.85	0.17	4.26	8.61	3.19	0.39	0.14	1.15	3.40	3.74		87
4	1155	52.77	1.28	16.45	1.81	10.14	0.18	3.94	8.33	3.29	0.41	0.15	1.24	2.94	3.54		80
5	1145	52.95	1.36	16.21	1.86	10.40	0.20	3.63	8.06	3.39	0.44	0.16	1.34	2.54	3.07		75
6	1135	53.14	1.44	15.96	1.91	10.65	0.21	3.34	7.80	3.48	0.47	0.17	1.43	2.21	2.69		70
7	1125	53.32	1.52	15.72	1.96	10.88	0.23	3.07	7.55	3.56	0.50	0.18	1.52	1.95	2.38		66
8	1115	53.50	1.60	15.48	2.00	11.08	0.24	2.81	7.30	3.64	0.53	0.19	1.62	1.74	2.11		62
9	1105	53.68	1.68	15.25	2.05	11.27	0.25	2.56	7.06	3.72	0.56	0.20	1.71	1.56	1.89		58
10	1095	54.92	1.52	15.04	1.97	10.60	0.28	2.30	6.80	3.87	0.61	0.22	1.87	1.62	2.25	1.03	54
11	1085	56.17	1.37	14.80	1.89	9.90	0.30	2.06	6.57	4.01	0.66	0.24	2.03	1.30	2.04	0.91	49
12	1075	57.33	1.23	14.54	1.81	9.27	0.32	1.86	6.35	4.13	0.71	0.26	2.19	1.04	1.81	0.73	46
13	1065	58.43	1.11	14.26	1.73	8.68	0.35	1.68	6.15	4.23	0.75	0.28	2.34	0.84	1.63	0.60	43
14	1055	59.46	1.01	13.97	1.66	8.14	0.37	1.52	5.96	4.32	0.80	0.30	2.49	0.69	1.47	0.49	40

Table A-15 continued

Index	T (°C)	Upper sequence – Group 4 Model 4												Crystal-Melt proportion			
		SiO ₂	TiO ₂	Al ₂ O ₃	Fe ₂ O ₃	FeO	MnO	MgO	CaO	Na ₂ O	K ₂ O	P ₂ O ₅	H ₂ O	Cpx	Plag	Spinel	Melt
1	1196	46.76	1.08	14.46	2.44	14.76	0.21	6.45	10.11	2.52	0.07	0.15	1.00				100
2	1186	46.65	1.11	14.79	2.46	15.01	0.22	6.10	9.79	2.61	0.07	0.15	1.04	3.97			96
3	1176	46.55	1.13	15.17	2.48	15.29	0.23	5.71	9.41	2.72	0.08	0.16	1.09	4.30			92
4	1166	46.47	1.16	15.53	2.49	15.54	0.24	5.32	9.04	2.82	0.08	0.17	1.14	3.99			88
5	1156	46.38	1.19	15.71	2.52	15.90	0.25	5.01	8.65	2.93	0.08	0.18	1.20	3.54	0.75		83
6	1146	46.18	1.27	15.49	2.61	16.52	0.27	4.73	8.34	3.04	0.09	0.19	1.29	3.10	2.71		78
7	1136	45.98	1.34	15.24	2.69	17.12	0.29	4.44	8.07	3.15	0.09	0.21	1.38	2.79	2.49		72
8	1126	46.63	1.28	15.13	2.70	16.92	0.32	4.03	7.79	3.35	0.10	0.23	1.52	3.39	2.03	1.27	66
9	1116	48.06	1.11	15.10	2.63	15.95	0.36	3.57	7.51	3.64	0.12	0.25	1.71	3.41	1.86	2.09	58
10	1106	49.41	0.95	15.02	2.56	15.03	0.40	3.17	7.25	3.91	0.13	0.28	1.90	2.56	1.78	1.62	53
11	1096	50.67	0.81	14.88	2.49	14.18	0.44	2.84	7.00	4.16	0.14	0.31	2.09	1.95	1.66	1.26	48
12	1086	51.84	0.69	14.70	2.42	13.39	0.48	2.54	6.77	4.39	0.15	0.34	2.29	1.52	1.53	1.00	44
13	1076	52.95	0.59	14.47	2.35	12.65	0.52	2.29	6.56	4.61	0.17	0.37	2.48	1.20	1.41	0.81	40

Appendix C: Chapter 5

Table A- 16 Selected samples for Zircon separation in attempted Zircon crystallisation age dating.
Zircon separation was carried out by Geotrack International Pty Ltd Australia.

Sample ID	Lithology	Zr (ppm)	Method	Zircon Yield
GS_054	Monomictic Breccia	50.36	pXRF	Zero
GS_080	Polymictic Breccia	54.86	pXRF	Zero
GSA041B	Dolerite	30.15	pXRF	Ten
GSA083	Hornblende-Feldspar Porphyritic Andesite	195.8	ICPMS	Few



Figure A- 2 Photographs of samples used in zircon separation. Note: Samples GSA041B and GSA083 were heated to 1050 °C to anneal zircons

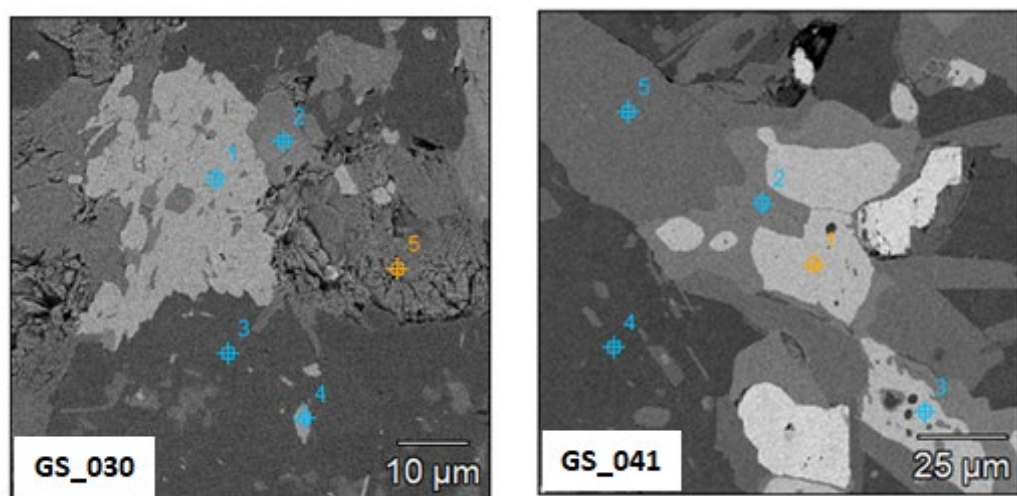


Figure A- 3 BSE images of samples Gs_030 and Gs_041 showing the targeted spot of major element analysis using the SEM. Note this analysis was carried out without standard reference material.

Table A- 17 Results of major elements SEM quantification for GS_030 and GS_041

GS_030					
Element (wt.%)	Point 1	Point 2	Point 3	Point 4	Point 5
O	41.33	41.24	44.86	49.55	44.54
Al	0.81	6.26	9.85	1.23	9.55
Si	14.82	20.2	13.74	2.91	13.87
Ca	19.88	7.77		42.29	
Ti	23.17	1.54			0.16
Fe		14.58	18.95		18.84
Mn					
Mg		8.42	12.61		12.66
F				4.02	
GS_041					
Element (wt.%)	Point 1	Point 2	Point 3	Point 4	Point 5
O	27.8	41.11	29.48	49.18	44.29
Al		0.72		16.15	4.39
Si	0.15	14.63	0.2	25.6	16.73
Ca		19.81	0.28	9.08	12.45
Ti	31.58	23.73	31.33		10.34
Fe	38.24		37.16		9.29
Mn	2.11		1.55		
Mg	0.11			2.51	

Note: This analysis was standardless

Table A- 18 U-Pb in-situ LA-ICPMS titanite data of standard reference materials (SRM) in analytical session for Gs_030 and Gs_041.

Analysis number	Radiogenic Ratios										Apparent Ages (Ma)	
	$^{207}\text{Pb}/^{235}\text{U}$	$\pm 2\delta$	$^{206}\text{Pb}/^{238}\text{U}$	$\pm 2\delta$	Error Correlation	$^{238}\text{U}/^{206}\text{Pb}$	$\pm 2\delta$	$^{207}\text{Pb}/^{206}\text{Pb}$	$\pm 2\delta$	Error Correlation	$^{206}\text{Pb}/^{238}\text{U}$	$\pm 2\delta$
G_NIST610_1	33	0.45	0.2568	0.0036	0.25873	3.894081	0.05458992	0.927	0.016	0.59511	1473	18
G_NIST610_2	32.91	0.47	0.2513	0.0034	0.14775	3.979308	0.05383862	0.942	0.017	0.62178	1445	17
G_NIST610_3	32.86	0.54	0.2538	0.0035	0.16469	3.94011	0.05433564	0.931	0.018	0.57322	1458	18
G_NIST610_4	32.49	0.58	0.2533	0.0033	0.31674	3.947888	0.0514332	0.921	0.016	0.3745	1455	17
G_NIST610_5	33.08	0.56	0.2555	0.0036	0.45932	3.913894	0.05514685	0.928	0.016	0.40714	1466	19
G_NIST610_6	33.3	0.57	0.2539	0.0041	0.469	3.938558	0.0636002	0.943	0.017	0.47666	1458	21
G_NIST610_7	32.94	0.53	0.2561	0.0035	0.41594	3.904725	0.05336406	0.924	0.015	0.38989	1470	18
G_NIST610_8	32.77	0.44	0.2594	0.0038	0.29446	3.85505	0.05647336	0.908	0.015	0.61566	1486	20
G_NIST610_9	32.82	0.47	0.2592	0.0042	0.28875	3.858025	0.06251429	0.914	0.017	0.63748	1485	22
G_NIST610_10	32.66	0.59	0.2622	0.0042	0.41641	3.813883	0.06109194	0.895	0.016	0.41666	1500	21
G_NIST610_11	33.38	0.47	0.2616	0.0032	0.48309	3.82263	0.04676	0.914	0.012	0.41618	1497	16
G_NIST610_12	33.52	0.54	0.2668	0.004	0.20359	3.748126	0.05619379	0.903	0.018	0.57184	1524	20
G_NIST610_13	33.28	0.51	0.2647	0.0042	0.34338	3.777862	0.0599434	0.904	0.016	0.52795	1513	21
G_NIST610_14	33.3	0.55	0.2684	0.004	0.48857	3.725782	0.05552582	0.894	0.014	0.38216	1532	20
G_NIST610_15	33.93	0.49	0.2652	0.0047	0.38515	3.770739	0.06682682	0.923	0.017	0.60434	1516	24
G_NIST610_16	33.34	0.56	0.2705	0.0046	0.61421	3.696858	0.06286708	0.885	0.015	0.4599	1543	23
G_NIST610_17	33.87	0.52	0.2666	0.0038	0.4965	3.750938	0.05346423	0.912	0.013	0.40463	1523	19
G_NIST610_18	33.2	0.64	0.2684	0.0041	0.31956	3.725782	0.05691396	0.885	0.017	0.3756	1532	21

G_NIST610_19	34.15	0.54	0.2743	0.0048	0.43616	3.645643	0.06379544	0.895	0.016	0.59448	1562	24
G_NIST610_20	33.8	0.6	0.2685	0.0048	0.36828	3.724395	0.06658136	0.909	0.017	0.559	1532	25
G_NIST610_21	33.5	0.48	0.2685	0.0047	0.37748	3.724395	0.06519425	0.901	0.017	0.61666	1533	24
G_NIST610_22	33.93	0.47	0.2716	0.0034	0.23054	3.681885	0.04609135	0.897	0.015	0.58537	1549	17
G_NIST610_23	33.81	0.55	0.2719	0.0047	0.5487	3.677823	0.06357399	0.893	0.015	0.54112	1550	24
T_OLT1_1	2.15	0.13	0.1668	0.0042	0.27856	5.995204	0.1509584	0.0923	0.0051	0.15573	998	24
T_OLT1_2	2.032	0.093	0.1673	0.004	0.053178	5.977286	0.1429118	0.0888	0.0047	0.45201	997	22
T_OLT1_3	1.99	0.11	0.1694	0.0038	-0.048658	5.903188	0.132421	0.0843	0.0049	0.4382	1008	21
T_OLT1_4	2.037	0.092	0.166	0.0038	0.14165	6.024096	0.137901	0.0885	0.0042	0.35003	990	21
T_OLT1_5	1.999	0.096	0.1713	0.0041	0.25845	5.837712	0.1397234	0.0841	0.0039	0.26863	1018	23
T_OLT1_6	2.043	0.096	0.1688	0.0041	-0.055928	5.924171	0.1438928	0.0877	0.0048	0.2594	1005	23
T_OLT1_7	4.53	0.24	0.1973	0.0051	0.44474	5.068424	0.1310135	0.1669	0.0089	0.060862	1165	29
T_OLT1_8	2.04	0.13	0.1719	0.0049	0.065769	5.817336	0.1658228	0.0852	0.0054	0.17573	1022	27
T_OLT1_9	2.41	0.13	0.1784	0.0045	0.072266	5.605381	0.1413913	0.0969	0.0054	0.35955	1057	25
T_OLT1_10	2.07	0.1	0.1787	0.0041	0.45194	5.595971	0.1283911	0.0829	0.0037	0.022623	1059	22
T_OLT1_11	1.98	0.11	0.1808	0.0047	0.1761	5.530973	0.1437808	0.0791	0.0044	0.20962	1070	25
T_OLT1_12	2.09	0.1	0.1781	0.0045	0.10296	5.614823	0.1418681	0.0837	0.0041	0.42991	1056	25
T_OLT1_13	2.062	0.089	0.1825	0.0047	0.067603	5.479452	0.1411147	0.0825	0.0041	0.46354	1079	25
T_OLT1_14	2.03	0.13	0.1747	0.0047	0.40271	5.724098	0.1539969	0.0841	0.0043	-0.063728	1037	26
T_OLT1_15	2.1	0.11	0.1786	0.0039	0.23165	5.599104	0.1222649	0.0845	0.0047	0.19755	1059	22
T_OLT1_16	2.02	0.096	0.173	0.0037	0.097705	5.780347	0.1236259	0.0842	0.0042	0.33414	1028	20
T_OLT1_17	2.07	0.1	0.1738	0.0039	-0.10097	5.75374	0.1291115	0.0856	0.0046	0.21098	1033	21

T_OLT1_18	2.14	0.11	0.1811	0.0039	-0.038079	5.521811	0.1189126	0.0854	0.0049	0.37873	1072	21
T_OLT1_19	2.05	0.096	0.1818	0.0042	0.16095	5.50055	0.1270754	0.0814	0.0041	0.37777	1076	23
T_OLT1_20	2.041	0.081	0.1778	0.0038	0.25253	5.624297	0.1202043	0.0829	0.0035	0.32577	1054	21
T_OLT1_21	2.03	0.12	0.1734	0.0047	0.22655	5.767013	0.1563146	0.0835	0.0049	0.31981	1030	26
T_OLT1_22	2.05	0.1	0.1796	0.0037	0.16294	5.567929	0.1147068	0.0818	0.004	0.28928	1064	20
T_OLT1_23	2.069	0.087	0.1787	0.0037	0.25053	5.595971	0.1158651	0.0829	0.0035	0.30972	1059	20
T_TBC_1	1.637	0.088	0.1633	0.0033	0.14523	6.123699	0.123749	0.0731	0.0041	0.21902	975	18
T_TBC_2	1.67	0.11	0.1646	0.0038	0.091414	6.075334	0.1402568	0.0733	0.0049	0.2606	981	21
T_TBC_3	1.653	0.075	0.1645	0.0034	0.03562	6.079027	0.1256456	0.0733	0.0037	0.39179	981	19
T_TBC_4	1.651	0.08	0.1621	0.0038	0.19437	6.169031	0.1446164	0.0734	0.0037	0.18873	968	21
T_TBC_5	1.65	0.077	0.1637	0.0032	0.18772	6.108735	0.1194133	0.0725	0.0034	0.21559	977	18
T_TBC_6	1.671	0.061	0.1658	0.0036	-0.015515	6.031363	0.1309584	0.0733	0.0034	0.54063	988	20
T_TBC_7	1.698	0.083	0.1674	0.0041	0.11179	5.973716	0.1463096	0.0733	0.0038	0.38764	997	23
T_TBC_8	1.759	0.094	0.1718	0.004	0.04356	5.820722	0.1355232	0.0732	0.0039	0.379	1021	22
T_TBC_9	1.72	0.082	0.171	0.0042	0.20756	5.847953	0.1436339	0.0724	0.0035	0.25259	1017	23
T_TBC_10	1.718	0.073	0.1692	0.0038	0.13181	5.910165	0.1327342	0.0733	0.0034	0.41647	1007	21
T_TBC_11	1.78	0.1	0.1737	0.0037	0.11183	5.757052	0.1226315	0.0738	0.0042	0.21328	1032	20
T_TBC_12	1.732	0.083	0.173	0.0033	0.027941	5.780347	0.110261	0.0731	0.004	0.34941	1028	18
T_TBC_13	1.77	0.099	0.1747	0.0042	0.11141	5.724098	0.1376143	0.0743	0.0047	0.28461	1037	23
T_TBC_14	1.77	0.1	0.176	0.0038	0.31091	5.681818	0.1226756	0.0729	0.0043	0.048477	1045	21
T_TBC_15	1.788	0.09	0.1764	0.0037	0.024428	5.668934	0.1189062	0.0732	0.004	0.40288	1047	20

T_TBC_16	1.789	0.091	0.1744	0.0042	0.26242	5.733945	0.1380881	0.0735	0.0039	0.25971	1036	23
T_TBC_17	1.787	0.091	0.1758	0.0044	0.26168	5.688282	0.1423688	0.0733	0.0038	0.20879	1043	24
T_TBC_18	1.809	0.096	0.1775	0.0043	0.33252	5.633803	0.1364809	0.0733	0.0037	0.16659	1052	24
T_TBC_19	1.795	0.093	0.1767	0.0043	0.13946	5.65931	0.1377195	0.0724	0.0038	0.37428	1048	23
T_TBC_20	1.771	0.084	0.1751	0.0042	0.093777	5.711022	0.1369863	0.0728	0.0037	0.38158	1039	23
T_TBC_21	1.801	0.097	0.1763	0.0046	0.18364	5.67215	0.1479971	0.0731	0.0041	0.35651	1046	25
YILT_2_1	13.18	0.36	0.497	0.012	0.47116	2.012072	0.04858123	0.1906	0.0052	0.46429	2596	53
YILT_2_3	15.2	0.67	0.507	0.016	0.37936	1.972387	0.06224494	0.2149	0.0088	0.37601	2637	69
YILT_2_4	14.13	0.53	0.507	0.014	0.37372	1.972387	0.05446432	0.2001	0.0077	0.38662	2651	62
YILT_2_5	14.17	0.5	0.507	0.015	0.40165	1.972387	0.05835463	0.2034	0.0075	0.32334	2640	62
YILT_2_6	13.97	0.39	0.527	0.012	0.46922	1.897533	0.04320759	0.1899	0.0045	0.35023	2724	49
YILT_2_7	14.13	0.38	0.522	0.011	0.43707	1.915709	0.04036934	0.1936	0.0048	0.35689	2706	47
YILT_2_8	14.1	0.43	0.529	0.014	0.45644	1.890359	0.05002841	0.192	0.0057	0.36174	2734	57
YILT_2_9	14.89	0.53	0.516	0.013	0.24218	1.937984	0.04882519	0.2079	0.0085	0.42214	2677	57
YILT_2_10	14.2	0.6	0.518	0.014	0.31808	1.930502	0.05217573	0.1967	0.0084	0.30369	2688	58
YILT_2_11	13.93	0.43	0.537	0.014	0.55543	1.862197	0.04854891	0.1868	0.0052	0.35161	2766	60
YILT_2_12	14.09	0.46	0.53	0.013	0.61026	1.886792	0.04627981	0.1911	0.005	0.22788	2736	56
YILT_2_13	14.41	0.45	0.544	0.013	0.39862	1.838235	0.04392842	0.1901	0.006	0.41963	2794	54
YILT_2_14	15.17	0.59	0.552	0.016	0.31592	1.811594	0.05250998	0.202	0.0086	0.40598	2827	66
YILT_2_15	13.46	0.38	0.515	0.011	0.4129	1.941748	0.04147422	0.1883	0.0054	0.42288	2677	48
YILT_2_16	14.01	0.34	0.55	0.013	0.47156	1.818182	0.04297521	0.1843	0.0047	0.50381	2822	55
YILT_2_17	13.41	0.42	0.524	0.015	0.57346	1.908397	0.05462968	0.1825	0.0049	0.41344	2711	61

YILT_2_18	15.08	0.62	0.54	0.016	0.303	1.851852	0.05486968	0.2017	0.0087	0.39369	2778	65
YILT_2_19	14.94	0.63	0.543	0.018	0.38943	1.841621	0.0610482	0.1968	0.0078	0.45029	2790	74
YILT_2_20	13.79	0.48	0.531	0.013	0.58123	1.883239	0.04610567	0.1857	0.0052	0.239	2740	56
YILT_2_21	13.71	0.41	0.535	0.013	0.62316	1.869159	0.04541881	0.1831	0.0043	0.2976	2759	55
YILT_2_22	14.91	0.68	0.548	0.018	0.31675	1.824818	0.05993926	0.1988	0.0094	0.34981	2808	77
YILT_2_23	14.87	0.52	0.534	0.015	0.48254	1.872659	0.05260279	0.2007	0.0064	0.35091	2752	60

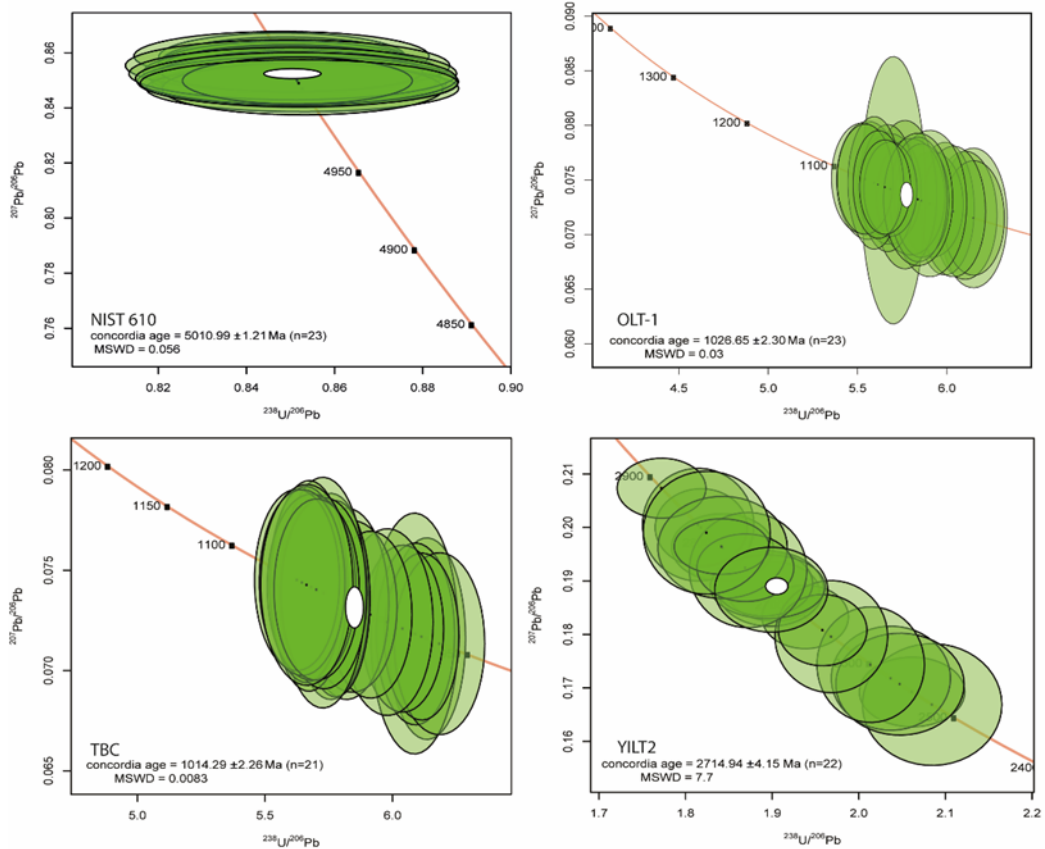


Figure A- 4 Terra-Wasserberg Concordia plots for reference materials. Error ellipses are at the 2-sigma level. Plots and age calculations achieved using IsoplotR free online geochronology plugin designed by Vermeesch (2018).